EFFECTS OF DYNAMIC SURFACE WETTABILITY ON POOL BOILING BEHAVIOR

by

Taylor P. Allred

A Dissertation

Submitted to the Faculty of Purdue University

In Partial Fulfillment of the Requirements for the degree of

Doctor of Philosophy

School of Mechanical Engineering

West Lafayette, Indiana

December 2019

THE PURDUE UNIVERSITY GRADUATE SCHOOL
STATEMENT OF COMMITTEE APPROVAL

Dr. Suresh V. Garimella, Co-Chair
School of Mechanical Engineering
Dr. Justin A. Weibel, Co-Chair
School of Mechanical Engineering
Dr. Amy M. Marconnet
School of Mechanical Engineering
Dr. Sangtae Kim
Davidson School of Chemical Engineering
Dr. Partha Mukherjee
School of Mechanical Engineering

Approved by:

Dr. Nicole Key
Head of the Graduate Program

TABLE OF CONTENTS

LIST OF TABLES

LIST OF FIGURES

ABSTRACT

Wettability has been shown to play a critical role in the pool boiling behavior of a surface. In this thesis, the effects of surface wettability on boiling behavior are further examined, with a particular focus on understanding the role of dynamic surface wettability (*i.e.* receding contact angle, advancing contact angle, and contact angle hysteresis). Hydrophobic and superhydrophobic surfaces are shown to have favorable boiling performance if the receding contact angle of the surface is sufficiently low, contrary to previous reports that found them to be ineffective boiling surfaces when considering only the static contact angle. To explain this behavior, the roles of both the receding and advancing contact angles during boiling are clarified. Additionally, the effect of different dynamic wetting behaviors on heat transfer mechanisms during single bubble growth are established in order to develop a comprehensive, mechanistic understanding of the role of wettability during boiling.

The critical importance of dynamic surface wettability is first demonstrated through studying boiling from superhydrophobic surfaces. These surfaces have stark differences in boiling behavior depending on the initial wetting state of the surface, which determines the effective dynamic wettability. Superhydrophobic surfaces are fabricated on metal test blocks and evaluated in a controlled pool boiling environment. Two degassing procedures are utilized to achieve one of two different initial wetting states prior to the start of a pool boiling experiment. The low-hysteresis Cassie-Baxter state leads to film boiling as a result of vapor spreading readily over the surface. The high-hysteresis Wenzel state leads to efficient nucleate boiling, never before seen on a superhydrophobic surface.

Biphilic surfaces, with alternating superhydrophobic and hydrophilic stripes, are investigated to control and enhance pool boiling hydrodynamics. Surfaces are fabricated such that half of the surface area on each surface is superhydrophobic but stripe widths differ across surfaces. Superhydrophobic regions are brought into the Wenzel state prior to boiling to prevent premature film boiling. Boiling occurs preferentially on the superhydrophobic regions, demonstrating control over the location of vapor generation by the surface patterning. Both the critical heat flux and heat transfer coefficient are shown to increase as the stripe size decreases, indicating performance enhancement due to changes in the hydrodynamic ordering during boiling. Ultimately, a uniform

superhydrophobic surface in the Wenzel state provides better performance than any of the patterned surfaces.

The boiling behavior of hydrophobic surfaces is further investigated to elucidate the surface properties responsible for vapor spreading and premature onset of film boiling. Smooth and textured hydrophobic surfaces with high and low contact angle hysteresis are studied. The results show that the receding contact angle dominates bubble growth dynamics, rather than the static contact angle which is typically considered. These bubble dynamics, in turn, indicate whether premature critical heat flux will occur. Hydrophobic surfaces with low receding contact angles are shown to decrease surface temperatures compared with hydrophilic surfaces while reaching similar critical heat fluxes. The boiling behavior of parahydrophobic surfaces, those with high static contact angle as well as high contact angle hysteresis, is investigated for the first time, revealing untapped potential for these surfaces to minimize surface temperatures during boiling.

Numerical simulations of single bubble dynamics are performed to explore the role of receding and advancing contact angle in determining the bubble morphology during growth. The findings show that the receding contact angle governs the bubble shape during the early stages of growth and is the dominant factor in determining the maximum base diameter and departure diameter of the bubble. The advancing contact angle governs the bubble shape during the departure process and determines the departure mechanism. Three new wettability regimes are classified in the context of boiling based upon the dynamic contact angles. Hygrophilic surfaces are redefined as those with receding and advancing contact angles less than 90 deg. Hygrophobic surfaces are redefined as those with receding and advancing contact angles greater than 90 deg. Ambiphilic surfaces are defined as those with receding contact angles less than 90 deg and advancing contact angles greater than 90 deg. Each of these wettability regimes has unique and identifiable bubble characteristics. A new correlation is developed for the departure diameter that incorporates the dynamic contact angles and significantly improves the predictive accuracy compared with conventional approaches based on the static contact angle.

Following, heat transfer and phase change are incorporated into the simulation to evaluate the influence of dynamic wetting behavior on the prevalent heat transfer mechanisms during bubble growth. The three regimes of wettability are demonstrated to exhibit notably different heat transfer behavior during bubble growth. Hygrophilic surfaces are shown to have the most effective heat transfer on a per bubble basis due to extremely high microlayer heat transfer during the early

stages of bubble growth. Ambiphilic surfaces have less effective heat transfer on a per bubble basis but have more favorable nucleation characteristics than hygrophilic surfaces. Hygrophobic surfaces are shown to be ineffective due to a large amount of vapor spreading and the absence of microlayer formation. Dynamic contact angle design targets for the development of enhanced hygrophilic and ambiphilic surfaces are proposed.

Taken together, this work demonstrates the role and importance of dynamic wetting behavior during boiling. Experimental investigations were used to demonstrate the importance of dynamic wetting behavior and the promise of surfaces with tailored dynamic wetting characteristics. Numerical studies were used to probe further into the mechanistic understanding regarding how dynamic wetting behavior influences bubble dynamics and heat transfer during boiling. These advances pave the way for improved prediction of bubble dynamics and development of enhanced surfaces with tailored dynamic wetting characteristics.

1. INTRODUCTION

1.1 Background

Boiling is a critical process in staple industries such as power generation and water distillation and has emerged as the primary choice when extremely high heat fluxes need to be dissipated from high-power electronic systems and nuclear reactors due to extremely efficient heat transfer during phase change. While boiling has been implemented in practical systems for decades, a lack of understanding of several fundamental aspects and key phenomenological limits has prevented the rational design of enhanced surfaces for use in industry. In particular, a key limiting phenomenon that constrains system operation is the critical heat flux, a catastrophic point of failure at which the surface is blanketed completely by vapor and the efficiency of heat transport is severely throttled. As result of the difficulty in accurately predicting surface temperatures and critical heat flux during boiling, fundamental investigations on boiling behavior and mechanisms remain widespread and important.

While initial theories to predict critical heat flux were based purely on hydrodynamic considerations [1], it has become apparent through numerous studies that surface characteristics play an important role [2,3]. Surface modifications such as area enhancement (*e.g.*, fins), porous coatings, and re-entrant cavities have a significant impact on the critical heat flux and heat transfer coefficient of a surface. More recently, surface wettability modifications have gained notoriety for their impact on boiling behavior. Hydrophilic surfaces (static contact angle less than 90 deg) are generally preferred due to their ability to rewet [4–7], delaying critical heat flux and maintaining efficient nucleate boiling; however, hydrophobic surfaces (static contact angle greater than 90 deg) generally have better heat transfer performance in the nucleate boiling regime [8,9]. This comes with the caveat that vapor spreading has been commonly observed on hydrophobic surfaces, resulting in premature critical heat flux [5,10–14]. Due to the necessity of avoiding critical heat flux in boiling applications, hydrophobic surfaces have been largely dismissed and have not been subject of the detailed investigations that hydrophilic surfaces have.

Additionally, the existing framework for understanding the effects of wettability on boiling behavior is built around static contact angle characterization. Dynamic wettability characterization, including receding and advancing contact angles, is not typically considered. Boiling is a very

dynamic process. Thus, constraining the interpretation of the complex interfacial interactions that occur during boiling to the static contact angle of the surface is limiting, especially considering that the static contact angle can take any angle between the advancing and receding contact angles, depending on the history of the droplet used for static contact angle characterization. By considering the dynamic wettability and investigating the behavior of surfaces with drastically different dynamic wetting characteristics, a more complete picture of the effect of wettability on boiling is possible, enabling rational design of enhanced boiling surfaces.

1.2 Objectives and Major Contributions

The overall goal of this work is the develop a framework for understanding the effects of dynamic surface wettability on boiling behavior. This is accomplished by 1) studying the effect of initial wetting state on the boiling behavior of superhydrophobic surfaces, 2) exploring the ability of surface wettability patterns to control and enhance pool boiling hydrodynamics, 3) experimentally examining the bubble dynamics on hydrophobic and parahydrophobic surfaces with differing dynamic contact angles, 4) numerically studying the individual roles of receding and advancing contact angle during adiabatic single bubble growth, and 5) numerically evaluating the effect of different dynamic wetting behavior on the heat transfer mechanisms during bubble growth.

Through studying the effect of the initial wetting state on the boiling behavior of superhydrophobic surfaces, the importance of the dynamic wettability in dictating the boiling behavior was demonstrated. The low-contact-angle-hysteresis Cassie-Baxter state promoted premature film boiling while the high-contact-angle-hysteresis Wenzel state promoted efficient film boiling up to high heat fluxes never before reached on a superhydrophobic surface, despite both wetting states exhibiting a high static contact angle. By evaluating surfaces with alternating superhydrophobic and hydrophilic stripes, we demonstrated the ability to control hydrodynamics during boiling. Boiling occurred preferentially on superhydrophobic surfaces, providing spatial control of vapor generation. The superhydrophobic and hydrophilic areas were maintained constant, but stripe widths were varied from test to test, showing that the heat transfer coefficient and critical heat flux increased as the stripe width decreased. In studying the boiling behavior of hydrophobic surfaces with differing dynamic wettability, including the first boiling study involving parahydrophobic surfaces with rose-like wettability, we demonstrated that the receding

contact angle plays a dominate role in bubble growth and indicates whether premature critical heat flux will occur. Hydrophobic and parahydrophobic surfaces were shown to exhibit exceptional boiling performance when the receding contact angle was minimized.

Numerical simulations were used to assess the role of dynamic wetting behavior on bubble dynamics and heat transfer mechanisms in ways that would be experimentally inviable. In the adiabatic simulations, a wide range of dynamic contact angles were evaluated to get a clear picture of the role of the advancing and receding contact angles during bubble growth. This led to the reclassification of wettability regimes and the development of new correlations for the maximum base diameter and the departure diameter based on the dynamic contact angles rather than static contact angles. The diabatic simulations investigated the effect of differing dynamic wetting behaviors on heat transfer during bubble growth. They showed that the heat transfer behavior in different wettability regimes is notably different and provided insight into the precise dynamics that are favorable for heat transfer.

1.3 Organization

This dissertation is divided into eight chapters. Chapter 1 introduces the background, motivation, and contributions of this work. Chapter 2 provides a literature review of pool boiling heat transfer mechanisms, critical heat flux, and surface wettability. Chapter 3 discusses a study on the effect of initial wetting state on the boiling behavior of superhydrophobic surfaces. Chapter 4 presents an investigation into the ability to control and enhance pool boiling hydrodynamics using surface wettability patterning. Chapter 5 includes details of a study on the role of dynamic wettability on boiling behavior of hydrophobic and parahydrophobic surfaces. Chapter 6 presents the numerical study of adiabatic bubble dynamics and the role of the dynamic contact angles during bubble growth. Chapter 7 discusses the study on the impact of dynamic wetting behavior on the heat transfer mechanisms via diabatic numerical simulations. Chapter 8 summarizes the key conclusions for the work and provides suggested pathways for future studies.

2. LITERATURE REVIEW

This chapter provides a detailed review of the literature pertinent to the work performed in this dissertation. The key areas discussed are pool boiling heat transfer, critical heat flux, surface wettability, and wettability effects on boiling.

2.1 Pool Boiling Heat Transfer

Boiling is central to heat exchange processes in staple industries such as power generation and water distillation and has emerged as the primary choice when extremely high heat fluxes need to be dissipated from high-power electronic systems and nucleate reactors. While boiling has been implemented in practical systems for decades, a lack of understanding of several fundamental aspects and key phenomenological limits has prevented the rational design of enhanced surfaces for use in industry. For this reason, boiling heat transfer remains an area of active research [3,15–17].

In heat transfer applications, boiling technologies are commonly characterized as either pool boiling, where boiling occurs from a surface in a stagnant pool, or flow boiling, where boiling occurs from a surface in the presence of a forced flow. Compared with single-phase technologies, boiling technologies benefit from increasing heat transfer coefficients as the heat flux is increased [18]. This enables high heat fluxes to be dissipated with minimal surface temperature rises. Flow boiling technologies are generally able to sustain higher heat fluxes, but come with added complexity and pumping requirements [18].

For the work in this dissertation, the focus will be on pool boiling. Pool boiling has two key regimes: nucleate boiling and film boiling [19]. With increasing heat flux, boiling begins in the nucleate regime at boiling incipience and transitions to film boiling at the critical heat flux. The nucleate boiling regime is characterized by bubbles growing and departing from isolated nucleation sites on the surface. This results in extremely effective heat transfer due to efficient heat transfer mechanisms that occur during bubble growth. In the nucleate boiling regime, high heat fluxes can be maintained with minimal increases in surface temperature. In film boiling, the surface becomes completely blanketed in vapor, limiting the ability of liquid to reach the surface. This vapor film is highly insulating. Thus, the surface temperature increases significantly with

increases in heat flux. Due to the drastic different in heat transfer efficacy between nucleate boiling and film boiling, critical heat flux is marked by a drastic surface temperature increase. For this reason, it is essential to remain in the nucleate boiling regime and avoid critical heat flux in practical applications.

2.1.1 Pool Boiling Heat Transfer Mechanisms

In an attempt to understand and enhance the heat transfer occurring during nucleate boiling, the heat transfer mechanisms present during the bubble ebullition cycle have been carefully studied. While natural convection and conduction are the primary forms of heat transfer in the absence of bubble ebullition, various heat transfer mechanisms have been proposed to explain the high heat transfer near the bubble during boiling [20–22]. Potential modes of heat transfer during bubble ebullition include: evaporation of the microlayer (a thin liquid layer underneath the growing bubble), evaporation of superheated liquid surrounding the bubble cap, evaporation at the three-phase contact line, microconvection heat transfer due to perturbation of the surrounding liquid during bubble growth, and transient conduction as subcooled liquid rewets the surface after bubble departure. Each of these mechanisms has been individually studied and shown to play an important role in the overall heat transfer, as discussed in the following paragraph. However, the overall contribution of each mechanism remains up for debate and no single theory has accurately incorporated each of them [21].

Early theories suggested that latent heat transfer was not sufficient and relied on improved sensible heat transfer mechanisms such as convective effects from liquid agitation as the bubble departs [23] or transient conduction as bubbles acted to pump cooler liquid close to the surface [24]. Mikic and Rohsenow [25] suggested that the dominant mode of heat transfer is transient conduction to the subcooled liquid that rewets the surface after bubble departure. Moore and Mesler [26] first suggested the presence of the microlayer, a thin liquid layer under the bubble, and proposed that it was responsible for the majority of evaporative heat transfer. Judd and Hwang [27] modeled this microlayer heat transfer and suggested it could be responsible for up to a third of the overall heat transfer during boiling. Utaka *et al.* [28] directly measured the microlayer thickness during boiling and found that the microlayer evaporation accounts for up to 44% of the total evaporation, depending on the specific conditions. Stephan and Hammer [29] modeled the micro-region near the three-phase contact line as well as the macro-region away from the contact

line and suggested that the micro-region near the three phase contact line played a dominate role in the heat transfer during bubble ebullition. Wayner *et al.* [30] posited that high heat fluxes are possible very close to the adsorbed layer (*i.e.* near the contact line). Wagner and Stephan [31] utilized infrared temperature measurements on the backside of a foil heater to obtain a temperature map of the heater during boiling. They determined that the area near the three-phase contact line was responsible for up to 50-60% of the overall heat transfer.

Some studies have sought to determine the specific contribution of each individual heat transfer mechanism through novel experimental methods. Moghaddam and Kiger [32] utilized local heat flux sensors to determine the heat transfer contribution due to the microlayer, transient conduction and microconvection separately. They concluded that the microlayer contributed between 16.3% and 28.8% of the overall heat transfer, transient conduction between 32.1% and 45.4%, and microconvection between 25.8% and 51.6%. Yabuki and Nakabeppu [33] utilized local MEMS sensors to obtain high frequency temperature measurements and found that the contribution of the microlayer increased after nucleation to a maximum contribution of nearly 60% midway through bubble growth, followed by a sharp decrease to 5-10% until departure.

2.1.2 Bubble Ebullition Characteristics

Because the heat transfer mechanisms discussed in Chapter 2.1.1 are dependent on the stage of the bubble ebullition cycles, bubble ebullition characteristics such as departure diameter, active nucleation site density, waiting time, growth time, and departure frequency are critically important. The bubble ebullition cycle consists of nucleation, bubble growth, bubble departure, and waiting time until the next bubble nucleates. The bubble departure diameter is a key characteristic that indicates the size at which a bubble departs from the surface. Fritz [34] developed one of the first and most widely used correlations for bubble departure diameter by considering a static force balance between buoyant and surface tension forces. While the Fritz correlation provides a reasonable estimate, it has been shown to deviate significantly from observations in various situations, particularly in high pressure systems [20]. Since then, many correlations have been developed for bubble departure diameter [35]; however, they commonly rely on many of the same parameters such as the densities of the liquid and vapor, surface tension, surface wettability, gravitational constant, and the Jakob number, with differences to accommodate specific situations or data sets. No single correlation is universally applicable.

The active bubble nucleation site density on a surface is known to generally increase as the heat flux is increased [20]. The active nucleation site density has also been shown to correlate with the cavity size and distribution on the surface [25,36]. Wang and Dhir [37] demonstrated that the active nucleate site density increased as the contact angle of the surface increased. Hibiki and Ishii [38] developed a model for the nucleation site density that accounts for the role of critical cavity size and contact angle. Applying correlations for the nucleation site density is difficult due to the required knowledge of the cavity sizes and distributions across the surfaces. Even when these are accounted for, the ability to accurately predict the nucleation site density is still lacking [35].

The bubble waiting period is the time between bubble departure and inception of a new bubble at the nucleation site. Han and Griffith [39] showed that the waiting period was influenced by the bulk liquid temperature and the wall superheat. As the liquid temperature and wall superheat increase, the waiting time decreases. Surface wettability has also been shown to play a role, as some hydrophobic surfaces have been observed to exhibit no waiting period at all [8,40]. The bubble growth period is the other portion of the bubble ebullition cycle, the time when a bubble a present on the surface and growing. The bubble growth period has been shown to correlate with the bubble departure diameter, the Jakob number, the thermal diffusivity of the liquid, and the cavity size [35,41]. Together, the waiting period and the growth period provide the overall bubble departure frequency. Mohanty and Das [35] compared many correlations that have been developed to predict the bubble departure frequency and found heavy reliance on knowledge of the bubble departure diameter, bubble waiting period, bubble growth period, surface tension, heat flux, and thermophysical properties of the fluids, making a priori predictions very difficult.

2.1.3 Numerical Modeling of Bubble Ebullition

As computational capabilities have progressed, numerical simulations have become a key tool for probing the physical understanding of bubble ebullition and heat transfer mechanisms that occur during the boiling process. While some alternatives exist, the majority of numerical studies on boiling utilize level set or volume of fluid (VOF) methods [42]. One of the first numerical simulations was performed by Lee and Nydahl [43] assuming a simplistic hemispherical geometry for the bubble. They accounted for the microlayer heat transfer and found the microlayer responsible for 87% of the overall heat transfer. Welch [44] developed an interface tracking

method to more accurately model the bubble shape and fluid flow during bubble ebullition. Son *et al.* [45] developed a level-set technique to model the complete bubble ebullition cycle for a single nucleation site and showed reasonable agreement with experimental bubble dynamics; successive studies within the same group advanced this technique and utilized it to probe more complex boiling situations. Son *et al.* [46] added vertical merging of bubbles departing from a single nucleation site. Wu *et al.* [47] coupled the level set method with a moving mesh method to more accurately model the interfacial heat transfer. Son and Dhir [48] simulated higher heat fluxes with multiple nucleation sites. The model was able to predict the formation of vapor columns and mushroom-like bubbles at higher heat fluxes as observed in experiments. They concluded that the improvement in the heat transfer coefficient with increased heat fluxes results from higher nucleation site densities and decreased waiting times. Aktinol and Dhir [49] incorporated the thermal response of the heater wall, as opposed to assuming a constant wall superheat. They found that the heat transfer was highest near the contact line and lowest under the center of the bubble where it had dried out. Significant temperature fluctuations were observed on the wall near the three-phase contact line.

Kunkelmann and Stephan [50] developed a VOF model incorporating the micro-region heat transfer model developed by Stephan and Busse [51] to accurately model the heat transfer near the contact line which is not appropriately resolved by the numerical grid. Additionally, they modeled the wall temperature profile and showed promising, although limited, agreement with experiments. The same authors later improved the temporal and spatial resolution of the model to resolve transient phenomena during bubble ebullition [52]. Building on these key advances, additional numerical studies have been performed concerning nucleate boiling to probe the influence of factors such as surface wettability [9,40,53,54], surface structure [55–58], among others [59,60].

2.2 Critical Heat Flux

It is vital to avoid critical heat flux in applications, due to the rapid temperature excursion that occurs. Accordingly, significant research effort has been focused on understanding the mechanistic cause of critical heat flux in an effort to predict at what heat flux it will occur and develop means to avoid it. The early, and still widely used, theory proposed by Zuber [1] proposed that critical heat flux occurs as a result of hydrodynamic instabilities that develop at high heat

fluxes. In this theory, vapor columns rise from nucleation sites while liquid moves toward the surface to rewet. Vapor columns are spaced according to the Rayleigh-Taylor wavelength. When a critical relative velocity between the liquid and vapor is reached at the liquid-vapor interface, Helmholtz instabilities develop resulting in disruption of the interface and vapor blanketing of the surface. Importantly, critical heat flux predictions based upon this theory rely purely on fluid properties and are unaffected by the characteristics of the surface. It has since been clearly demonstrated that the surface characteristics play an important role in the occurrence of critical heat flux [3], which cannot be captured by Zuber's model. Additionally, while this theory reasonably predicts critical heat flux for a number of studies, the specific hydrodynamic mechanisms suggested remain unproven during boiling. Modifications to Zuber's model have been made in an attempt to expand its applicability such as adjustments for different surface geometries and sizes [61,62], electric fields and contact angle [63], and nucleation site density [64].

Other critical heat flux theories have emerged based on a variety of mechanisms [17]. Haramura and Katto [65] proposed a hydrodynamics model in which critical heat flux is caused by dryout of the macrolayer, a thin liquid layer on the surface with vapor stems that feed rise vapor bubbles, within the hovering time of a large vapor bubble. Nikolayev *et al.* [66–68] and Kandlikar [69] suggested that the vapor recoil force, or evaporative momentum force, at the three-phase contact line leads to vapor spreading and critical heat flux at high evaporative fluxes. Theofanous *et al.* [70] and Yagov [71] pointed to the growth of dry spots on the surface as the triggering mechanism for critical heat flux. Many authors have recently attributed critical heat flux to the inability of the surface to rewet rapidly enough at high heat fluxes [6,7,72]. While all these mechanisms, and more, have been proposed, Zuber's hydrodynamic theory remains the predominant model.

2.3 Surface Wettability

Engineered surface wettability has become a key consideration in areas such as self-cleaning surfaces [73], drag reduction [74,75], condensation [76–78], and boiling [6,8–10]. Surface wettability is commonly characterized by the contact angle. The contact angle is defined as the angle between the liquid-vapor interface and the solid-liquid interface at the three-phase contact line for a droplet viewed from the side. On an ideal, smooth surface, the contact angle is defined as the equilibrium contact angle given by Young's equation [79], $\gamma_{lv}\cos\theta_E = \gamma_{sv} - \gamma_{sl}$,

where γ_{lv} is the liquid-vapor interfacial tension, γ_{sv} is the solid-vapor interfacial tension, γ_{sl} is the solid-liquid interfacial tension, and θ_E is the equilibrium contact angle. However, for real surfaces, there are three common contact angles that are considered: static contact angle, advancing contact angle, and receding contact angle.

The static contact angle is the simplest to measure and most commonly used to characterize surface wettability. The static contact angle is determined by first depositing a small droplet (small enough such that surface tension effects dominate gravitational effects) gently on the surface. The droplet is then imaged from the side and the contact angle is measured from the image. The advancing and receding contact angle are referred to as dynamic contact angles, as they are measured while the contact line is moving. These angles are commonly measured in two ways. Using the first method, after a droplet is placed on the surface, the surface is tilted until the droplet rolls off. The advancing contact angle is taken as the contact angle at the leading edge of the droplet just after it begins to roll off the surface. The receding contact angle is taken as the contact angle at the trailing edge of the droplet just after it begins to roll off the surface. In the second method, a small syringe tip is inserted into the droplet. Volume is gradually added to the droplet until the contact line begins to move and a steady advancing contact angle is observed. Then, volume is gradually removed from the droplet until the contact line begins to move and a steady receding contact angle is observed. The difference between the advancing contact angle and the receding contact angle is known as the contact angle hysteresis. For real surfaces, the static contact angle can take any angle between the advancing and receding contact angles depending on the droplet history. Therefore, it should not be considered equivalent to the equilibrium contact angle and does not accurately describe the intrinsic wettability of the surface, particularly in cases of high contact angle hysteresis.

The wettability of a surface is governed by two key factors: the intrinsic wettability of the material and the surface texture [80]. The intrinsic wettability of a material is defined based upon the equilibrium contact angle of a material system and is practically approximated based on a static contact angle measurement of a smooth surface. Considering water as the liquid, a surface is considered hydrophilic if the static contact angle is less than 90 deg and hydrophobic if the static contact angle is greater than 90 deg. Examples of common hydrophilic materials include glass, most metals, and silicon while common hydrophobic materials include polymers and waxes.

By texturing surfaces, the wettability can become more extreme. For intrinsically hydrophilic materials, roughening the surface generally decreases the contact angle, making the surface more wettable. The liquid fully wets the surface texture, a wetting condition known as the Wenzel state, and the contact angle can be described by the Wenzel relation [81–83],

$$\cos\theta_W = r\cos\theta \tag{2.1}$$

where θ_W is the apparent contact angle in the Wenzel state, r is the roughness ratio, and θ is the contact angle on a smooth surface of the same material. Based on this relation, the apparent contact angle generally decreases as the roughness ratio increases, assuming the contact angle of the smooth surface is less than 90 deg. If the roughness is high enough, hemiwicking, or simply "wicking", can occur, during which liquid spontaneously spreads over the surface. Bico *et al.* [84] derived a criterion for the occurrence of hemiwicking on textured hydrophilic surface,

$$\cos\theta_c = \frac{1-\phi_s}{r-\phi_s} \tag{2.2}$$

where θ_c is the critical contact angle, r is the roughness ratio, and ϕ_s is the solid fraction that remains dry during hemiwicking (*e.g.* the tops of micropillars with liquid wicking between them). If the contact angle of the material is less than the critical contact angle hemiwicking will occur. Surfaces upon which hemiwicking occurs are commonly called superhydrophilic. Because liquid spreads on superhydrophilic surfaces, resulting in a contact angle approaching 0 deg, further characterization is required to differentiate superhydrophilic surfaces. In our work, discussed in Appendix A, we developed a metric to describe the degree of superhydrophilicity of a surface by characterizing the volumetric rate at which liquid wicks into the surface texture [85].

Upon texturing hydrophobic materials, a variety of unique wetting behaviors are possible. While several wetting states have been proposed [86], the two most common are the Wenzel state [81,82], as described above and in equation (2.1), and the Cassie-Baxter state [87]. In the Wenzel state, the surface texture under a droplet is completely wetted and the apparent contact angle increases with the roughness ratio. In the Cassie-Baxter state [87], the droplet rests on top of the surface structures with a relatively small amount of solid-liquid interface, resulting in extremely high static contact angles (>150 deg) and droplets that readily slides off the surface with minimal contact angle hysteresis [88,89]. The contact angle in this state can be determined based on a specific form of the Cassie-Baxter model,

$$\cos\theta_{CB} = \phi_s\cos\theta + \phi_s - 1 \tag{2.3}$$

where θ_{CB} is the apparent contact angle in the Cassie-Baxter state, ϕ_s is the wetted fraction, and θ is the static contact angle on a smooth surface of the same material. Surfaces capable of sustaining a Cassie-Baxter wetting state are commonly called superhydrophobic. Due to their unique water-repellant properties that mimic those of the lotus leaf [90,91], superhydrophobic surfaces have been widely investigated for engineering applications [73,92–94]. However, the Cassie-Baxter state which instills these unique properties is commonly metastable, meaning that if sufficient force is exerted, the liquid penetrates the surface texture transitioning to the Wenzel state [95–97]. While the Cassie-Baxter and Wenzel states both promote high static contact angles on hydrophobic materials, they exhibit contrasting dynamic behavior [98–100]. As mentioned, surfaces in the Cassie-Baxter state have minimal contact angle hysteresis. Surfaces in the Wenzel have comparatively high contact angle hysteresis due to pinning on surface structures.

Parahydrophobic surfaces are an additional class of hydrophobic surfaces that have received less attention. Parahydrophobic surfaces exhibit high contact angles (>150 deg), but have very high contact angle hysteresis such that a droplet can stay adhered to the surface even when tilted at 90-180 deg [101]. This wetting behavior, commonly known as the "petal effect", has recently come to the attention of the scientific community due to it being observed on biological surfaces such as the rose petal [102,103] and the peanut leaf [104], among others [101]. While minimal applications have been investigated for parahydrophobic surfaces, they have been shown to have favorable performance in water collection [104] and a unique ability to pin droplets and air bubbles in place [105].

2.4 Enhancing Pool Boiling Performance

Many researchers have attempted to improve bubble dynamics and heat transfer by modifying boiling surfaces. Common and reliable approaches include area enhancement via fins or grooves, addition of artificial nucleation sites through roughening or fabricating cavities, applying porous coatings, and microstructuring or nanostructuring. For a review of these technologies refer to Refs [2,15,106]. This section will focus on two key methods of enhancement – controlling boiling hydrodynamics and altering surface wettability.

2.4.1 Controlling Boiling Hydrodynamics

Methods to enhance pool boiling performance via control of pool boiling hydrodynamics has two main thrusts. First, Zuber's hydrodynamic instability theory for critical heat flux [1] is dependent on the spacing between rising vapor columns. By controlling this spacing, it is theoretically possible to delay critical heat flux. As discussed in Chapter 2.1.1, convective and transient conductive effects resulting from subcooled liquid circulating near the surface can be a significant source of heat transfer. The second goal in controlling hydrodynamics is to order the liquid and vapor flows in such a way that promotes this circulation and improves heat transfer from the surface.

Liter and Kaviany [107] fabricated modulated porous coatings such that liquid is brought to the surface through tall porous peaks and vapor exits through shorter valleys. This ordering of liquid and vapor flows resulted in the enhancement of CHF by 59% compared to a uniform porous surface. The authors proposed this critical heat flux enhancement results from modulation of the hydrodynamic instabilities. Jaikumar and Kandlikar studied microchannels with selective sintered coatings [108,109] and surfaces with defined nucleating regions and non-nucleating feeder channels [110]. In both cases, the location of vapor generation is controlled, and the boiling heat transfer coefficient and CHF enhancement observed is attributed to induced convection effects generated by the ordered flows. It is suggested that this impingement-like induced convection improves CHF by rewetting the surface and increases convective heat transfer, resulting in a measured decrease in wall superheat with increasing heat fluxes. Rahman *et al.* [111] utilized low-conductivity, epoxy-covered strips on a plain copper surface to promote bubble nucleation on the higher-conductivity, higher-temperature regions. The heat transfer coefficient and CHF were shown to change significantly with the pitch between the low-conductivity regions. At the optimum pitch, introduction of these low-conductivity regions enhanced the heat transfer coefficient by five times and doubled the CHF when compared to a plain copper surface. This enhancement is suggested by the authors to be a resonance-like effect resulting from ordering the vapor-liquid pathways with a spacing that correlates with the capillary length and the approximate bubble departure diameter. By introducing wettability patterning in combination with low-conductivity regions, the enhancement can be amplified [112]. These studies have demonstrated that surface features can be used to manipulate boiling hydrodynamics to improve both CHF and heat transfer coefficient, but the specific enhancement mechanisms are speculative.

2.4.2 Effects of Surface Wettability on Boiling Performance

The wettability of boiling surfaces has emerged as a key factor in their heat transfer efficacy. Considering smooth surfaces, those that are hydrophilic have been reported to delay critical heat flux through improved rewetting [113,114]; however, at lower heat fluxes in the nucleate boiling regime, they have less efficient heat transfer than hydrophobic surfaces [8,115,116]. Hydrophobic surfaces exhibit boiling incipience at lower surface temperatures [40,116] and yield higher nucleation site densities in the nucleate boiling regime, which leads to efficient heat transfer at low heat fluxes, but are commonly reported to promote premature film boiling leading to prohibitive surface temperatures at moderate to high heat fluxes [8,9,12].

Textured superhydrophilic surfaces have garnered significant interest in boiling applications for their ability to actively rewet the surface, significantly delaying critical heat flux [4,6,7,72,117,118]. The delay in critical heat flux has been demonstrated to correlate with the volumetric rate at which liquid wicks into the surface structures [6]. While this makes superhydrophilic surfaces ideal for applications with extremely high heat fluxes, the intrinsic hydrophilicity of the surfaces still results in heat transfer disadvantages at lower heat fluxes compared to hydrophobic surfaces that exhibit nucleate boiling.

Initial studies on the boiling behavior of textured superhydrophobic surfaces revealed that these surfaces promoted premature film boiling, often observed just after boiling incipience, resulting in ineffective heat transfer [5,10,11,13,14]. Because of this, superhydrophobic surfaces, and wholly hydrophobic surfaces altogether, have been largely dismissed for boiling applications despite their advantageous boiling characteristics in the nucleate boiling regime. However, engineered surfaces with patterned wettability have emerged in an attempt to capitalize on the preferable nucleation characteristics of hydrophobic and superhydrophobic surfaces along with the beneficial rewetting ability of hydrophilic and superhydrophilic surfaces. On these surfaces, small hydrophobic islands typically act as nucleation sites on mostly hydrophilic surfaces [119]. This generally improves the heat transfer coefficient compared to a hydrophilic surface with minimal detriment to the critical heat flux, due to the mixture of the favorable incipience behavior of the hydrophobic islands and the rewetting ability of the hydrophilic surface [8,12,120,121]. Due to the ability of hydrophobic regions to trap air, the incipience behavior of hydrophobic regions has been shown to be highly dependent on the degassing approach [122]. Jo *et al.* [123] observed that hydrophobic spots on patterned surfaces never rewet after boiling incipience. Due to these dry

spots, critical heat flux was shown to decrease proportionally as the hydrophobic area ratio increased. On the contrary, Betz *et al.* [115] presented evidence that hydrophilic surfaces with hydrophobic islands actually significantly improve the critical heat flux compared to fully hydrophilic surfaces; however, they were unable to provide a conclusive explanation for the behavior. Thus, the critical heat flux behavior of surfaces with patterned wettability remains unclear. Additionally, although the dynamic wettability of a surface has been shown to influence bubble dynamics [124,125], nearly all studies on the effects of wettability on boiling consider only the static contact angle of the surface. This risks neglecting important dynamic interfacial processes during boiling.

3. ENABLING HIGHLY EFFECTIVE BOILING FROM SUPERHYDROPHOBIC SURFACES

This chapter focuses on an experimental investigation of the boiling behavior of superhydrophobic surfaces. The dynamic wettability is shown to have an important role in boiling dynamics through examining the boiling behavior of superhydrophobic surfaces with different initial wetting states. The Cassie-Baxter wetting state (low contact angle hysteresis) results in premature critical heat flux while the Wenzel (high contact angle hysteresis) wetting state leads to exceptionally efficient nucleate boiling heat transfer. The material from this chapter was published in *Physical Review Letters* [126].

3.1 Surface Fabrication and Characterization

Microstructured and nanostructured superhydrophobic surfaces were each fabricated on copper test blocks. The copper surfaces were first sanded with 320 and 600 grit sandpaper to a roughness of 400-600 nm and cleaned with acetone, methanol, and isopropyl alcohol before being rinsed with deionized water. The microstructured copper surface was fabricated through laser-etching with a 1.06 μm wavelength fiber laser (ULS, PLS6MW). The nanostructured copper surface was fabricated by chemical etching at room temperature in a solution of 2.5 M NaOH and 0.1 M $(NH_4)_2S_2O_8$ for 30 min to produce copper oxide nanowires. To impart superhydrophobic behavior, the surfaces were coated with PDMS by first priming (Dow Corning, 92-023) to promote adhesion to the surface. The primer was deposited on the surface, the excess removed, and the primer allowed to cure for 30 min. The surface was then submerged at room temperature in a solution of PDMS (10:1 base to curing agent) and hexane for 1 hr and cured at 180°C for 2 hr. Scanning electron microscopy images of each surface are presented in Figure 3.1. More detailed accounts of the surface fabrication procedures are provided in Appendix B.

Static contact angles were measured using an automated goniometer (ramé-hart, 290-F1) after gently depositing a 5 μL drop of deionized water on the surfaces. Cassie-Baxter state roll-off angles were measured by gently depositing a droplet on the surface and tilting the goniometer stage in 1-deg increments until the droplet rolled off the surface. Wenzel state roll-off angles were measured by releasing a droplet from a significant height such that the momentum allowed it to

impinge into and infiltrate the surface structures. The surface was then tilted until the tilt angle reached 90 deg without the droplet rolling off. Surfaces were also inverted 180 deg to demonstrate that the droplet in the Wenzel state was adhered to the surface. This characterization is reported in Table 3.1.

3.2 Experimental Facility

The experimental facility consists of a boiling chamber, a copper test block, a coolant flow loop, a high-speed camera, lighting equipment, and data acquisition equipment. The boiling chamber (Figure 3.2a) has polyether ether ketone (PEEK) walls that have low thermal conductivity (0.25 W/mK) and good durability under operation up to high temperatures (260°C). Two 170 W immersion heaters are inserted into the pool for degassing and maintaining saturated pool conditions. Six pool thermocouples monitor the pool conditions to ensure that the liquid is at a uniform temperature. A pressure transducer (Omegadyne, PX409) measures the pressure of the chamber. The facility is equipped with two condensers: the Graham condenser is used to purge noncondensables during degassing, and the coiled condenser is used to condense vapor during the boiling experiment. Borosilicate glass windows (5.1 cm × 7.6 cm) are located in the front and back of the chamber to allow for lighting and visualization.

The copper test block is inserted into the bottom of the pool boiling chamber and has twelve 150 W cartridge heaters inserted from below that are powered with a 2700 W DC power supply (Ametek, XFR 150-18). The cross-sectional area the test block base (8.2 cm × 8.2 cm) is made wide enough to accommodate the heaters, and it narrows to a 2.7 cm × 2.7 cm neck on top of which the textured surfaces are directly fabricated. The block is designed to ensure that a uniform heat flux is supplied at the surface. The test block neck is instrumented with twelve T-type thermocouples, configured in linear rakes as shown in Figure 3.2c to measure the temperature gradient, which is used to calculate the surface temperature and heat flux. The thermocouples are referenced to a physical ice-point junction in an isothermal dry block (Fluke, 9101) to minimize measurement error due to the joining of dissimilar metals at junctions. After the textured surface has been prepared on the test block, the block is sealed into the chamber; a bead of silicone RTV (Momentive, RTV 106) is applied around the outer top edge of the heater block neck for sealing and then encapsulated with a smooth layer of epoxy (3M, DP110) to prevent nucleation and outgassing from the silicone.

Visualizations are recorded through the front window using a high-speed camera (Phantom, VEO 710L) and a macro lens (Zeiss, Makro-Planar T* 2/100). Uniform high-intensity backlighting (Advanced Illumination, BT200100) is provided over the entire rear window; additional front lighting (Sunoptics, Titan300) improves visibility near the surface. For these experiments, deionized water is used as the working fluid. A more detailed account of the experimental facility is provided in Appendix C.

3.3 Experimental Procedure and Data Analysis

The first step of each experiment involves degassing the chamber. The process used for degassing the liquid in the chamber is critical to determining the initial wetting state of the surface, and has been shown to impact the incipience behavior of textured hydrophobic surfaces [122]. Two alternative degassing processes are used to achieve different initial wetting states on each textured superhydrophobic surface. *If the Cassie-Baxter state is desired,* the cartridge heaters in the test block are powered to ~100 W to boil water from its surface after the pool is filled with liquid; boiling from the surface is maintained throughout the degassing process. The immersion heaters are powered to heat the pool to the saturation temperature with the chamber open to the ambient through the Graham condenser; coolant (water) is pumped through the Graham condenser such that the vapor condenses and reenters the chamber while noncondensable gas is allowed to escape. Boiling is maintained until no noncondensables are observable in the chamber. Throughout this process, film boiling is observed on the surface. At the end of the degassing process, noncondensables have been removed from the system, but the vapor remains trapped in the surface texture. *If the Wenzel state is desired*, the pool is heated to saturation and degassed exclusively using the immersion heaters, without any heating of the test block or boiling from the test surface. As the pool degasses, the trapped gas film on the surface during initial filling of the pool was observed to gradually disappear until no gas remained on the surface. Again, the liquid is boiled until no noncondensables are observable in the chamber.

Once the system is degassed, the chamber is sealed from the environment and the coiled condenser in the vapor space is used to maintain a constant pressure of 101 kPa in the chamber. If the test surface is undergoing boiling from the degassing procedure (namely, when preparation of the surface in a Cassie-Baxter wetting state is desired), the test block heaters were turned off and the surface allowed to cool to just below saturation, upon which boiling was observed to cease.

The immersion heaters remain powered throughout the test to maintain uniform, saturated conditions in the chamber.

To obtain a boiling curve showing the steady-state surface superheat as a function of heat flux, the power supplied to the cartridge heaters in the test block is incremented in steps and the system is allowed to reach a steady state at each increment (defined as when the surface temperature changes at less than 0.25°C/hr). At steady state, the temperature/pressure data are recorded (Agilent, 34970A; National Instruments, LabVIEW); high-speed visualizations at 3000 fps are also recorded. The heat flux increments continue until the test is stopped or critical heat flux is reached.

For each steady-state point, the temperature and pressure data are averaged over ~75 sec. The pressure is used to determine the saturation temperature of the water. The surface temperature and heat flux are determined from the thermocouple rakes. This is done by first performing a linear least-squared fit to the spatial temperature gradient along each rake. The fitted temperature gradient and thermal conductivity of copper (390 W/mK) are used to determine the heat flux based on Fourier's law. The surface temperature is determined by extrapolating the gradient to the surface location. Assuming that the temperature distribution in the block is symmetric, the area-averaged surface temperature and heat flux are determined by taking an area-weighted average of the surface temperature and heat flux obtained from each thermocouple rake. The areas that correlate to each thermocouple rake are shown in Figure 3.2b, which correspond to area-based weights of 0.25 for the central rake and 0.375 for each of the side rakes. The surface superheat is determined as the difference between the area-averaged surface temperature and the saturation temperature that correlates to the measured pressure value. The heat transfer coefficient is a measure of the boiling heat transfer efficiency at a steady-state point and is calculated by dividing the heat flux by the surface superheat.

Uncertainties of the heat flux, surface superheat, and heat transfer coefficient are assessed. The ice-point-referenced thermocouples were all calibrated simultaneously in a dry-block calibrator (Isotech, Jupiter 4852) over a temperature range of 50°C to 250°C. An RTD is used to accurately measure the dry block temperature during the calibration. The manufacturer-quoted uncertainty for the RTD is ±0.15°C and the ice point uncertainty is ±0.05°C. A linear offset from the NIST ITS-90 [127] standard is fitted to the calibration data for each thermocouple. The uncertainty in this linear calibration curve is determined through analyzing the regression

uncertainty as laid out in Brown *et al.* [128]. Because the results are averaged over many data points, random errors are neglected; the uncertainties are assumed to vary independently, eliminating the covariance uncertainties. The thermocouple uncertainty was determined to be approximately ±0.35°C.

The heat flux and surface temperature uncertainties are determined based on the uncertainty of the linear regression of the temperature gradient along the thermocouple rakes, taking into account the temperature measurement uncertainty (±0.35°C) and the positional uncertainty of each thermocouple ±0.04 mm. The uncertainty of the slope and intercept of the linear fit correlates directly to the heat flux and surface temperature, assuming there is no uncertainty in the material thermal conductivity. The heat flux uncertainty generally increases with heat flux and the maximum uncertainty was 2.6 W/cm^2. The uncertainty in the saturation temperature is evaluated based on the manufacturer-quoted uncertainty for the pressure transducer and is estimated to be ±0.12°C. The surface superheat uncertainty, which depends on both the surface and saturation temperature uncertainties, ranges from 0.52°C to 0.56°C. Finally, the heat transfer coefficient uncertainty is determined based on the heat flux and surface superheat uncertainties. It depends heavily on the performance of the surface and is much larger for low surface superheats. The maximum heat flux uncertainty is ±4.9 kW/m^{2}K. The uncertainties for each of these parameters are shown as error bars in the plotted data.

3.4 Results

For both the microstructured and nanostructured surfaces, a contrast in the boiling behavior was observed between an initial Cassie-Baxter state and an initial Wenzel state. The behavior is demonstrated in Figure 3.3 for the nanostructured surface, which exhibits the more extreme nonwetting nature. When the experiment started with the surface in the Cassie-Baxter state, film boiling occurred shortly after incipience, prior to reaching steady-state conditions for the first heat flux test point of 2.1 W/cm^2, matching the behavior commonly observed for superhydrophobic surfaces in the literature; film boiling continued as the heat flux was increased (Figure 3.3d). In contrast, for an initial Wenzel wetting state, a nucleate boiling mode consisting of individual bubbles nucleating and departing from the surface at a high density was observed (Figure 3.3h). This hitherto unreported nucleate boiling behavior on a nanostructured superhydrophobic surface continued up to a heat flux of 45 W/cm^2, at which point testing ceased. The boiling data for this

surface are presented in Figure 3.4. Critical heat flux was avoided in order to prevent damage to the surface associated with the sharp temperature excursion, in order to allow confirmation that the observed nucleate boiling behavior was not a result of a loss of superhydrophobicity. After the test, the surface remained superhydrophobic.

The contrast in boiling behavior between the two initial wetting states is explained by differences in the resistance to three-phase contact line motion in the two states. The contact line moves freely in the Cassie-Baxter state, as demonstrated by the small droplet roll-off angles (see Table 3.1). During boiling, this free movement of the contact line is sustained; the contact diameter of each bubble is free to grow until the bubble becomes large enough (several millimeters in size) to experience necking, pinch-off and departure, leaving behind a vapor patch on the surface (Figure 3.5b). As a result, a single active nucleation site covers a significant amount of surface area with vapor; a small number of nucleation sites can thus coalesce to coat the entire surface in vapor resulting in film boiling at a minimal heat flux. Conversely, the three-phase contact line is strongly pinned in the Wenzel state, as evidenced by the adherence of a droplet to the surface even when inverted (Table 3.1). As the bubble grows, the contact diameter remains fixed, covering a small region on the surface, and the bubble maintains a spherical shape as a result of the contact line pinning (Figure 3.5d). This observation is in contrast to all prior reports of bubble growth on nominally superhydrophobic surfaces in the literature (Table 3.2). These results reveal that the *static* contact angle of a droplet, which would be large in both Cassie-Baxter and Wenzel states, is not representative of the bubble characteristics following nucleation on textured superhydrophobic surfaces during boiling. Rather, the boiling behavior is governed by contact line *dynamics*, which are in turn driven by the initial wetting state of the surface.

This demonstration of the ability to maintain nucleate boiling on superhydrophobic surfaces changes our perspective on their potential use as enhanced surfaces. To illustrate that this behavior is not unique to the nanostructured surface shown, the boiling performance is investigated for a microstructured surface in the Cassie-Baxter and Wenzel initial states. For reference, a bare microstructured copper surface without the PDMS coating is also included in the comparison. Boiling curves for the three cases are shown in Figure 3.6a. The reference microstructured bare copper surface has relatively few active nucleation sites at low heat fluxes (< 50 W/cm^2), leading to a significant temperature increase with increasing heat flux. Above ~50 W/cm^2, active nucleation over a majority of the surface leads to a sharp increase in the slope of the boiling curve.

Nucleate boiling is observed until CHF occurs at 110 W/cm^2, matching the limit predicted by Zuber [1]. The nucleate boiling behavior observed is not a fleeting condition; nucleate boiling on the surface was observed for durations of over 5 hr during acquisition of the data. For the case with the initial Cassie-Baxter wetting state, film boiling occurs for all heat fluxes along the boiling curve, with no nucleate boiling regime being observed. Much higher levels of superheat result as compared to the reference bare copper surface, the disparity increasing as the heat flux is increased. The surface in the initial Wenzel wetting state displays nucleate boiling behavior over the entire range of heat fluxes, displaying a minimal rise in surface temperature with increasing heat flux all the way to the critical heat flux. A 100% increase in the maximum heat transfer coefficient (as shown in Figure 3.6b) is achieved compared to the bare copper reference; importantly, no reduction in CHF is observed. The substantial increase in heat transfer coefficient is a result of the lower energy requirement for nucleation on hydrophobic substrates [129] leading to a higher nucleation site density. Because of the pinned contact lines of bubbles on the surface in the Wenzel state, bubbles are observed to grow and depart readily, rather than permanently blanketing regions in vapor and diminishing heat transfer, as has been observed for boiling from superhydrophobic surfaces in past studies [123].

This is first report of sustained, efficient nucleate boiling on a superhydrophobic surface. An initial Wenzel wetting state allows this microstructured superhydrophobic surface to operate in the nucleate boiling regime up to a CHF of 115 W/cm^2, a value comparable to that typical of hydrophilic wetting surfaces; the transition to film boiling occurs at a heat flux over an order of magnitude higher than previous reports for superhydrophobic surfaces [10]. By removing the limiting characteristic of superhydrophobic surfaces of reaching CHF prematurely, their advantageous ability to promote a high nucleation site density can be fully utilized in practical applications that call for high heat transfer coefficients. Heterogeneous surface concepts can utilize superhydrophobic regions primed to operate in the Wenzel state without concern for hot spots or significant deterioration of CHF. It is likely that this Wenzel state behavior would naturally occur in many industrial applications where surfaces are submerged in water over long periods of time, due to the natural diffusion of air trapped in the surface into the degassed liquid, as has been observed in drag reduction studies [74].

3.5 Conclusions

Superhydrophobic surfaces are shown to yield two distinct boiling behaviors based on the wetting state of the surface prior to boiling. Boiling initiated from the Cassie-Baxter state leads to film boiling immediately after incipience, as has been observed in prior studies. For the first time, nucleate boiling is achieved here on a superhydrophobic surface by initiating boiling from a superhydrophobic surface initially brought into the Wenzel state. The strong contact line pinning in the Wenzel state limits contact-line spreading, allowing individual bubbles to grow and depart without coalescing into a vapor film. The behavior is demonstrated on two superhydrophobic surfaces of vastly different texture scales – microstructured and nanostructured – and is shown to be governed by the initial wetting state of the surface rather than a unique surface structure. Boiling is extremely efficient on superhydrophobic surfaces operating in this mode owing to their promotion of high nucleation site densities; a nucleate boiling mode is maintained on a superhydrophobic surface up to an unprecedented critical heat flux on the order of the classical Zuber limit [1]. These results indicate the importance of contact line dynamics during boiling.

Table 3.1. Cassie-Baxter and Wenzel Wetting Behavior Characterization.

Surface	Cassie-Baxter Contact Angle	Cassie-Baxter Roll-Off Angle	Wenzel Roll-Off Angle
Microstructured superhydrophobic	158 deg	10 deg	No roll-off
Nanostructured superhydrophobic	165 deg	~1 deg	No roll-off

Table 3.2. Summary of Boiling Behavior of Water from Textured Superhydrophobic Surfaces.

Author(s)	Surface Modification	Contact Angle	Onset of Film Boiling
Takata *et al.*[10]	Nickel plated surface with PTFE microparticle coating	150-170 deg	~5-6°C superheat; ~5 W/cm^2
Hsu and Chen[5]	Silica nanoparticles with fluorosilane coating	149-155 deg	Upon incipience
Malavasi *et al.* [11]	Stainless steel with commercial hydrophobic coating (Glaco Mirror Coat Zero, Soft99 Co)	~150 deg	Upon incipience
Li *et al.*[13]	Silicon nanowires with PTFE coating	>150 deg	Upon incipience
Teodori *et al.*[14]	Stainless steel with commercial nanoparticle coating (Glaco Mirror Coat Zero, Soft99 Co)	~165 deg	Upon incipience at ~1°C superheat
Current Study	Laser-etched copper surface with PDMS coating	158 deg	Initial Cassie-Baxter state: < 2 W/cm^2 Initial Wenzel state: 115 W/cm^2

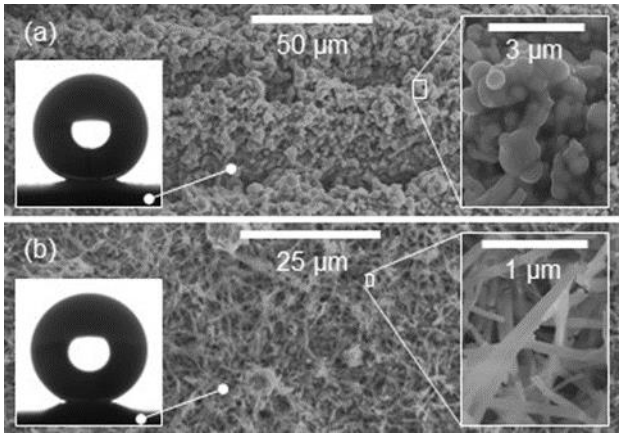

Figure 3.1. Scanning electron microscope (SEM) images of (a) the laser-etched microstructured copper surface (300X; top-right inset at 4,000X) and (b) the chemically-etched nanostructured copper surface (800X; top-right inset at 15,000X). Insets at bottom-left of each frame show a static 5 µl droplet resting on the respective surface in the Cassie-Baxter state.

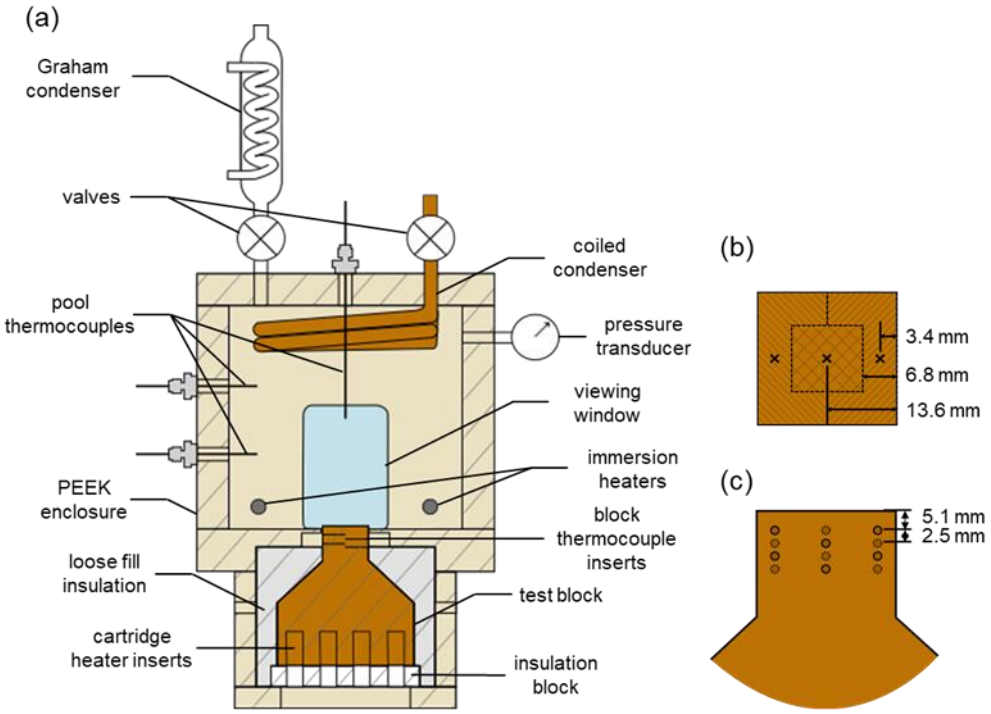

Figure 3.2. (a) Schematic diagram of the pool boiling test chamber. (b) Plan and (c) side views of the neck of the test block showing the surface regions attributed to each thermocouple rake and the locations of the thermocouples (dotted lines represent thermocouples inserted from the back side).

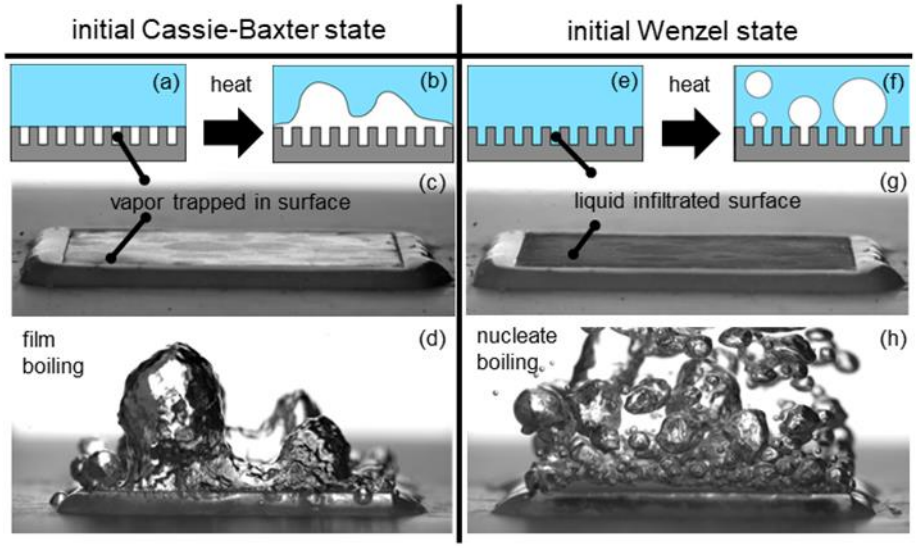

Figure 3.3. Illustrations of (a) the initial Cassie-Baxter state progressing to (b) film boiling upon heating, and (e) the initial Wenzel state progressing to (f) nucleate boiling upon heating. Visualization of (c) the initial Cassie-Baxter state and (d) subsequent film boiling from a submerged nanostructured superhydrophobic surface (heat flux 9 W/cm^2, surface superheat 17.7°C). Visualization of (g) the initial Wenzel state and (h) subsequent nucleate boiling from a submerged nanostructured superhydrophobic surface (7.6 W/cm^2, 7.4°C).

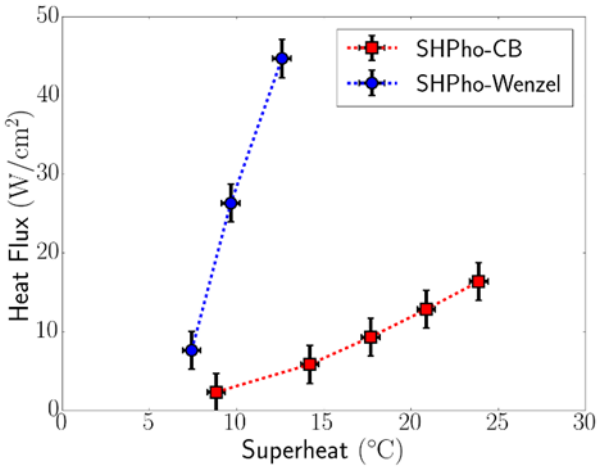

Figure 3.4. Boiling curves for both an initial Cassie-Baxter (SHPho-CB) state and initial Wenzel state (SHPho-Wenzel) on a nanostructured superhydrophobic surface.

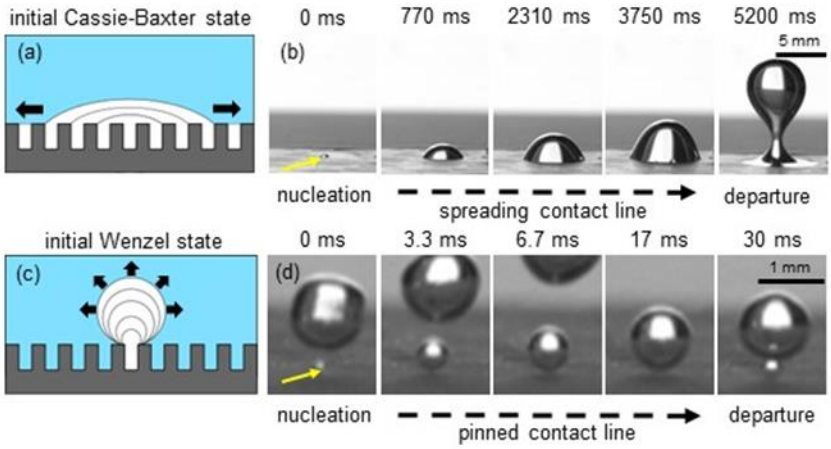

Figure 3.5. Illustrations showing the bubble growth and departure behavior from an (a) initial Cassie-Baxter state and (c) initial Wenzel state and (b,d) respective image sequences of these behaviors on a nanostructured superhydrophobic surface just after incipience (note the different length and time scales indicated).

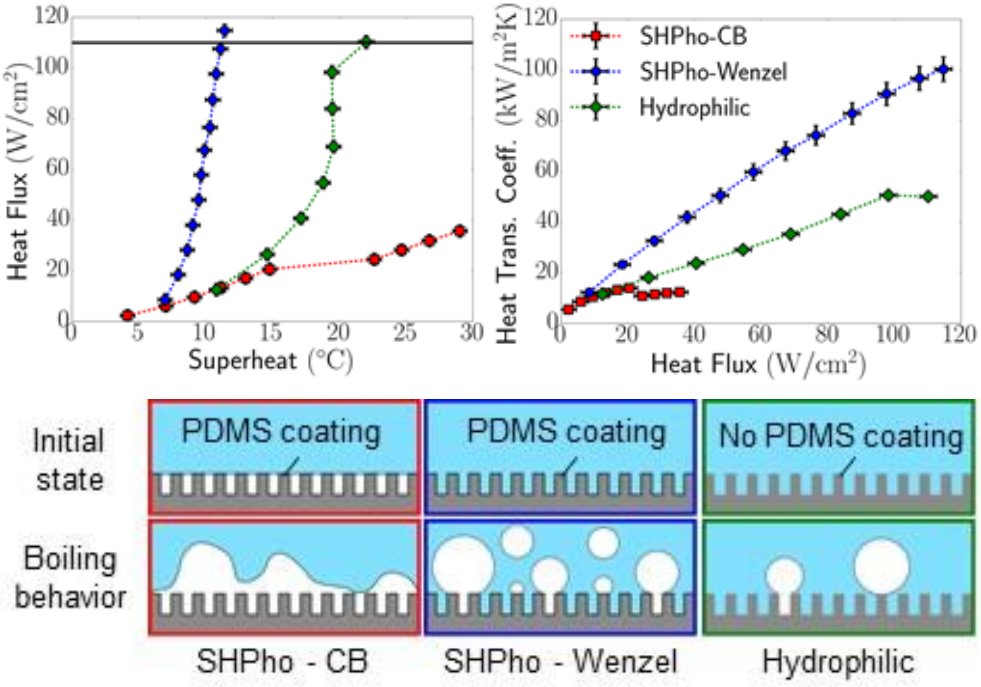

Figure 3.6. (a) Boiling curves (surface heat flux as a function of superheat) and the associated (b) heat transfer coefficients for the three microstructured surface cases: superhydrophobic in the Cassie-Baxter state (SHPho-CB), superhydrophobic in the Wenzel state (SHPho-Wenzel), and bare copper (Hydrophilic). Illustrations below the graphs indicate the relationship between the initial wetting state and the boiling behavior.

4. CONTROL OF POOL BOILING HYDRODYNAMICS THROUGH SURFACE WETTABILITY PATTERNING

This chapter details an experimental study on controlling pool boiling hydrodynamics using surface wettability patterning and its effects on the boiling performance. Surfaces are patterned with superhydrophobic and hydrophilic stripes. Boiling preferentially occurs on the superhydrophobic regions allowing spatial control of vapor generation. The boiling performance is shown to improve as the pitch and width of the stripes decreases. The material in this chapter was published in the *Proceedings of the 16th International Heat Transfer Conference* [130].

4.1 Surface Fabrication and Characterization

Surfaces are directly fabricated onto the top surface of copper test blocks. The surface is first sanded to a roughness of ~500 nm. The surface is then laser-etched (ULS, PLS6MW) to create a stochastically roughened topology having a roughness of ~10 μm. An adhesion-promoting primer (Dow Corning, 92-023) is applied to the surface, the excess removed, and the primer allowed to cure for 30 min. Polydimethylsiloxane (PDMS) is applied to the surface via submersion for 1 hr in a solution of hexane and PDMS (10:1, base to curing agent). The PDMS coating is cured for 2 hr in an oven at 180°C. At this point in the fabrication, the entire surface is rendered superhydrophobic with a static contact angle of 158 deg and a roll-off angle of ~10 deg. Laser-etching is used to selectively remove the PDMS coating from some areas to create the desired wettability pattern. A detailed account of the surface fabrication procedures is presented in Appendix B. Prior to testing, the etched regions are observed to be hydrophilic (contact angle less than 90 deg) but do not exhibit capillary wicking; a significant wettability contrast exists between the PDMS-coated (superhydrophobic) and laser-etched (hydrophilic) regions, as shown in Figure 4.1.

A uniform superhydrophobic surface and a uniform hydrophilic surface (without the coating) are fabricated as reference samples. Biphilic surfaces are evaluated that each have alternating superhydrophobic and hydrophilic stripes of equal width such that half of the surface is superhydrophobic in each case. As shown in Figure 4.2, four biphilic surfaces were fabricated with stripe widths of 0.21, 0.85, 2.27, and 13.63 mm. The 13.63 mm case is a baseline where the

surface consisted of one large superhydrophobic region in the center with hydrophilic regions on each side. Because there is minimal boiling on the outer hydrophilic regions, the hydrodynamics would resemble those of a typical 13.63 mm wide superhydrophobic surface. The local boiling characteristics and percentage of boiling area are the same in this case as for the other biphilic surfaces, but the potential for enhancement due to hydrodynamic ordering is removed, providing a clear contrast and hence a clearer understanding of the impact of hydrodynamics.

4.2 Experimental Procedure

The experimental facility, procedure and data analysis are the same as is discussed in Chapters 3.2 and 3.3. One key distinction is that in this study, degassing is always performed by boiling from the immersion heaters to promote the Wenzel state.

4.3 Results

The boiling curves (superheat versus heat flux) for each surface are shown in Figure 4.3a. The curves for the biphilic surfaces are bounded by the uniform reference tests; the superhydrophobic surface generally maintains the lowest superheat while the hydrophilic surface has the highest superheat. Both uniform cases and the two biphilic cases with smaller stripes (0.21 mm and 0.85 mm) have similar CHF values of 110-118 W/cm^2 while the two cases with larger stripes (2.27 mm and 13.63 mm) have diminished CHF values of 97-99 W/cm^2. Both the CHF and heat transfer coefficient (Figure 4.3b) increase with decreasing stripe width on the biphilic surfaces, despite constant proportions of superhydrophobic area being maintained (Table 4.1). The superhydrophobic surface and best-performing biphilic surface (0.21 mm-wide stripes) exceed the maximum heat transfer coefficient of the hydrophilic surface by 91% and 74% respectively.

While it is well-established that nucleation occurs at a lower superheat on superhydrophobic surfaces as compared to hydrophilic ones [8,12,115], this advantage is typically counteracted by early occurrence of film boiling on superhydrophobic surfaces [10,5,11,13,14]. In the present work, the superhydrophobic regions on the surface are brought into the Wenzel state prior to boiling, leading to contact line pinning and prevention of vapor spreading and film formation. This behavior, first reported in our work in Ref. [126], coupled with the ease of activating nucleation sites on the superhydrophobic surface, allows nucleate boiling to be

maintained at a low surface superheat up to a CHF on the order of Zuber's limit (110 W/cm^2) [1]. This mitigation of film boiling also prevents the development of hotspots at superhydrophobic regions on biphilic surfaces reported in past studies [12].

Minimal nucleation is observed on the hydrophilic surface until higher heat fluxes (greater than 50 W/cm^2) where the boiling curve slope begins to increase. As a result of the earlier nucleation on superhydrophobic regions, boiling preferentially occurs on the superhydrophobic regions of biphilic surfaces, as shown in Figure 4.4 for a representative case (2.27 mm-wide stripe). Vapor generation does not take place on the hydrophilic regions of the biphilic surfaces in most cases, even at high heat fluxes, and vapor leaving the surface maintains a periodic structure corresponding to the position of the superhydrophobic stripes. One exception is the case with a single 13.63 mm-wide superhydrophobic stripe in the center of the surface, for which vapor generation was observed near the edges of the hydrophilic regions furthest from center, likely due to an elevated superheat over the large feature.

All of the biphilic surfaces have a higher superheat than the uniform superhydrophobic surface at the same heat flux (Figure 4.3a) resulting in lower heat transfer coefficients (Figure 4.3b). This superheat increase is expected, because the actively boiling area is limited to the superhydrophobic regions which cover only a half of the surface area (compared to the entire surface being uniformly superhydrophobic in the reference case). This decrease in performance, specifically the heat transfer coefficient, is expected to scale based on the reduction in boiling area when comparing the uniform superhydrophobic surface and the single, large 13.63 mm superhydrophobic stripe (which, as stated earlier, is expected to experience minimal impact on the hydrodynamics compared to the other surfaces with multiple interacting stripes). The maximum heat transfer coefficient is indeed found to decrease from 96 kW/m^{2}K to 57 kW/m^{2}K. The heat transfer coefficient is not strictly cut in half due to convective heat transfer from the hydrophilic regions. The CHF also decreases from 115 W/cm^2 to 97 W/cm^2. Likewise, the decrease in superheat for the biphilic surface when compared with the hydrophilic surface is expected; the addition of superhydrophobic regions increases the active nucleation site density on the surface, improving the heat transfer coefficient.

All of the biphilic surfaces have the same surface topography, local wettability, and percentage of superhydrophobic area. Thus, the amount of boiling area (superhydrophobic regions) and boiling characteristics within this area (*e.g.*, nucleation site density, local bubble dynamics)

should be similar, with the key difference being the change in hydrodynamic ordering. We note that controlling this ordering led to an increase in CHF with decreasing stripe width in this study (Table 4.1). Various explanations have been proposed for boiling performance enhancement based on ordering of counter-current liquid and vapor flows. As described by Liter and Kaviany [107], it is possible that ordering these flows constrains the length scales that lead to the development of instabilities that in turn result in CHF. They proposed a modified hydrodynamic choking limit that is proportional to $\lambda_m^{-1/2}$, where λ_m is the center-to-center distance between boiling regions. However, this theory would vastly overpredict the CHF enhancement compared to the results obtained in the present study. It is unlikely that this mechanism is dominant for the cases in this study. Rahman *et al.* [111] reported maximum CHF and heat transfer coefficient enhancement when the pitch between boiling regions approaches the capillary length (~2.5 mm for saturated water at 101 kPa). However, minimal enhancement over the 13.63 mm case is observed near the capillary length in the present study.

An alternative explanation offered in the literature proposed that the maximum CHF and heat transfer coefficient enhancement occurs when the spacing approaches the bubble departure size [110,111]. The bubble departure size (d_{oF}) can be approximated using the Fritz correlation [34]

$$d_{oF} = 0.0208\theta_{rec}\left[\frac{\sigma}{g\left(\rho_l - \rho_g\right)}\right]^{1/2} \tag{4.1}$$

where θ is the receding contact angle in degrees, σ is the surface tension, g is the gravitational constant, and ρ_l and ρ_g are the liquid and vapor densities, respectively. In order to compute a departure size from this expression, a receding contact angle measurement was attempted for a droplet in the Wenzel state on the superhydrophobic surface via sessile drop goniometry; however, the contact line exhibited stick-slip behavior during recession and no stable receding contact angle was observed. Additionally, there are no reliable models to estimate the receding contact angle of a surface in the Wenzel state. He *et al.* [99] reported similar difficulty in determining the receding contact angle of a droplet in the Wenzel state. For the bubble departure diameter to approach the stripe width for which the largest enhancement was observed (0.21 mm), the receding contact angle would need to be less than 4 deg. Due to the high contact angle hysteresis and pinning

behavior observed in the Wenzel state on these superhydrophobic surfaces [131], it is possible that the receding contact angle could take a low value of this magnitude, and the optimal ordering length scale corresponds to the bubble departure diameter.

Jaikumar and Kandlikar [108,110] proposed that the enhancement observed on surfaces with ordered hydrodynamics was a result of improved convective heat transfer. They proposed an induced jet impingement effect resulting from the separated liquid and vapor flows. For the surfaces tested in this study, a large vapor plume is formed above the surfaces (as shown in Figure 4.4d) that would seemingly inhibit significant liquid flow and impingement from above. It is, however, possible that the surfaces in our study have induced convective flows from the ends of the stripes into the interior of the surface.

4.4 Conclusions

Biphilic surfaces with alternating superhydrophobic and hydrophilic stripes were used to control counter-current liquid and vapor flows during pool boiling to study the effects of this flow ordering on pool boiling performance. The superhydrophobic regions were brought into the Wenzel wetting state prior to boiling, which prevented vapor film formation upon nucleation, and allowed for sustained nucleate boiling. Boiling occurred preferentially on superhydrophobic regions of biphilic surfaces, effectively controlling the liquid-vapor hydrodynamics during boiling. Both the CHF and heat transfer coefficient were observed to increase as the width of the stripes decreased. Decreasing the stripe width from 13.63 mm to 0.21 mm led to a 22% improvement in CHF and a 53% improvement in the maximum heat transfer coefficient. Because other key surface parameters were kept fixed across surfaces, this enhancement is attributed to the changing length scale of the hydrodynamic ordering. While the precise enhancement mechanism is uncertain, it may be related to the bubble departure diameter length scale or induced convection effects. The biphilic surface with the smallest stripe width (0.21 mm) outperformed the uniform hydrophilic surface in terms of heat transfer coefficient by 74%. The enhancement may be due to induced convection effects or hydrodynamic ordering at the scale of bubble departure but does not correspond to the expected enhancement for either the mitigation of hydrodynamic instabilities or hydrodynamic ordering at the scale of the capillary length.

Table 4.1 Comparison of boiling performance of the uniform and biphilic surfaces

Surface	CHF (W/cm^2)	Maximum Heat Transfer Coefficient (kW/m^2K)
Uniform superhydrophobic	115	96
Uniform hydrophilic	110	50
Biphilic (13.63 mm)	97	57
Biphilic (2.27 mm)	99	65
Biphilic (0.85 mm)	113	83
Biphilic (0.21 mm)	118	87

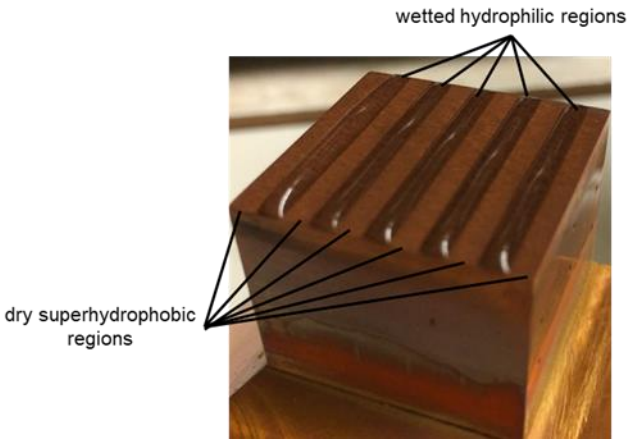

Figure 4.1. Photograph demonstrating the wettability contrast on a biphilic surface with eleven alternating superhydrophobic and hydrophilic stripes. Water deposited on the surface is confined to the hydrophilic regions while the superhydrophobic regions remain dry.

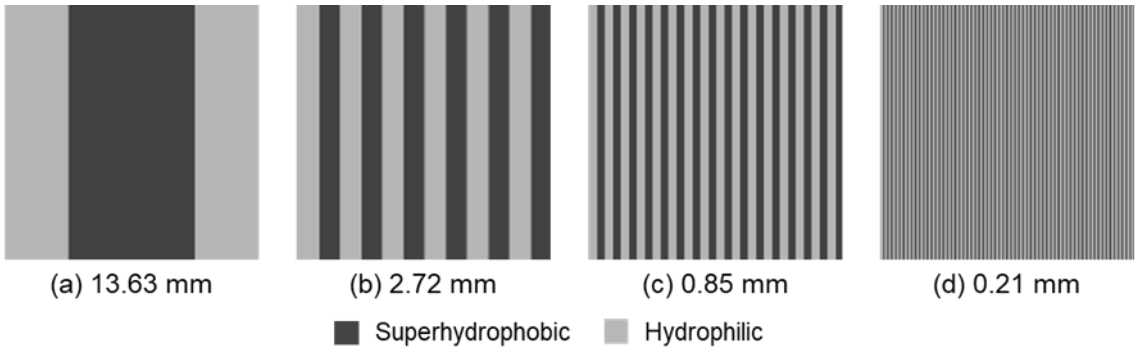

Figure 4.2. Diagram of the biphilic surfaces evaluated in this work (to scale).

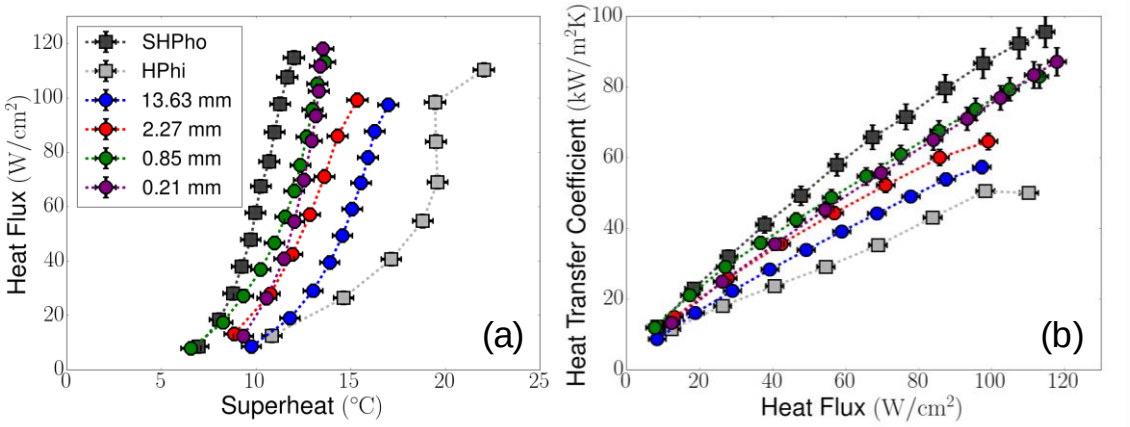

Figure 4.3. Pool boiling curves showing (a) heat flux versus superheat and (b) heat transfer coefficient versus heat flux for the uniform superhydrophobic (SHPho), uniform hydrophilic (HPhi), and biphilic surfaces evaluated in this work. The last point in each boiling curve marks where CHF occurs.

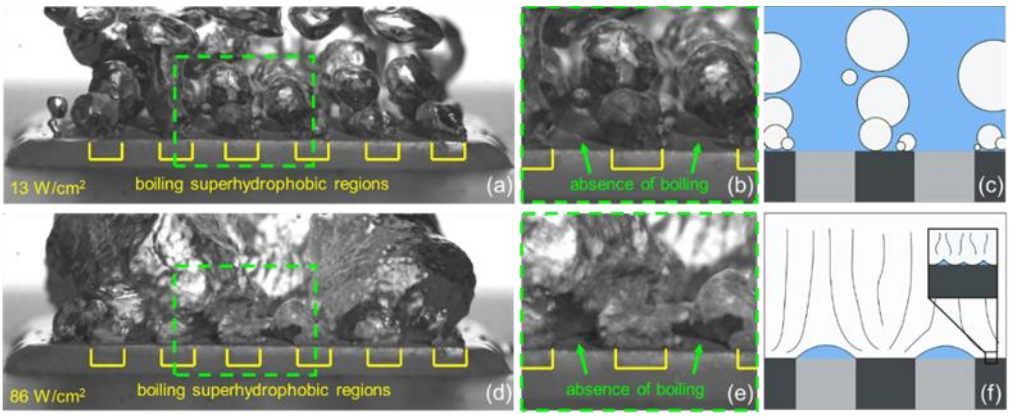

Figure 4.4. Visualization of boiling behavior on the biphilic surface with 2.27 mm-wide stripes at 13 W/cm^2 with (b) a zoomed-in view and (c) illustration portraying the boiling behavior featuring bubble coalescence and departure over superhydrophobic regions. (d) Visualization of the same surface at 86 W/cm^2 with (e) zoomed-in view and (f) illustration showing boiling on superhydrophobic regions and vapor coalescence directly above hydrophilic regions with an inset showing the local nucleate boiling behavior on the superhydrophobic regions.

5. EXPERIMENTAL INVESTIGATION OF THE ROLE OF DYNAMIC WETTING BEHAVIOR DURING BOILING

This chapter discusses a study on the boiling behavior of smooth and textured hydrophobic surfaces with differing dynamic wettability. Hydrophobic surfaces are shown to display ineffective film boiling behavior if they have high receding contact angles, but highly effective nucleate boiling if they have low receding contact angles. The boiling behavior of parahydrophobic surfaces with rose-like wetting behavior is investigated for the first time revealing exceptional heat transfer characteristics if the surface has a sufficiently low receding contact angle. This work demonstrates that the receding contact angle dominates bubble growth behavior and indicates whether premature critical heat flux will occur on a surface. The material from this chapter was published in the *International Journal of Heat and Mass Transfer* [132].

5.1 Surface Fabrication and Characterization

In this work, both smooth and textured hydrophobic surfaces with differing dynamic wettability were fabricated for boiling experiments. Both smooth and textured surfaces are coated with either polydimethylsiloxane (PDMS), a hydrophobic material with high contact angle hysteresis, and Teflon, a hydrophobic material with low contact angle hysteresis. All PDMS-coated and Teflon-coated surfaces were fabricated on aluminum test blocks while a copper test block was used for the smooth copper baseline surface. All surfaces were prepared by first wet-sanding a metal test block to a roughness of 400-600 nm (R_a) and cleaning with acetone, methanol, and isopropyl alcohol prior to any fabrication steps. Surface textures for the parahydrophobic surfaces were fabricated via chemical etching of aluminum [133]. The surface was etched for 4 hr in a 0.25 M solution of NaOH at room temperature, then rinsed with deionized water and blown dry with nitrogen. The surface texture for the superhydrophobic surface was created via laser etching (ULS, PLS6MW, 1.06 μm fiber laser). Smooth surfaces were not etched. Scanning electron microscope images of the metallic textured surfaces, along with a rose petal, are presented in Figure 5.1. Scanning electron microscopy images of the metal surfaces were taking using a Hitachi S-4800 field emission microscope. To obtain scanning electron microscope images of the rose petal with surface structures intact, the petal was fixed and critical point dried prior to

scanning. Specimens were fixed in 2% paraformaldehyde and 2% glutaraldehyde in 0.1 M sodium cacodylate buffer. They were then post-fixed in buffered 1% osmium tetroxide, dehydrated in a graded ethanol series, and dried in a Tousimis Autosamdri-931 critical point dryer. Dried specimens were coated with platinum in a Cressington 208HR sputter coater and imaged in a FEI Nova NanoSEM 200.

Hydrophobic wetting properties were attained by coating the surface with low-surface-energy polymers. For PDMS coatings, the surface was submerged for 1 hr at room temperature in a 1:10 base to curing agent solution of PDMS diluted in hexane; the surface was removed and cured at 150°C for 30 min. For Teflon coatings, the surface was submerged in a 1% wt/wt solution of Teflon powder dissolved in a fully-fluorinated liquid (Performance Fluid PF-5060, 3M) for 30 s and then cured at 150°C for 2 hr.

The wettability of each surface was characterized by static, advancing, and receding contact angles, with the measured values reported in Table 5.1. Static contact angles were measured by gently depositing a 5 µL droplet on the surface and measuring the angle with the solid surface using an automated goniometer (ramé-hart, 290-F1). Advancing and receding contact angle measurements were obtained via the same goniometer by inserting a 0.3 mm outer-diameter stainless steel syringe tip into the 5 µL droplet and adding or removing liquid in 0.25 µL increments until a steady contact angle was observed. In the case of the textured surfaces with low receding contact angle, stick slip behavior was observed during dynamic contact angle measurements which prevented the formation of a steady receding contact angle, as reported by He *et al.*[99]. In this case, the lowest receding contact angle observed before the droplet became too small to accurately measure is reported. For the parahydrophobic surfaces, an additional test was performed to evaluate the adhesion of a droplet to the surface. A 5 µL droplet was gently placed on the surface. The surface was then tilted to 90° to see if the droplet remains adhered. The wettability of PDMS has been observed to change after boiling in water[134]. We observed that the wettability of PDMS changes significantly within the first hour of boiling and then remains stable. Thus, the contact angles reported are those of a representative surface after being subjected to boiling water for 2 hr. For all other surfaces, the wettability did not change significantly after boiling and pre-test contact angles are reported. The rose characterized in this study was a red Freedom hybrid tea rose.

5.2 Experimental Procedure

The experimental facility, experimental boiling procedure and data analysis are the same as is discussed in Chapters 3.2 and 3.3 with the exception of the following details. Because the copper test block and aluminum test block have different hole depths for the corner thermocouple rakes, only the center and side rakes are considered in the data analysis. The water is degassed by initially heating the test surface to the boiling point via twelve 150 W cartridge heaters inserted into the base of the test block and then bringing the pool to saturation using the immersion heaters. This degassing procedure, which boils the surface while air is still trapped in the surface, maintains the Cassie-Baxter wetting state for the superhydrophobic surfaces; the procedure is chosen to demonstrate that parahydrophobic surfaces cannot form the Cassie-Baxter state, which would promote premature film boiling.

Bubble departure diameters and maximum base diameters were measured directly from high-speed videos taken during boiling, with pixel size calibrated based on the known surface width. For each surface, a high-speed video was recorded immediately after boiling incipience. The diameters are reported based on the average of measurements taken from the first unobscured nucleation site that activates on the interior of the surface and does not coalescing with other sites during the bubble ebullition cycle. For surfaces with repeated bubble departures from the same initial nucleation site (smooth PDMS and smooth copper), departure diameters and maximum base diameters were observed to vary by less than 10%. On the smooth Teflon surface, due to the long ebullition cycle and surface-level coalescence, only one isolated bubble departure was observed.

5.3 Results for Smooth Surfaces

Boiling experiments with smooth surfaces were carried out to determine the impact of the unique wetting behavior of two different hydrophobic coating materials in comparison with a hydrophilic copper baseline. The boiling curves for each of these surfaces (smooth copper, smooth PDMS-coated, and smooth Teflon-coated), along with the static and receding contact angle measurements, are shown in Figure 5.2. The hydrophilic copper baseline surface, having a static contact angle of 52 deg and a receding angle of ~10 deg, behaves as expected, exhibiting nucleate boiling behavior and reaching critical heat flux near Zuber's predicted limit [1]. The PDMS-coated surface has a high static contact angle (106 deg), but a similarly low receding contact angle (~10

deg). This surface sustains nucleate boiling and a cooler surface temperature than the baseline copper surface at all steady-state points on the boiling curve and reaches a similar critical heat flux. The Teflon-coated surface has high static and receding contact angles (123 deg and 111 deg, respectively). This surface exhibits low-temperature boiling incipience, but transitions to film-like boiling shortly after incipience, resulting in very high superheats as the heat flux is increased.

The boiling behavior at a low heat flux below 10 W/cm^2 is shown for each of these smooth surfaces in Figure 5.3. The different vapor formation characteristics that result in the differing boiling performance of the surfaces are evident. The copper and PDMS-coated surfaces both exhibit nucleate boiling; more active nucleation sites are observed on the hydrophobic PDMS-coated surface, resulting in a lower surface superheat (7.9 K) on this surface compared to the smooth copper (9.9 K). The Teflon-coated surface is blanketed in insulating vapor, resulting in high surface superheats. Remarkably, even though the two hydrophobic PDMS-coated and Teflon-coated surfaces have similar wettability in terms of the static contact angle, their boiling behavior is drastically different. The bubble dynamics observed on the PDMS-coated surface align more closely with the hydrophilic baseline surface.

As a bubble grows and the contact line expands outward from the nucleation site, the liquid is receding away. Thus, the receding contact angle could logically be expected to play a dominant role in the dynamics of bubble growth. The importance of the receding contact angle is clearly demonstrated in the single bubble dynamics at incipience, shown in Figure 5.4. The bubble behavior on the PDMS-coated and Teflon-coated surfaces is drastically different despite their similar static contact angles (106 deg and 123 deg, respectively). On both surfaces, the contact angle of a receding droplet (Figure 5.4a and Figure 5.4d) closely matches the contact angle of liquid receding away from the site of a growing bubble (Figure 5.4b and Figure 5.4e) during the early stages of bubble growth before buoyancy begins to distort the bubble shape. As a result, on the PDMS-coated surface, the base diameter of the bubble remains small during low-receding-angle growth (Figure 5.4c), which allows most of the surface to remain wetted. Once the bubble becomes large enough, buoyancy forces exceed the surface tension forces and the bubble departs. The minimal dewetting that occurs during bubble growth allows the notionally hydrophobic PDMS-coated surface to maintain nucleate boiling. On the Teflon-coated surface, the base diameter of the bubble spreads as the bubble grows with a high receding contact angle (Figure 5.4f). A single bubble reaches a base diameter of several millimeters, covering a large area of the

surface with vapor prior to departure. Once the bubble has reached some maximum base diameter, the bubble stretches upward due to buoyancy as it continues to grow and the liquid-vapor interface becomes nearly perpendicular to the solid surface as the bubble shape becomes dominated by buoyancy effects. The base diameter begins to recede, followed by the bubble departing by pinching off above the surface, leaving behind a small vapor bubble. Due to the extensive vapor spreading during bubble growth, active nucleation sites readily coalesce resulting in premature film boiling at a low heat flux.

5.4 Model Development

To explain the role of the receding contact angle during bubble growth, a simple analytical model is derived to predict the bubble departure diameter and maximum base diameter. The bubble growth model considers a balance between the buoyancy force acting upward on the bubble

$$F_b = (\rho_l - \rho_v)Vg \tag{5.1}$$

(where ρ_l and ρ_g are the densities of the liquid and vapor, V the bubble volume, and g the gravitational constant) and the surface tension force holding it to the surface

$$F_s = \gamma(\pi D_b)\sin\theta \tag{5.2}$$

(where γ is the liquid-vapor surface tension, D_b the base diameter of the bubble, and θ the contact angle). It is assumed that the bubble grows with the liquid at the receding contact angle as a spherical cap. The volume of a spherical cap can be calculated according to [135] (variables defined in Figure 5.5):

$$V_{cap} = \frac{1}{3}\pi R^3\left(2 - 3\sin\alpha + \sin^3\alpha\right) \tag{5.3}$$

The sphere radius, R, and the angle, α, are substituted for the bubble base diameter, D_b, and the liquid receding contact angle, θ_{rec}, which can be readily measured in the experiments. The sphere radius is related to the bubble base diameter as $\cos\alpha = D_b / 2R$. The angle α can be related to the liquid receding contact angle as $\alpha = \theta_{rec} - \pi/2$. Substituting these expressions into equation (5.3):

$$V_{cap} = \frac{1}{24}\pi\left(\frac{D_b}{\sin\theta_{rec}}\right)^3\left(2 + 3\cos\theta_{rec} - \cos^3\theta_{rec}\right) \tag{5.4}$$

Substituting equation (5.4) into the relation for the buoyancy force (equation (5.1)), and setting the buoyancy force equal to the surface tension force (*i.e.* the condition for bubble departure), the balance between buoyancy and surface tension forces is

$$\frac{1}{24} g\left(\rho_l - \rho_v\right)\pi\left(\frac{D_b}{\sin\theta_{rec}}\right)^3\left(2+3\cos\theta_{rec}-\cos^3\theta_{rec}\right) = \gamma_{lv}\pi D_b \sin\theta_{rec} \qquad (5.5)$$

Equation (5.5) can be simply solved to obtain an expression for the bubble base diameter immediately prior to departure:

$$D_b = \sqrt{\frac{24\gamma_{lv}\sin^4\theta_{rec}}{g\left(\rho_l-\rho_v\right)\left(2+3\cos\theta_{rec}-\cos^3\theta_{rec}\right)}} \qquad (5.6)$$

Once this base diameter and spherical cap volume are known, the bubble departure diameter can be obtained assuming the bubble departs as a sphere,

$$D_{depart} = \sqrt[3]{6V_{cap}/\pi} \qquad (5.7)$$

For a surface with a low receding contact angle (less than 90 deg), the bubble growth progression can be approximated as illustrated in Figure 5.6a-c. The bubble grows as a spherical cap with the liquid at the receding contact angle until it reaches a critical size at which the buoyancy and surface tension forces are balanced (Figure 5.6a). Then, the base diameter begins to retract as the bubble begins to rise (Figure 5.6b), and ultimately departs from the surface as a sphere (Figure 5.6c). Based on this progression, the maximum vertical component of the surface tension forces occurs when the buoyancy and surface tension forces first become balanced (Figure 5.6a). Thus, the maximum base diameter and departure diameter of the bubble can be determined by evaluating equation (5.6), (5.4) and (5.7), using the receding contact angle of the surface. This results in a trend of increasing bubble departure diameter and maximum base diameter with increasing receding contact angle from 0 to 90 deg as shown in Figure 5.6g.

For a surface with a high receding contact angle (greater than 90 deg), the bubble growth progression can be approximated as illustrated in Figure 5.6d-f. The bubble grows as a spherical cap at the receding contact angle until it reaches a size at which the buoyancy force and the vertical component of the surface tension force become balanced (Figure 5.6d). The bubble base diameter begins to retract, and the bubble begins to deform upward due to buoyancy effects (Figure 5.6e). As a result, the liquid contact angle decreases, causing the vertical component of the surface

tension forces to increase as the bubble continues to grow. Ultimately, the bubble departs by pinching-off just above the surface, leaving behind a small vapor bubble on the surface (Figure 5.6f). Because of the pinch-off mechanism, the limiting surface tension force, after which departure process begins via the retracting of the diameter at the pinch-off height, is expected to occur at the point where the interface is perpendicular to the surface. Thus, the bubble size is determined based on the elongated bubble represented by Figure 5.6e, with the interface assumed to be perpendicular to the surface at the height at which the pinch-off occurs. The departure volume is determined using equation (5.4) and (5.6) based upon a receding contact angle of 90 deg, assuming the bubble above the pinch-off height can be approximated as a spherical cap and the volume below the pinch-off location remains on the surface. The departure diameter can then be trivially determined using equation (5.7). Because the limiting surface tension forces occur at an angle perpendicular to the surface rather than at the receding contact angle, all surfaces with a receding contact angle greater than 90 deg are predicted to have the same departure diameter. The maximum base diameter is estimated by considering the volume of the departed bubble as a spherical cap with a contact angle equal to the receding contact angle of the surface, resulting in an increasing trend in maximum base diameter with increasing receding contact angle above 90 deg; this is expected to be an overestimate due to neglect of the bubble deformation by buoyancy.

The experimental results closely follow the trends of bubble departure diameter and base diameter with increasing receding contact angle and match the expected magnitudes, as shown in Figure 5.6g. The model slightly underpredicts the departure diameter on a surface with a low receding contact angle and, as expected, overpredicts the maximum base diameter on a surface with a high receding contact angle. This agreement confirms the dominant role of the receding contact angle on bubble growth and departure dynamics.

5.5 Results for Textured Surfaces

This newfound understanding that the receding contact angle governs bubble growth dynamics is next used to design textured hydrophobic surfaces that provide favorable bubble dynamics to avoid premature critical heat flux while further enhancing nucleate boiling. Based on the results of the previous sections, it is evident that previously observed vapor spreading on hydrophobic surfaces [5,8,10–12,14,136] can be mitigated by minimizing the receding contact angle of the surface. To further demonstrate this understanding, the wettability characteristics and

boiling performance of a high-hysteresis parahydrophobic surface versus a low-hysteresis superhydrophobic surface (in the Cassie-Baxter state) are reported in Figure 5.7. These surfaces feature the same PDMS coating material, but different textures give rise to their drastically different dynamic wetting behaviors. The parahydrophobic PDMS-coated surface, which is textured to provide wetting properties similar to those of the rose petal (as shown in Figure 5.7), has a high static contact angle (144 deg) and a low receding contact angle (~30 deg). Due to the high contact angle hysteresis, a 5 μL droplet deposited on this surface remains adhered even when tilted at a 90 deg angle or inverted. Textured to minimize contact angle hysteresis, the superhydrophobic PDMS-coated surface also has a high static contact angle (151 deg) but paired with a high receding contact angle (147 deg). Due to the minimal contact angle hysteresis, droplets readily roll off this surface when tilted, similar to the classical behavior of the lotus leaf [90].

As hypothesized, the contrast in the receding contact angles results in stark differences in the boiling behavior and heat transfer performance. The superhydrophobic PDMS-coated surface exhibits film boiling behavior immediately upon incipience and throughout the boiling curve, resulting in large surface superheat increases with small increases in heat flux. The parahydrophobic PDMS-coated surface maintains nucleate boiling to a high heat flux and even further reduces surface temperatures compared to the smooth PDMS-coated surface; at a low heat flux of ~ 8 W/cm^2, a 60% increase in the heat transfer coefficient (heat flux divided by surface superheat) is observed compared to the smooth copper surface.

By tailoring the wettability to resemble that of the rose petal, the boiling performance is enhanced considerably due to favorable bubble dynamics. As presented in Figure 5.8, the low receding contact angle characteristic of the parahydrophobic PDMS-coated surface minimizes the bubble base diameter during bubble growth; tiny bubbles have a near-perfect spherical shape as they grow and readily depart from the surface (Figure 5.8a). This behavior sustains nucleate boiling even under conditions with dense, vigorous vapor formation across the entire surface by minimizing surface dewetting (Figure 5.8b). On the superhydrophobic surface, the base diameter of the bubbles spreads freely as the bubble grows at the receding contact angle. As a result, the first bubble that forms covers much of the surface in vapor and extensive surface-level coalescence occurs prior to a single bubble departure (Figure 5.8c). Due to the promotion of the Cassie-Baxter state, this region traps vapor in the interstices of the surface structures and is never able to rewet.

Thus, the surface becomes blanketed in vapor easily, resulting in premature film boiling (Figure 5.8d).

In the previous work from Chapter 3 [126], superhydrophobic surfaces were shown to promote effective nucleate boiling if brought into the Wenzel state prior to boiling, but to suffer ineffective film boiling if in the Cassie-Baxter state prior to boiling. The initial wetting state on the surfaces in Chapter 3 was controlled via the degassing procedure. Importantly, the parahydrophobic PDMS-coated surface in the current study maintains nucleate boiling even under conditions that promote a Cassie-Baxter wetting state on superhydrophobic surfaces. Parahydrophobic surfaces can thereby remove the risk of premature film boiling, because they do not support a Cassie-Baxter wetting state. These surfaces capitalize upon the advantages of hydrophobicity (*i.e.*, promotion of boiling incipience at low superheats and high nucleation site densities that yield efficient heat transfer) while mitigating the vapor spreading and premature film boiling that commonly plague hydrophobic boiling surfaces. With further geometric optimization of the texture geometry to promote nucleation and reduce the receding contact angle, parahydrophobic surfaces offer a very promising approach to minimize surface temperatures during boiling without negatively affecting the critical heat flux.

We caution that a surface satisfying the notional criteria for 'parahydrophobicity' does not automatically ensure that it will yield advantageous boiling characteristics. There is no consensus in the research community on the specific wetting characteristics that define parahydrophobicity, but a surface is typically regarded as being parahydrophobic if it has a high static contact angle (approaching or exceeding 150 deg) and a droplet can remain adhered to the surface when tilted at 90 deg or inverted. Because adhesion of a droplet to a surface when tilted is governed by the contact angle hysteresis, all notionally parahydrophobic surfaces do not necessarily possess the low receding contact angle required for maintaining nucleate boiling. This is demonstrated next by evaluating the boiling performance of a parahydrophobic Teflon-coated surface with the same textured surface morphology as the parahydrophobic PDMS-coated surface, presented in Figure 5.9d. Like the rose petal and the parahydrophobic PDMS-coated surface (Figure 5.9a and Figure 5.9c, respectively), the Teflon-coated surface is considered parahydrophobic owing to a high static contact angle (135 deg) and the adherence of a 5 μL droplet to the surface when tilted at 90 deg (attributable to a high contact angle hysteresis of ~40 deg), shown in Figure 5.9b. However, unlike for a PDMS coating, the parahydrophobic Teflon-coated surface has a high receding contact angle

(105 deg) and was observed to undergo premature film boiling, resulting in significant increases in surface superheat with increasing heat flux. This reinforces the assertion that the receding contact angle governs vapor spreading during boiling, rather than the contact angle hysteresis which is used to identify parahydrophobicity.

5.6 Conclusions

The set of experiments described in this chapter has clarified the roles of different wettability characteristics on boiling behavior. The intrinsic wettability of the surface, as indicated by static contact angle measurements, plays a role in the nucleation behavior and heat transfer efficacy of a surface during boiling; however, the receding contact angle is the dominant factor governing the bubble growth dynamics and, ultimately, the critical heat flux on surfaces in the absence of capillary wicking. The hydrophobic surfaces with low receding contact angles evaluated in this study maintain the advantageous low-superheat boiling incipience and high active nucleation site densities commonly observed on hydrophobic surfaces, but prevent the vapor spreading during bubble growth that commonly plagues these surfaces. This results in decreased surface temperatures during nucleate boiling compared to hydrophilic surfaces and little to no detriment to critical heat flux.

Texturing hydrophobic surfaces to minimize the receding contact angle provides a further avenue for boiling performance enhancement. For the first time, the boiling behavior of parahydrophobic surfaces with rose-petal-like wettability is studied. Textured parahydrophobic surfaces with low receding contact angles are demonstrated to improve the boiling efficacy compared to smooth hydrophobic surfaces of the same material through further reduction in surface temperatures.

The understanding obtained in this study ushers in a new class of surfaces with wide applicability for enhanced boiling: hydrophobic surfaces that have low receding contact angles. Additional investigation is warranted into hydrophobic coating materials with high contact angle hysteresis and texturing approaches to promote parahydrophobic behavior while minimizing the receding contact angle.

Table 5.1. Average contact angle measurements for each surface studied

	static contact angle	receding contact angle	advancing contact angle	contact angle hysteresis
smooth copper	52°	~10°	66°	56°
smooth PDMS	106°	~10°	110°	100°
smooth Teflon	123°	111°	129°	18°
rose petal	145°	~30°	154°	~120°
parahydrophobic PDMS	144°	~30°	161°	~130°
superhydrophobic PDMS	151°	147°	156°	9°
parahydrophobic Teflon	135°	105°	146°	41°

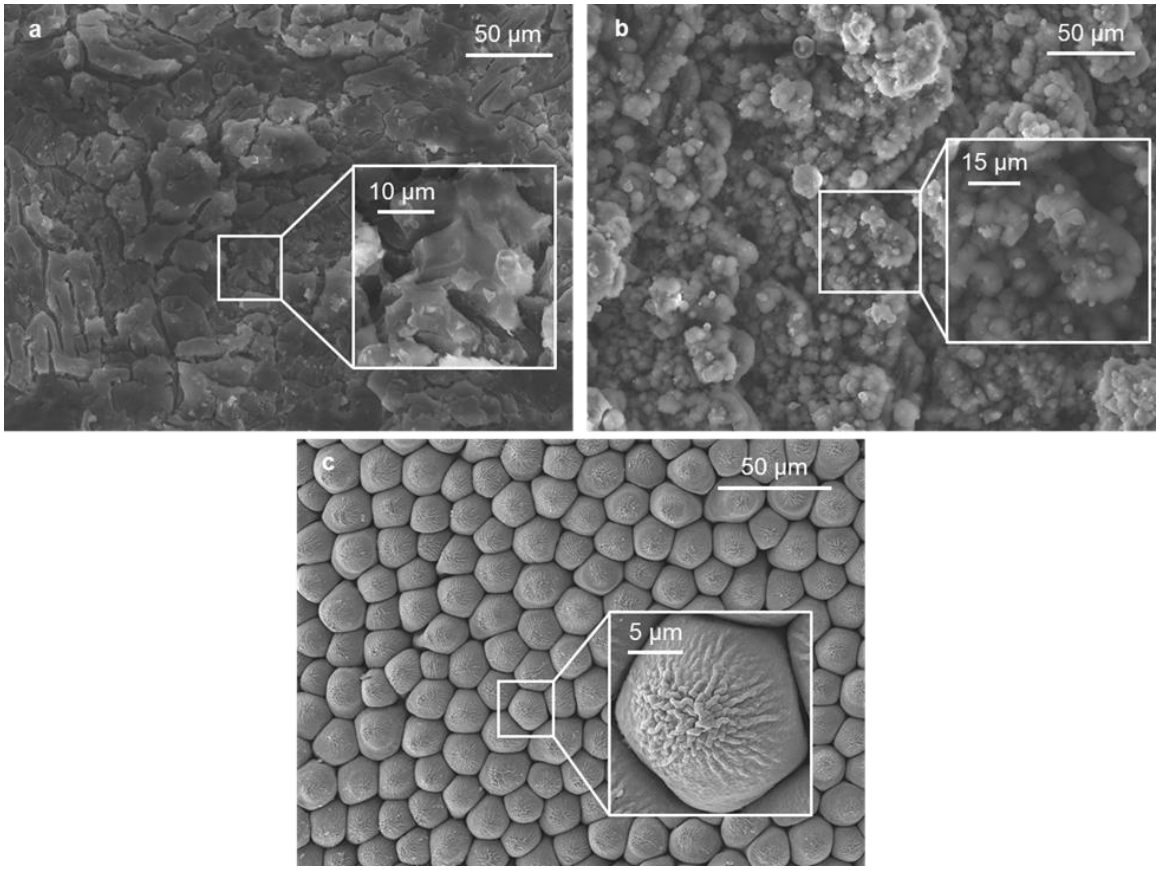

Figure 5.1. Scanning electron microscope images of the aluminum textured surfaces fabricated in this study. **a** Chemically-etched parahydrophobic surface texture with large (tens of microns) relatively smooth structures separated by fissures. **b** Laser-etched superhydrophobic surface texture with stochastic roughness made up of fused spheroidal particles; structures range in size from ones to tens of microns. **c** Rose petal surface with micron-sized ridges on top of microscale bumps on the order of tens of microns.

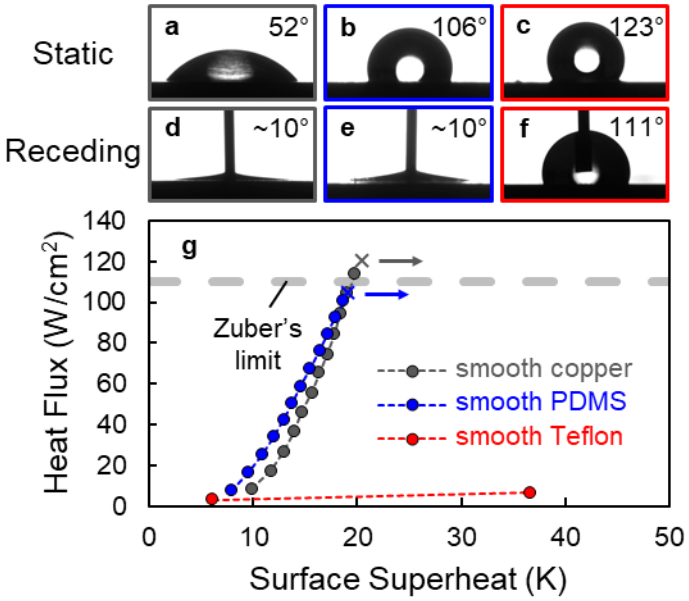

Figure 5.2. Wettability characterization and boiling results for smooth hydrophilic and hydrophobic surfaces. Static 5 µL droplets on **a** smooth copper, **b** smooth PDMS-coated, and **c** smooth Teflon-coated surfaces. Receding droplets on **d** smooth copper, **e** smooth PDMS-coated, and **f** smooth Teflon-coated surfaces. **g** Boiling curves (heat flux versus surface superheat) for each of the smooth surfaces. Calculated uncertainties in heat flux and surface superheat are less than 3 W/cm^2 and 0.7 K, respectively. Crosses with a rightward arrow indicate critical heat flux and subsequent temperature excursions. The horizontal dashed line indicates the critical heat flux predicted by Zuber's proposed hydrodynamic limit.

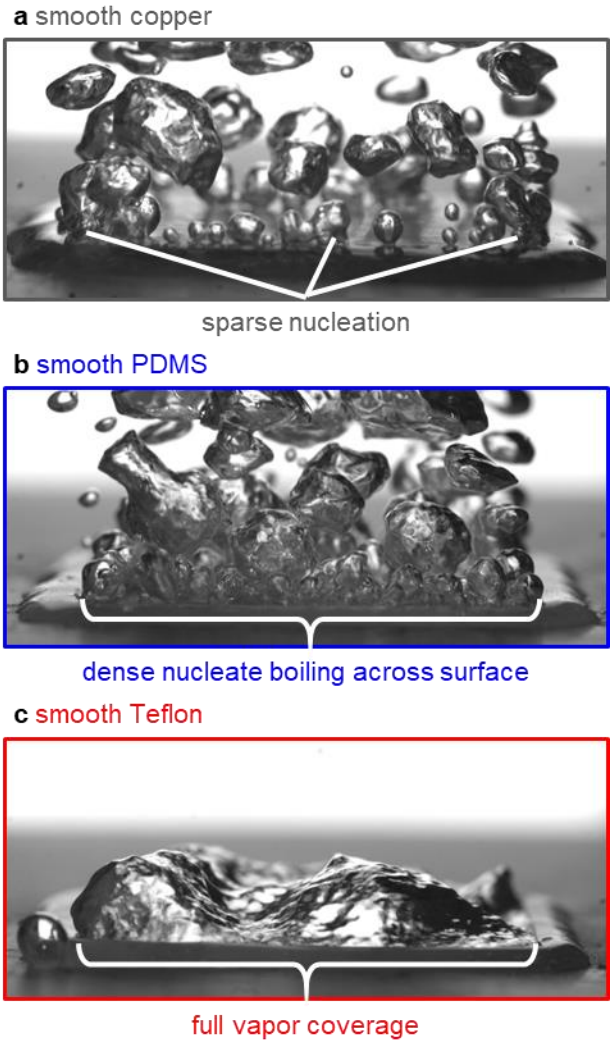

Figure 5.3. Images comparing the boiling behavior on smooth surfaces. **a** Sparse nucleate boiling from the smooth copper surface (heat flux: 8.3 W/cm^2; superheat: 9.9 K), **b** dense nucleate boiling from the smooth PDMS-coated surface (7.5 W/cm^2; 7.9 K), and **c** film boiling from the smooth Teflon-coated surface (6.7 W/cm^2; 36.7 K).

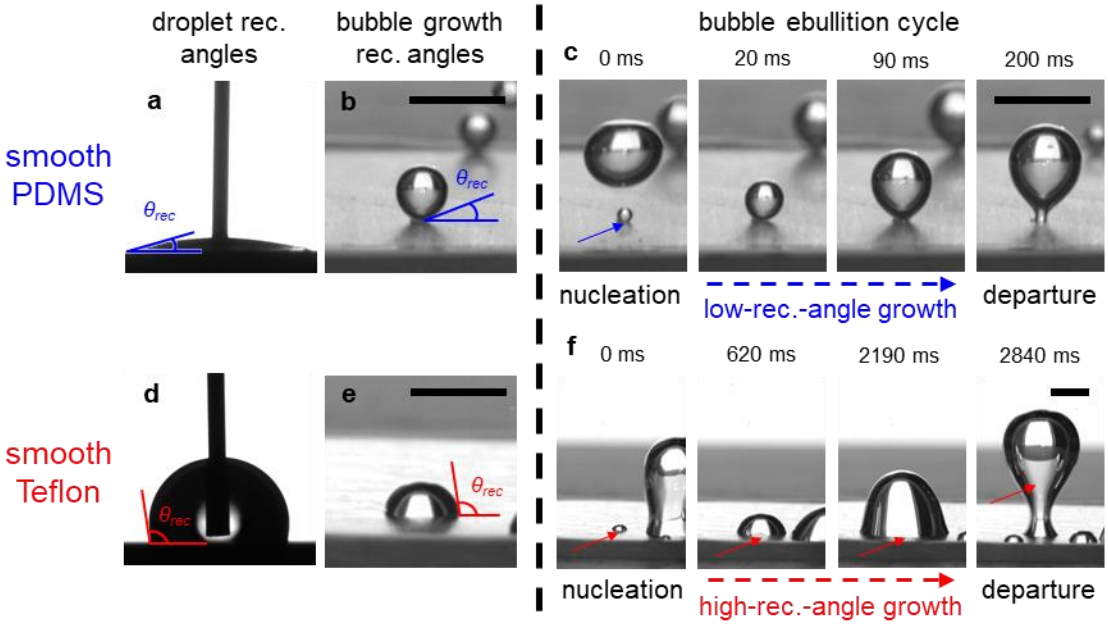

Figure 5.4. Bubble growth dynamics and ebullition cycle. **a** Receding contact angle measurement of a droplet on the smooth PDMS-coated surface and **b** image showing a similarly small receding contact angle during bubble growth on the same surface. **c** Bubble ebullition cycle on a PDMS-coated surface exhibiting low-receding-angle growth. **d** Receding contact angle measurement of a droplet on the Teflon-coated surface and **e** image of a growing bubble on the same surface showing a similarly large receding contact angle. **f** Bubble ebullition cycle on a Teflon-coated surface exhibiting high-receding-angle growth. Scale bars, 3 mm. Note the different length and time scales indicated on **c** and **f**.

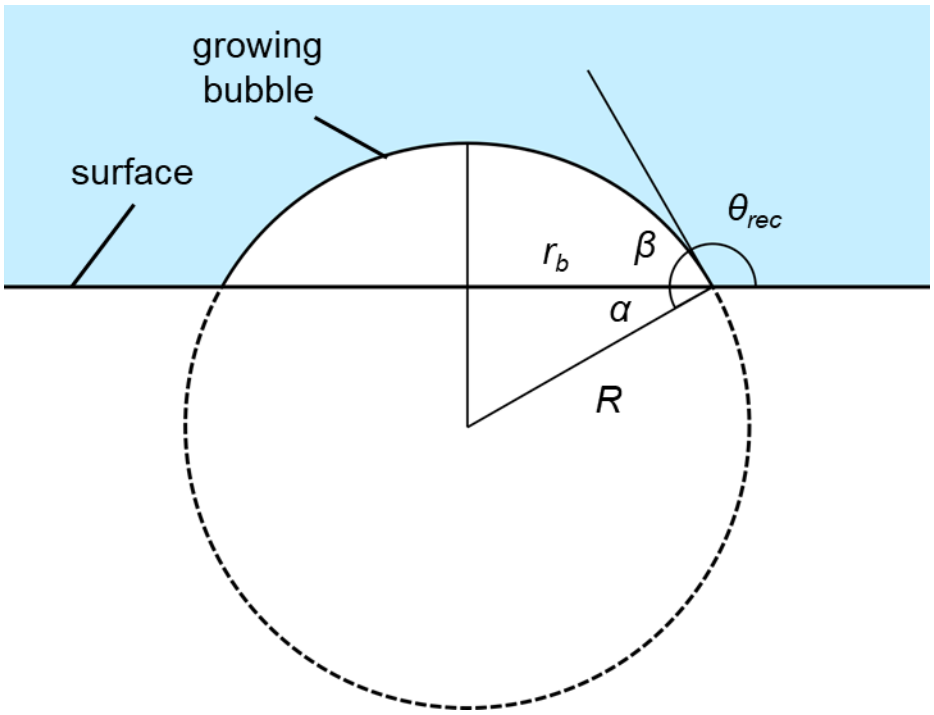

Figure 5.5. Schematic illustration of the geometry of a spherical cap bubble at the receding contact angle.

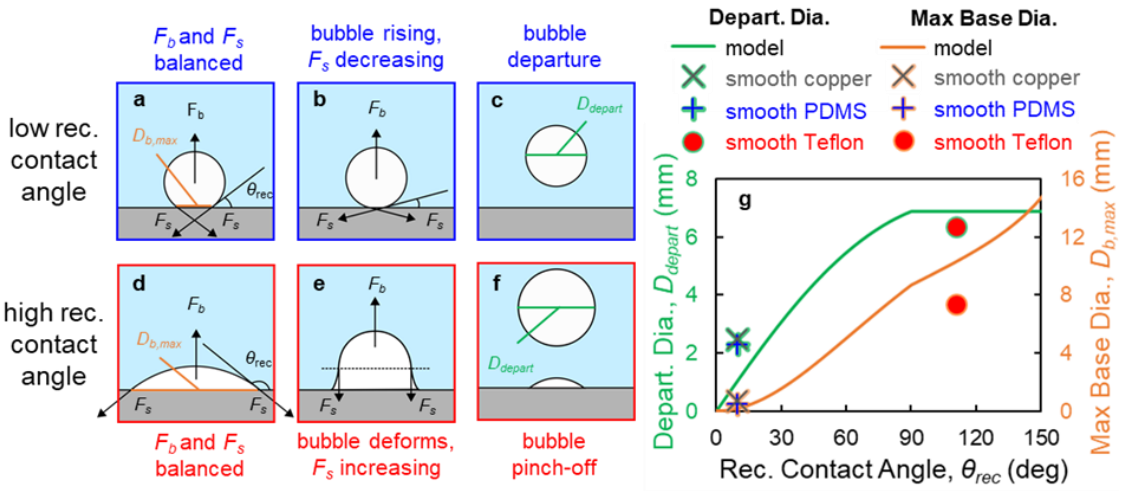

Figure 5.6. Illustration of approximate bubble growth progressions and results of bubble growth model. Bubble growth and departure on a surface with **a-c** low receding contact angle and **d-f** high receding contact angle. **g** Model results for the bubble departure diameter and maximum bubble base diameter plotted along with experimental results from the smooth surfaces.

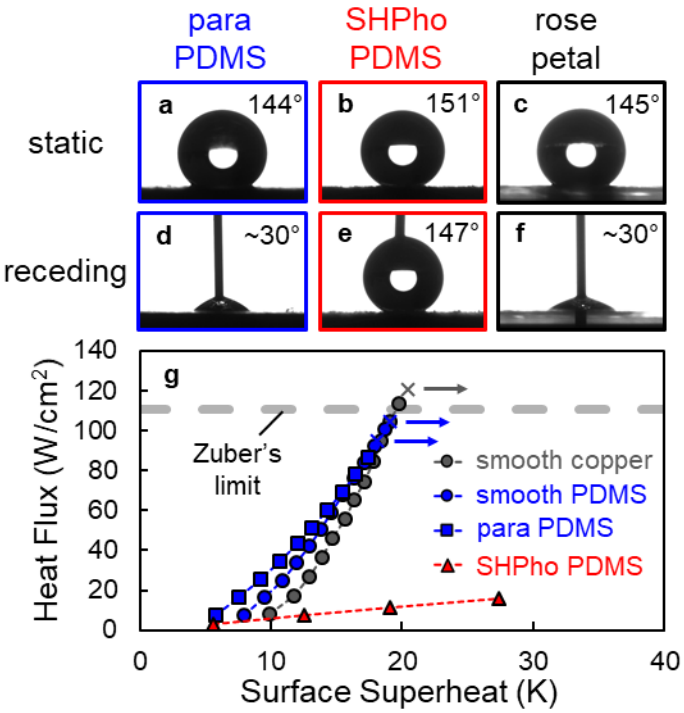

Figure 5.7. Wettability characterization and boiling results for textured PDMS-coated surfaces. Static 5 µL droplets on **a** parahydrophobic PDMS-coated surface (para PDMS), **b** superhydrophobic PDMS-coated surface (SHPho PDMS), and **c** rose petal. Receding droplets on **d** parahydrophobic PDMS-coated surface, **e** superhydrophobic PDMS-coated surface, and **f** rose petal. **g** Boiling curves (heat flux versus surface superheat) for the textured PDMS-coated surfaces compared with the smooth copper and PDMS-coated surfaces. Calculated uncertainties in heat flux and superheat are less than 3 W/cm^2 and 0.7 K, respectively. Crosses with a rightward arrow indicate critical heat flux and subsequent temperature excursions. The horizontal dashed line indicates the critical heat flux predicted by Zuber's proposed hydrodynamic limit.

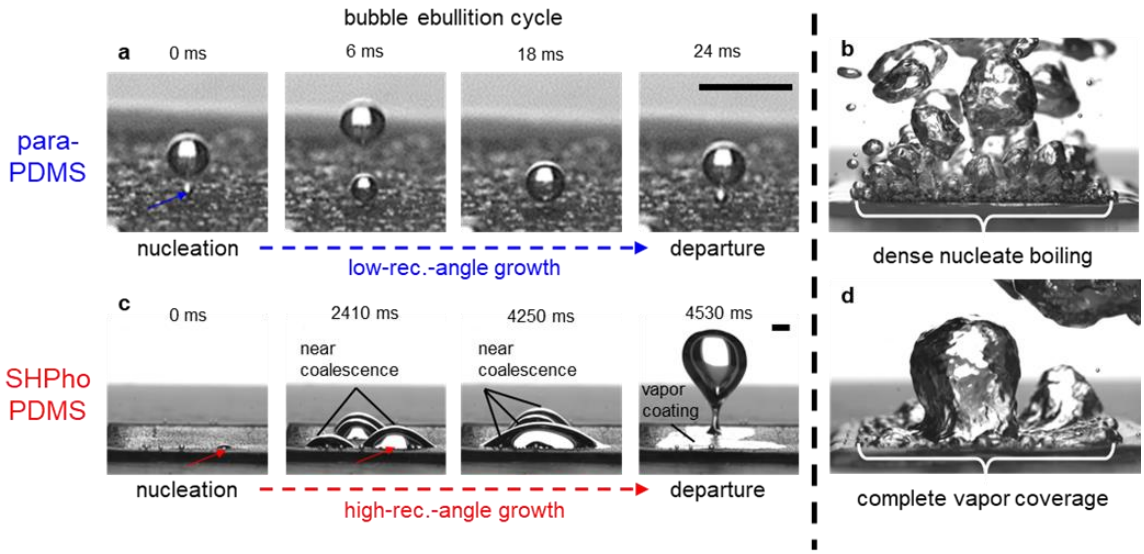

Figure 5.8. Comparison of the bubble ebullition cycle and boiling behavior of the textured PDMS-coated surfaces. **a** Bubble ebullition cycle on the parahydrophobic PDMS-coated and **c** growth, coalescence and departure of first bubbles on the superhydrophobic PDMS-coated surface at incipience. Low-heat-flux boiling behavior of **b** the parahydrophobic PDMS-coated surface (heat flux: 7.8 W/cm^2; superheat: 5.8 K) and **d** the superhydrophobic PDMS-coated surface (7.3 W/cm^2; 12.5 K). Scale bars, 2 mm.

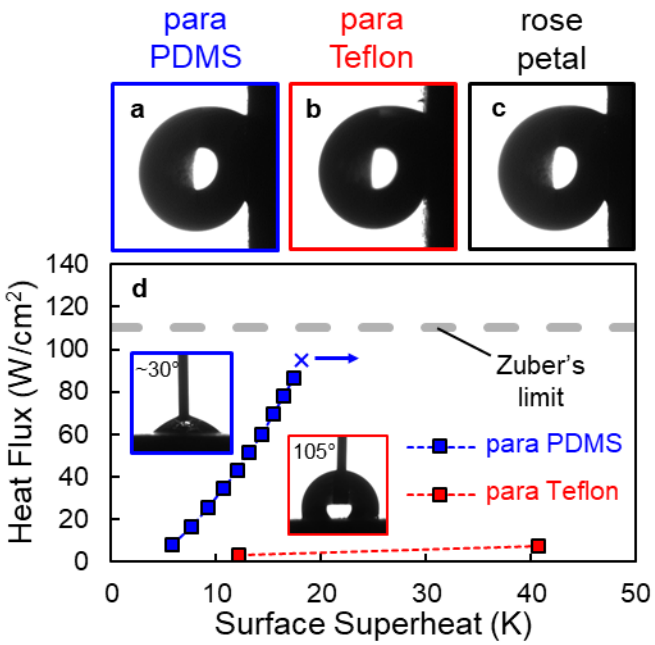

Figure 5.9. Wetting behavior and boiling results for parahydrophobic PDMS-coated (para PDMS) and Teflon-coated (para Teflon) surfaces. A 5 µL droplet adhered to **a** parahydrophobic PDMS-coated surface, **b** parahydrophobic Teflon-coated surface, and **c** rose petal while tilted at 90°. **d** Boiling curves (heat flux versus surface superheat) for the two parahydrophobic surfaces with insets showing the receding contact angle measurements for each surface. Calculated uncertainty for the heat flux and superheat are less than 3 W/cm^2 and 0.7 K, respectively. Cross with a rightward arrow indicates critical heat flux and the subsequent temperature excursion. The horizontal dashed line indicates the critical heat flux predicted by Zuber's proposed hydrodynamic limit.

6. NUMERICAL INVESTIGATION OF THE ROLES OF RECEDING AND ADVANCING CONTACT ANGLES DURING SINGLE BUBBLE DYNAMICS

In this chapter, a new theoretical framework for the wetting and dewetting processes occurring during single bubble growth is developed based upon the dynamic advancing and receding contact angles. Adiabatic volume-of-fluid simulations, which integrate this framework to accurately capture the influence of the surface wettability on contact line and contact angle dynamics during bubble growth and departure, are performed for a variety of fluids across a large range of dynamic wetting behaviors. The receding contact angle is shown to govern the early stages of growth as the liquid recedes from the bubble site and is the dominant wetting characteristic that determines the maximum contact diameter and the departure diameter. The advancing contact angle dictates the departure morphology and plays a supporting role is determining the departure size. Based upon the simulation results, new models for the maximum contact diameter and departure diameter are developed and are shown to improve predictive accuracy compared to existing standards. The resulting understanding reveals the need to redefine hygrophilicity and hygrophobicity in the context of boiling applications based on the dynamic contact angles rather than the static contact angle. Additionally, a new regime of surface wettability, ambiphilicity, is defined for surfaces exhibiting low receding contact angles and high advancing contact angles which results in unique bubble dynamics sharing elements of both hygrophilicity and hygrophobicity.

6.1 Methods

6.1.1 Theoretical Framework for Dynamic Wetting during Bubble Growth and Departure

We propose an intuitive framework for the contact angle and contact line dynamics during bubble growth that is based on fundamental wetting dynamics [137]. The key assertion is that contact line motion is governed by the dynamic contact angles. If the liquid is at the receding contact angle, it can recede if the acting forces so dictate, but it cannot advance. Similarly, the liquid can advance when at the advancing contact angle but cannot recede. At any contact angle

between the advancing and receding contact angles, the contact line will be pinned in place and will not move. Instead, acting forces will alter the contact angle and bubble morphology.

When discussing the proposed framework for the case of bubble growth and departure, the contact angles referenced are always with respect to the liquid. The dominant forces considered during quasisteady growth are the buoyant force ($F_b = \Delta\rho V g$) and the surface tension force ($F_s = \sigma\pi D_c \sin\theta$). For the initial stage of bubble growth, the contact line expands from the nucleation site as the bubble grows (*i.e.* the liquid recedes from the nucleation site). During this dewetting process, the liquid is expected to be at the receding contact angle as shown in Figure 6.1(a). Eventually, an initial force balance is reached between the buoyant and surface tension forces at the receding contact angle and receding stops. However, because the liquid cannot *advance* at the *receding* contact angle, it will not immediately depart. Instead, the contact angle will start to increase with a pinned contact line, as shown in Figure 6.1(b), to accommodate the increasing buoyant force of the growing bubble. Once the bubble has grown such that the advancing contact angle is reached, advancing can occur. Thus, the liquid rewets the surfaces as the contact line advances at the advancing contact angle, as shown in Figure 6.1(c). In short, the bubble initially grows in a constant contact angle mode at the receding contact angle, followed by a constant contact radius mode as the contact angle spans the contact angle hysteresis, and finally a constant contact angle mode at the advancing contact angle as the bubble departs. Kim *et al.* [138] reported a similar three stage process based on experimental measurements and attributed the transitions between stages to differences in free energy rather than the dynamic contact angles. These resulting dynamics are analogous to those commonly reported for droplet evaporation featuring constant contact radius and constant contact angle modes [139].

Following this framework, the bubble morphology during growth and departure is governed by the dynamic contact angles; the static contact angle is not considered as it has no role in contact line or contact angle dynamics. The bubble morphology during the early stages of growth is governed by the receding contact angle, the time spent in the pinned mode is governed by the contact angle hysteresis, and the departure morphology is governed by the advancing contact angle. The effect of contact line velocity on the dynamic contact angles is neglected, though it may have an influence during rapid bubble growth [140,141]. The growth is assumed to be quasisteady and dominated by surface tension and buoyancy effects.

6.1.2 Numerical Simulation of Bubble Growth and Departure with Dynamic Wetting Effects

The proposed theoretical framework for the contact line and contact angle dynamics during bubble growth and departure is implemented within a transient two-phase continuum surface force volume-of-fluid (CSF-VOF) simulation (ANSYS Fluent) to determine the roles of the advancing and receding contact angles on the bubble morphology, departure diameter, and maximum contact diameter. The simulations are performed using a rectangular, 2D axisymmetric domain as shown in Figure 6.2. A uniform square mesh with cell widths of 0.01 mm is applied throughout the domain. The domain size is adjusted from case to case based on the bubble size to minimize computational time while avoiding interactions with the side walls. The top boundary acts as a mixed outlet with a constant pressure of 1 atm. The outer radial boundary is a no-slip wall. The bottom boundary, which has contact with the bubble, is used to apply a user-defined boundary condition for the contact angle and contact line based on the proposed dynamics. The simulation is completely adiabatic; no heat transfer or phase change is considered.

For VOF simulations, the phases are tracked based on the volume fraction, ϕ, within each individual cell. In this work, the phases are defined based upon the vapor volume fraction. As labeled in Figure 6.2, liquid is present where $\phi = 0$ (shown in blue) and vapor is present where $\phi = 1$ (shown in red). The interface is found anywhere $0 < \phi < 1$. In VOF solvers, a single set of the Navier-Stokes equations, which incorporates the volume fraction, is solved to determine the flow field. Using a geometric reconstruction interpolation scheme (Geo-Reconstruct) and a well-resolved mesh, the interface is accurately tracked in time. The volume fraction is useful in determining the location of the contact line and the value of the contact angle throughout the simulation. The contact line location is considered to be at the cell adjacent to the bottom boundary with a volume fraction closest to 0.5. The contact angle can be calculated based on the gradient of the volume fraction at the contact line ($\theta = \cos^{-1}\left((\nabla\phi)_z / |\nabla\phi|\right)$). The contact angle is measured at the interface cells in the second row from the bottom boundary to ensure an accurate gradient calculation. Both of these values are tracked and recorded every 50 time steps throughout the simulation. A variable time step is implemented to ensure the Courant number remains less than 0.25, with a maximum time step of 1×10^{-6} s to mitigate the development of spurious current.

The domain is initialized to be entirely liquid, except for the initial bubble. For each case, the bubble is initialized as a spherical cap at the receding contact angle where is overall sphere

radius would be 0.3 mm. This provides a stable bubble with a contact radius smaller than the smallest maximum bubble radius observed to ensure that the maximum bubble radius and departure size are not influenced by the initial condition. The bubble grows as a result of a user-defined mass source that is evenly distributed volumetrically across all vapor cells where $\phi = 1$. It is well known that inertia can play a dominant role in the bubble growth and departure process at high growth rates. In this study, the goal is to obtain quasisteady bubble growth that is independent of inertial effects. Thus, the growth rate is scaled based on the contact diameter. Oguz and Prosperetti [142] defined a critical volumetric growth rate for bubbles growing adiabatically from a needle, below which the departure size is independent of growth rate. It was adapted here based on the contact diameter rather than the needle diameter and is shown in equation (6.1) where g is the gravitational acceleration, σ is the surface tension, D_c is the contact diameter, and ρ_l is the liquid density.

$$Q_{cr} = \pi \left(\frac{16}{3g} \right)^{1/6} \left(\frac{\sigma D_c}{\rho_l} \right)^{5/6} \tag{6.1}$$

To be conservative, the growth rate for the simulations is set to be 10% of the critical growth rate given by equation (6.1) in all cases with the exception the water cases with a 30 deg receding contact angle. In these cases, the variable growth rate led to numerical instability. Instead a constant growth rate of 50 mm^3/s was used, which is varies between 8-12% of the critical growth rate given in equation (6.1).

The contact angle boundary condition and the contact line motion at the bottom boundary are controlled using a user-defined function. This consists of two key components: a variable contact angle boundary condition and a contact line pinning mechanism. The contact angle boundary condition is native to ANSYS Fluent and sets the volume fraction gradient at the cell adjacent to the wall accordingly. To pin the contact line, a momentum source is applied at the contact line, similar to the approach by Malgarinos *et al.* [143] during droplet impingement. The momentum source is somewhat analogous to a proportional-derivative (PD) controller and takes the form $S_m = \pm k_1 \left(r_{CL} - r_{pin} \right)^2 - k_2 \rho_{CL} \dot{r}_{CL}$, where k_1 and k_2 are proportionality constants, r_{CL} is the radial position of the contact line, r_{pin} is the location the contact line should be pinned at, ρ_{CL} is the density of the cell that contains the contact line, and $\dot{r}_{CL}$ is the radial velocity of the contact line. The magnitude of the momentum source increases as the distance between the current contact line

location and the target pinning location increases and as the velocity increases. To distribute the momentum source and minimize instabilities, the source is applied in a total of six cells (the cells at and adjacent to the radial location of the contact line within the two mesh rows closest to the surface). The constants, k_1 and k_2, are tuned such that the contact line generally remains within one cell from the target pinning location during a pinning mode.

In implementing these two tools, the goal is to simply ensure that the contact line is only able to recede if it is at the receding contact angle and is only able to advance if it is at the advancing contact angle. In this way, appropriate wetting dynamics are ensured, but the proposed framework for bubble growth is not artificially forced. If the contact angle is less than or equal to the receding contact angle and the contact line is moving toward the liquid, the contact angle boundary condition is set to the receding contact angle and no momentum source is applied. If the measured contact angle is greater than or equal to the advancing contact angle and the contact line is moving toward the vapor, the contact angle boundary condition is set to the advancing contact angle and no momentum source is applied. If either the contact angle or contact line motion is incongruent with these criteria (*e.g.* the contact angle is less than the receding contact angle but the contact line is moving toward the vapor, or the contact angle is between the advancing and receding contact angles), the contact line is pinned by applying the momentum source and the contact angle boundary condition is set to the measured contact angle at the end of each time step. This combination keeps the contact line pinned in place but allows the contact angle to change each time step. For cases with no contact angle hysteresis, $\theta_{adv} = \theta_{rec}$, no pinning condition is applied, and the contact angle boundary condition remains constant throughout the simulation. This is essentially what is assumed when using a static contact angle to describe the contact line dynamics.

A wide range of dynamic contact angles were evaluated for three different fluids, as shown in Table 6.1. Water, propane, and HFE-7100 were chosen due to their extensive use in two-phase systems and their differences in capillary length ($\lambda_c = \sqrt{\sigma / \Delta\rho g}$). The fluid properties at saturation at a pressure of 1 atm were used for each fluid, with the exception of the viscosity. The viscosity is not generally considered to play a notable role in quasisteady bubble dynamics [35], but low viscosity increases the proliferation of spurious currents during numerical simulations [144,145]. For this reason, an increased liquid viscosity of $\mu_l = 2.79 \times 10^{-3}$ N/m, one order of magnitude larger than the saturation viscosity of water, was used for every fluid.

6.2 Results and Discussion

The progression of a typical bubble simulation with contact angle hysteresis is shown in Figure 6.3 for water with a receding contact angle of 30 deg and an advancing contact angle of 120 deg. In the first stage of growth (receding, shown in Figure 6.3(c)), the bubble grows at the receding contact angle. The contact radius increases during this stage (see Figure 6.3(a)) while the contact angle remains constant (see Figure 6.3(b)). Once the maximum contact diameter is reached, the second stage of bubble growth (pinning, shown in Figure 6.3(d)) begins. The contact line is pinned in place and the contact angle increases as the bubble grows. Eventually, the third stage (advancing, shown in Figure 6.3(e)) commences as the contact angle reaches the advancing contact angle. The contact radius decreases rapidly at the advancing contact angle and the bubble quickly departs from the surface. The length of each of these stages varies depending on the dynamic contact angles and the fluid, but the general behavior remains the same. In cases with no contact angle hysteresis, which are analogous to simulations which impose a single static contact angle, the pinning stage does not occur, and the contact angle is constant throughout the bubble ebullition process.

6.2.1 The Role of Receding Contact Angle during Bubble Growth

As described, the receding contact angle is theorized to dictate the morphology of the bubble during the early stage of bubble growth as the liquid is receding away from the nucleation site. Therefore, the receding contact angle is expected to govern the maximum contact diameter, which occurs as the bubble transitions from the receding mode to the pinning mode. For low receding contact angles, the contact diameter remains small compared to the equivalent diameter of the bubble as it grows, as shown in Figure 6.4(a). Thus, the contact line length over which the surface tension forces act is short and buoyant forces balance the surface tension forces at small bubble sizes, resulting in an early transition to the pinning mode and a small maximum contact diameter. As the receding contact angle increases, shown in Figure 6.4(b,c), the bubble morphology changes such that the contact diameter becomes increasingly larger compared to the equivalent diameter of the bubble. The increased contact line length increases the overall surface tension force and delays the balance between surface tension and buoyancy. As a result, the receding mode in prolonged and the maximum contact diameter increases. Obviously, with the dramatic increase in contact diameter, the overall bubble size also increases substantially with

increasing receding contact angle. Figure 6.4(d) shows influence, or lack thereof, of advancing and receding contact angle on the maximum contact diameter for water. The receding contact angle is shown to have a dominant role. The contact diameter changes by more than an order of magnitude when the receding contact angle is increased from 30 deg to 140 deg. The advancing contact angle has no influence on the contact diameter. The maximum contact diameter remains constant even when the advancing contact angle is increased from 30 deg to 150 deg. Because the receding contact angle governs the bubble morphology during the initial bubble growth stages prior to pinning of the contact line, it is the key aspect of surface wettability which determine the maximum contact diameter of a bubble.

6.2.2 The Role of Advancing Contact Angle during Bubble Departure

The advancing contact angle is theorized to govern the bubble departure process as the liquid advances to rewet the surface. Effectively, the advancing contact angle acts as threshold which marks the end of the pinning stage when the contact line is allowed to advance. As a result, the bubble morphology during departure is determined by the advancing contact angles. Figure 6.5(a,b) show water bubble morphologies at the moment the contact line begins to advance for cases with a constant receding contact angle of 30 deg and advancing contact angles of 30 deg and 90 deg, respectively. For an advancing contact angle of 30 deg, there is no contact angle hysteresis. Thus, there is no pinning stage and the bubble morphology does not differ from that of the receding stage shown in Figure 6.4(a). The contact line is able to advance upon reaching the maximum contact diameter and the bubble departs. As the advancing contact angle is increases to 90 deg, the bubble goes through the receding stage followed by contact line pinning until the contact angle increases to 90 deg. This keeps the bubble attached to the surface for longer as the bubble continues to grow, resulting in an increased departure size. Because the contact diameter remains constant during the pinning stage of growth, the bubble morphology changes significantly as the bubble deforms and the region near the base begins to neck. If the advancing contact angle is increased further to 150 deg, as shown in Figure 6.5(c), the bubble actually pinches off above the surface during the pinning stage before the advancing contact angle is reached, leaving a residual vapor bubble behind on the surface. This pinch-off mechanism, with or without partial advancement of the contact line, was observed in all simulations with advancing contact angles greater than 90 deg and has been reported experimentally on hydrophobic and high contact angle hysteresis surfaces

[8,40,132]. As a result of this phenomenon, bubbles will repetitively grow and depart at this location with no waiting time for nucleation to occur.

Figure 6.5(d) shows the bubble contact radius plotted against the bubble volume for a constant receding contact angle of 30 deg and increasing advancing contact angles to reveal the impact of advancing contact angle on the bubble ebullition process. All five cases exhibit identical bubble contact radii as the volume increases during the receding stage when the contact diameter is increasing, indicating that the bubble morphologies are identical during this stage due to having identical receding contact angles. After the maximum contact radius is reached, the cases differ in the length of the pinning stage and the contact radius at which departure occurs. As the advancing contact angle increases from 30 deg to 150 deg, the amount of time spent in the pinning mode increases allowing the bubble to stay attached to the surface and grow. Thus, an increased advancing contact angle leads to a larger departure diameter. For advancing contact angles of 30, 60, and 90 deg, the contact radius reduces to zero as the bubble departs from the surface indicating that the bubble completely departs from the surface. The contact line partially advances for an advancing contact angle of 120 deg, but the bubble pinches off as the contact diameter approaches 0.1 mm, leaving behind a residual bubble. As mentioned previously, with an advancing contact angle of 150 deg (Figure 6.5(c)), the contact line does not advance at all and the bubble pinches off at the maximum contact radius. The advancing contact angle plays two keys roles in bubble ebullition. First, it determines the amount of time the bubble spends in the pinned mode, affecting the final departure diameter. Second, it determines the departure morphology, namely, whether the bubble fully departs from the surface or pinches off, leaving behind a residual bubble.

6.2.3 Redefining Wettability Regimes Based upon Dynamic Contact Angle

With this understanding of the roles of advancing and receding contact angle, three fluid-independent classes of surfaces can be defined based upon the dynamic contact angles and the resulting qualitative bubble morphologies. First, hygrophilic surfaces (where “hygro-“ refers to any arbitrary liquid [146]) can be redefined as having a low receding contact angle (less than 90 deg) and a low advancing contact angle (less than 90 deg). This refines the definition of hygrophilicity for boiling such that it is linked to dynamic contact angle measurements rather than static contact angle measurements. In this way, the terminology better represents the wetting dynamics and resulting bubble morphologies that are important to boiling.

A single bubble simulation for a hygrophilic surface (θ_{rec} = 30°, θ_{adv} = 30°) is shown alongside experimental bubble visualizations for a smooth aluminum surface in Figure 6.6. The aluminum surface was sanded to an Ra roughness of ~400 nm and tested in facility and manner as described in prior work [126]. The static, receding, and advancing contacts angles were measured to be 10 deg, <5 deg, and 29 deg, respectively. The simulation accurately replicates the progression of the bubble morphology through bubble ebullition. Hygrophilic surfaces have relatively small contact diameters, owing to the low receding contact angle, and fully vacate the surface upon departure due to the low advancing contact angle. This behavior ultimately results in small, quickly departing bubbles.

Similarly, hygrophobic surfaces can be redefined as those having high receding contact angles (greater than 90 deg) and high advancing contact angles (greater than 90 deg). A single bubble simulation for a hygrophobic surface (θ_{rec} = 120°, θ_{adv} = 120°) is shown alongside experimental visualization of the bubble ebullition process on a hygrophobic smooth Teflon surface [132] in Figure 6.7. Again, the simulations accurately capture the changes in the bubble morphology as it grows and compares favorably with the experimental results. Bubbles on hygrophobic surfaces grow with contact diameters that are larger than the equivalent bubble diameter due to the large receding contact angle. As a result, vapor readily spreads along the surface and surface-level coalescence events can occur with neighboring bubbles in boiling applications [8,10,126,132]. Due to the large advancing contact angles, the bubbles depart by pinching off above the surface, leaving behind a pocket of vapor which can immediately begin to grow with the absence of a nucleation waiting period. These characteristics lead to large bubbles which can quickly cover an entire surface during boiling processes, resulting in premature film boiling.

Lastly, in the context of boiling, we define ambiphilic surfaces ("ambi-" meaning both) as those having a low receding contact angle (less than 90 deg) but a high advancing contact angle (greater than 90 deg). These surfaces display attraction to both the liquid (via low receding contact angle) and the vapor (via high advancing contact angle) of a given fluid. A single bubble simulation for an ambiphilic surface (θ_{rec} = 30°, θ_{adv} = 120°) is shown alongside experimental visualization of the bubble ebullition process on an ambiphilic smooth PDMS surface (θ_{rec} = 10°, θ_{adv} = 110°) [132] in Figure 6.8. The low receding contact angle results in a small contact diameter as the bubble grows. The contact line then pins, and the contact angle increases beyond 90 deg to a high

advancing contact angle; the bubble necks resulting in pinch-off at departure and a residual bubble left behind on the surface.

Often, surfaces with extreme contact angle hysteresis, such as parahydrophobic and Wenzel-state superhydrophobic surfaces, will fall under this classification. These surfaces are particularly poorly represented by static contact angle characterization making it critical to consider the dynamic wetting behavior of the surfaces. Most often, these surfaces will appear to be hygrophobic based on static contact angle characterization [126,132] due to the contact line advancing during the deposition of a sessile droplet. However, in comparing the bubble morphologies shown in Figure 6.7 and Figure 6.8, the simulated and observed maximum contact diameters and departure sizes are in stark contrast with those of hygrophobic surfaces.

6.2.4 Semi-Analytical Bubble Growth and Departure Models

In addition to defining these qualitative classes based on the dynamic contact angles, the simulations provide valuable quantitative data regarding the dependency of both maximum contact diameter and departure diameter on the dynamic contact angles. In order to determine the fluid-independent relationship between the dynamic contact angles and these parameters, the maximum contact diameter and departure diameter are nondimensionalized using the Bond number ($\mathrm{Bo}(L) = \Delta\rho g L^2 / \sigma$), where the length scale L is either the maximum contact diameter ($D_{c,max}$) or the departure diameter (D_d). The bubble growth and departure processes are dominated by buoyant and surface tension forces. This nondimensionalization removes the influence of the fluid properties that affect buoyant and surface tensions forces, isolating the role of the bubble morphology which is governed by the dynamic contact angles.

Figure 6.9 shows the relationship between the maximum contact diameter and the receding contact angle. As previously demonstrated, the advancing contact angle does not play a role in determining the maximum contact diameter. Rather, the receding contact angle is the governing wetting characteristic. Figure 6.9(a) shows the dimensional results for the three different fluids. For each fluid, the trend of increasing contact diameter with increasing receding contact angle is observed, though the magnitude of the contact diameter varies significantly. Upon nondimensionalizing the results using the Bond number (Figure 6.9(b)), the results for the three fluids collapse cleanly onto a single curve.

Buoyant deformation of the bubble plays a significant role in determining the bubble shape and precludes the use of the spherical cap assumption in evaluating the force balance, making it difficult to obtain an analytical solution for the maximum contact diameter based on the receding contact angle. Instead, a correlation, provided in equation (6.2), is determined by fitting the nondimensionalized simulation data shown in Figure 6.9(b)).

$$\frac{\Delta\rho g D_c^2}{\sigma} = 5.2\times10^{-8}\theta_{rec}^4 \tag{6.2}$$

Equation (6.2) can be explicitly solved to obtain a correlation for the departure diameter as given in equation (6.3).

$$D_c = 2.28\times10^{-4}\theta_{rec}^2\lambda_c \tag{6.3}$$

This equation provides a novel correlation for the maximum base diameter based on the dynamic wetting behavior of a surface. The prediction of the maximum contact diameter is critical in the understanding of the wetting and coalescence dynamics during boiling.

A bubble departure diameter model can be developed based on the dynamic contact angles using a force balance between buoyant and surface tension forces. The buoyant force ($F_b = \Delta\rho V g$) and the vertical component of the surface tension force is given as ($F_s = \sigma\pi D_{c,\max}\sin\theta$). The buoyant force will, of course, continue to increase as the bubble grows. On the other hand, the surface tension force can increase and decrease depending on the contact diameter and contact angle. The limiting surface tension force for departure, at which the buoyant force insurmountably overcomes surface tension, is expected to be the maximum surface tension force possible for a given set of dynamic contact angles. As established, the receding contact angle establishes the maximum contact diameter, which corresponds to the maximum contact line length and thereby largest surface tension force. Additionally, the surface tension is maximized when contact angle approaches 90 deg. Because the advancing contact angle governs when the contact line is allowed to advance and the bubble will depart, it is considered to be the critical contact angle in this situation. Thus, if the advancing contact angle is less than or equal to 90 deg, the limiting surface tension force occurs at the maximum contact diameter and the advancing contact angle. After this condition is reached, departure is unhindered because the contact line will begin to advance and the contact line length will decrease, further reducing the surface tension force. If the advancing contact angle is greater than 90 deg, the limiting surface tension force occurs when the contact angle is 90 deg at the maximum contact diameter. After this point, the bubble begins to rise, but

still must undergo morphological changes for the contact line to advance. Incorporating the correlation from equation (6.3), this gives a piecewise relation for the departure diameter of a bubble based upon only the receding contact angle, the advancing contact angle, and the capillary length of the fluid as shown in equation (6.4).

$$\begin{aligned} \theta_{adv} < 90\,\text{deg} &\rightarrow D_d = 0.111\theta_{rec}^{2/3}\sin^{1/3}\theta_{adv}\lambda_c \\ \theta_{adv} > 90\,\text{deg} &\rightarrow D_d = 0.111\theta_{rec}^{2/3}\lambda_c \end{aligned} \tag{6.4}$$

The simulation results and model prediction for the departure diameter, nondimensionalized as the Bond number, are shown for each fluid in Figure 6.10. The model from equation (6.4) captures two keys trends based upon the advancing and receding contact angles. First, across a constant advancing contact angle, the departure diameter increases strongly with receding contact angle. The increase in the receding contact angle leads to a larger contact diameter and longer contact line which ultimately increases the surface tension force keeping the bubble attached to the surface to larger bubble sizes. Second, across a constant receding contact angle, there is a lesser increase in the departure diameter as the advancing contact angle increases up to 90 deg, after which the departure diameter remains constant. Overall, the model matches the simulation results very well. At receding contact angles of greater than 90 deg, the model less accurately captures the interfacial dynamics during departure, but still reasonably predicts the departure diameter. From the simulations, the departure diameter is considered to be the equivalent diameter based on the bubble volume just after the bubble pinches off or leaves the surface. The model, which predicts departure to occur immediately when the buoyant force balances the maximum surface tension force, does not account for the time it takes for the bubble to rise and leave the surface. For low contact angles, this time is negligible and does not notably affect the departure size. However, for high contact angles, the bubble can grow significantly during this process. For example, for a surface with a receding contact angle of 120 deg and an advancing contact angle of 150 deg for water, the bubble grows an additional 7% between the point at which contact line advancing begins and the fully bubble departs from the surface.

The predicted maximum contact diameter and departure diameter from equation (6.3) and equation (6.4), respectively, are compared with experiments [40,53,132,147] for a wide range of dynamic contact angles in Figure 6.11. Equation (6.3) accurately captures the trends in maximum contact diameter with dynamic contact angle as shown in Figure 6.11(a). The contact diameter for cases with very low receding contact angle (~10 deg or less) are notably underpredicted. This is

likely due to the quasisteady nature of the simulations which ignores the inertia-controlled growth period commonly observed in the early stages of bubble growth [148]. It is possible that the contact diameter expands past the very small predicted quasisteady maximum diameter during this inertia-controlled stage of growth. Nonetheless, the overall magnitude and trends in the maximum contact diameter with respect to dynamic contact angle are accurately captured by the model.

Figure 6.11(b) show the comparison between the newly developed bubble departure diameter model (equation (6.4)) and experimental measurements, alongside the Fritz correlation. The newly proposed model reduces the mean absolute error in the departure diameter for these cases from 73% to 29% when compared against the Fritz correlation. The starkest improvement is obtained for ambiphilic surfaces with substantial contact angle hysteresis due to the Fritz correlation's reliance on the static contact angle. For example, on the flat PDMS surface from Allred *et al.* [132] (R10A110), the departure diameter is reported as 2.3 mm. The Fritz correlation predicts a departure diameter of 7.8 mm (239% error) based on the static contact angle of 106 deg. Accounting for both the advancing and receding contact angles, the present model predicts a bubble departure diameter of 1.3 mm (43% error). Due to the underprediction in the contact diameter for cases with very low receding contact angles, the departure diameter is also underpredicted based on the experimental measurements. Overall, the developed models improve upon existing models for departure diameter and accurately capture the relationship between surface wettability and bubble size.

6.2.5 Implications and Limitations of the Model

This new understanding of the role of surface wettability during bubble growth and departure alters the design goals for surfaces in boiling applications. First, it is clear that the static contact angle is not an adequate predictor of the bubble dynamics during boiling. While it may provide a reasonable estimate for surfaces with very low contact angle hysteresis, static contact angle characterization runs the risk of dramatically overpredicting the departure size for surfaces with moderate to high contact angle hysteresis. Instead, the dynamic contact angles should be characterized as indicators of the bubble morphology and departure size due to their role in the dewetting and rewetting processes throughout bubble ebullition.

The refined wettability regimes of hygrophilic, hygrophobic, and ambiphilic based on the dynamic wetting behavior of the surface provide a more complete understanding of how these

surfaces will behavior in boiling applications. Hygrophilic surfaces both minimize dewetting during bubble growth and readily rewet upon bubble departure. This results in small, rapidly departing bubbles and complete rewetting upon bubble departure. This maintains their reputation as the ideal surfaces for applications in which the surface must remain wetted to very high heat fluxes [6,7]. Hygrophobic surfaces both maximize dewetting during bubble growth and mitigate rewetting upon bubble departure. While they have exhibited advantages with high nucleation site densities and low boiling incipience temperatures, this behavior leads to premature insulating vapor film coverage over the surface and precludes their use in most boiling applications [8,10,40,115,132]. The unique bubble dynamics of ambiphilic surfaces have been clearly revealed through this study. While ambiphilic surfaces are prone to minimal rewetting during bubble departure similarly to hygrophobic surfaces, they also minimize the amount of dewetting as the bubble is growing similarly to hygrophilic surfaces. As a result, these surfaces produce small bubbles that pinch off above the surface upon departure. The majority of the surface remains wetted, explaining the observed critical heat flux values on par with those of hygrophilic surfaces [126,132]. However, ambiphilic surfaces are also reported to exhibit higher heat transfer coefficients than hygrophilic surfaces [126,132]. Based on the minimal rewetting on these surfaces, it is expected that they trap gas within cavities on the surface very easily, replicating the favorable nucleation characteristics of hygrophobic surfaces. Additionally, bubbles pinch off from the surface instead of the surface fully rewetting upon bubble departure. This completely eliminates the waiting time between bubbles and may result in more efficient heat transfer. These findings call for additional development of ambiphilic surfaces for boiling applications for a variety of fluids.

While the model proposed herein captures the contact line and contact angle dynamics very well across a wide range of dynamic wetting behaviors, it does have limitations based on the model assumptions. First, as mentioned, the quasisteady assumption may not be valid for all situations during boiling, particularly for low receding contact angles. The growth rate of a bubble can be highly dependent on the surface superheat during boiling [148]. Based on the analysis by Oguz and Prosperetti [142], the growth rate threshold under which the quasisteady assumption is valid is expected to scale with the contact diameter. Thus, surfaces with low receding contact angles are more prone to inertia-dominated growth and the effect will increase with higher surface superheats. Additionally, this model uses an adiabatic analysis based purely on wetting dynamics. Thus,

contact line evaporation, which may have an influence on the maximum contact diameter over time, is ignored. Convective currents which may influence the force balance acting on the bubble are also ignored. Despite these simplifications, it is expected that the newly developed models for the maximum contact diameter and departure diameter will provide the accurate estimates of these parameters for most surfaces due to its consideration of the full spectrum of dynamic wetting behavior. Additional studies on the contact line and contact angle dynamics during inertia-controlled growth would provide a pathway for improved accuracy at low receding contact angles.

6.3 Conclusions

This study defines a new theoretical framework for the contact line and contact angle evolution during bubble growth that is based on fundamental wetting dynamics. The bubble growth process is divided into three stages: receding, pinning, and advancing. The bubble initially grows as the liquids recedes away at the receding contact angle, followed by contact line pinning as the contact angle increases from the receding contact angle to the advancing contact angle, and finally the contact line advances at the advancing contact angle as the bubble departs. Models for the maximum base diameter and departure diameter of a bubble are developed requiring inputs of only the dynamic contact angles and the fluid properties. The receding contact angle is the key wetting characteristic that determines the maximum contact diameter. The receding contact angle is also the dominant wetting characteristic that dictates the departure diameter, but the advancing contact angle also plays a notable role. In general, lower contact angles result in smaller contact diameters and departure diameters. These findings reinforce the assertion that dynamic contact angles should be considering when modeling boiling behavior rather than the static contact angle. For boiling applications, the definitions for hygrophilic and hygrophobic regimes are refined based on the dynamic contact angles rather than static contact angle measurements. Additionally, a new class of ambiphilic surfaces is defined as having receding contact angles less than 90 deg and advancing contact angles greater than 90 deg. These surfaces display unique bubble dynamics that combine elements from hygrophilic and hygrophobic surfaces and warrant further investigation.

Table 6.1. Matrix of Simulations performed where “W” indicates a simulation using water, “P” propane, and “H” HFE-7100.

Receding Contact Angle (deg) \ Advancing Contact Angle (deg)	30	60	90	120	150
30	WP	WPH	WPH	WPH	WPH
60	-	WPH	WPH	WPH	WPH
90	-	-	WPH	WPH	WPH
120	-	-	-	W	WPH
140	-	-	-	-	WPH

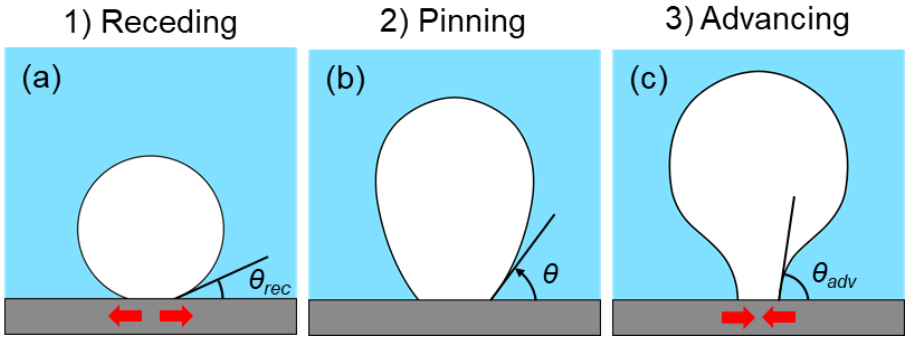

Figure 6.1. Illustration of the wetting dynamics during bubble growth. (a) The receding mode during which the contact line is moving away from the bubble at the receding contact angle. (b) The pinning mode during which the contact angle is increased and there is no contact line motion. (c) The advancing mode during which the contact line moves toward the bubble at the advancing contact angle.

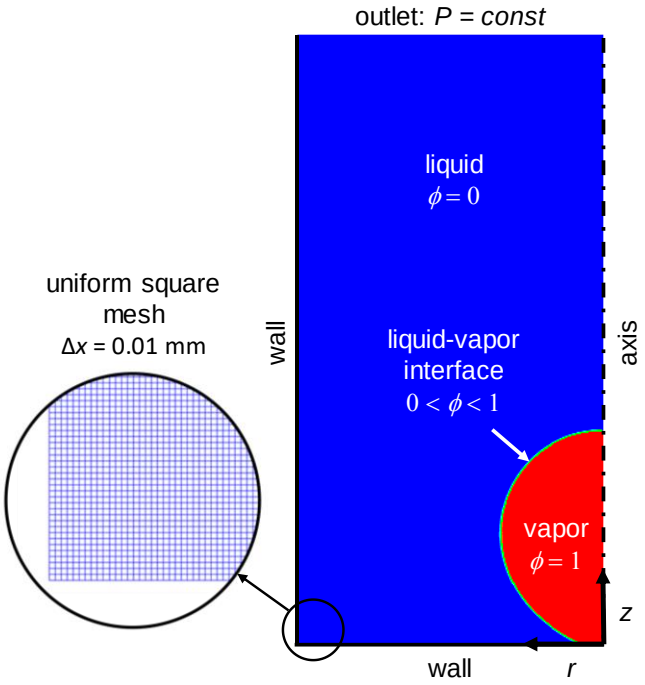

Figure 6.2. The rectangular, axisymmetric simulation domain. The zoomed view shows the mesh geometry.

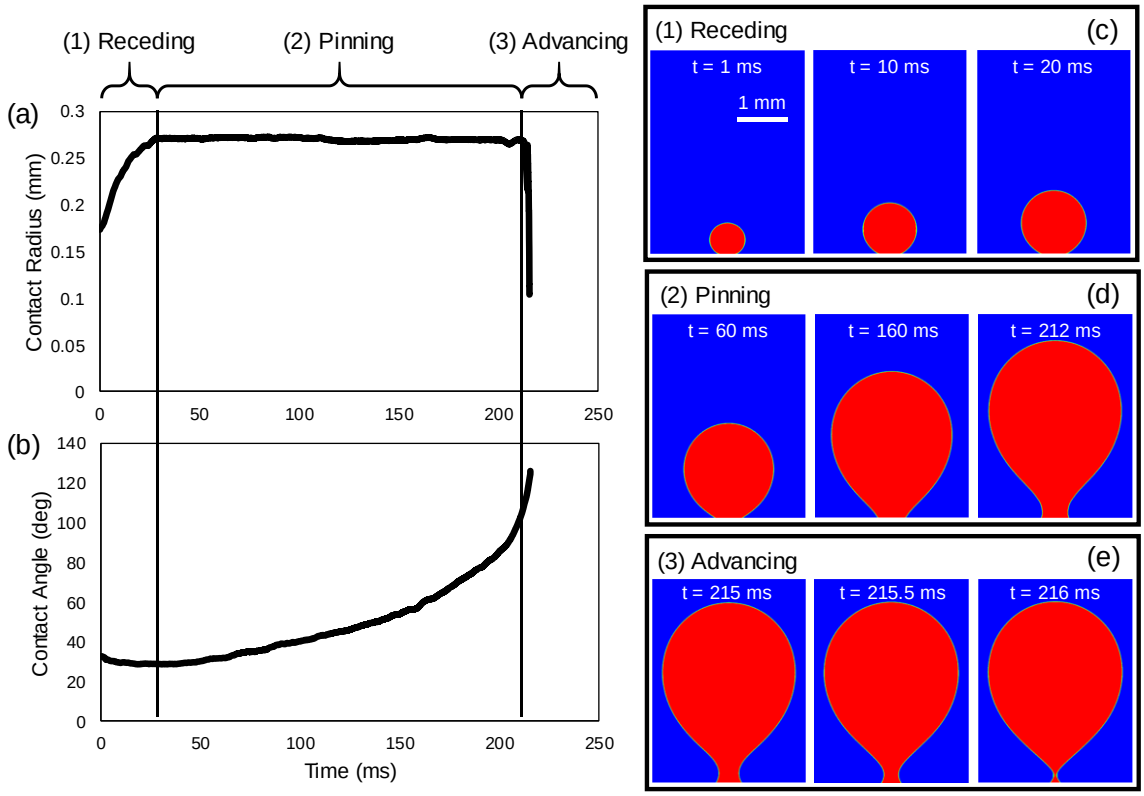

Figure 6.3. Characterization of the simulation of the bubble ebullition cycle with a receding contact angle of 30 deg and advancing contact angle of 120 deg for water. Plots show the change in (a) contact radius and (b) contact angle over time during bubble growth and departure. Simulation snapshot series show the bubble morphologies progressions during (c) the receding mode, (d) the pinning mode, and (e) the advancing mode.

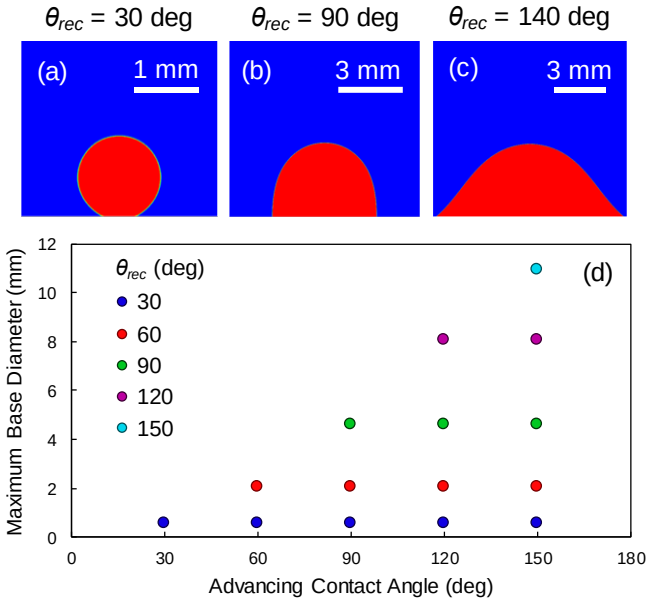

Figure 6.4. The morphology of water bubbles upon reaching the maximum contact diameter with receding contact angles of (a) 30 deg, (b) 90 deg, and (c) 140 deg. (d) Maximum contact diameter plotted versus advancing contact angle with differing receding contact angles for water.

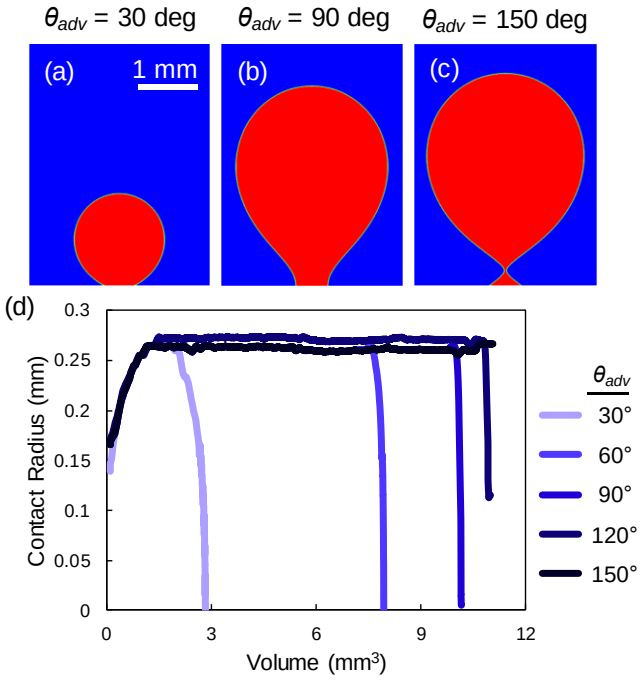

Figure 6.5. Simulation snapshots showing the morphology of water bubbles when contact line advancing begins, or pinch-off occurs in lieu of contact line advancing, with constant receding contact angles of 30 deg and differing advancing contact angles of (a) 30 deg, (b) 90 deg, and (c) 150 deg. (d) Bubble contact radius plotted versus bubble volume for water cases with a receding contact angle of 30 deg and differing advancing contact angles.

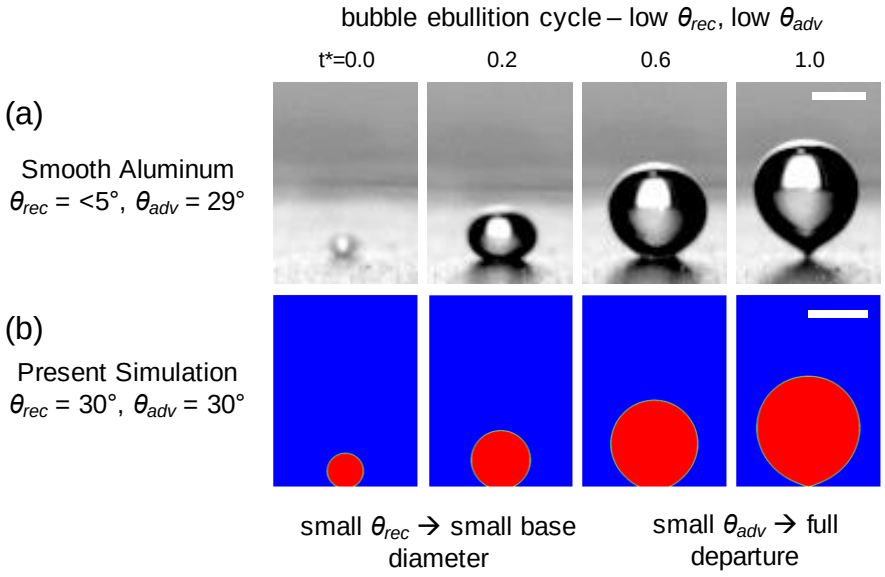

Figure 6.6. Progressions of (a) experimental images and (b) simulation snapshots showing the bubble morphology evolution during the ebullition cycle on a hygrophilic surface.

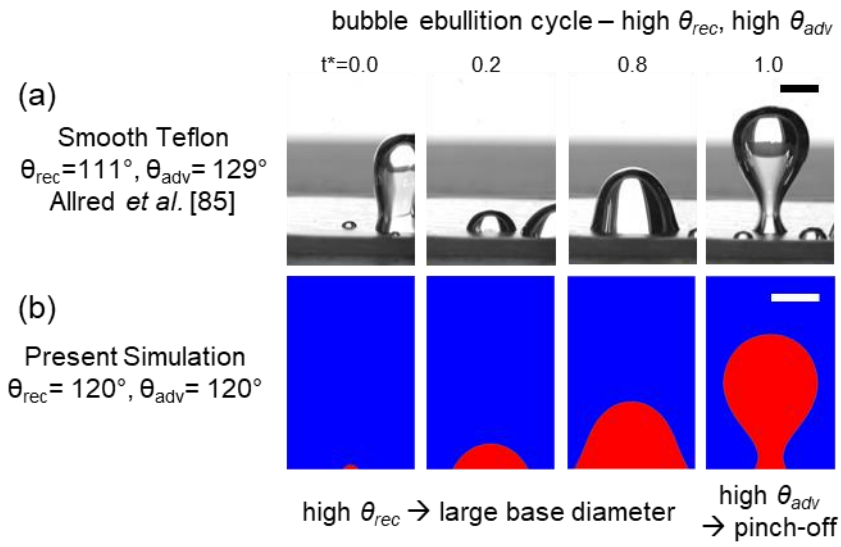

Figure 6.7. Progressions of (a) experimental images[132] and (b) simulation snapshots showing the bubble morphology evolution during the ebullition cycle on a hygrophobic surface.

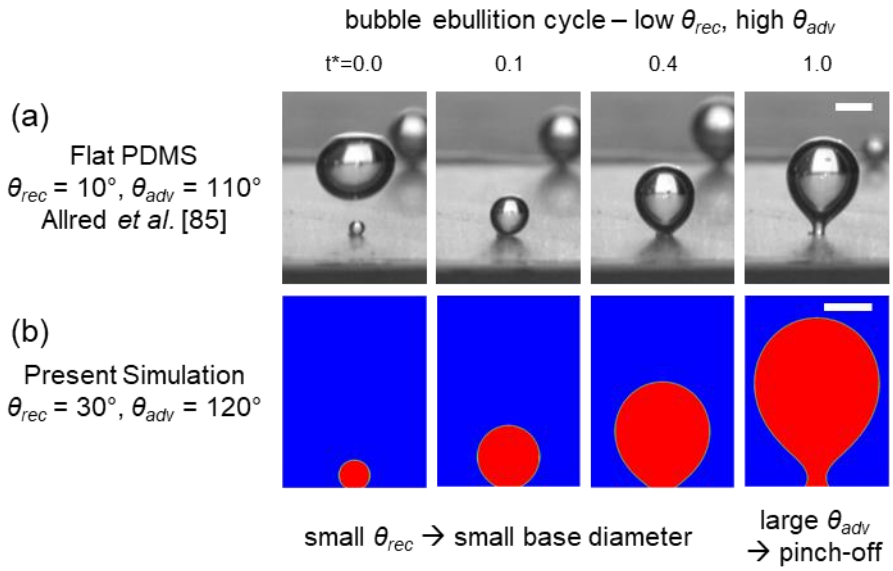

Figure 6.8. Progressions of (a) experimental images[132] and (b) simulation snapshots showing the bubble morphology evolution during the ebullition cycle on an ambiphilic surface. Scale bars are 1 mm.

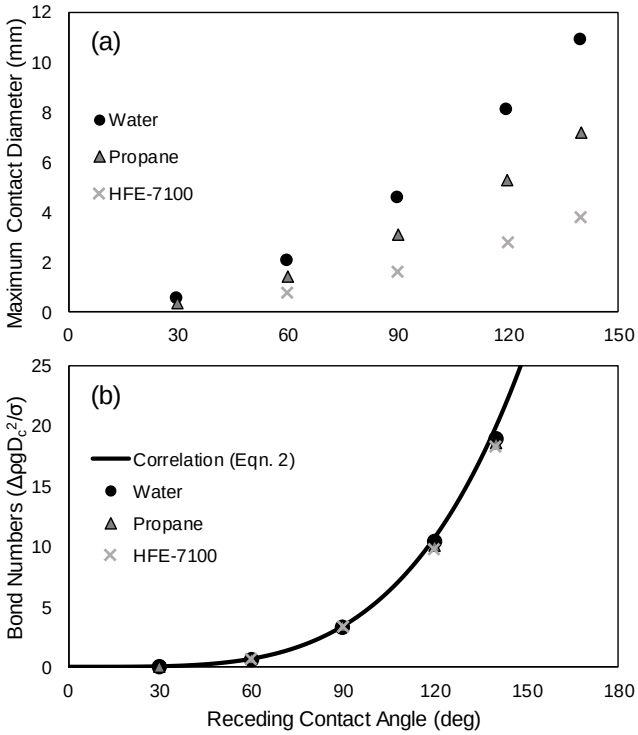

Figure 6.9. The maximum contact diameter, shown dimensionally in (a) and nondimensionalized by the Bond number in (b), plotted versus receding contact angle for water, propane, and HFE-7100.

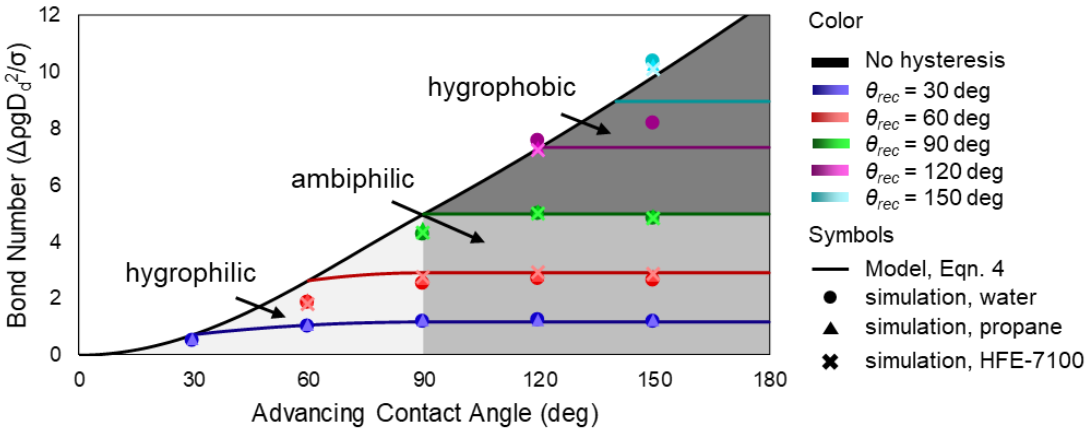

Figure 6.10. Simulation results and model predictions for the departure diameter, nondimensionalized as the Bond number, for water, propane, and HFE-7100 with differing advancing and receding contact angles.

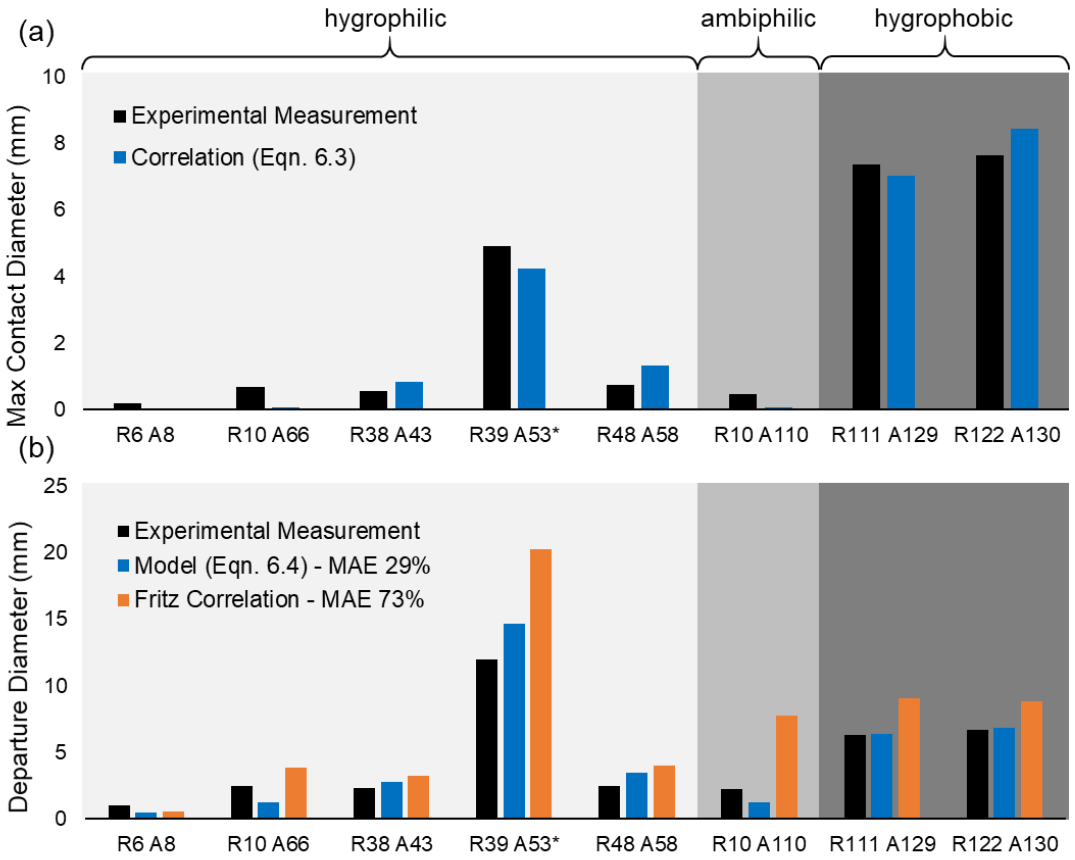

Figure 6.11. Comparisons between experimental results and model predictions for (a) maximum contact diameter and (b) departure diameter using water. (*The case "R39 A53" is at reduced gravity, $g' = 0.04g$).

7. THE EFFECT OF DYNAMIC WETTING BEHAVIOR ON HEAT TRANSFER MECHANISMS DURING BUBBLE GROWTH

This chapter builds upon the numerical simulations discussed in Chapter 6 by incorporating heat transfer and phase change. This simulation framework is then used to explore the heat transfer behavior of hygrophilic, hygrophobic, and ambiphilic surfaces during single bubble growth. The differing bubble dynamics resulting from the differences in dynamic wetting behavior are shown to alter the heat transfer mechanisms that dominate during bubble growth. Hygrophilic surfaces are shown to have the most effective heat transfer on a per bubble basis due to highly effective microlayer heat transfer. Ambiphilic surfaces have less effective microlayer heat transfer as a result of the pinch-off departure mechanism limiting rewetting and formation of a new microlayer. However, they exhibit advantages including favorable nucleation characteristics and no waiting period between bubble departure and nucleation of the next bubble due to pinch-off. Hygrophobic surfaces are shown to perform poorly due to significant vapor spreading and the development of hot spots beneath the bubble. Based on the observations from the simulations, design targets for the dynamic contact angles within the hygrophilic and ambiphilic regimes are suggested to maximize their respective performance.

7.1 Methods

The heat transfer associated with single bubble growth from a solid surface was modeled by implementing heat transfer and phase change into the simulation framework described in section 6.1.2. The modified 2-D axisymmetric domain, shown in Figure 7.1, is defined for this work. A uniform square mesh with 0.01 mm cells was used throughout the domain to maximize the accuracy of the interface reconstruction. The overall domain consists of a solid region at the base and a two-phase fluid region that makes up the rest of the domain. The solid region is 0.5 mm thick with material properties of silicon. The solid region is included to incorporate the effects of the thermal response of the surface on local heat transfer during bubble growth. The two-phase fluid region has material properties to approximate water. The viscosity of the liquid was artificially increased by an order of magnitude to 0.00279 N-s/m^2 in order to improve the stability of the simulation. This has a mild impact on the convective heat transfer and bubble dynamics, but

does not affect the qualitative conclusions of the study. All material properties are assumed to be constant with respect to temperature. Thus, natural convection is neglected.

A constant heat flux of 3 W/cm^2 is applied at the base of the solid surface for all simulation cases. The outer wall is considered to be no-slip and adiabatic. Axial symmetry is enforced at the central axis. The top of the domain acts as a constant pressure (1 atm) outlet and thermal outflow condition. Any backflow at the outlet comes in at the saturation temperature (373.15 K). Three custom submodels are implemented via user-defined functions to dictate the more complex aspects of the simulation: phase change at the interface, the contact angle and contact line dynamics, and the microlayer evaporation and heat transfer. These submodels are discussed in detail in the subsequent subsections.

An initial vapor bubble is initialized as a spherical cap at the receding contact angle with a sphere radius of 0.27 mm. The solid region is initialized at a 5 K superheat for all cases (378.15 K). The initial thermal boundary layer in the liquid is assumed to have a thickness of 1 mm and a linear temperature profile that spans the difference between the surface superheat and the saturation temperature. Because the thermal boundary layer can only be accurately captured through many bubble ebulltion cycles and only one cycle is observed for each case in this study, the choice of the initial thermal boundary layer is somewhat arbitrary [50]. Additionally, a 1 mm radial boundary layer is introduced around the bubble to prevent large temperature discontinuities at the liquid-vapor interface, which result in instabilities. Similarly, this radial boundary layer has a linear profile that spans the saturation temperature at the liquid-vapor interface and the local temperature in the axial thermal boundary layer. The rest of the two-phase fluid region is initialized at at the saturation (373.15 K). The pressure throughout the two-phase region is initialized at 1 atm. Figure 7.2 shows an initialized case with a receding contact angle of 30 deg.

This study evaluates one surface from each of the three dynamic wetting regimes identified in Chapter 6: hygrophilic, hygrophobic, and ambiphilic. The hygrophilic surface has receding and advancing contact angles equal to 30 deg, the hygrophobic surface has receding and advancing contact angles equal to 120 deg, and the ambiphilic surface has a receding contact angle of 30 deg and an advancing contact angle of 120 deg. The domain size for each case is designed such that the bubble does not interact significantly with the wall and is able to fully depart prior to interacting with the outlet. The domain radius for both the hygrophilic and ambiphilic surfaces is set to 2 mm.

The domain radius for the hygrophobic case is 5 mm. The domain height for the hygrophilic and ambiphilic surfaces is 4.5 mm, and the height for the hygrophobic surface is 14 mm.

7.1.1 Saturated-Interface-Volume Phase Change Model

The saturated-interface-volume phase change model, developed previously in Pan *et al.* [149], is utilized to fix the liquid-vapor interface to the saturation temperature throughout the simulation and calculate the appropriate amount of liquid-vapor phase change. The key advantage of this model is that it reduces temperature oscillations during numerical iterations by explicitly setting the local interface temperature to the saturation temperature. Importantly, this leads to compatibility with non-iterative time advancement schemes, which are used in this study, and can significantly reduce computational cost of simulations that incorporate phase change. The model is briefly described here. In each time step, the amount of sensible heat needed to change each interface cell to the saturation temperature is calculated locally based on the current temperature, volume fraction, and material properties. Correspondingly, the amount of latent heat needed to balance this sensible heat defines the amount of phase change during that time step. An energy source/sink is applied locally to supply the sensible heat to explicitly set the interface cells to the saturation temperature. Mass source/sinks for both the liquid and the vapor are applied to account for the phase change and maintain mass conservation. The vapor source is uniformly applied over the entire interior volume of the bubble, and the liquid source is uniformly applied over the interfacial cells.

7.1.2 Dynamic Contact Angle Model

The contact angle boundary condition is applied at the solid-liquid boundary in the domain. In this work, simulations with and without contact angle hysteresis are considered. Cases with no contact angle hysteresis ($\theta_{rec} = \theta_{adv}$) are simply considered to have a constant contact angle and utilize the contact angle boundary condition that is native to ANSYS Fluent. Cases with contact angle hysteresis ($\theta_{rec} \neq \theta_{adv}$) utilize the custom dynamic contact angle framework described in Chapter 6. It is briefly described again here for clarity.

The dynamic contact angle framework acts to ensure realistic contact angle and contact line dynamics during bubble growth. It asserts three main conditions: the contact angle is at the receding contact angle when the contact line is receding, the contact angle is at the advancing

contact angle when the contact line is advancing, and the contact line remains pinned when the contact angle is between the advancing and receding contact angles. The effects of contact line velocity are neglected. During receding and advancing, the contact angle boundary condition is simply set to the receding or advancing contact angle, respectively. During pinning, the contact angle boundary condition is allowed to change by resetting it to match the current contact angle at the end of each time step. Additionally, a momentum source is applied at the contact line to keep it pinned at the appropriate radial location. The momentum source is proportional to the radial distance between the current contact line location and the set pinning location and the current contact line velocity and acts to move the contact line toward the pinning location and resist any current contact line velocity. This framework results in a bubble growth cycle that begins with a constant contact angle receding stage at the receding contact angle, followed by a constant contact radius pinned stage as the contact angle increases to the advancing contact angle, and finally a constant contact angle stage at the advancing contact angle as the contact line advances and the bubble departs.

7.1.3 Microlayer Heat Transfer Model

Microlayer heat transfer is a very significant component of the overall heat transfer during bubble growth and cannot be neglected [27,28]. However, due to the thinness of the microlayer (on the order of μm), it is computationally intensive to develop a mesh that can accurately model the microlayer along with the larger scale bubble features. Thus, a submodel was developed to approximate the microlayer heat transfer without requiring the full resolution of the microlayer numerically. This submodel tracks the local microlayer thickness and determines the appropriate amount of heat transfer and phase change accordingly.

The initial microlayer thickness at a given radial location is determined based on the Cooper and Lloyd, $\delta_0 = 0.8\sqrt{\nu t_R}$, where ν is the kinematic viscosity and t_R is the time required for the contact line to reach that radial location [150]. The goal of this work is make broad conclusions about the heat transfer behavior in each of the wettability regimes discussed rather than determine the accurate quantative contribution from each specific heat transfer mechanism. Thus, the model developed by Cooper and Lloyd [150] is used due to its simplicity and popularity. It is worth noting that the kinematic viscosity used in the microlayer submodel is based on the saturation properties of water, not the artificially increased dynamic viscosity utilized to improve numerical stability.

The microlayer thickness is tracked by storing this data at each time step using user-defined memory within the top row of cells in the solid region, the same location where the energy sink to account for the microlayer heat transfer is ultimately applied. The local microlayer heat transfer is calculated based on the conduction resistance across the microlayer thickness according to

$$q''(r) = -k_l \frac{T_{surf}(r) - T_{sat}}{\delta(r)} \tag{7.1}$$

This heat transfer is spatially averaged and applied uniformly as an energy sink to the top row of cells in the solid surface with a nonzero microlayer thickness. Additionally, it is assumed that all of the microlayer heat transfer results in evaporation of the local microlayer. The amount of phase change within the microlayer is calculated based on the local heat transfer, and the local microlayer thickness is adjusted accordingly. This phase change is incorporated into the distributed liquid and vapor mass sources/sinks. If the microlayer is thin enough such that the entire local microlayer would evaporate within a given time step, the local heat transfer applied during that time step is capped based on the latent heat transfer that would result from full evaporation of the local microlayer thickness. Any flow within the microlayer region is neglected, so each cell within the microlayer region is treated independently. By tracking the microlayer thickness in this manner, the microlayer dryout is modeled and the microlayer heat transfer evolves qualitatively as expected based on observations from the literature [151]. There is a wide band of high heat transfer over the entire microlayer during bubble growth. As the microlayer dries out, an inner dryout radius forms where there is no microlayer heat transfer. The microlayer heat transfer gradually decreases as a result of thin, low-thermal-resistance microlayer regions drying out and thicker, higher-resistance microlayer regions being formed as time advances.

The initialization of the microlayer differs depending on the dynamic wettability of the surface being considered. For a hygrophilic surface, it is important to consider that the microlayer formation begins upon nucleation, rather than the initiation of the simulation which begins with a initialized bubble. Thus, time required for the bubble to reach a particular radial location, which is used to determine the initial microlayer thickness, must account for the approximate time required for the bubble to reach the initialization condition. The initial growth rate is approximated based on the average growth rate over the first 1000 time steps (~0.5 ms). This is used to determine the approximate time needed for the bubble to grow to the initialized volume. This time, t_{offset}, is used as an offset from the simulation time for the determination of the microlayer thickness. The initial

microlayer under the initialized bubble is assumed to have a linear profile spanning from $\delta_0 = 0$ at $r = 0$ to $\delta_0 = 0.8\sqrt{\nu t_{offset}}$ at the initial contact radius. The thickness of the microlayer also affects the early growth rate. So, an iterative process was used until change in the offset time was less than 10%. As the simulation progresses, the initial microlayer thickness at a given radial location for the hygrophilic surface is given by $\delta_0 = 0.8\sqrt{\nu(t_{sim} + t_{offset})}$

For ambiphilic surfaces, those with a low receding contact angle but a high advancing contact angle, the microlayer has not been explicitly studied. However, the microlayer is theorized to form as a result of the hydrodynamics as the contact radius expands outwards [150]. Because the growth dynamics of bubbles on ambiphilic surfaces during this receding stage match those of hygrophilic surfaces, which are known to form a microlayer, it is expected that a microlayer will form under bubbles on ambiphilic surfaces as well. For these surfaces, bubbles pinch off above the surface at departure and leave behind a residual bubble on the surface. The surface under this residual bubble will not rewet, and thus, a new microlayer will not form in this area. To simulate a representative bubble, rather than the first bubble that occurs at a given location, the initial base diameter is set to have approximately the same base diameter as the residual bubble left upon bubble departure, and it is assumed that no microlayer exists within this region. As a result, time zero for the simulation can be approximated as time zero for the determination of the microlayer thickness (*i.e.* the offset time is set to zero). Bubbles growing on hygrophobic surfaces are generally not considered to form a microlayer [9]. Thus, microlayer heat transfer is neglected for the hygrophobic surface in this study.

As a result of the microlayer framework and the numerical discretization, slight fluctuations in the surface temperature were observed in the hygrophilic and ambiphilic cases. This is due to the increase in the microlayer heat transfer in a given cell as the microlayer become very thin, followed by a sharp decrease in heat transfer when the microlayer dries out. It is not expected that these events alter the representative behavior of each surface. For the discussion of the results, the times presented are selected to be away from these spikes such that the interpretation of the results is minimally affected by this numerical aberration.

7.2 Results and Discussion

7.2.1 Bubble Ebullition Characteristics

Significant differences in the bubble dynamics result from the differences in the dynamic contact angle in the three wettability regimes. The effects of dynamic contact angle on bubble dynamics were extensively explored in Chapter 6. The bubble dynamics observed in the three cases studied are described herein to facilitate understanding of the impact that these dynamics have on heat transfer during bubble growth. Table 7.1 summarizes the bubble ebullition characteristics for each case. Figure 7.3 shows the bubble morphology for each case at key points in the bubble ebullition process.

The receding contact angle governs the bubble morphology during the initial stages of bubble growth. The low receding contact angle in the hygrophilic and ambiphilic cases leads to a small base diameter compared to the equivalent diameter as the bubble grows to the maximum base diameter of 0.53-0.55 mm. Because the receding contact angles are identical, the bubble morphologies of these two cases are very similar up to the maximum base diameter. The high receding contact angle of the hygrophobic surface results in a bubble morphology with a large base diameter compared with the equivalent diameter as the bubble grows to a large maximum base diameter of 7.71 mm.

The stage between when the maximum base diameter is reached and contact line advancing begins is the pinned stage where the contact angle increases from the receding contact angle to the advancing contact angle. Because the hygrophilic and hygrophobic cases do not have any hysteresis, the bubble morphology does not change significantly between the time the maximum base diameter is reached and contact line advancing begins. However, for the ambiphilic surface, the contact line pins as the contact angle increases from 30 deg to 120 deg. Thus, the bubble grows significantly during this stage and begins to stretch upward forming a necking region at the base of the bubble.

Once the advancing stage begins, the advancing contact angle governs the bubble morphology as the contact line begins to move with a constant contact angle. The bubble on the hygrophilic surface maintains a sphere-like shape and the bubble departs completely from the surface as a result of the contact line reaching $r = 0$. Because of the high advancing contact angles, the hygrophilic and ambiphilic surfaces have an elongated shape with a significant necking region.

The interface in the necking region reaches $r = 0$ prior to the contact line which results in a pinch-off departure mechanism which leaves a residual bubble behind on the surface.

Because the receding contact angle governs the initial growth period up to the maximum base diameter, it plays a dominant role in determining the departure diameter as demonstrated in Chapter 6. The advancing contact angle also plays a minor role in determining the departure diameter and plays a significant role in determining the time spent in the pinning mode and ultimately the departure time. This results in the departure time on the ambiphilic surface being over twice as long as on the hygrophilic surface. Despite the substantially larger bubble volume, the hygrophobic surface only has a slightly longer departure time than the ambiphilic surface. Most of the phase change that leads to bubble grow occurs at the three-phase contact line, and the hygrophobic surface has a much larger base diameter, and therefore contact line length. Thus, the average volumetric growth rate on the hygrophobic surface is much higher.

7.2.2 Heat Transfer in the Hygrophilic Case

Figure 7.4 presents the temperature evolution of the simulated domain throughout bubble growth on a hygrophilic surface. Figure 7.4(a-c) show the temperature contours of the domain during the receding growth, pinned growth, and advancing growth stages. Figure 7.4(d) shows the surface temperature profile at each of these respective stages. Figure 7.5 displays the surface heat flux profiles at the same times. Both the heat transfer from the microlayer submodel (dot-dash line style) and the conduction and convection heat transfer calculated natively in ANSYS Fluent (solid line style) are shown separately. By analyzing this information carefully, insight about the dominant heat transfer mechanisms in each growth stage can be ascertained.

As the bubble begins to grow in the receding stage, the surface temperature directly under the bubble is reduced to approximately 2 K less than the outer surface due to high local heat transfer (Figure 7.4(a)). As shown in Figure 7.5(a), this stage is dominated by microlayer heat transfer. The instantaneous microlayer thickness at each of the times shown in Figure 7.4 and Figure 7.5 is plotted in Figure 7.6. During the receding stage, the microlayer thickness is very small due to rapid radial growth. This results in a minimal thermal resistance across the microlayer and extremely effective heat transfer. The local heat transfer ($\sim 3.4\times10^6$ W/m^2) during this early growth stage on the hygrophilic surface is by far the highest observed in any of the simulated cases. However, this ultrathin microlayer also dries out quickly. So, this highly effective heat transfer is short-lived.

During the pinning stage, the average microlayer thickness is much larger (see Figure 7.6), and the microlayer heat transfer is roughly an order of magnitude lower than that observed during the early receding growth, as shown in Figure 7.5(b). The total of the convective and conductive heat transfer near the contact line are comparable in magnitude to the microlayer heat transfer at this stage. Because the most efficient heat transfer still occurs near the contact line, the surface temperature in this region remains reduced compared to the temperature away from the bubble, as seen in Figure 7.4(b,d). As the contact line begins to advance, it moves past any remaining microlayer and there is no longer microlayer heat transfer. The heat transfer resulting from convection and conduction increases marginally as a result of contact line motion and cooler liquid being brought toward the surface near the contact line.

Throughout the bubble growth process, the region near the contact line displays the greatest heat transfer. The microlayer dominates during the early receding stage of growth, but convection and conduction beyond the apparent contact radius become a larger proportion of the overall heat transfer as the bubble grows and the thin regions of the microlayer dry out. Within the dried out region, there is minimal heat transfer which corroborates observations of central hot spots in experimental studies [12,151].

7.2.3 Heat Transfer in the Ambiphilic Case

The temperatures and surface heat fluxes for the ambiphilic case are presented in Figure 7.7 and Figure 7.8, respectively, for the receding, pinned, and advancing growth stages in the same manner as shown previously for the hygrophilic case. Despite having similar bubble dynamics to the hygrophilic surface in the receding stage, the heat transfer during this stage is much different for the ambiphilic surface. As described previously, there is no microlayer formation under the initial bubble because this region does not rewet during the ebullition cycle on ambiphilic surfaces. In the hygrophilic case, the evaporation of the thin microlayer in this region dominates heat transfer and contributes significantly to rapid growth of the bubble. The absence of this thin microlayer region, evident in Figure 7.9 which shows the instantaneous microlayer thickness, results in slower growth and diminished heat transfer.

The rate of contact line expansion during early receding growth and the initial microlayer thickness at each radius are plotted in Figure 7.10 and Figure 7.11, respectively, for the hygrophilic and ambiphilic surfaces. The contact radius rapidly expands during early growth on the hygrophilic

surface, as shown in Figure 7.10, due to the rapid evaporation of the microlayer. As a result of this inertia-controlled growth, the contact radius actually goes beyond the stable value and advances backward slightly between 1 and 2 ms to reestablish a stable bubble shape. In Figure 7.11, it is evident that this rapid initial growth leads to a much thinner initial microlayer in the hygrophilic case between radii of 0.165 mm and 0.225 mm and a slightly thinner microlayer beyond 0.225 mm when compared with the ambiphilic case. Thus, the ambiphilic surface has diminished microlayer heat transfer into the pinning stage and through the entire bubble growth process. The increasing contact angle during the pinning stage also results in a larger film thickness and a less extreme temperature gradient which reduces conduction heat transfer near the contact line. The stagnant contact line also minimizes any convection during this stage. As a result of all of these factors, the heat transfer around the bubble is poor during the pinned growth stage for the ambiphilic surface and results in a nearly constant surface temperature, as seen in Figure 7.7(d).

The most effective heat transfer from the ambiphilic surface is observed as the contact line is advancing and the bubble departs. As observed in Figure 7.7(d) and Figure 7.8(c), respectively, the largest local dip in the surface temperature and the largest peak in heat flux are observed during this stage. Once the contact line begins to advance, the bubble quickly departs from the surface within ~1 ms as shown in Figure 7.3. This rapid contact line motion induces convection and brings cooler liquid into contact with the surface near the contact line, increasing the overall heat transfer.

7.2.4 Heat Transfer in the Hygrophobic Case

Figure 7.12 and Figure 7.13 present the respective surface temperature and heat flux profiles for the hygrophobic surface in the receding, pinning, and advancing stages in the same manner as shown for the previous cases. It is assumed that the microlayer does not form on a hygrophobic surface. This results in the majority of the heat transfer being sharply localized at the contact line as the bubble grows through the receding (Figure 7.13(a)) and pinned (Figure 7.13(b)) stages. Early in the receding stage, the surface remains nearly isothermal with only a slight dip in temperature due to the heat transfer at the contact line, as shown in Figure 7.12(a,d). The peak heat flux remains relatively constant through the receding and pinned stages, as evident in Figure 7.13, and the surface steadily heats up throughout this process. Due to the large base diameter, a substantial surface area becomes covered in vapor. Due to the lower conductivity of vapor compared with liquid, the surface underneath the bubble away from the contact line becomes hotter

than the bulk surface outside the contact radius. This occurrence of hot spots underneath the bubble is evident in the pinned (Figure 7.12(b,d)) and advancing (Figure 7.12(c,d)) stages.

The highest heat transfer is observed as the contact line is advancing, as shown in Figure 7.13(c). The contact line advances from the maximum contact radius of 3.86 mm to the pinch off radius of 0.42 mm, traversing a large portion of the surface. During this process, cooler liquid is brought into contact with this entire span of the surface resulting in a significantly thinner thermal boundary layer, as seen Figure 7.12(c). This moderately improves the heat transfer over a large area due to an increased amount of transient conduction and induces a convective flow. Additionally, the peak heat flux at the contact line is roughly doubled compared with the receding and pinning stages.

7.2.5 Advantages and Disadvantages of Different Wetting Behaviors

Based on the heat transfer behavior of the surfaces presented, broad conclusions can be made about the relative advantages and disadvantages of hygrophilic, hygrophobic, and ambiphilic surfaces. Hygrophobic surfaces have the most obvious drawbacks due to the lack of microlayer heat transfer and the large dryout region with minimal heat transfer. These features, coupled with previous conclusions that hygrophobic surfaces transition to ineffective film boiling prematurely due to large bubble base diameters [8,10,132], make hygrophobic surfaces undesirable for boiling applications. Hence, the following discussion will focus on hygrophilic and ambiphilic surfaces.

Compared with ambiphilic surfaces, hygrophilic surfaces have more effective microlayer heat transfer, particularly at the beginning stages of bubble growth. Because of the pinch-off departure mechanism observed in ambiphilic surfaces, the residual bubble left behind prevents formation of a microlayer in this area. Additionally, the existence of the thin microlayer near the center of the bubble on hygrophilic surfaces results in an increased growth rate which decreases the average microlayer thickness even in regions where the microlayer does form in the ambiphilic case. These advantages in microlayer heat transfer are the major contributing factor which allows the hygrophilic surface to maintain the lowest temperatures observed during bubble growth in this study.

When assessing the heat transfer performance during the bubble ebullition cycle, it is important to consider the full cycle which consists of nucleation, the growth period, and the waiting period. Due to the lack of predictive understanding of nucleation, the nucleation process and

waiting period were not directly modeled in this study; however, generalizations about these aspects can be made based on existing understanding. For instance, while the pinch-off mechanism of ambiphilic surfaces reduces the efficacy of microlayer heat transfer, it completely eliminates the waiting time before another bubble nucleates. It is expected that the waiting time would exhibit diminished heat transfer compared with any stage of the bubble growth process for either of these surface types due to the lack of a three-phase contact line, where the peak heat transfer is always observed. Thus, the lack of a waiting time is seen as a benefit for ambiphilic surfaces [8,40]. Of course, the value of eliminating the waiting time is dependent on the length of the waiting time on a specific hygrophilic surface. Additionally, nucleation typically occurs at a lower superheat on ambiphilic surfaces compared to hygrophilic surfaces [115,116,126,132]. This leads to a higher nucleation site density at a given heat flux. Thus, even though the heat transfer is generally less effective per bubble on ambiphilic surfaces, more bubbles will likely be present on the surface at a given heat flux. These tradeoffs between hygrophilic and ambiphilic surfaces make it difficult to claim that one surface type is definitively better for boiling heat transfer.

7.2.6 Implications for Enhanced Surface Design

Because both hygrophilic and ambiphilic surfaces are viable for the development of enhanced surfaces, the focus of surface design with regards to wettability should be focused on maximizing the advantages and minimizing the disadvantages for each surface type. The tradeoffs with different receding and advancing contact angles and potential design targets for hygrophilic surfaces are summarized in Figure 7.14, which illustrates the trends in heat transfer behavior with changes in the receding and advancing contact angle. As discussed, hygrophilic surfaces have the most effective heat transfer on a per bubble basis due to high microlayer heat transfer, particularly early in the growth process. One potential design target is to maximize the proportion of time spent in this early receding stage of growth by producing small bubbles that quickly depart from the surface. To achieve this, based on the results presented in Chapter 6, the receding and advancing contact angles should be minimized. The receding contact angle is the key factor that determines the bubble departure diameter. Reducing the receding contact angle will reduce the bubble departure diameter and, correspondingly, the time to departure. Reducing the advancing contact angle also plays a minor role in decreasing the departure diameter because it limits the length of the pinning stage of growth. This design target corresponds with the lower left area in Figure 7.14.

The disadvantages of hygrophilic surfaces revolve primarily around their nucleation characteristics. They exhibit a waiting time during which a bubble is not present at the nucleation site and the nucleation site density on these surfaces is typically lower than that of hygrophobic and ambiphilic surfaces at the same heat flux. Nucleation characteristics have been largely speculated to correspond to either the static or advancing contact angle [116,132]. Therefore, designing a surface such that the advancing contact angle approaches 90 deg may be a viable path for improving nucleation characteristics, and thereby performance, in the hygrophilic regime. This stands in contrast with the previous point of minimizing the advancing contact angle to promote rapid departure. However, the nucleation site density plays a major role in the overall heat transfer efficacy of a surface. For this reason, it is possible that any improvement to the nucleation site density would outweigh the increase in the departure time. If the receding contact angle were also maximized within the hygrophilic regime, this would lead to significantly larger bubbles which, in turn, would increase the contact line length and likely the departure time. While increased contact line length is favorable for heat transfer, it may have a detrimental impact on the critical heat flux of the surface and reduces the proportion of time spent in the efficient early receding growth stage. Based on this conjecture, hygrophilic surfaces should be designed either to minimize both the advancing and receding contact angles (bottom left in Figure 7.14) or minimize the receding contact angle and increase the advancing contact angle to near 90 deg (bottom right in Figure 7.14).

The tradeoffs with different receding and advancing contact angles and potential design targets for ambiphilic surfaces are summarized in Figure 7.15. Ambiphilic surfaces generally have favorable nucleation characteristics due to high advancing contact angles. As discussed for hygrophilic surfaces, it may be possible to maximize the nucleation site density by maximizing the advancing contact angle as much as possible. It is important to consider that an increase in the advancing contact angle also increases the size of the residual bubble left behind upon bubble departure. In Chapter 6, a case with a receding contact angle of 30 deg and an advancing contact angle of 150 deg was shown to pinch off from the surface with the contact line still at the maximum contact diameter. A typical bubble ebullition cycle on such a surface would not exhibit a receding stage or an advancing stage, but rather the entire bubble growth period would have a pinned contact line. This would completely eliminate microlayer heat transfer once the initial microlayer dries out. Thus, the trade-off between nucleation characteristics and microlayer heat transfer must be

considered, but one path to heat transfer enhancement would be to maximize the advancing contact angle in an attempt to maximize the nucleation site density on the surface while maintaining a low receding contact angle to limit vapor coverage on the surface, as shown in the bottom right of Figure 7.15.

Another potential design target for ambiphilic surfaces would be to reduce the detriment to microlayer heat transfer caused by the lack of rewetting of the surface by the minimizing the size of the residual bubble left behind upon departure. To achieve this, the advancing contact angle should be reduced to just above 90 deg such that pinch off still occurs, but the residual bubble is very small. Then, the bubble should behave more like those on hygrophilic surfaces because almost the entire surface is allowed to rewet, but still preserve the benefit of removing the waiting time until another bubble nucleates. Notably, this target, shown in the bottom left of Figure 7.15, aligns with the goal of balancing microlayer heat transfer and nucleation characteristics for hygrophilic surfaces via a low receding contact angle and an advancing contact angle near 90 deg.

Ambiphilic surface can be prone to the development of dry spots due to the pinch-off departure mechanism. Thus, high receding contact angles that lead to large contact diameters should generally be avoided, particularly when coupled with high advancing contact angles. High receding and advancing contact angles (top right region of Figure 7.15) would result in large dry spots that do not rewet upon bubble departure, leading to large hot spots on the surface. This would likely significantly reduce the critical heat flux of the surface.

7.3 Conclusions

The heat transfer behavior during single bubble growth was investigated for hygrophilic, hygrophobic, and ambiphilic surfaces. Differences in the dynamic contact angles in each case result in significantly different bubble dynamics and heat transfer mechanisms. Hygrophilic surfaces are shown to have extremely effective heat transfer during the early receding stage of growth resulting from a thin microlayer. This results in the most effective heat transfer observed on a per bubble basis. Ambiphilic surfaces exhibit lessened microlayer heat transfer due to the pinch-off mechanism at departure which prevents portions of the surface from rewetting and forming a new microlayer. However, this pinch-off mechanism completely eliminates the waiting time between bubble departure and nucleation of a new bubble. This maintains constant contact line heat transfer, as opposed to less effective transient conduction as the thermal boundary layer

is reestablished during the waiting period. Additionally, ambiphilic surfaces have been shown to have favorable nucleation characteristics. Bubbles on hygrophobic surfaces grow to large contact diameters which result in large dry spots beneath the bubble. These dry spots have particularly poor heat transfer due to the poor conductivity of vapor, resulting in large hot spots on the surface. Additionally, this vapor spreading has previously been shown to lead to premature critical heat flux.

Hygrophilic and ambiphilic surfaces were identified as promising choices for the development of enhanced surfaces. Specific dynamic contact angle design targets were identified based on maximizing and minimizing the advantages and disadvantages within each class of surfaces. Broadly, this resulted in the same two targets for each class – maximizing nucleation site density or maximizing microlayer heat transfer. In both cases, low receding contact angles are preferred in order to limit vapor spreading and the departure size. For the hygrophilic regime, the advancing contact angle can either be minimized to encourage rapid bubble departure and increase the proportion of time spent in the highly effective early receding stage, or the advancing contact angle can be increased near 90 deg to maximize the nucleation site density. Similarly for ambiphilic surfaces, the advancing contact angle can be reduced near 90 deg to minimize the size of the residual bubble and increase the area over which the microlayer forms, or the advancing contact angle can be maximized to improve the nucleation site density. It is difficult to predict which precise conditions are ideal due to uncertainty in the impact that varying the dynamic contact angles has on the waiting time, nucleation site density, and other factors. Overall, this work provides design rationale for the dynamic wetting behavior of a surface in order to improve heat transfer.

Table 7.1. Key Bubble Ebullition Characteristics for Each Case Studied

Case	Receding Contact Angle (deg)	Advancing Contact Angle (deg)	Maximum Base Diameter (mm)	Departure Diameter (mm)	Departure Time (ms)
Hygrophilic	30	30	0.55	1.87	25.9
Hygrophobic	120	120	7.71	7.83	123.9
Ambiphilic	30	120	0.53	2.71	115.1

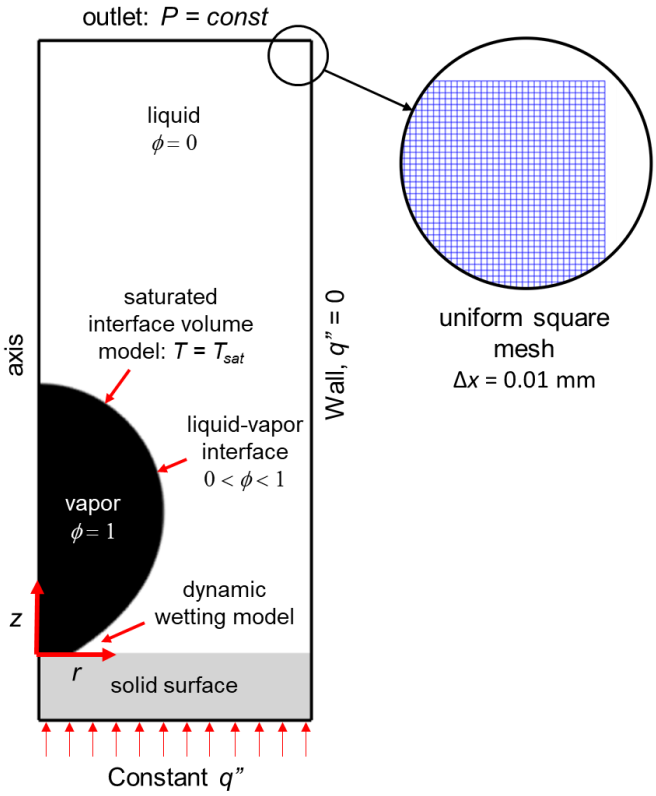

Figure 7.1. The axisymmetric simulation domain including specified boundary conditions. The zoomed view in the top right shows the uniform square mesh.

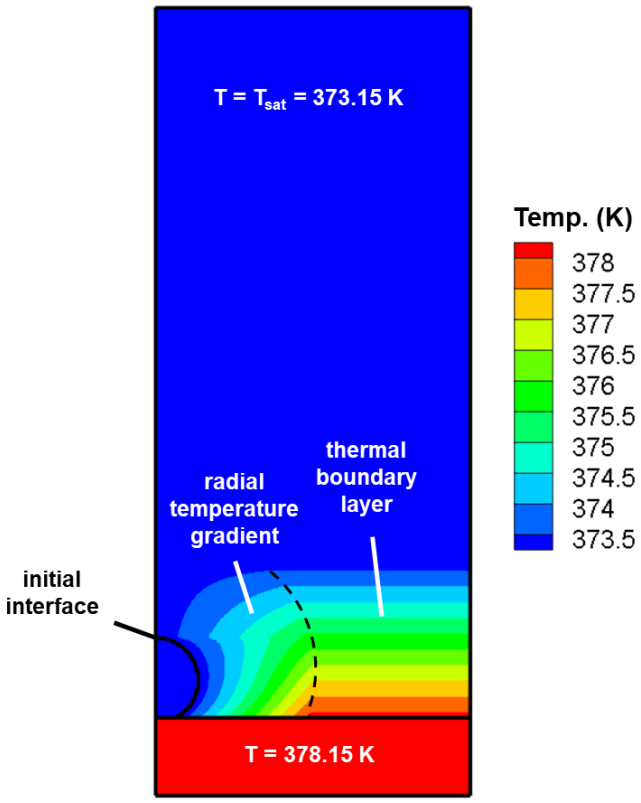

Figure 7.2. The conditions at initialization for the hygrophilic case with key aspects labeled.

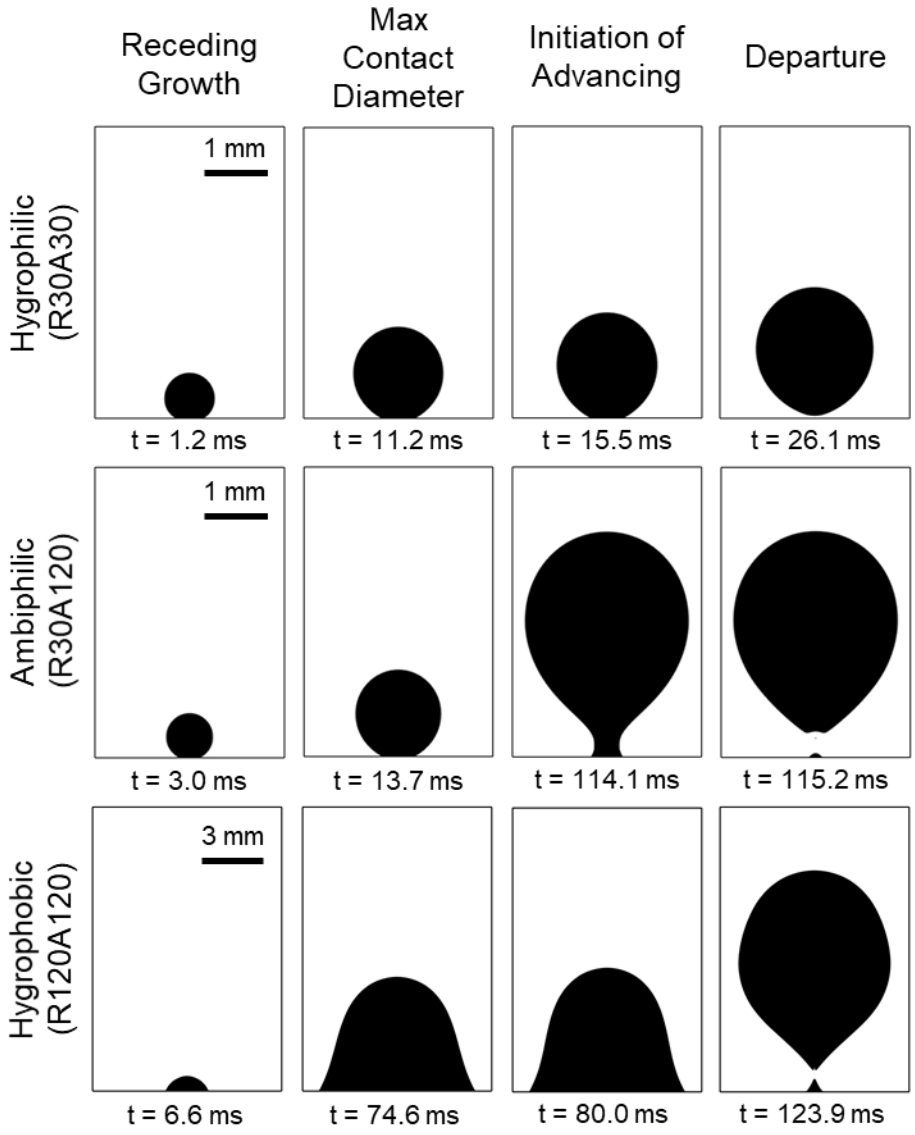

Figure 7.3. Snapshots of the bubble morphology at key points along the bubble ebullition cycle for each case. Vapor is shown in black and liquid is shown in white. Note that the full simulation domain is not shown here.

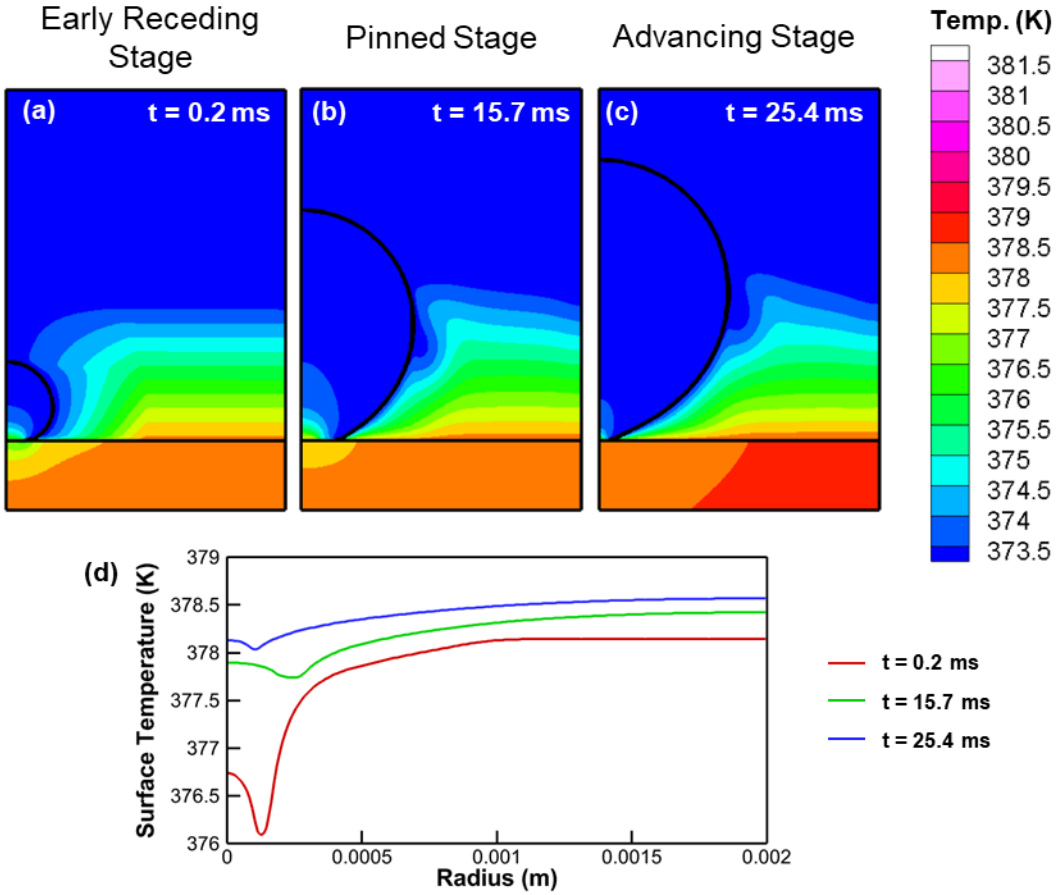

Figure 7.4. Temperature contours for a bubble growing on the hygrophilic surface in the (a) early receding stage, (b) pinned stage, and (c) advancing stage. The interface of the bubble and the solid-liquid boundary are denoted by black lines. The full domain width of 2 mm is shown, but with a reduced frame height. (d) The surface temperature plotted versus radius for the same times.

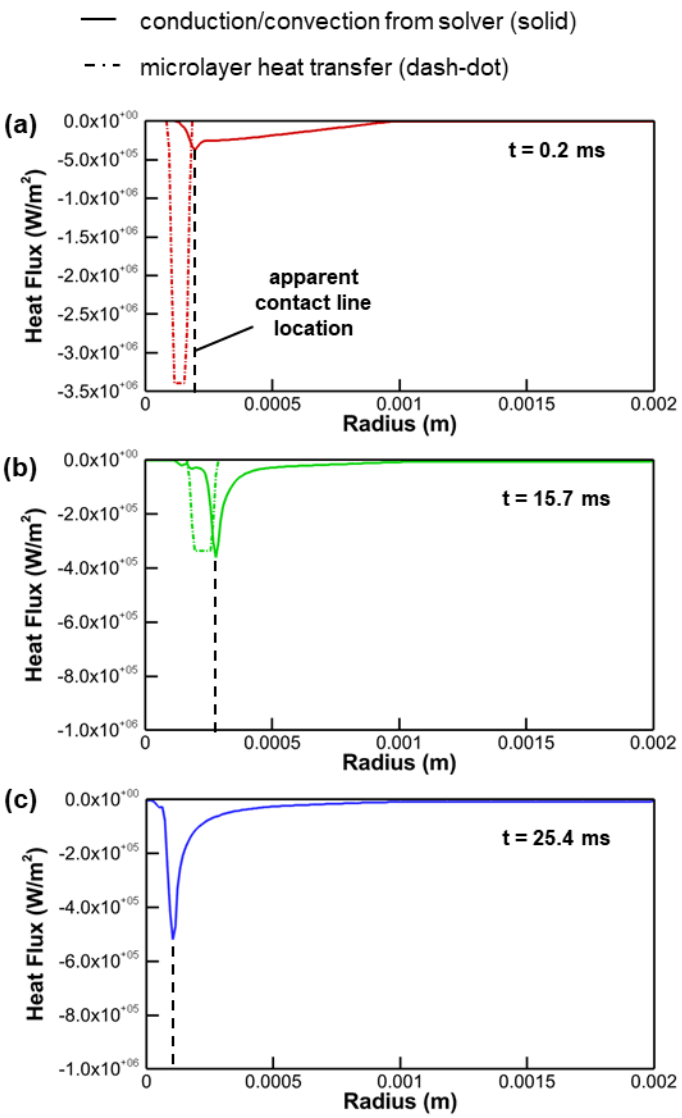

Figure 7.5. The surface heat flux profiles for the microlayer and the conductive and convective heat transfer calculated by the simulation for the hygrophilic case during the (a) early receding stage, (b) pinning stage and (c) advancing stage. Note that (a) has a larger y-axis range than the other plots.

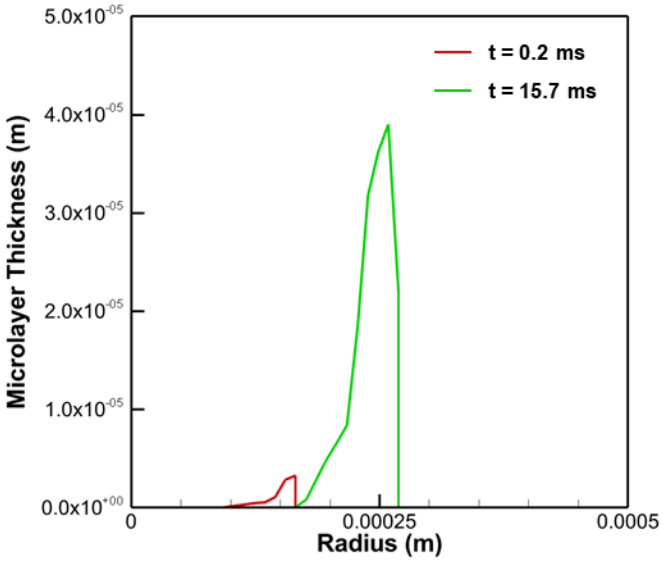

Figure 7.6. The instantaneous microlayer thickness during early receding stage (t = 0.2 ms) and the pinned stage (t = 15.7 ms) for the hygrophilic surface.

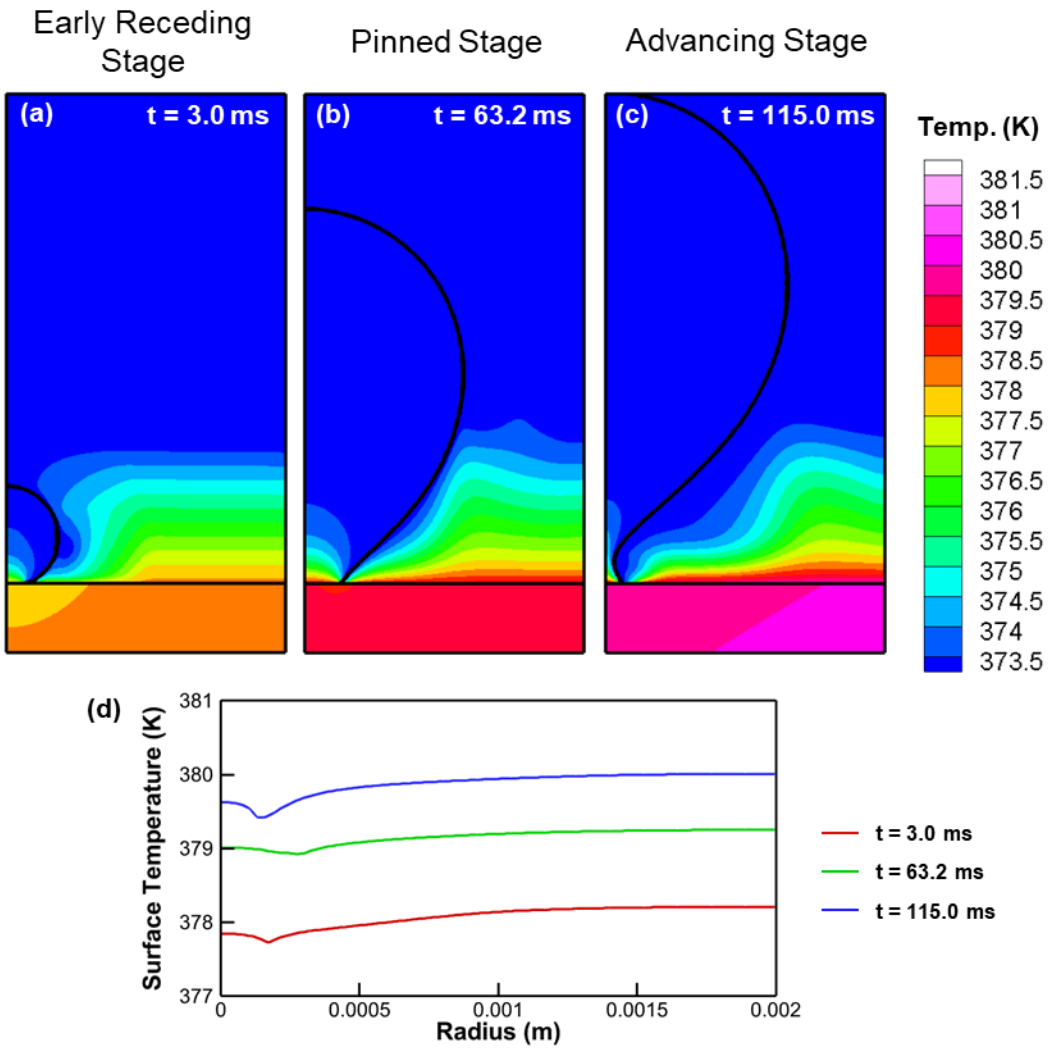

Figure 7.7. Temperature contours for a bubble growing on the ambiphilic surface in the (a) early receding stage, (b) pinned stage, and (c) advancing stage. The interface of the bubble and the solid-liquid boundary are denoted by black lines. The full domain width of 2 mm is shown, but with a reduced frame height. (d) The surface temperature plotted versus radius for the same times.

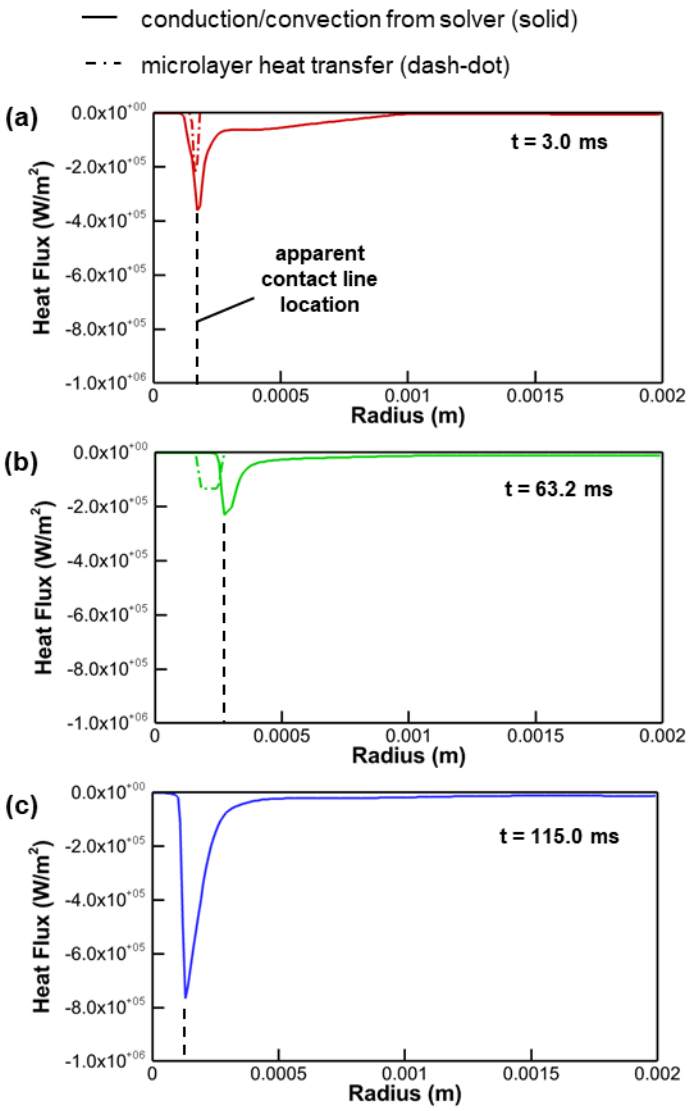

Figure 7.8. The surface heat flux profiles for the microlayer and the conductive and convective heat transfer calculated by the simulation for the ambiphilic case during the (a) early receding stage, (b) pinned stage and (c) advancing stage.

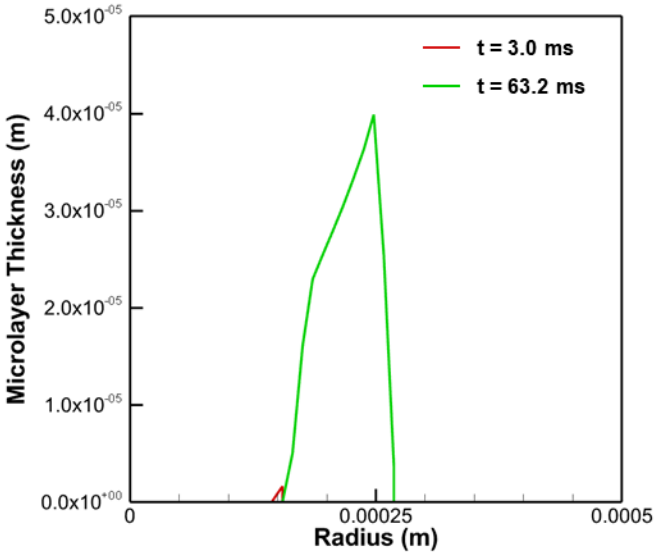

Figure 7.9. The instantaneous microlayer thickness during early receding stage (t = 3.0 ms) and pinned stage (t = 63.2 ms) for the ambiphilic surface.

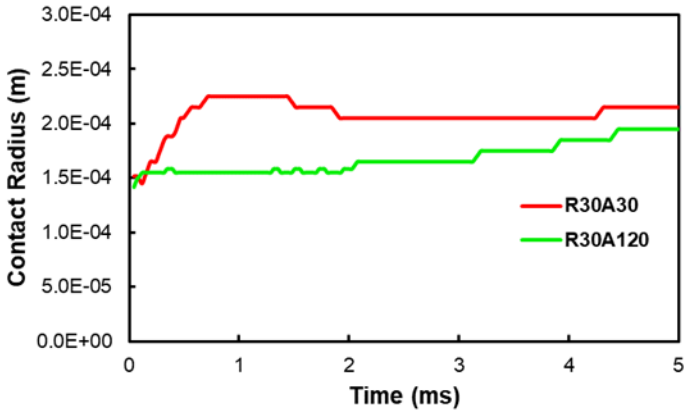

Figure 7.10. The contact radius of the bubble during the first 5 ms of the hygrophilic and ambiphilic simulations.

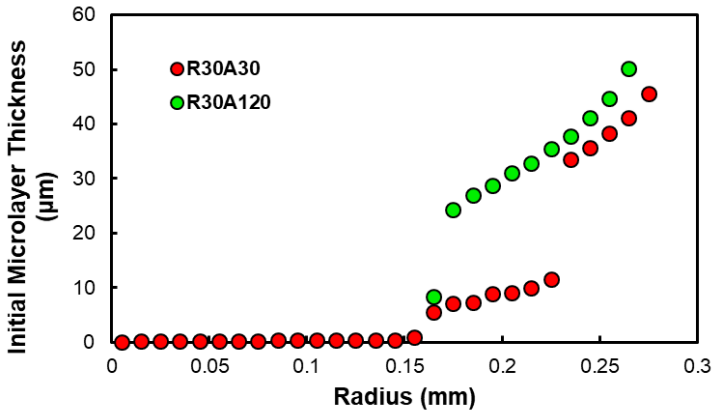

Figure 7.11. The initial microlayer thickness at each radial location for the hygrophilic and ambiphilic cases. Each point shown has a nonzero thickness.

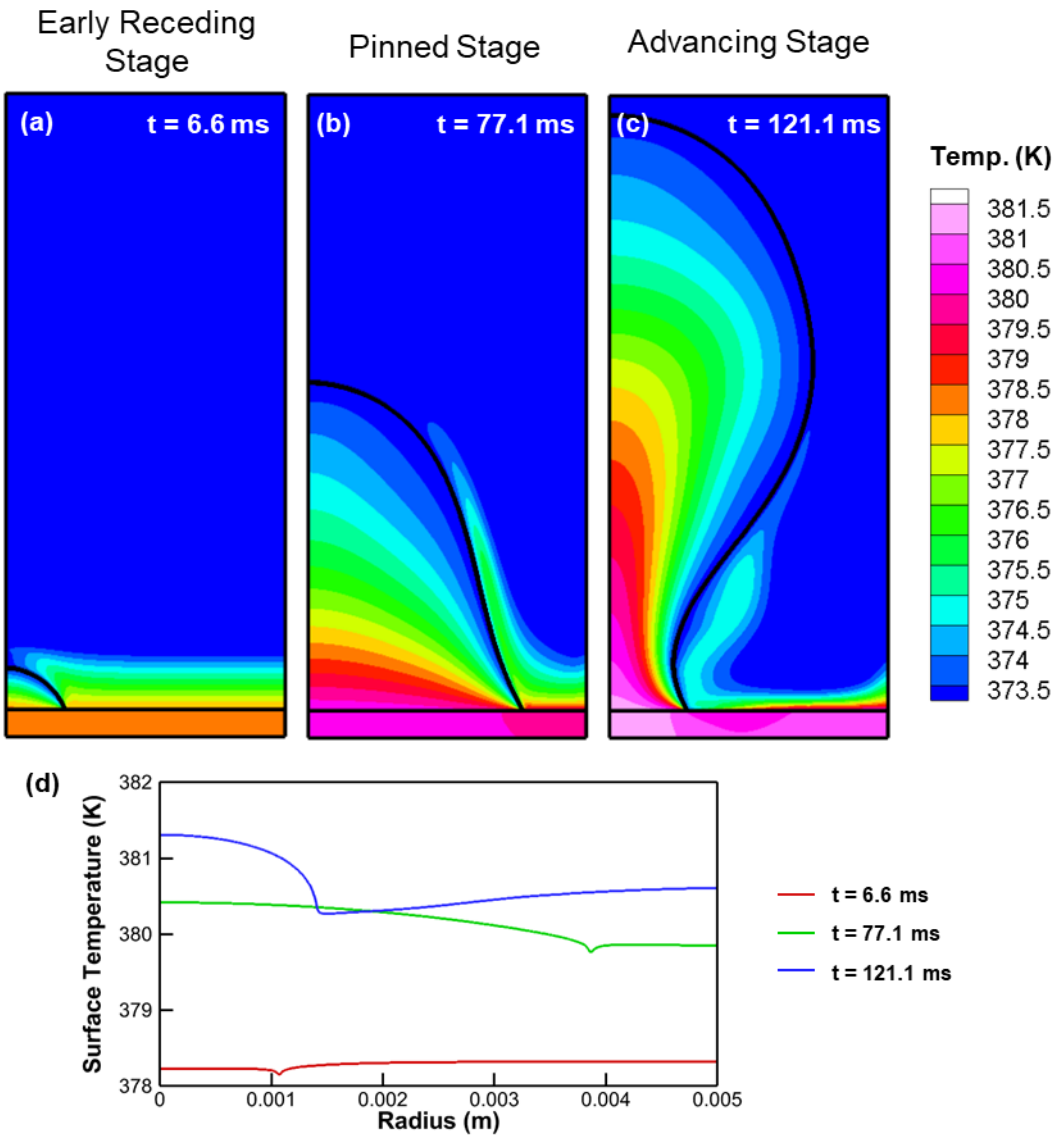

Figure 7.12. Temperature contours for a bubble growing on the hygrophobic surface in the (a) early receding stage, (b) pinned stage, and (c) advancing stage. The interface of the bubble and the solid-liquid boundary are denoted by black lines. The full domain width of 5 mm is shown, but with a reduced frame height. (d) The surface temperature plotted versus radius for the same times.

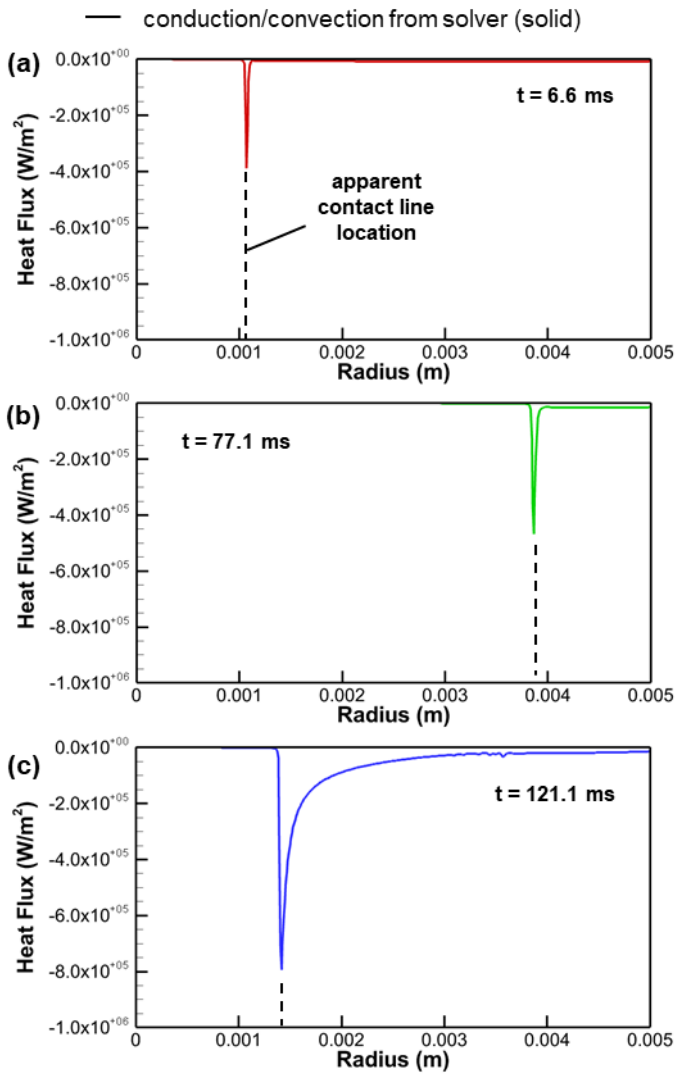

Figure 7.13. The surface heat flux profiles for hygrophobic case during the (a) early receding stage, (b) pinned stage, and (c) advancing stage.

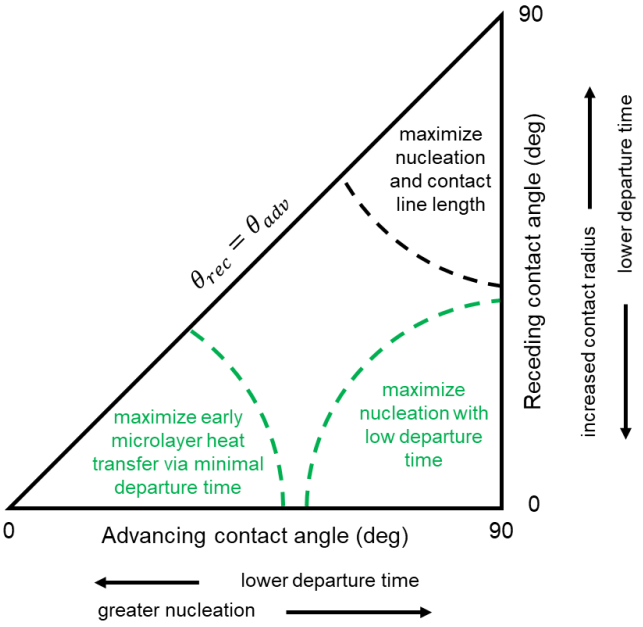

Figure 7.14. Summary of the tradeoffs that occur at different receding and advancing contact angles within the hygrophilic regime. Favorable design targets are shown in green.

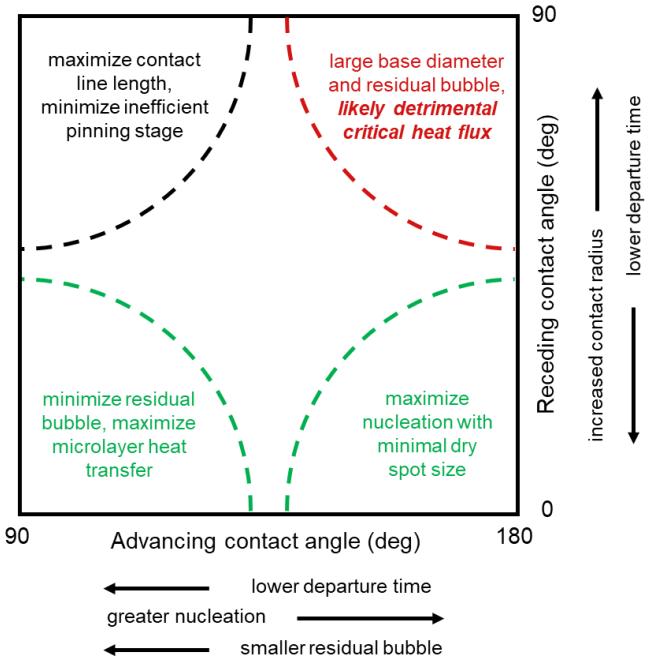

Figure 7.15. Summary of the tradeoffs that occur at different receding and advancing contact angles within the ambiphilic regime. Favorable design targets are shown in green. Particularly detrimental regions are shown in red.

8. SUMMARY AND FUTURE WORK

8.1 Summary

This work has greatly advanced the understanding of the effects of surface wettability on bubble dynamics and boiling performance. The findings provide a strong foundation upon which enhanced surfaces and additional studies can be built. The key conclusions are summarized as follows:

- **Dynamic wetting behavior is extremely important to consider for boiling surfaces.** This point is strongly reinforced throughout this work, but is most clearly demonstrated in Chapter 3, which focuses on boiling from superhydrophobic surfaces. From the same surface, drastically different boiling behaviors were observed depending on the wetting state of the surface. Despite the wetting states having similar static wettability, the contrast in the dynamic wetting behavior of the wetting states clearly dictated the performance. This, among other results, clearly shows that wetting dynamics play a critical role during boiling.
- **The receding contact angle plays the dominant role in dictating bubble morphology and critical heat flux.** It was shown to control the bubble morphology during the early stage of growth up to the point at which the maximum contact diameter is reached. Thus, it is the major factor in determining the amount of vapor spreading from a given bubble and the departure size. This finding informed the development of enhanced ambiphilic surfaces, which would have previously been considered “hydrophobic” and expected to perform poorly.
- **The advancing contact angle determines the bubble departure mechanism.** Surfaces with advancing contact angles greater than 90 deg exhibit a pinch-off departure mechanism while those with advancing contact angles less than 90 deg fully depart from the surface. The pinch-off mechanism results in complete removal of the waiting period between bubble departure and nucleation of the next bubble because a residual bubble is left behind on the surface upon departure.
- **Surface wettability in the context of boiling was reclassified into three regimes: hygrophilic, hygrophobic, and ambiphilic.** Based on the findings presenting throughout

this work, it became evident that wettability regimes in the context of boiling should be based upon dynamic wetting behavior rather than static wetting behavior such that these classifications correlate with boiling characteristics. Thus, hygrophilic surfaces are redefined as those having receding and advancing contact angles of less than 90 deg. These surfaces have small base diameters and departure diameters and fully depart from the surface upon departure. Hygrophobic surfaces are redefined as those having receding and advancing contact angles of greater than 90 deg. These surfaces have large base and departure diameters and pinch-off at departure. Ambiphilic surfaces are defined as those having receding contact angles less than 90 deg and advancing contact angles greater than 90 deg. These surfaces are unique in that, according to static contact angle characterizations, they might be considered hygrophobic, but the bubble morphologies and sizes are more similar to hygrophilic surfaces due to the low receding contact angle. These surfaces also exhibit a pinch-off departure mechanism.

- **Hygrophilic surfaces were identified as candidates for the development of enhanced surfaces due to highly effective heat transfer on a per bubble basis, and a pathway for further enhancement was identified.** Based on the results presented in Chapter 7, hygrophilic surfaces promote highly effective microlayer heat transfer during the early stages of bubble growth. The drawback of hygrophilic surfaces is that they have less favorable nucleation characteristics than ambiphilic surfaces. To maximize the performance of hygrophilic surfaces, two pathways were proposed. First, receding and advancing contact angles can be minimized to reduce departure time and increase the proportion of time spent in the early growth stage where the microlayer heat transfer is highly effective. Second, the receding angle can be minimized to keep departure time low while the advancing contact angle is increased to near 90 deg to improve nucleation characteristics.
- **Ambiphilic surfaces were identified as candidates for the development of enhanced surfaces due to favorable nucleation characteristics and bubble dynamics, and a pathway for further enhancement was identified.** Ambiphilic surfaces were shown to have less effective heat transfer than hygrophilic surfaces on a per bubble basis, but the nucleation characteristics are much more favorable. Additionally, they maintain small bubble contact diameters and departure sizes which promote high critical heat fluxes. To

maximize the performance of ambiphilic surfaces, two pathways were proposed. In both cases, the receding contact angles should be minimized to maintain small bubble sizes and prevent vapor spreading. One option is to reduce the advancing contact angle to near 90 deg. This reduces the size of the residual bubble left behind upon bubble departure, allowing the majority of the surface to rewet. This leads to the development of a new, thin microlayer, maximizing microlayer heat transfer. The second option is the maximize the advancing contact angle in an attempt to achieve the best possible nucleation characteristics. This is the path under which the "superhydrophobic surfaces" (Wenzel state), presented in Chapter 3, and the "parahydrophobic surfaces", presented in Chapter 5, fall. Both of these can now be redefined as special cases of ambiphilic surfaces, and both were shown to exhibit enhanced boiling performance.

8.2 Future Work

The foundational understanding obtained throughout this work provides clear pathways for further advances, several of which are briefly summarized here.

- In the diabatic single bubble simulations presented in Chapter 7, there are a number of approximations and assumptions, particularly with respect to the microlayer behavior, that can have a major influence on the overall heat transfer. Thus, an experimental study to validate the heat transfer behavior for bubbles growing on hygrophilic, hygrophobic, and ambiphilic surfaces is warranted. These experiments should examine the single bubble dynamics on each type of surface, measure local surface temperatures using techniques such as infrared imaging, and measure the microlayer thickness using interferometry. This data would provide a basis for comparison with the simulation framework. If necessary, the simulations could be adapted to better account of the local heat transfer and microlayer behavior during the bubble ebullition cycle.
- This work clearly identifies pathways for the development of enhanced hygrophilic and ambiphilic surfaces. Four viable dynamic contact angle targets, in all, are described: hygrophilic surfaces with minimized receding and advancing contact angles, hygrophilic surfaces with minimized receding contact angles and advancing contact angles approaching 90 deg, ambiphilic surfaces with minimized receding contact angles and maximized advancing contact angles, and ambiphilic surfaces with minimized receding

contact angles and advancing contact angles approaching 90 deg. All of these options should be explored and optimized to achieve new classes of enhanced surfaces.

- The key aspect regarding the role of wettability during boiling for which understanding is still lacking is the role during the nucleation process. It is still unclear exactly how surface wettability affects the nucleation behavior and whether the static, equilibrium, or advancing contact angle is the governing wetting characteristic. Further studies should be carried out in order to gain this understanding and develop model for nucleation based on dynamic wetting behavior. This would allow integration of the nucleation process into the numerical simulations and better analysis of the overall bubble ebullition cycle.

APPENDIX A. A WETTABILITY METRIC FOR CHARACTERIZATION OF CAPILLARY FLOW ON TEXTURED SUPERHYDROPHILIC SURFACES

This appendix discusses the development of a metric to characterize superhydrophilic surfaces based on the rate of capillary flow on the surface. Superhydrophilic surfaces are of interest in practical applications for their ability to rapidly pump or spread liquid and, thus, any wettability metric should characterize this trait. An expression for the radial capillary-driven flow is developed from which a lumped metric is identified that includes all of the key surface characteristics that govern liquid pumping. A simple characterization technique is proposed to experimentally determine this metric for any highly wetting, textured surface. This simple approach is demonstrated to be accurate and repeatable in distinguishing surfaces based on their liquid pumping performance. The work discussed in this appendix was published in *Langmuir* [85].

INTRODUCTION

The practice of engineering surfaces to obtain desirable wetting behavior has grown extensively over the past couple of decades [93,152]. The wettability of a surface depends not only on the intrinsic surface energy of the material, but also on the surface topology. By texturing surfaces with nano- or microstructures, extremely wetting or non-wetting behavior can be imparted [92,93]. Extremely wetting surfaces offer advantageous properties for textiles [153,154], microfluidics [155–157], and boiling [4,115] applications due to their ability to promote capillary-driven flow on the surface. Extremely non-wetting surfaces can be useful in condensation [76,158,159] and self-cleaning surfaces [160,161], among other applications [162], due primarily to their water-repellence.

The wettability of a surface is most commonly characterized by the equilibrium contact angle, *i.e.*, the angle between the solid-liquid interface and the liquid-gas interface formed at the three-phase contact line. The equilibrium contact angle on a flat surface is a manifestation of the balance of surface energies in the system as defined by Young's equation [79], and is typically measured using a sessile droplet deposited on the surface. While the situation is more complex for textured surfaces [82,84,87,163], the static contact angle is often used to define nominal

regimes of wettability, *viz*., superhydrophilic, hydrophilic, hydrophobic, and superhydrophobic, when water is the wetting liquid (and the hydro- prefix is modified for different liquids). While various definitions for these regimes are found in the literature [164], the most common contact-angle-based definition specifies that superhydrophilic surfaces have a contact angle of 0 deg, hydrophilic surfaces a contact angle of less than 90 deg, hydrophobic a contact angle of greater than 90 deg, and superhydrophobic a contact angle greater than 150 deg (note that to be considered superhydrophobic, a surface also typically must have a low roll-off angle). In the case of the superhydrophilic behavior, water spreads completely on a textured surface into a thin liquid layer with an apparent contact angle of zero.

Contact angle is a simple and effective metric that indicates the relative wettability of surfaces ranging from hydrophilic to superhydrophobic. However, following this metric, all surfaces exhibiting superhydrophilic behavior are mapped to a single value of contact angle that does not necessarily reflect the liquid pumping ability of the surface. Thus, an apparent contact angle value of zero can identify a surface as superhydrophilic, but it is not a sufficient descriptor of the extent of superhydrophilicity of a surface.

Several alternative measures have been used to characterize the behavior of highly wetting surfaces; however, there is no universally accepted metric to describe highly wetting surfaces. One such approach tracks the transient contact angle of a droplet after it is placed on the surface [165,166]. Surfaces are then differentiated based on how rapidly the contact angle of the droplet diminishes from an initial value to below a threshold value, typically 5 deg. This approach allows the performance of different surfaces to be compared side-by-side, but the behavior is difficult to predict *a priori* based on the surface characteristics so as to extract a performance metric that is not dependent on the specific experiment.

For porous materials, the rate of capillary rise method places a sample vertically into a liquid reservoir and measures the liquid that wicks up into the sample by either direct visualization or weight [167]. By modeling these capillary flow dynamics [168], a factor such as K/R_{eff} [169,170] or $\Delta P_{cap}K$ [171] is often obtained that contains key parameters that govern the flow (where K is permeability, ΔP_{cap} is capillary pressure, and R_{eff} is the effective pore radius which is inversely related to the capillary pressure). While these factors quantify the tradeoff between the permeability and capillary pressure, they are not the only surface properties important to capillary-driven liquid pumping. Additionally, the rate of rise technique requires samples to have a straight

edge at which liquid must be introduced, which prohibits the testing of certain geometries, such as disk-shaped samples.

Other studies have characterized highly wetting surfaces by measuring the radial spreading of liquid introduced at a point location on the surface [117,172]. Rahman *et al.* [6] measured the maximum volume flux drawn by wicking into a superhydrophilic substrate from a vertical liquid-supply tube held just above the surface. The maximum volumetric flux occurs at the instant the liquid contacts the surface and was approximated with a linear fit of the initial data, rendering this metric sensitive to the precise manner in which the liquid contacts the surface and what initial period of data is considered for the fitting. Kim *et al.* [72] deposited a droplet on a superhydrophilic surface and tracked the wetting front from above. Applying a model derived for a linear rate of rise experiment [83] to this radial flow, the wicking coefficient, W, was extracted, but the difference between the radial and linear flow behavior was not reconciled. Kunkle and Carey [173] proposed a metric based on the ratio of the measured wetted footprint of a droplet on a surface to the footprint of a droplet of the same volume if it were to have a contact angle of 90 deg. This metric can accommodate surfaces ranging from superhydrophilic to superhydrophobic but does not capture the dynamic liquid spreading process on superhydrophilic surfaces, which is important in the relevant applications.

Superhydrophilic surfaces are of interest in practical applications for their ability to rapidly pump or spread liquid and, thus, any wettability metric should characterize this trait. In this study, an expression for the radial capillary-driven flow is developed from which a lumped metric is identified that includes all of the key surface characteristics that govern liquid pumping. A simple characterization technique is proposed to experimentally determine this metric for any highly wetting, textured surface. This simple approach is demonstrated to be accurate and repeatable in distinguishing surfaces based on their liquid pumping performance. While this approach is not fluid-specific, water is used for the experiments in this study.

METHODS

The characterization technique must accurately capture the volumetric flow rate into the highly wetting surface as a measure of the wetting behavior. The approach taken here is to bring a small tube filled with liquid into contact with the highly wetting substrate, such that the liquid is

drawn out of the open-ended tube and spreads radially across the surface, as is illustrated in Figure A-1. The meniscus level in the tube is tracked over time to determine the volumetric flow into the surface. Compared to rate of rise tests, this point-introduction method has the advantage of being able to accurately measure the volumetric flow rate without the need for visualizing the liquid front within the surface or making separate mass measurements [6]. Additionally, because it is does not require or assume a unidirectional flow, anisotropically wetting substrates can be evaluated. In this section, a capillary-flow model is developed to determine a superhydrophilicity metric that can be extracted from this characterization approach. An experimental procedure is then developed to characterize superhydrophilic surfaces with this metric. Finally, superhydrophilic surfaces are fabricated with a known geometry to demonstrate that the wetting behavior of surfaces can be predicted solely based on the surface characteristics included in the metric.

Capillary Flow Model

To model the capillary-driven flow, the surface is treated as a thin, porous layer such that there is one-dimensional radial flow outward from the tube location, as shown in Figure A-2. The gravitational pressure head, capillary pressure of the tube, and flow resistance in the tube are assumed to be negligible compared to the capillary pressure and viscous resistance of the surface. To verify, the relative magnitude of each of these terms is compared to the surface capillary pressure to determine whether they would have a significant effect on the flow behavior. The capillary pressure in the tube can be approximated as

$$\Delta P_{cap,tube} = \frac{2\sigma\cos(\theta)}{r} \tag{A.1}$$

where σ is the surface tension of water, θ is the receding contact angle of water on polytetrafluoroethylene (PTFE), and r is the inner radius of the tube. The receding contact angle of water on PTFE has been shown by Yasuda and Okuno [174] to be as low as 70 deg, which is used in this analysis to be conservative. The capillary pressure of the tube is calculated to be a constant $\Delta P_{cap,tube}$ = 92 Pa. This value is between 2-13% of the surface capillary pressure for the different arrays evaluated in this study. The gravitational pressure head of the suspended water column can be approximated by

$$\Delta P_g = \rho g l \tag{A.2}$$

where ρ is the mass density of water, g is the gravitational constant, and l is the height of the liquid column of water. The height of 5 μL of water in the tube, used for testing in this study, is ~6.4 mm, resulting in a maximum gravitational pressure head of ΔP_g = 63 Pa assisting the flow rate out of the tube. This maximum value is between 2-9% of the surface capillary pressure for the different arrays tested; we note that this is a conservative estimate, as the actual gravitational pressure head would decrease over the duration of the test to a value of zero. The pressure drop in the tube due to viscous resistance, ΔP_v, can be estimated using the Hagen-Poiseuille Law

$$q = \frac{\pi r^4 \Delta P_v}{8\mu L} \tag{A.3}$$

where q is the volumetric flow rate, r is the radius of the tube, μ is the dynamic viscosity of water, and L is the flow length. In the most extreme case, the pressure drop was evaluated at the maximum measured flow rate of 40 μL/s over the maximum flow length in the tube of 6.4 mm. The calculated pressure drop due to viscous resistance in the tube was ΔP_v = 21 Pa, or 0.6-3% of the capillary pressure in the micropillar arrays. It is additionally assumed that evaporation from the liquid layer drawn into the surface is negligible compared to the volumetric flow rate into the surface.

Under these assumptions, the creeping flow through the surface can be modeled using the one-dimensional radial form of Darcy's law:

$$\frac{dP_{cap}}{dr} = -\frac{\mu}{K} u_r(r) \tag{A.4}$$

where P_{cap} is capillary pressure, r is the radial coordinate direction, μ is the dynamic viscosity of the fluid, K is the permeability of the surface, and $u_r(r)$ is the radial Darcy velocity at radius r. Based on mass continuity, the radial velocity decreases with radial distance; the instantaneous volumetric flow rate, $q(t)$, must be substituted in to integrate with respect to radius. For the porous layer, $q(t) = A_c u_r(r) = 2\pi r(t) h u_r(r)$, where A_c is the cross-sectional area of a radial slice at the flow front, and h is the effective porous layer thickness. Integrating between the radius of the flow front, $r_{out}(t)$, and the radius at which liquid is being supplied, r_{in}, the instantaneous volumetric flow rate can be determined with a knowledge of the fluid properties, surface characteristics, and current radial position of the flow front:

$$q(t) = \frac{2\pi Kh\Delta P_{cap}}{\mu \ln\left(\frac{r_{out}(t)}{r_{in}}\right)} \tag{A.5}$$

The volumetric flow rate into the surface at any instant, $q(t)$, is maximized when the product of surface properties $Kh\Delta P_{cap}$ is maximized. Thus, this surface property product is deemed a superhydrophilicity metric, ω, that governs the wetting performance of a superhydrophilic surface and contains all the surface characteristics important to the flow:

$$\omega = Kh\Delta P_{cap} \tag{A.6}$$

By lumping all the important surface characteristics into a single metric, the need to determine these properties individually – a task that is challenging for stochastic superhydrophilic surfaces – is obviated. It is evident that while performance factors K/R_{eff} and $\Delta P_{cap}K$ would correlate strongly with wetting behavior, they do not account for the key factor of the effective porous layer thickness. It is noted that while the characterization approach developed here can be generally applied for any fluid that wets the surface with this behavior, the value of ω is fluid-specific.

Experimental Procedure

An experimental test facility and procedure were developed to determine the superhydrophilicity metric by measuring the liquid intake rate of the surface under test. A schematic representation of the experimental setup is shown in Figure A-3. An open-ended syringe (with the plunger removed) with a 1.07 mm inner-diameter, semi-transparent polytetrafluoroethylene (PTFE) tip is suspended above a textured superhydrophilic surface resting on a stage that can be translated vertically. The syringe tip is filled with approximately 5 µL of water; this fill volume is selected such that the radial flow is not obstructed by the outer boundaries of the surface. A high-speed camera (Photron, Ultima APX) is mounted to view the syringe tip in such a manner that both the top meniscus of the water column in the syringe tip and the surface are visible throughout the test. Uniform LED backlighting (Advanced Illumination, BL138) allows for a visual measurement of the liquid meniscus position in the tube.

Each test is carried out by slowly raising the test surface vertically until it just comes into contact with the bottom of the liquid column suspended in the tube. As contact occurs, a liquid meniscus is formed between the end of the tube and the surface; downward movement of the

meniscus in the tube is initiated as the liquid is drawn into the surface under test. The high-speed camera records the meniscus position in the tube until all the liquid has been drawn out. Figure A-4 shows an image frame from the high-speed video at an intermediate time during this process when the liquid is being drawn into the surface from the tube and the meniscus between the tube and the surface has reached a steady shape. The liquid propagation front can be seen as the liquid wets the surface. At any given time, the meniscus location is defined by its lowest point within the tube. By comparing the location of the meniscus at any time with the initial meniscus location, the volume that has spread into the surface can be determined.

To interpret the experimental data, the capillary flow dynamics captured by equation (A.5) are recast in terms of the measured volume of liquid drawn into the surface (as opposed to the flow rate and radial position of the liquid front in the surface) where $q(t) = dV_{out}(t)/dt$, $V_{out}(t) = \pi r_{out}^2(t) h\varepsilon$ (where ε is the porosity), and $V_{in} = \pi r_{in}^2 h\varepsilon$. Integrating between two arbitrary times, a form of the equation is obtained in terms of only known liquid properties, ω, and measured values.

$$\frac{\mu}{4\pi\omega}\left[\begin{array}{l} V_{out,2}\ln\left(\frac{V_{out,2}}{V_{in}}\right) - V_{out,2} - \\ \left(V_{out,1}\ln\left(\frac{V_{out,1}}{V_{in}}\right) - V_{out,1}\right)\end{array}\right] = t_2 - t_1 \qquad \text{(A.7)}$$

where $V_{out,a}$ represents the volume in the porous layer within r_{out} at time t_a and V_{in} is defined as the liquid volume in the porous layer within the radius where the meniscus contacts the surface, r_{in} (as shown in Figure A-4). With these values measured experimentally, a volume versus time plot can be prepared to determine ω by fitting to the model in equation (A.7).

Immediately upon contact between the liquid and the superhydrophilic surface, the liquid begins to propagate through the superhydrophilic surface and forms a meniscus between the tube and the surface. The formation of the meniscus between the tube and the surface is shown in Figure A-5; when the pendant droplet first contacts the surface, a capillary liquid bridge develops between the surface and tube, which then expands outward until a meniscus is formed between the tube and surface. The initial volumetric flow data during the transient formation of this meniscus are not used, as it clearly would not be accurately represented by the capillary-driven flow model.

After the progression shown in Figure A-5, the meniscus begins to recede slightly and fluctuates for a short time before reaching a steady shape. These fluctuations in the meniscus

shape and position affect the measurement of liquid volume wicked into the surface. Figure A-6 shows the meniscus shape fluctuations and wicked volume measurement oscillations early in the experiment. The local maxima and minima seen in the wicked volume measurement oscillations correspond directly to local maxima and minima in meniscus size. After 0.025 s, the volume fluctuations are reduced to the point of being negligible and the wicked volume data can be fitted to the capillary-driven flow model; the data prior to 0.025 s are rejected. These volume fluctuations were also observed to vary in intensity based on the size of the pendant drop suspended from the tube. While these oscillations were evident in nearly every case, the experiment shown in Figure A-6 was an extreme case and a data cutoff at 0.025 s was determined to be appropriate for all cases in this study. Thus, the initial time of contact between the liquid and the surface is not used as t_1. Instead, a time after the meniscus has reached a steady shape is used; for all trials in this study, a conservative value of $t_1 = 0.025$s was selected. An ω value is determined that minimizes the error between the model (equation (A.7)) and the experimental data for the full range of time after t_1.

Surface Fabrication

To validate this characterization technique, four different superhydrophilic micropillar arrays were fabricated for which the important surface characteristics of K, ΔP_{cap}, and h can be estimated *a priori* and ω therefore predicted. Demonstrating an accurate match between the predicted and measured values would affirm that ω alone is sufficient to characterize the liquid pumping performance. The silicon micropillar arrays were fabricated on a 4-inch (100) silicon wafer, each array having a 2 cm × 2 cm footprint. The wafer was cleaned using acetone, methanol, and isopropyl alcohol. Hexamethyldisilazane (HMDS) was applied to the wafer to act as an adhesion promoter for the spin-coated photoresist (PR) using spin coating. Next, AZ9260 positive PR was applied uniformly over the surface using spin coating at 5000 rpm (Specialty Coating Systems, G3). The PR was exposed (Karl Suss, MA6) under a photomask with an intensity of 14 mW/cm^2 for 72 s. The PR was developed in a 1:3 solution of AZ 400K in water for ~60 s. Deep reactive ion etching via the Bosch process (Surface Technology Systems, Advanced Silicon Etch System) was utilized to etch high-aspect-ratio pillars with straight sidewalls. This process uses SF_6 plasma during etching steps and C_4F_8 during passivation steps. After the etching, the surface was exposed to an oxygen plasma for 6 min to remove any remaining passivation material from the pillar sidewalls. The as-fabricated pillar diameters and pitches were measured using standard

optical microscopy and the heights were measured using an optical profilometer (Zygo, NewView 6200). The geometries of the samples, which are denoted D02P10, D09P20, D07P20, and D17P50 based on their respective micropillar diameters and array pitches, are given in Table A-1. Each of the micropillar geometries is shown in Figure A-7.

Each term in the metric (*viz.*, permeability, capillary pressure, and height) can be predicted for the micropillar arrays based on their geometric parameters assuming that the liquid completely fills the pillar interstices within the wetted footprint. To confirm this behavior, the optical profilometer was used to measure the liquid meniscus within the micropillar array, as shown in Figure A-8. The micropillars for this profilometry were wetted by depositing a droplet in the center of the array. The droplet volume was selected such that the liquid did not flood the entire array. The meniscus appears pinned along the top circumference of the pillars, and the bottom of the liquid meniscus is approximately 2 μm below, less than 5% of the pillar height. Thus, the assumption that the liquid fills the pillars interstices is appropriate.

The capillary pressure was determined based on the model developed by Xiao *et al.* [175], which requires a knowledge of the roughness of the pillar sidewalls and the intrinsic contact angle of the material. Due to the scalloping on the sidewalls produced by DRIE (Figure A-7b), the roughness factor on the pillar sidewalls is taken as $\pi/2$. The intrinsic contact angle on the pillar sidewalls is unknown and cannot be directly measured. Due to the difficulty in measuring this parameter, it was instead determined by minimizing the error between the model predictions and experimental results for the superhydrophilicity metric. The sum of the squared error (SSE) between the measured and predicted ω values for all four micropillar arrays was minimized and shown to be sensitive to the contact angle with a minimum at 60.7 deg. The permeability is determined using a model for viscous drag during creeping flow through a periodic array of cylinders developed by Sangani and Acrivos [176], which is recast here in terms of permeability

$$K = P^2 \frac{\ln c^{-1/2} - 0.738 + c - 0.887c^2 + 2.038c^3 + o(c^4)}{4\pi} \qquad \text{(A.8)}$$

where $c = \pi D^2/(4P^2)$ is the solid fraction. The porous layer thickness is equated to the pillar height. Thus, ω can be predicted for each micropillar array.

RESULTS AND DISCUSSION

Seven repeated wettability characterization trials were performed for each micropillar array, each resulting in a best-fit ω specific to each trial. The volume of liquid drawn into the surface as a function of time is shown in Figure A-9 for one representative case each; the modeled behavior for the best-fit ω value is overlaid on the experimental data points. The wicked-volume curves are clearly differentiable from each other, and the volumetric flow rate is proportional to the value of ω. The array with the lowest value of the superhydrophilicity metric, and correspondingly the slowest flow rate, was the D02P10 array ($\omega = 1.05\times10^{-12}$ Pa-m^3) with increasingly higher flow rates measured for D09P20, D07P30, and then D17P50 ($\omega = 2.03\times10^{-12}$ Pa-m^3, $\omega = 2.37\times10^{-12}$ Pa-m^3, and $\omega = 3.69\times10^{-12}$ Pa-m^3, respectively). The capillary-flow model captures the physical behavior of the surface very well, indicating that the superhydrophilic surface wetting behavior can be appropriately represented as wicking in a thin, porous layer. The data do not follow the $V \propto t^{1/2}$ behavior that is observed in rate-of-rise tests, confirming that linear flow models should not be extrapolated to such radial flow cases.

Figure A-10a shows a comparison between the predicted values for ω and the average measured values determined experimentally for each of the four arrays. The error bars on the experimental results indicate the range of measured values across the seven sets of repeated tests. There is no overlap between these ranges, indicating that the metric is sensitive enough to distinguish surfaces from one another based on flow behavior, even for samples with relatively small differences in volumetric flow rate such as D09P20 and D07P30. Additionally, the predicted values for ω closely match the measured values in both magnitude and in the trends of variation across the different samples. The average error between the predicted and measured values is 5%. Figure A-10b shows the wicked volume versus time profiles for the predicted and experimental ω values, constructed using the capillary-flow model in equation (A.7). The accurate prediction of ω leads to an accurate prediction of the flow behavior within the surface as well.

The proposed surface wettability characterization technique is facile, repeatable, and accounts for the capillary-driven flow dynamics that govern wettability in textured superhydrophilic surfaces. This flexible technique can be used to determine an effective superhydrophilicity metric for a large variety of stochastic or regular surface textures. The Supporting Information demonstrates application of this technique to the characterization of laser-etched superhydrophilic surfaces with irregular surface roughness. The metric is derived by

assuming the surface behaves as a thin porous layer and characterizes the performance based on the rate of capillary-driven liquid intake into the surface. Enhancing liquid pumping performance is the primary rationale for employing superhydrophilic or highly wetting surfaces. Thus, the metric has wide utility in characterizing superhydrophilic surfaces for applications such as critical heat flux enhancement in boiling, anti-fogging surfaces, and liquid pumping in microfluidics devices.

This technique can also be used to characterize surfaces with stochastic roughness where the surface geometry is largely unknown (*i.e.*, it would not be possible to predict the wetting performance *a priori*). The characterization approach is demonstrated using laser-roughened aluminum and copper superhydrophilic surfaces (Universal Laser Systems, PLS6MW). After fabrication, a water droplet placed on the surface immediately spreads out into a thin liquid layer, and the contact angle cannot be measured, as shown in Figure A-11. For such surfaces where the geometry is unknown, one additional step is required to estimate the $h\varepsilon$ term that appears in the definition of V_{in}, as an input to the model. This can be done by measuring the area over which a droplet with known volume spreads. The term $h\varepsilon$ is evaluated as $h\varepsilon = V_{liquid} / A_f$ where V_{liquid} is the volume of liquid that was deposited on the surface and A_f is the footprint area covered by the liquid.

Figure A-12 shows the measured volume wicked into both surfaces over time, along with the model fit, resulting from the characterization process. The model captures the flow behavior even for these surfaces with random microstructured roughness. The flow rate in the aluminum surface is significantly faster than that in the copper surface; this behavior is captured in the ω value, which is almost double for the aluminum surface (ω = 1.1 x 10^{-12} Pa-m^3) compared with the copper surface (ω = 5.6 x 10^{-13} Pa-m^3).

CONCLUSIONS

A capillary-flow model was developed to describe the volumetric liquid intake into highly wetting surfaces, which revealed a metric of superhydrophilicity ($\omega = Kh\Delta P_{cap}$) that captures the effects of the important surface characteristics on the flow rate and can be easily measured. This metric is proposed for characterization of superhydrophilic surfaces, as a supplement to the apparent static contact angle that can define surfaces as simply being superhydrophilic but cannot further distinguish the wetting performance. To demonstrate characterization of this proposed

metric, the volumetric liquid intake rate into four different micropillared superhydrophilic surfaces was experimentally measured to extract ω. The capillary-flow model showed an excellent match to the experimental behavior. The experimental technique accurately characterized the behavior of the highly wetting surfaces and the metric was shown to reliably distinguish such surfaces based on their liquid pumping ability. The superhydrophilicity metric defined in this work is recommended as an indicator of superhydrophilic surface performance in applications where rapid liquid pumping or spreading across the surface is desired.

Table A-1. Measured geometries of the micropillar arrays including the average measured micropillar diameter, *D*, pillar-to-pillar pitch, *P*, and pillar height, *H*.

	***D* (μm)**	***P* (μm)**	***H* (μm)**
D02P10	2.4	10	46
D09P20	8.5	20	50
D07P30	6.7	30	53
D17P50	17	50	55

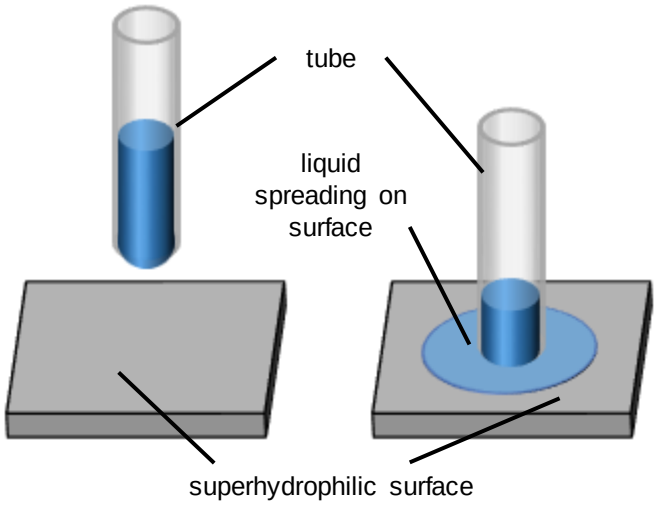

Figure A-1. Schematic illustration of the surface characterization approach.

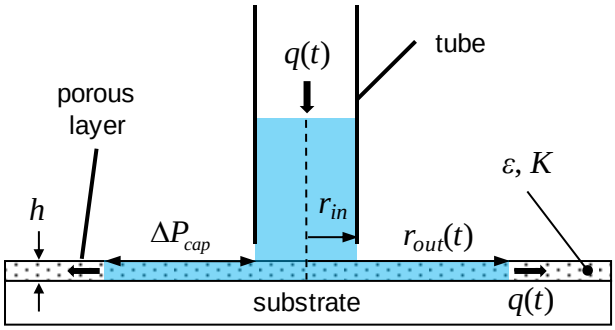

Figure A-2. Schematic diagram of capillary-driven radial flow due to drawing of liquid from a tube into a highly wetting surface.

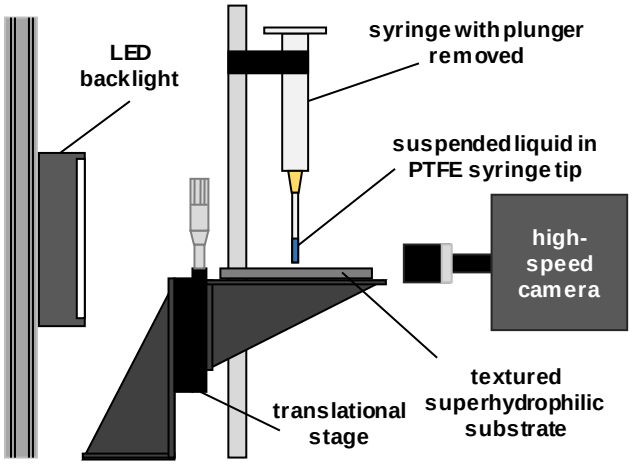

Figure A-3. Schematic diagram of the experimental setup used to measure the volumetric rate of liquid intake into a superhydrophilic surface.

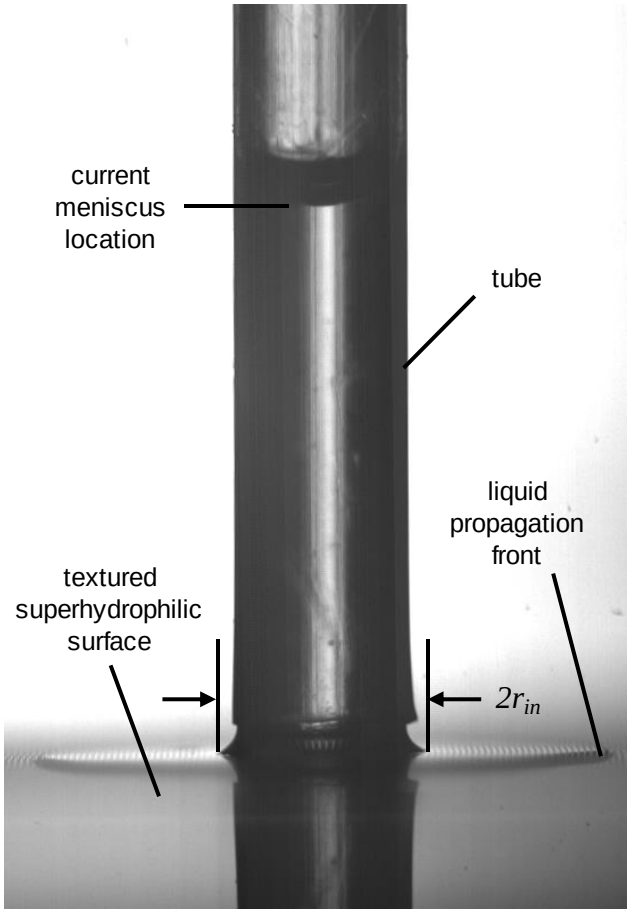

Figure A-4. Image of liquid being drawn from a tube into s superhydrophilic substrate.

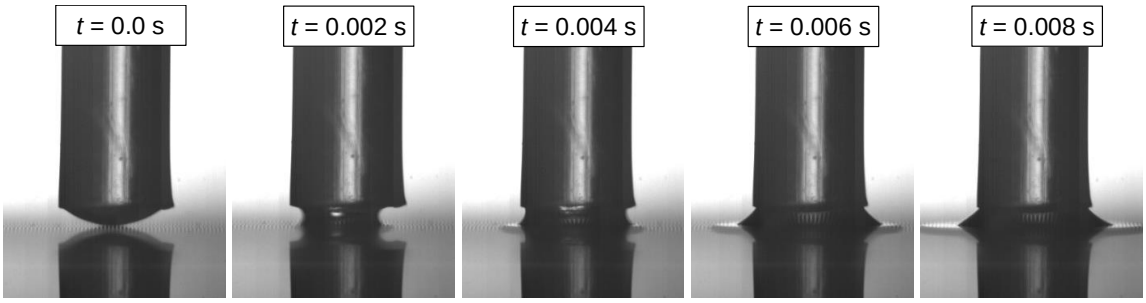

Figure A-5. Sequence of images showing the meniscus formation immediately after contact between the liquid and the D17P50 superhydrophilic surface. A pendant drop is suspended above the surface immediately before contact occurs (t = 0 s); after contact, a capillary bridge is formed (t = 0.002 s) that expands outward and forms a meniscus between the tube and surface (the largest span of the meniscus is reached at t = 0.008 s).

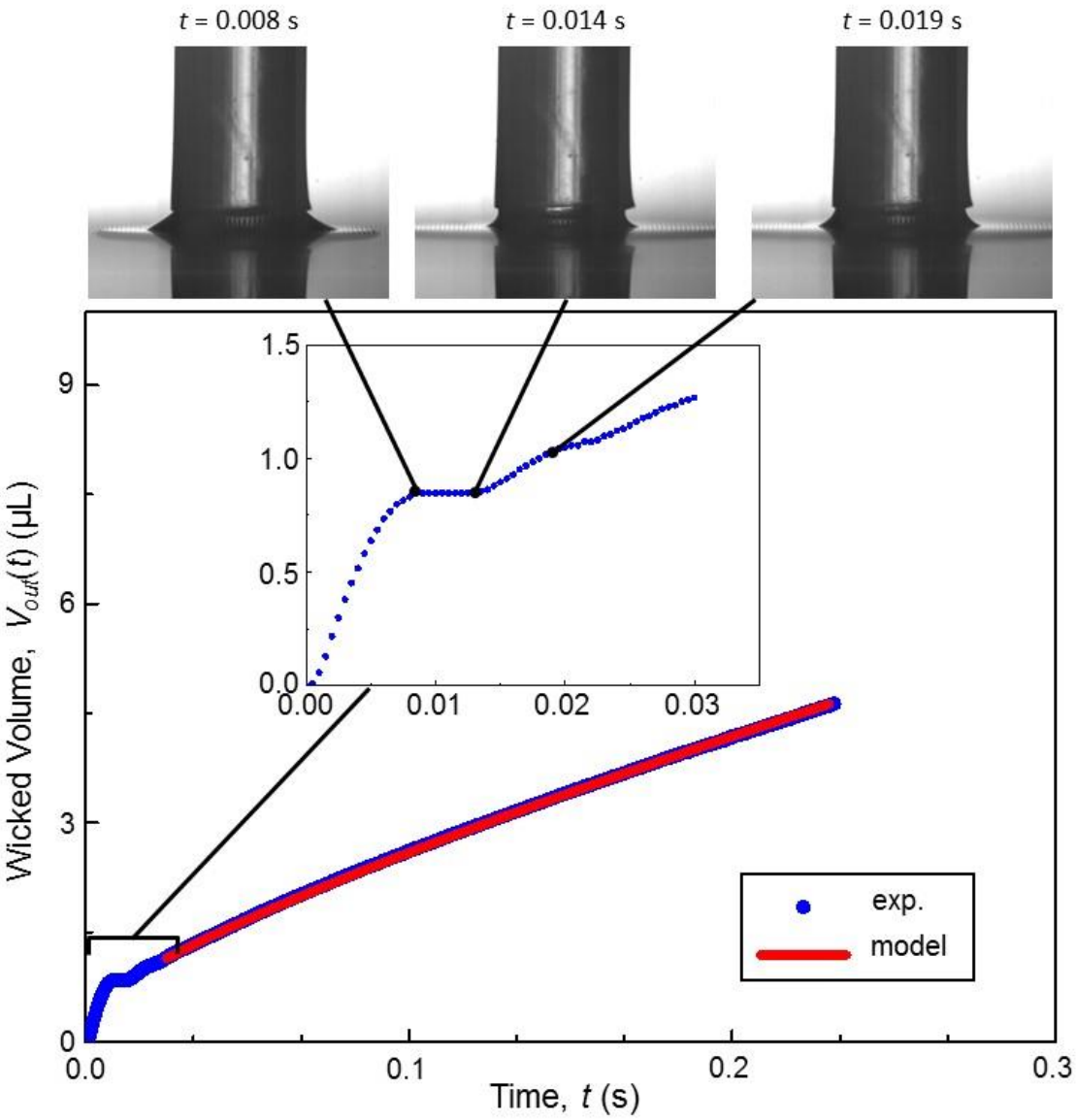

Figure A-6. Plot showing the wicked volume over time for a single D17P50 experiment fit with the capillary-flow model from equation (A.7) after t = 0.025 s. The inset graph shows a magnified view of the first 0.03 s of the test. The shape of the meniscus between the tube and the surface is shown at three times that correspond to local maxima and minima in the wicked volume profile.

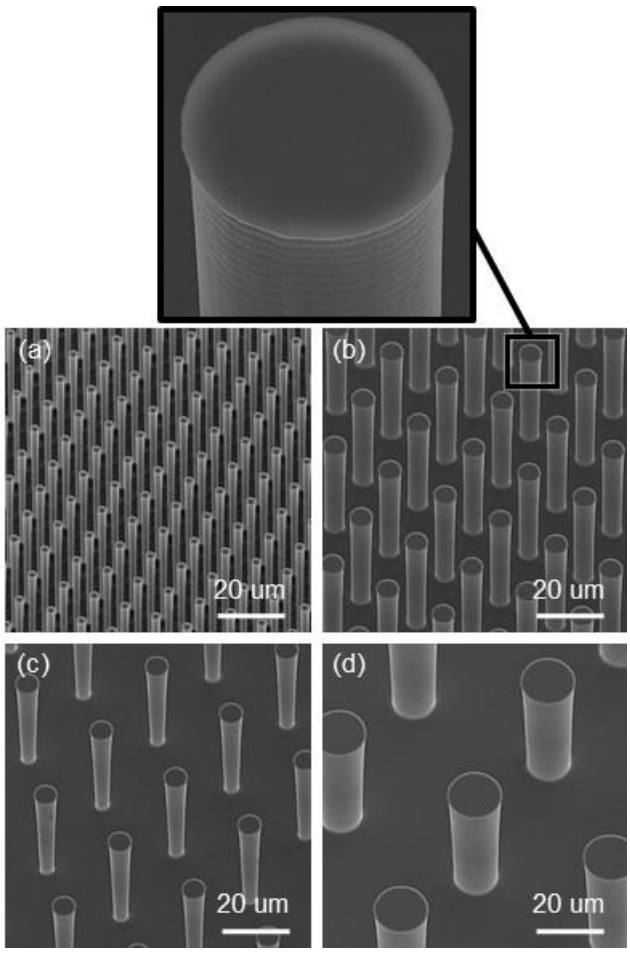

Figure A-7. Scanning electron microscope (SEM) images of the four superhydrophilic micropillar arrays: (a) D02P10, (b) D09P20, (c) D07P30, (d) D17P50. The inset in part (b) shows a high-magnification view of the micropillar sidewalls, revealing a semi-circular scalloping resulting from the etching during processing.

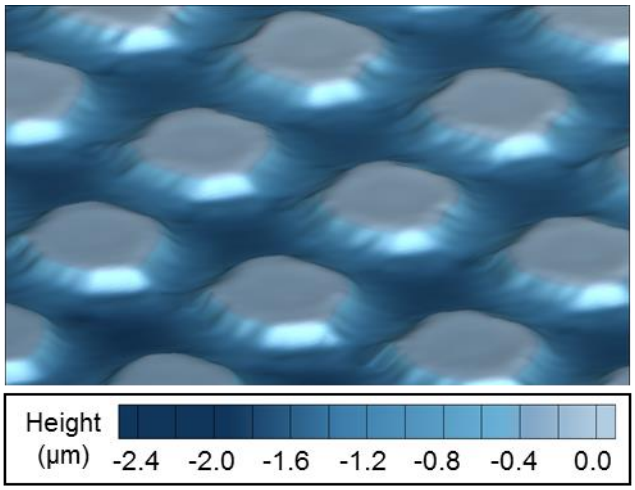

Figure A-8. Three-dimensional topography map of the D02P10 micropillar array with liquid filling the interstitial area between pillars. The color contours represent the height of the pillars and the liquid free surface, with the relative zero-height set at the tops of the pillars.

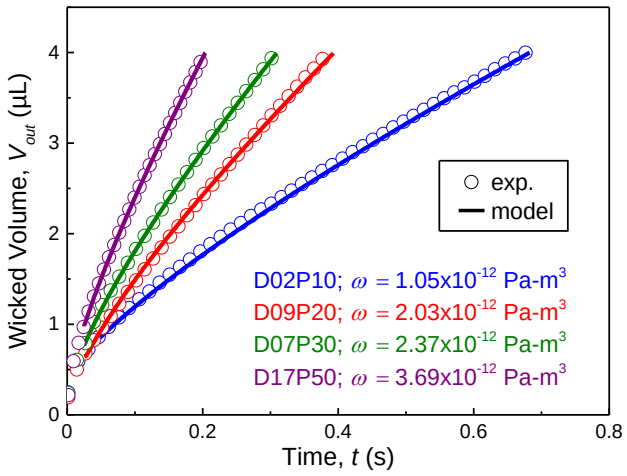

Figure A-9. Representative plots of the measured volume wicked into the surface over time (one experimental trial for each of the four different micropillar arrays) compared with the capillary-flow model for the fitted ω value.

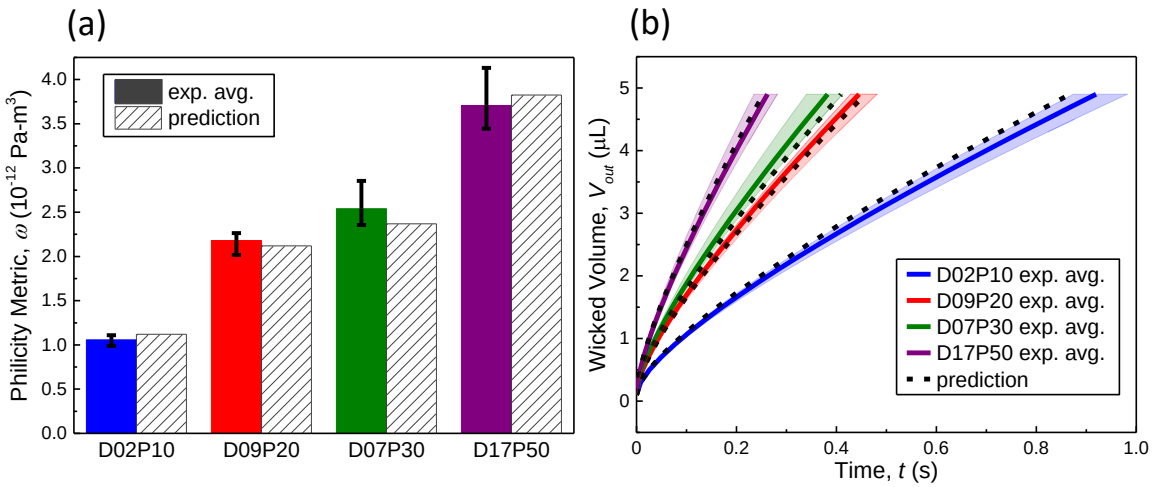

Figure A-10. (a) Comparison between the measured and predicted values of ω for each micropillar array; the error bars correspond to the range of measured values across the seven sets of repeated tests. (b) The capillary-flow model is used to calculate the characteristic volumetric flow curves corresponding to these measured and predicted ω values. The shaded regions in (b) correspond to the uncertainty in the wicked volume profiles based on the uncertainty in the measured values of ω shown in (a).

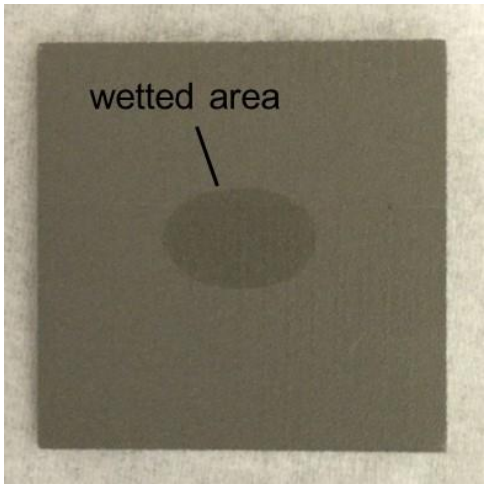

Figure A-11. Top-down view of a superhydrophilic aluminum surface with a 1.5 μL droplet deposited on the surface.

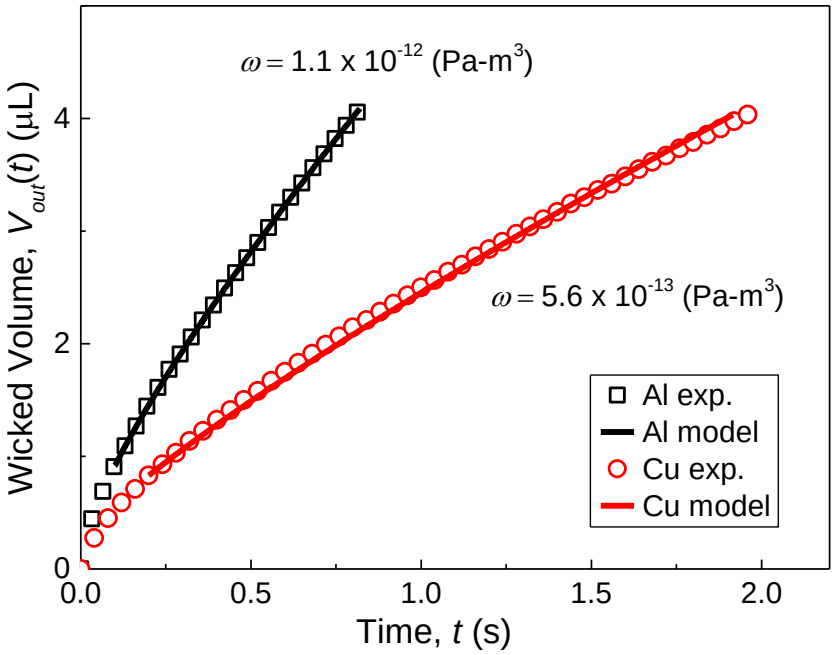

Figure A-12. Measured volume wicked into the superhydrophilic aluminum and copper surfaces over time compared with the capillary-flow model for the fitted ω value.

APPENDIX B. SURFACE FABRICATION PROCEDURES

B.1 Surface Preparation

In the experimental studies in Chapter 3-5, metallic surfaces are first prepared by sanding and cleaning the surface in order to obtain a consistent starting surface morphology for fabrication. A wet-sanding approach is utilized. Waterproof sand paper, starting with 320 grit, is wetted with deionized water and placed on a flat surface. With the sandpaper firmly held in place, the sample is inverted and dragged across the sandpaper ensuring even contact. To prevent surface waviness from nonuniform pressure, after several passes (~10) the sample is rotated 180 deg and sanding continues. Once the surface appears uniformly sanded and large defects are removed, the sandpaper is swapped for 600 grit. The same procedure is followed until the surface appears uniform. Then, the sample is rinsed, and the surface roughness is measured using a profilometer (Zygo, NewView 6200). If the Ra surface roughness is between 400-600 μm, it is deemed acceptable. If the roughness is greater than 600 μm, sanding with the 600 grit sandpaper is continued. If the roughness is less than 400 μm, the entire process is repeated with less time spent using the 600 grit sandpaper. Once the roughness is appropriate, the surface is cleaned using acetone, methanol, and isopropyl alcohol. In that order, the chemicals are sprayed onto the surface and wiped clean using a laboratory wipe. Finally, the surfaces are rinsed in deionized water and blown dry using nitrogen gas.

B.2 Laser etching

For the studies presented in Chapters 3-5, laser etching is used to create roughness on the surface. The laser (ULS, PLS6MW) has three main parameters that can be manipulated to control the roughness of the surface: power, speed, and waveform. The power indicates the laser power being pulsed at the surface, the speed indicates the speed of the laser head during rastering, and the waveform controls signature of the laser radiation. Additionally, the quality, which affects the space between passes of the laser head, can be changed from 1 to 7. For these studies, a high degree of uniform roughness is desired. In all cases, whether roughening to obtain a superhydrophobic surface or a hydrophilic surface, the parameters used are 100% power, 10%

speed, and waveform 2 (default frequency) with maximum quality (7). These etches are performed using the 1.06 μm fiber laser and the 2.0 MW lens, focused manually.

When creating patterns using laser etching in Chapter 4, it was observed that the laser overetched, leading to inaccurate feature widths. Thus, the amount of overetching was calibrated. A copper sample divided into 9 regions with stripes of differing widths, shown in Figure B-1, was fabricated via laser etching using the parameters described previously. The nominal stripe widths were 0.05 mm, 0.1 mm, 0.2 mm, 0.3 mm, 0.5 mm, 0.75 mm, 1 mm, 1.5 mm, and 2 mm. After etching, the unetched stripe widths between the etched stripes were measured and plotted against the expected nominal stripe widths, shown in Figure B-2. A very linear trend was observed and the total amount of overetch was determined to be 140 μm or 70 μm on each side. It is important to note that this value is likely specific to these etching parameters and the material used (copper). This also makes it clear that the minimum feature size is ~150 μm when using these parameters.

B.3 Nanostructuring Copper via Chemical Etching

In Chapter 3, nanostructured surfaces were etched to provide texture for the development of superhydrophobic surfaces. First, a 2.5 M NaOH and 0.1 M $(NH_4)_2S_2O_8$ solution is prepared. This is done by weighing out 8.0 g of NaOH flakes and 1.83 g of $(NH_4)_2S_2O_8$ powder and placing them in a beaker. The beaker is then filled with 80 mL of deionized water and stirred until the NaOH and $(NH_4)_2S_2O_8$ are fully dissolved and solution is fully transparent with a slight blue/purple hue. Then, the copper sample is placed in the solution. For the test blocks, the block is inverted, and the surface is place in the beaker such that the angled neck of the test block rests on the lip of the beaker. Aluminum foil is used to cover the opening of the beaker around the test block. Etching occurs for 30 minutes. Then, the sample is removed, rinsed with deionized water, and blown dry. After the etch, the surface should appear light-blue or black and be superhydrophilic. It was found that this etch can be sensitive to contamination. Thus, it is important to maintain clean glassware used solely for this process.

B.4 PDMS Coating

Polydimethylsiloxane (PDMS) coatings were used in Chapters 3-5 to instill intrinsic hydrophobicity. Prior to coating a metallic surface in PDMS, an adhesion promoting primer (Dow Corning, 92-023) must be applied. The primer is deposited on the surfaces using a dropper,

ensuring that the entire surface is completely wetted. For smooth surfaces, a laboratory wipe is then also wetted with primer and then used to wipe the excess primer off evenly. For textured surfaces, the excess primer is gently dabbed off with a laboratory wipe. The primer is then allowed to cure at room temperature for 30 min. While the primer is curing, the PDMS (Dow Corning, Sylgard 184) solution is prepared. A 10:1 ratio of base to curing agent is used (2.67 g base and 0.27 g of curing agent). These components are weighed in the beaker using a balance and then the beaker is filled with 80 mL of hexane. The solution is magnetically stirred for 1 hr. The primed surface is placed in the solution for 1 hr and then cured in an oven at 150°C for 30 min. PDMS was observed to be a pesky contaminant when reusing glassware. Using glassware previously used for PDMS coatings for any other process results in contamination issues.

B.5 Teflon Coating

In Chapter 5, Teflon coatings were used to instill intrinsic hydrophobicity. First, a 1% wt/wt solution of Teflon powder dissolved in a fully-fluorinated liquid (3M, PF5060) is made. The Teflon powder (1.36 g) is added to 80 mL of PF-5060 and stirred magnetically for 24 hr. The surface is then immersed in the solution for approximately 30 s, removed, and the excess liquid is shaken off. The sample is then placed in an oven at 150°C for 2 hr for curing.

B.6 Chemical Etch for Parahydrophobic Surfaces

Parahydrophobic surfaces were fabricated in Chapter 5. To obtain the surface morphology for parahydrophobic surfaces, an aluminum surface is etched in 0.25 M NaOH. The solution is prepared using 0.8 g of NaOH and 80 mL of water. The solution is stirred until it appears completely transparent. The aluminum test block is inverted, and the surface is submerged in the solution. The opening around the test block is covered using aluminum foil. Etching occurs for 4 hr, after which the sample is removed and blown dry. During rinsing and drying, flecks of surface material are observed to flake off of the surface. The rinsing and drying procedure is repeated until the surface no longer appears to change.

B.7 Wet Etching Silicon V-Grooves

Low aspect ratio silicon V-grooves were fabricated for the work published in Hu *et al.* [177]. Experimental measurements of the meniscus shape of a thin water film on a silicon V-

groove substrate were performed to validate the newly developed continuum model at the microscale. The silicon V-groove substrate was fabricated by wet-etching anisotropically along the slanted (111) planes of a (110) oriented silicon wafer. The slanted (111) planes intersect the (110) planes at an angle of $\theta_0 = 35.26°$. A silicon dioxide hard mask was grown through thermal oxidation and patterned using standard photolithography techniques and a 1:6 Buffered Oxide Etch (BOE). The mask was designed such that the channels were at an angle of 54.74° with respect to the primary wafer flat in order to properly align the channels with the slanted (111) planes. Then, the wafer was wet-etched using 25% tetramethylammonium hydroxide (TMAH) in water at 90°C for 6 min. The resulting geometry was a V-groove channel with a width of L = 18.81 μm. The depth of the V-groove channel is calculated based on the V-groove structure as $D = L \tan \theta_0/2 = 6.65$ μm. To ensure a clean surface, the remaining oxide was removed with BOE and the wafer was cleaned with a piranha solution (KMG Nano-strip 2X) for 10 min. The resulting V-groove channels are shown in Figure B-3.

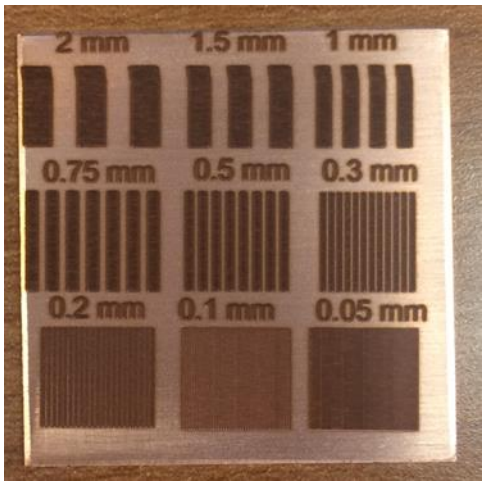

Figure B-1. Etched copper sample used for laser patterning calibration.

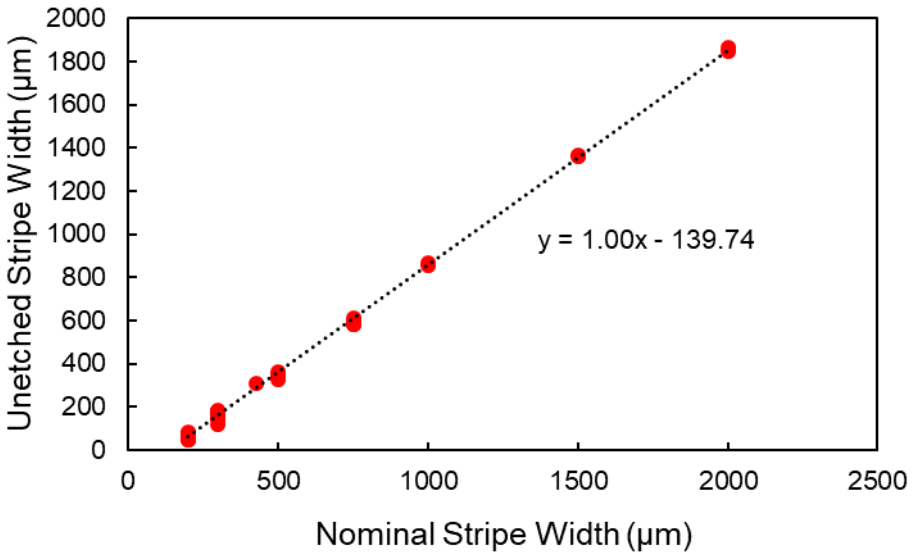

Figure B-2. Plot showing the width of the unetched stripes between two etched stripes versus the nominal stripe width.

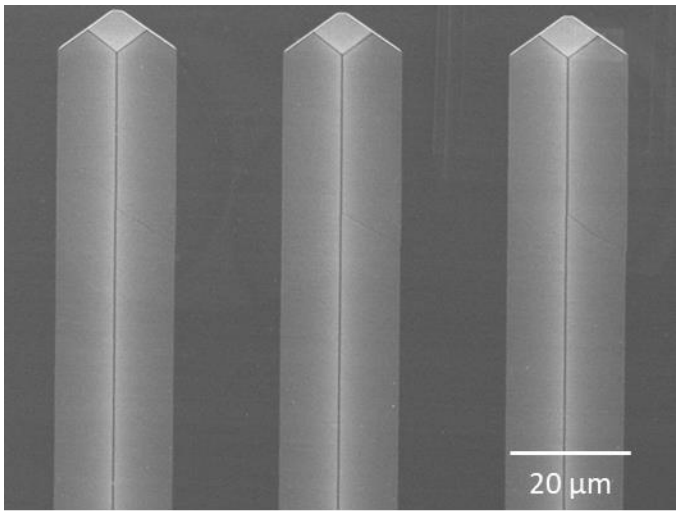

Figure B-3. Scanning electron microscope image of low aspect ratio V-groove channels in silicon obtained via anisotropic wet etching.

APPENDIX C. EXPERIMENTAL BOILING FACILITY

SUMMARY OF FACILITY COMPONENTS

Table C-1 summarizes all of the key equipment utilized during the pool boiling experiments. A photograph of the boiling facility is shown in Figure C-1. The boiling chamber has inner dimensions of 5.5" wide, 5.5" long, and 5.25" tall and is constructed with polyether ether ketone (PEEK) walls. The PEEK walls are sealed using Momentive RTV 118 between each interface and fastened together with screws. The lid of the boiling chamber is sealed using a flexible silicone gasket that is compressed uniformly with evenly distributed screws.

On the front and back of the chamber are borosilicate glass windows used for visualization during boiling. The windows are sealed using silicone O-rings. A uniform LED light source (Advanced Illumination, BT200100) provides backlighting over the entire rear window. Front lighting is also provided from the front window (Sunoptics, Titan300). The camera (Phantom, VEO 710L; Zeiss, Makro-Planar T* 2/100 lens) views the boiling process through the front window. It is mounted to the optical table using optical railing and three 1-D micrometer stages to allow for fine tuning of the camera position. Additionally, a tilt stage is used to control the viewing angle. Two 170 W pool heaters are inserted symmetrically into the chamber, one from the front and one from the back. The pool heaters are powered with an 840 W power supply (Sorensen, XG 150-5.6). A drain pipe with a ball valve is installed at the bottom of the front side to drain the liquid from the chamber after testing.

On the sides of the boiling chamber, four pool thermocouples and a pressure transducer (Omegadyne, PX409) are inserted into the chamber and sealed using Swagelok fittings. Additionally, a translatable spout is installed. The spout is connected to a pump and reservoir such that it can be used to actively cooled the surface upon reaching critical heat flux. The spout is made translatable by attaching it to the wall via a bored-through fitting and replacing the ferrules with O-rings. A ball valve is attached to the spout outside of the chamber such that it is sealed off unless needed. When not in use, the spout is retracted near the wall. When critical heat flux occurs, the spout is moved above the surface, the valve is opened, and the pump is turned on to cool the surface.

On the lid, two additional pool thermocouples are inserted, the two condensers are attached, and a ball valve for pressure relief are installed. One condenser is a Graham condenser on top of

the lid, used during degassing, and the other is a coiled copper tube condenser that sits inside the chamber, used during sealed operation. A ball valve is attached between the Graham condenser and the lid such that it can be sealed off after degassing. Attached to the inlet of the coiled condenser is a voltage-controlled solenoid valve (Aalborg Instruments, PSV-5) used to regulate the flow rate through the coiled condenser and thereby control the pressure in the chamber during sealed operation. The valve is connected to a power supply (BK Precision, 1786B) that is controlled via a PID module in NI LabVIEW that reads the pressure in the chamber and adjusts the flow rate accordingly. In parallel with the solenoid valve, a manual needle valve is installed in case the solenoid valve malfunctions. The coolant for the condensers is supplied using a magnet pump (Iwaki, MD-30RZ-115NL). The heat from the coolant is dissipated using an air-liquid heat exchanger and a fan.

The test block is installed into the bottom of the boiling chamber within the PEEK test block shroud. Within the shroud, the test block rests on top of a ceramic insulator and is surrounded by mineral wool loose fill insulation. The twelve T-type test block thermocouples are inserted into the test block through slots in the test block shroud. These test block thermocouples are additionally connected to an ice point reference (Fluke, 9101) to ensure accurate measurement. Additionally, a single K-type thermocouple is inserted into the bottom of the test block to monitor the temperature at the base. The twelve 150 W cartridge heaters used to heat the test block are inserted into the bottom of the test block through the ceramic insulator. The heaters are powered using a 2700 W power supply (Ametek, XFR 150-18). The test block is sealed into the chamber using a bead of RTV (Momentive, RTV 106) covered by epoxy (3M, DP 110) to fill the groove, cover the test block side walls to reduce unwanted sidewall nucleation, and prevent contamination and outgassing from the RTV.

All of the data from thermocouples, the pressure transducer, and power supplies is measured using a data acquisition unit (Agilent, 34970A) coupled with NI LabVIEW. Data is saved continuously throughout experiments and steady state data is flagged. Additionally, the LabVIEW program is set up to trigger shut down of the cartridge heat power supply when a drastic increase in temperature is measured at critical heat flux.

TEST BLOCK THERMAL DESIGN

The test block was carefully designed to provide uniform heating conditions to the surface during pool boiling experiments. The width of the surface was selected to be 1.073", the Rayleigh-Taylor wavelength for water, to allow studying of hydrodynamic instabilities during boiling. The rest of the test block geometry was designed to ensure that the heat flux at the surface would be uniform and high heat fluxes could be reached without overheating occurring at the bottom of the block. The test block was designed to handle a maximum heat flux of ~250 W/cm^2 at the surface. Cartridges heaters were selected that would be capable of supplying this heat flux and arranged in a way that supplied a uniform heat flux to the surface, shown in Figure C-2. The final geometry, shown in Figure C-3, has a neck region that is the same width as the surface and then flares out to a wider base to accommodate the cartridge heaters and reduce the temperature drop across the block.

A numerical simulation of the conduction in the block was performed to evaluate the thermal performance of the test block. A quarter-symmetric geometric model was created, including the insulation around the test block. A constant heat flux boundary condition was applied on the walls of the cartridge heater holes. A high convective heat transfer coefficient of 80,000 W/m^{2}K was applied to the surface to approximate boiling. To approximate natural convection, convective boundary conditions of 10 W/m^{2}K were applied to the side and bottom walls of the insulation in contact with air, and a convective boundary condition of 20 W/m^{2}K was applied to the top side of the insulation in contact with liquid. Heat fluxes of 250 W/cm^2 and 10 W/cm^2 were evaluated to verify the uniformity of the heat flux in high and low cases. All of the simulations were performed using the properties of aluminum for the test block as it was considered to be the limiting case, particularly with respect to the temperature limit at the bottom of the block. At 10 W/cm^2, the heat flux at the surface varied by approximately 1%, and at 250 W/cm^2, the heat flux at the surface varied by approximately 2.5%. These results are shown in Figure C-4 and Figure C-5, respectively. The maximum temperature in the block in the 250 W/cm^2 case, as shown in Figure C-6, was slightly above 900 K. This exceeded the melting point of aluminum by ~50 K, but 250 W/cm^2 was expected to be higher than the operational heat flux. To ensure safety, a thermocouple was used to measure the temperature at the bottom of the block.

THERMOCOUPLE CALIBRATION

The twelve T-type test block thermocouples were calibrated in a dry-block calibrator (Isotech, Jupiter 4852). The thermocouples were inserted into the block, along with an RTD, and the temperature was varied from 75°C to 175°C in 25°C increments. The difference between the thermocouple reading and the RTD was plotted against the RTD temperature for each thermocouple across the range of temperature. These results are shown in Figure C-7, Figure C-8, and Figure C-9 for the corner rake, center rake, and side rake thermocouples, respectively. The slope and intercept for each thermocouple were then used to offset the temperature measurements from the standard ITS-90 curve for T-type thermocouples. The uncertainty of the thermocouple measurements was determined from these curves through an uncertainty analysis following Brown *et al.* [128].

Table C-1. Key components for pool boiling experiments.

Category	*Equipment*	*Brand*	*Model/Key Spec*	*Purpose*
Optics				
	LED light source	Advanced Illumination	BT200100	Backlighting for visualization
	Power supply	Electro Industries	3002A	Power backlight
	High-speed camera	Phantom (Ametek)	VEO 710L	High speed imaging
	Lens	Zeiss	Makroplanar T* 2/100	High speed imaging
	Xenon light source	Henke Sass Wolf GMBH	XL 300-M	Front lighting
	Xenon light source	Sunoptics Surgical	Titan 300	Front lighting
Heat Supply				
	Immersion heaters	Hotwatt	170 W, ¼" D, 5" L	Pool heating
	Cartridge heaters	McMaster	150 W, 3/8" D, 1" L	Block heating
	Power supply	Sorensen	XG 150-5.6	Power immersion heaters
	Power supply	Ametek	XFR 150-18	Power cartridge heaters
Measurements				
	Pressure transducer	Omegadyne	PX409	Chamber pressure
	Thermocouples	Omega	1/16", T-type, ungrounded	Pool temperature
	Thermocouples	Omega	0.032", T-type, ungrounded	Block temperature
	Ice point reference	Fluke	9101	0°C temperature reference
	Data acquisition unit	Agilent	34970A	Data acquisition
	Thermocouple calibrator	Isotech	Jupiter	Temperature calibration
	Pressure calibrator	Scandura	Pascal 100	Pressure calibration
Pressure Control				
	Solenoid valve	Aalborg Instruments	PSV-5	Control condenser flow rate
	Power supply	BK Precision	1786B	Power solenoid valve
	Pump	Iwaki	MD-30RZ-115NL	Coolant pump
	Heat exchanger w/ fan			Cool coolant
	Power supply	Kepco	JQE 150V 1.5A	Power heat exchanger fan

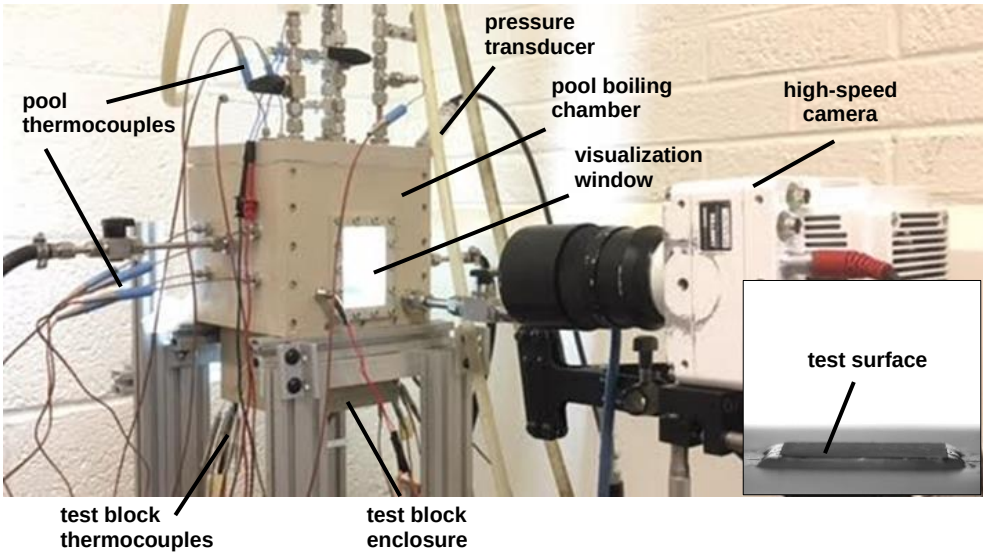

Figure C-1. Experimental Pool Boiling Facility

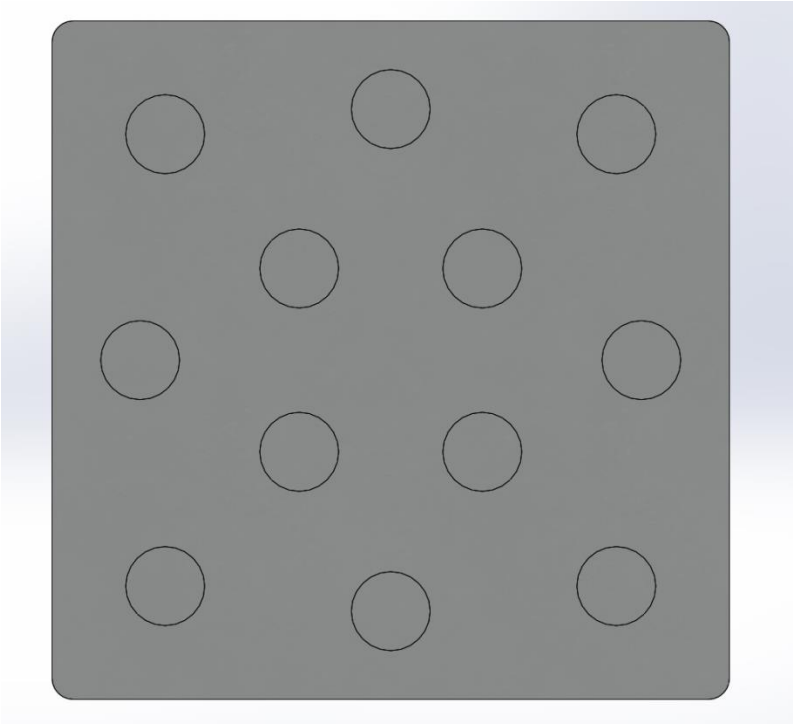

Figure C-2. Arrangement of cartridge heaters in the bottom of the test block.

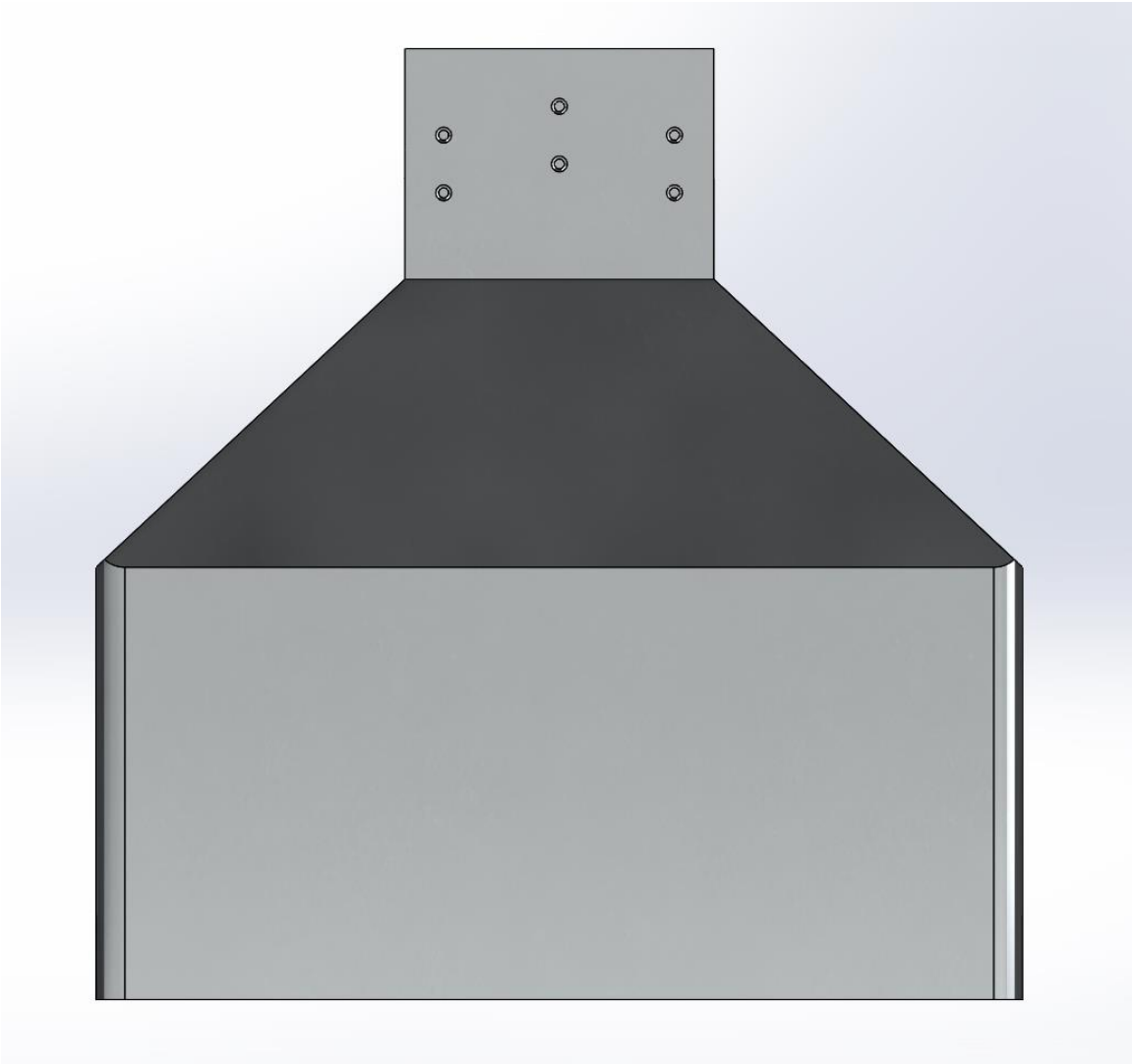

Figure C-3. Final test block geometry.

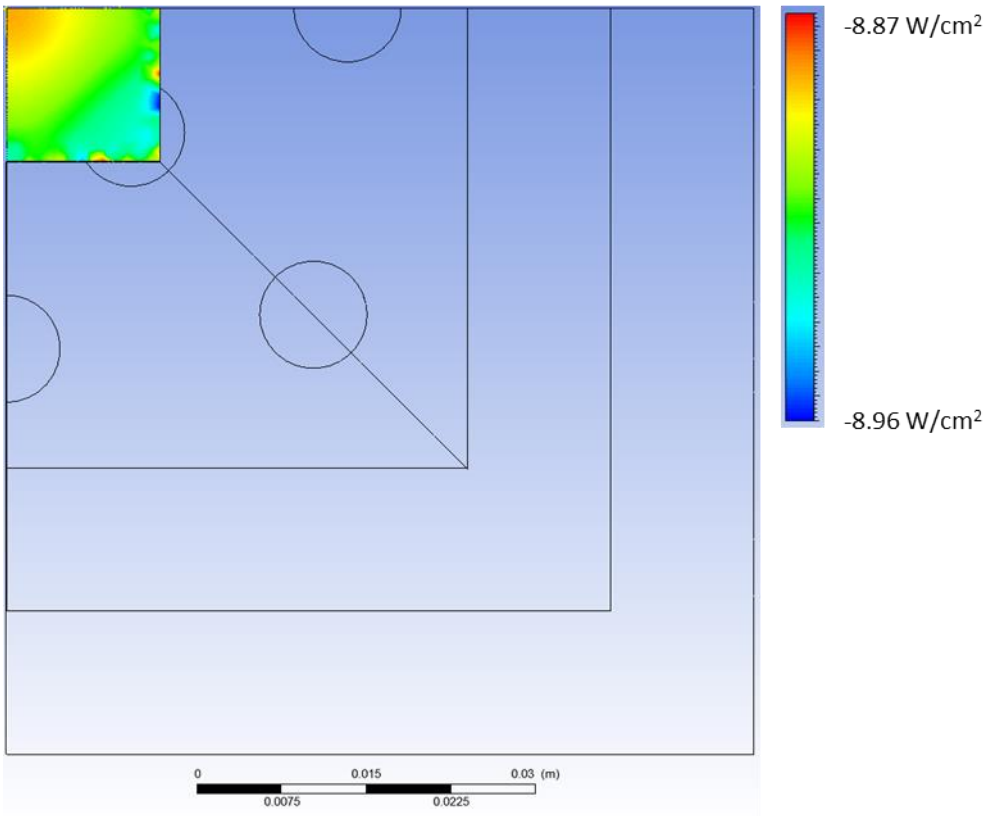

Figure C-4. Numerical results for the surface heat flux of the aluminum test block at 10 W/cm^2.

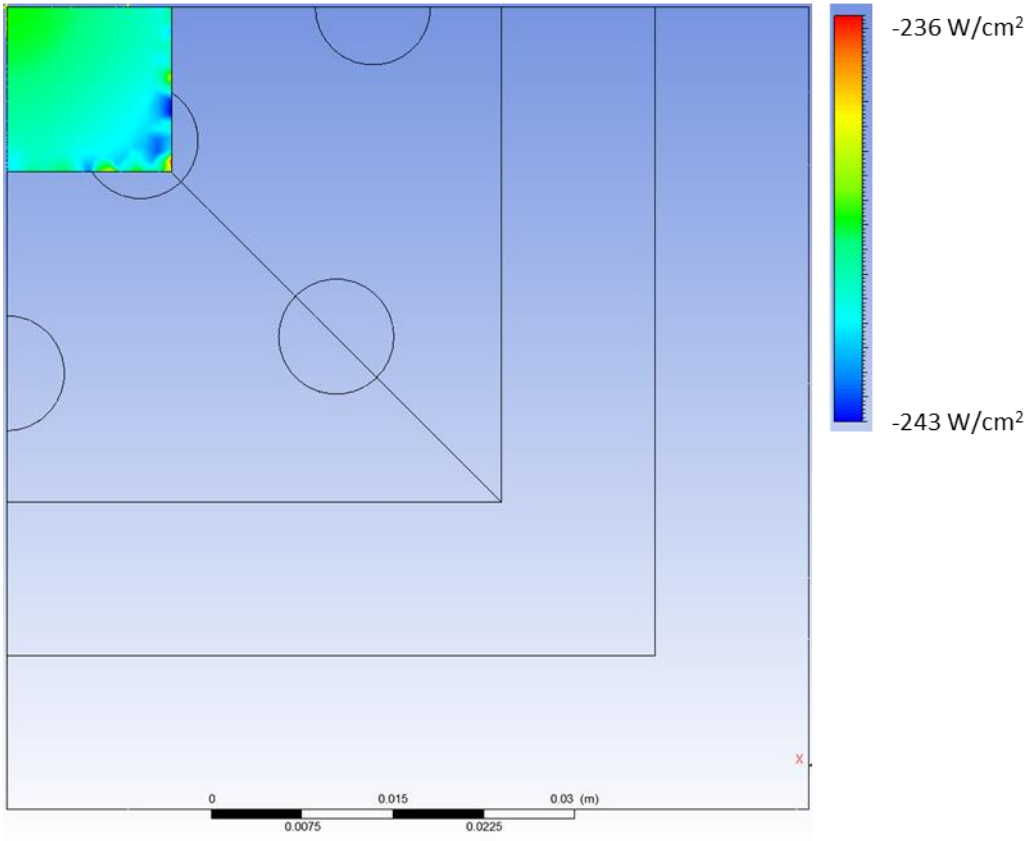

Figure C-5. Numerical results for the surface heat flux of the aluminum test block at 250 W/cm^2.

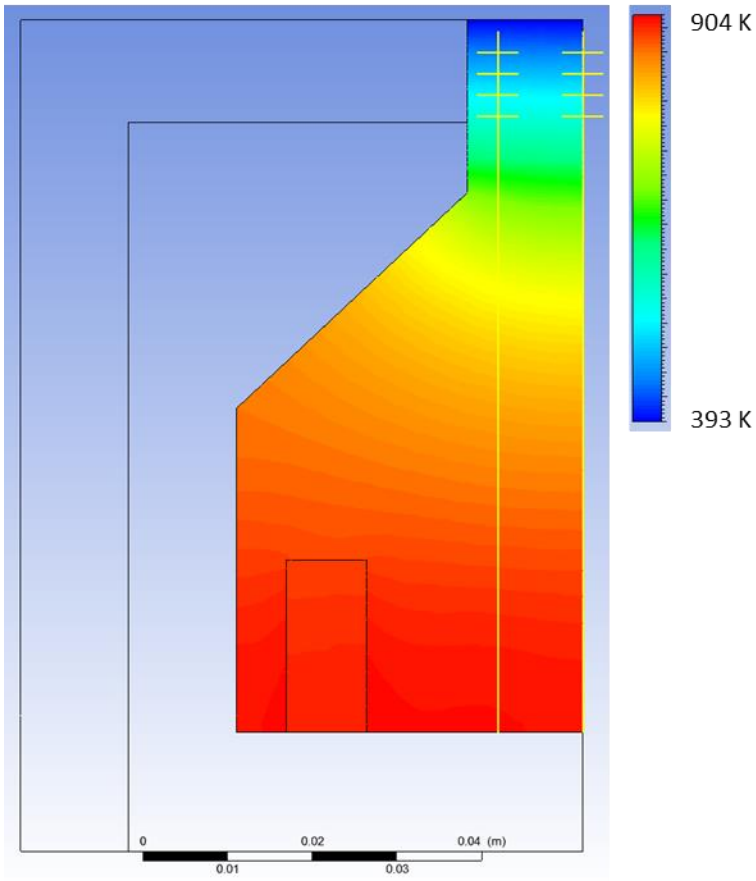

Figure C-6. Numerical results for the temperature profile along a center cut of the aluminum test block at 250 W/cm^2.

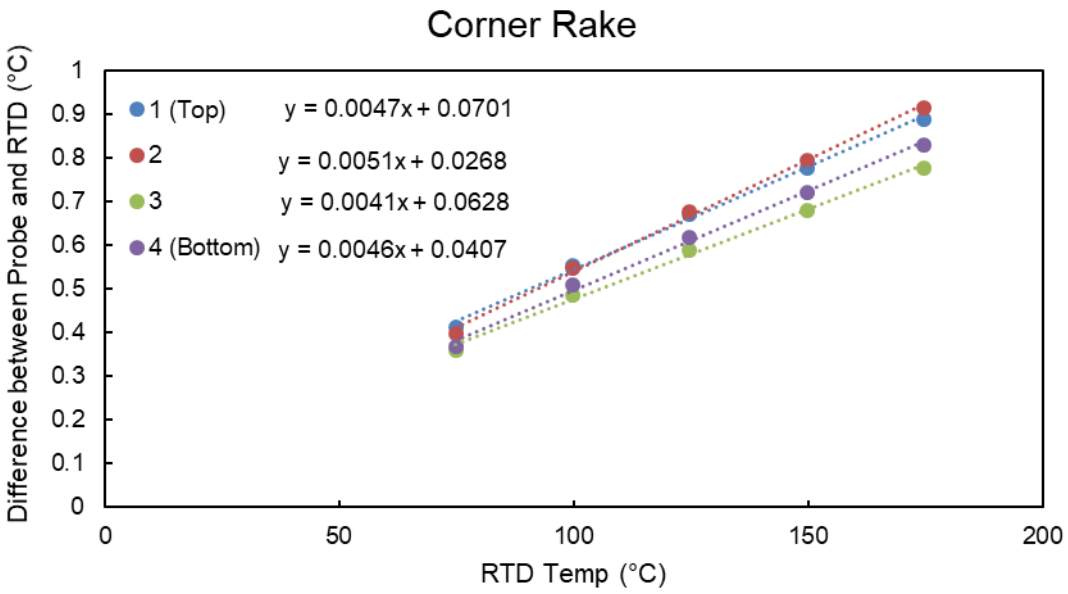

Figure C-7. Calibration results for the corner rake thermocouples.

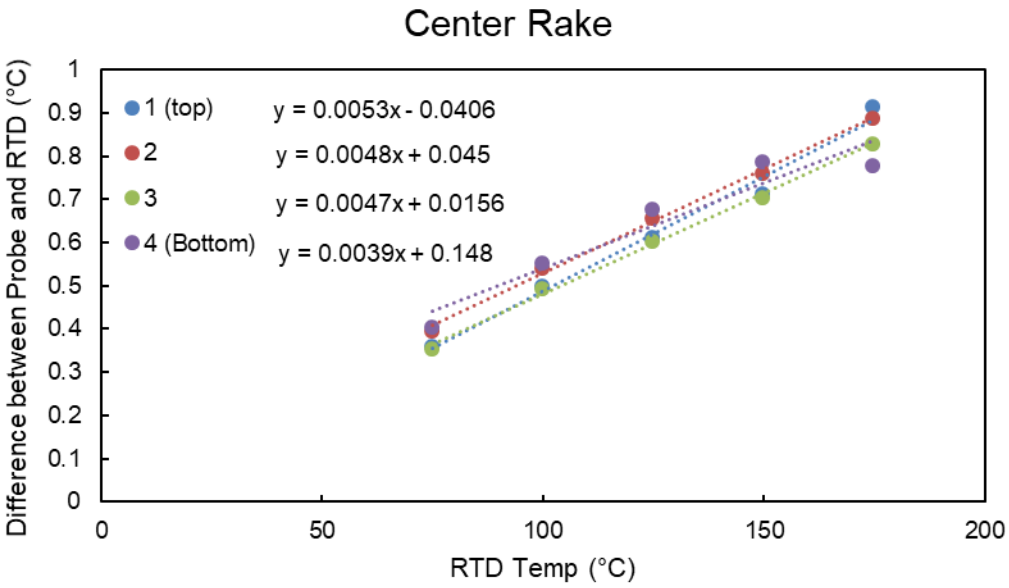

Figure C-8. Calibration results for the center rake thermocouples.

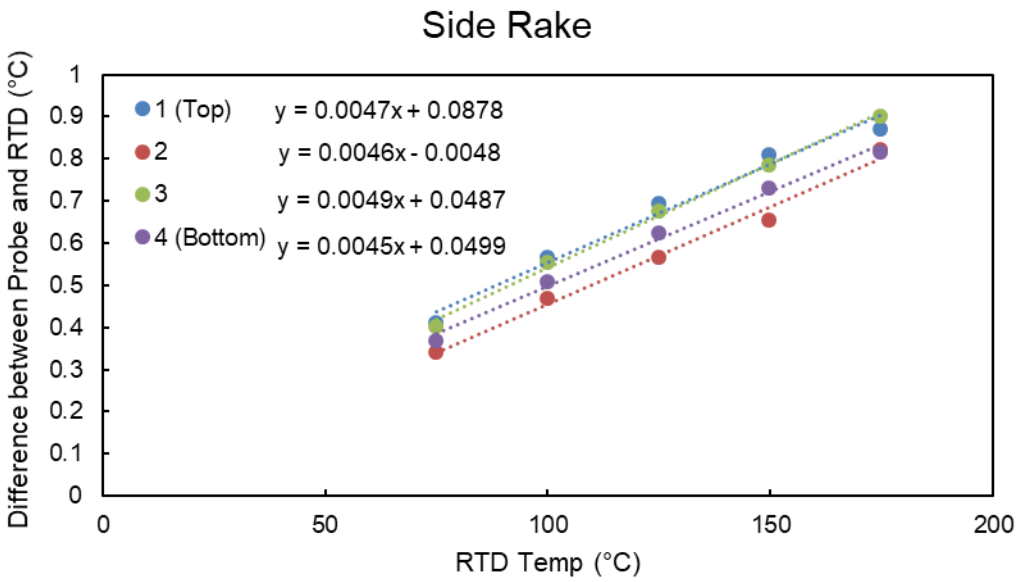

Figure C-9. Calibration results for the side rake thermocouples.

APPENDIX D. FLUENT USER-DEFINED FUNCTIONS FOR TWO PHASE VOLUME OF FLUID MODEL WITH DYNAMIC CONTACT ANGLE, PHASE CHANGE, AND MICROLAYER HEAT TRANSFER

```
#include "udf.h"
#include "sg.h"
#include "math.h"
#include "mem.h"
#include "para.h"

/************************************************************/
/************************************************************/

cell_t c_target;
cell_t c_target2;
real factor=20000.; /*For velocity based source, initially was 20000*/
real factorpos=4000000.; /*For position based source, initially was 4000000*/
real checksource;
real i=0;
real x_fix;
real r_target;
real r_target2;
real dx=0.00001;
real CA_adv = 120.; /* Advancing contact angle */
real CA_rec = 30.; /* Receding contact angle */
real contact_angle;
int const_CA;
int const_CL;
int adv;
int rec;
real CL_vel;
int constCAcount;
int constCLcount;
int transreq=5;
real factorrec = 1000000;
real factoradv = 1000000;
FILE *datafile;
int stepnum;
real totalsourcevol;
real totalvol;
real superheat = 5.;
real BLthickness = 0.001;
real ML_heat_tot;
real dryout_rad;
```

```
real tot_ML_area;
real tot_ML_vol;
real t_off = 0.;
real nu_l = 2.913E-7;

real gas_total, gas_total_1, gas_total_2; /*1 is on the interface, 2 is on the vapor bubble, total is the sum of 1 and 2*/
real liquid_total, liquid_total_1, liquid_total_2;
real time_step;
real renorm;
real scale_velocity=1;
real T_max, T_g_max;
real scale_liquid=1;
/*real moving_mesh_velocity=1.0;*/
real need_fix; /*1 is to fix, 0 is not to fix*/
real average_outlet_velocity;
real volume,volume_source, int_volume_source;
real MLSurfTemp;

/* domain pointer that is passed by INIT function is mixture domain */
DEFINE_INIT(bubble_initialization_90, mixture_domain)  /*This section initializes the bubble*/
{
   int phase_domain_index;
   cell_t cell;
   Thread *t_solid;
   Thread *t_fluid_mix;
   Thread *t_fluid_vapor;
   Domain *subdomain;
   real xc[ND_ND];
   real initial_radius = 0.00027;
   real cell_rad;
   real shell_rad = 0.001;
   real y_in_max;
   real x_inner;
   real x_shell;
   real T_sat = 373.15;
   real T_y;

   stepnum=0;
   x_fix = 0.;
   r_target = 0.;
   r_target2 = 0.;
   constCLcount=10;
   constCAcount=0;
   const_CA=1;
```

```
   const_CL=0;
   adv=0;
   rec=1;
   checksource=0.;
   contact_angle=CA_rec;
   dryout_rad = 0.;

   datafile=fopen("datafile.txt","w");
   fprintf(datafile,"TimeStep Time ContactDiameter Volume ContactAngle ConstCA ConstCL
DryoutRad \n");
   fclose(datafile);

   /* loop over all subdomains (phases) in the superdomain (mixture) */

   t_solid = Lookup_Thread(mixture_domain, 15);
   t_fluid_mix = Lookup_Thread(mixture_domain,16);

   begin_c_loop_all(cell,t_solid)
    {
        C_T(cell,t_solid) = T_sat+superheat;
        C_UDMI(cell, t_solid, 15) = -10.;
    }
   end_c_loop_all(cell,t_solid)

   begin_c_loop_all(cell,t_fluid_mix)
    {
        /*C_T(cell,t_fluid_mix)=373.15;*/
        C_UDMI(cell,t_fluid_mix,15) = -10.;
        C_CENTROID(xc,cell,t_fluid_mix);
        cell_rad = sqrt(ND_SUM(pow((xc[0]-initial_radius*cos(contact_angle*M_PI/180.)),2.),
pow(xc[1],2.), pow(xc[2],2.)));
        y_in_max = sqrt(pow(initial_radius,2.))+initial_radius*cos(contact_angle*M_PI/180.);
        if(xc[0]>BLthickness)
          C_T(cell,t_fluid_mix) = T_sat;
        else
          C_T(cell,t_fluid_mix) = superheat*((BLthickness-xc[0])/BLthickness)+T_sat;

        if(cell_rad <= initial_radius)
          C_T(cell,t_fluid_mix) = T_sat;

        /*THIS SECTION MAKES A LAYER OF SATURATED LIQUID AROUND THE
BUBBLE TO PREVENT NUMERICAL INSTABILITIES*/
        /*if((cell_rad < shell_rad)&&(cell_rad > initial_radius))
          C_T(cell, t_fluid_mix) = T_sat;*/
```

```
        /*THIS SECTION MAKES AN INITIAL TEMPERATURE GRADIENT AROUND
THE BUBBLE*/
        if ((xc[0]<BLthickness)&&(cell_rad < shell_rad)&&(cell_rad > initial_radius))
          {
            x_shell = sqrt(pow(shell_rad,2.)-pow(xc[0]-
initial_radius*cos(contact_angle*M_PI/180.),2.));
            T_y = superheat*((BLthickness-xc[0])/BLthickness)+T_sat;
            if(xc[0]<y_in_max)
              {
                  x_inner = sqrt(pow(initial_radius,2.)-pow(xc[0]-
initial_radius*cos(contact_angle*M_PI/180.),2.));
                  C_T(cell, t_fluid_mix) = (T_y-T_sat)*((xc[1]-x_inner)/(x_shell-x_inner))+T_sat;
              }
            else
              C_T(cell,t_fluid_mix) = (T_y-T_sat)*(xc[1]/x_shell)+T_sat;
          }
    }
   end_c_loop_all(cell,t_fluid_mix)

   sub_domain_loop(subdomain, mixture_domain, phase_domain_index)
    {
        /* loop if secondary phase */
        if (DOMAIN_ID(subdomain) == 3) /* loop over all cell threads in the secondary phase
domain */
          {
            t_fluid_vapor = Lookup_Thread(subdomain,16);
        {
            /* loop over all cells in secondary phase cell threads */
              begin_c_loop_all(cell,t_fluid_vapor)
            {
                    C_CENTROID(xc,cell,t_fluid_vapor);
                    if (sqrt(ND_SUM(pow((xc[0]-initial_radius*cos(contact_angle*M_PI/180.)),2.),
pow(xc[1],2.), pow(xc[2],2.))) < initial_radius) /* set volume fraction to 1 for centroid */
                      {
                        C_VOF(cell,t_fluid_vapor) = 1.;
                        /*C_UDMI(cell,t_fluid_vapor,0) = 1.;
                            C_UDMI(cell,t_fluid_vapor,1) = 0.;*/
                        /*Message("In vapor set loop \n");*/
                      }

                    else /* otherwise initialize to zero */
                      {
                        C_VOF(cell,t_fluid_vapor) = 0.;
                        /*C_UDMI(cell,t_fluid_vapor,0) = 0.;
                            C_UDMI(cell,t_fluid_vapor,1) = 0.;*/
                      }
```

```
                }
            end_c_loop_all(cell,t_fluid_vapor)
          }
        /*This loop assigns the initial x_fix location after the initial bubble has been patched
in*/
          begin_c_loop_all(cell,t_fluid_vapor)
            {
                C_CENTROID(xc,cell,t_fluid_vapor);
                if((xc[0]<dx)&&(C_VOF(cell,t_fluid_vapor)>0.99)&&(xc[1]>x_fix))
                  {
                    x_fix=xc[1];
                    r_target=xc[1];
                  }

        if((xc[0]>dx)&&(xc[0]<2.*dx)&&(C_VOF(cell,t_fluid_vapor)>0.99)&&(xc[1]>r_target
2))
                    r_target2=xc[1];
            }
          end_c_loop_all(cell,t_fluid_vapor)
        }
    }
  begin_c_loop_all(cell,t_solid)
    {
        C_CENTROID(xc, cell, t_solid);
        C_UDMI(cell, t_solid, 12) = 0.;
        if((xc[0]>-dx)&&(xc[1]<=r_target))
          C_UDMI(cell, t_solid, 15) = xc[1]/r_target*0.8*sqrt(nu_l*t_off);
    }
  end_c_loop_all(cell,t_solid)
}

DEFINE_ON_DEMAND(InitVars)
{
 #if !RP_HOST
  cell_t c;
  Thread *t;
  Domain *d;
  real x[ND_ND];

  d = Get_Domain(3);
  stepnum= N_TIME;
  x_fix = 0.;
  r_target = 0.;
  r_target2 = 0.;
  constCLcount=10; /*This may change from case to case */
  constCAcount=0;
```

```
   const_CA=1; /*This conditions may change from case to case */
   const_CL=0;
   adv=0;
   rec=1;
   checksource=0.;
   contact_angle=CA_rec; /*This may change from case to case*/

   /* loop over all subdomains (phases) in the superdomain (mixture) */

   /*This loop assigns the initial x_fix location after the initial bubble has been patched in*/
   thread_loop_c(t,d)
    {
        if(FLUID_THREAD_P(t))
          {
           begin_c_loop_all(c,t)
             {
                C_CENTROID(x,c,t);
                if((x[0]<dx)&&(C_VOF(c,t)>0.99)&&(x[1]>x_fix))
                  {
                    x_fix=x[1];
                    r_target=x[1];
                  }
                if((x[0]>dx)&&(x[0]<2.*dx)&&(C_VOF(c,t)>0.99)&&(x[1]>r_target2))
                  r_target2=x[1];
             }
           end_c_loop_all(c,t)
          }
    }
  #endif
}

DEFINE_SOURCE(vapormasssource, c, t, dS, eqn) /*This section supply the vapor source for
the adiabatic case*/
{
  #if !RP_HOST
   real xc[ND_ND];
   real sourcetot;
   real source;
   real growth_rate;
   real vapor_dens=0.5956;
   real time;

   time = CURRENT_TIME;

   /*This macro should be done on all nodes, but will need to have an accurate totalsourcevol for
the entire domain*/
```

```
   if(time<0.001)
     {
          source = 0.;
          dS[eqn]=0.;
     }
   else
     {
          /*growth_rate = 200.*time; /*(mm3/sec)*/
          /*growth_rate = 50.;*/
          growth_rate =
0.5*1000000000.*0.1*M_PI*pow((16./(3.*pow(9.81,2))),(1./6.))*pow((0.0589*r_target/957.854
4),(5./6.));

          sourcetot = vapor_dens*(growth_rate/1000000000.); /*kg/s*/
          C_CENTROID(xc,c,t);

          if(C_VOF(c,t)>0.99)
            {
              source =
(2*M_PI*C_VOLUME(c,t)/totalsourcevol)*sourcetot/(2*M_PI*C_VOLUME(c,t));
              /*source = (C_VOLUME(c,t)/totalvol)*sourcetot/(2*M_PI*C_VOLUME(c,t));*/
              dS[eqn] = 0.;
            }
          else
            {
              source = 0.;
              dS[eqn]=0.;
            }
     }
   return source;
  #endif
}

DEFINE_ADJUST(FindCTarget,domain) /*This section finds the location of the interface at the
boundary cell*/
{
  #if !RP_HOST
  Thread *t, *t_solid;
  cell_t c;
  real targetVOF;
  real x[ND_ND];
  real time;
  Domain *d;

  time = CURRENT_TIME;
  totalsourcevol=0.;
```

```
  d = Get_Domain(3);
  targetVOF = 1.;

  /*The totalsourcevol part needs to be done on all nodes, the rest only needs to be in the node
with the contact line, but shouldn't hurt to be performed elsewhere*/

  thread_loop_c(t,d)
  {
   if(FLUID_THREAD_P(t))
     {
          begin_c_loop(c,t)
           {
            C_CENTROID(x,c,t);
            if(x[0]<dx)
              {
                   if(ABS(C_VOF(c,t)-0.5)<ABS(targetVOF-0.5))
                    {
                     c_target = c;
                     targetVOF = C_VOF(c,t);
                     r_target = x[1];

                     if(const_CA==1)
                       {
                            if(rec==1)
                              {
                               if(r_target>x_fix)
                                 x_fix = r_target;
                              }
                            else
                              {
                               if(r_target<x_fix)
                                 x_fix=r_target;
                              }
                       }
                    }
              }
            if((x[0]<2.*dx)&&(x[0]>dx))
              {
                   if(ABS(C_VOF(c,t)-0.5)<ABS(targetVOF-0.5))
                    {
                     c_target2 = c;
                     targetVOF = C_VOF(c,t);
                     r_target2 = x[1];
                    }
              }
```

```
            if(C_VOF(c,t)>0.99)
              {
                totalsourcevol=totalsourcevol+2*M_PI*C_VOLUME(c,t);
              }
            }
          end_c_loop(c,t)
    }
  }
  totalsourcevol=PRF_GRSUM1(totalsourcevol);

  /*get the surface temperature at the microlayer*/
  t_solid = Lookup_Thread(domain, 15);
  begin_c_loop_all(c,t_solid)
    {
        C_CENTROID(x,c,t_solid);
        if((x[0]>-dx)&&(x[1]==r_target))
          {
            MLSurfTemp = C_T(c,t_solid);
            Message("Surface temp at microlayer is %g \n", MLSurfTemp);
          }
    }
  end_c_loop(c,t_solid)

  MLSurfTemp = PRF_GRHIGH1(MLSurfTemp);

  #endif
}

DEFINE_PROFILE(CAAdjust,t,i) /*This section sets the contact angle boundary condition
based on the values determined in the SaveVOF_grad function*/
{
  #if !RP_HOST
  face_t f;
  /*This should be fine to be run on all nodes, I imagine since it is applied to a specific boundary
condition, it will know which node to apply it to*/
  begin_f_loop(f,t)
    {
      if((const_CA==1)&&(rec==1))
      {
        F_PROFILE(f,t,i) = M_PI-CA_rec*M_PI/180.;
        /*Message("Receding condition set \n");*/
      }
      if((const_CA==1)&&(adv==1))
      {
        F_PROFILE(f,t,i) = M_PI-CA_adv*M_PI/180.;
        /*Message("Advancing Condition set \n");*/
```

```
    }
    if(const_CL==1)
    {
     F_PROFILE(f,t,i) = M_PI-contact_angle*M_PI/180.;
     /*Message("Pinned condition set \n");*/
    }
    if((const_CA!=1)&&(const_CL!=1))
     Message("Neither const_CA or const_CL specified...ERROR \n");
    if((const_CA==1)&&(adv==0)&&(rec==0))
        Message("Neither adv or rec specified...ERROR \n");
  }
 end_f_loop(f,t)
 #endif
}


DEFINE_SOURCE(MomSink,c,t,dS,eqn) /*This section supplies the force to keep the contact
line pinned if necessary*/
{
 #if !RP_HOST
  real x[ND_ND];
  real source;
  Thread *subt=THREAD_SUB_THREAD(t,1);
  real temp;
  real factorx;

  C_CENTROID(x,c,t);

  /*Need to make sure that the const_CL, const_CA, adv, rec, etc. are synced every time step.
Otherwise I don't think this should cause a problem to run on all nodes.*/

  if(const_CL==1)
  {
   if((C_VOF(c,subt)>0.01)&&(C_VOF(c,subt)<0.99))
        {
          if(((x[0]<dx)&&(ABS(r_target-
x[1])<1.5*dx))||((x[0]<2.*dx)&&(x[0]>dx)&&(ABS(r_target2-x[1])<1.5*dx)))
           {
              if(r_target>x_fix)
                factorx=-factorpos;
              if(r_target<x_fix)
                factorx=factorpos;
              temp = 2.5*ABS(r_target-x_fix)/dx;
              source = factorx*pow(temp,2.)-factor*C_V(c,t)*C_R(c,t);

              Message("Position source is %g \n", factorx*pow(temp,2.));
```

```
                Message("Velocity source is %g \n", -factor*C_V(c,t)*C_R(c,t));

                Message("r_target is %g \n", r_target);
                Message("x_fix is %g \n", x_fix);
                Message("Mom Source is %g \n", source);

                checksource=source;
            }
        }
        else
            source = 0.;
    }

    dS[eqn] = 0.;

    return source;
  #endif
}


DEFINE_EXECUTE_AT_END(SaveVOF_Grad) /*This section sets many important variables
for the next iteration such as the contact angle, and the const_CL or const_CA condition*/
{
  #if !RP_HOST
  Domain *d;
  Thread *t;
  cell_t c;
  real time;
  real x[ND_ND];
  real grad1;
  real grad2;
  real gradmag;
  real gradtotal=0.0;
  real gradnum=0.0;
  real veltotal=0.;
  real velnum=0.;
  int CLflag=0;

  time = CURRENT_TIME;
  i=0.;
  d = Get_Domain(3);
  stepnum=stepnum+1;
  totalvol=0.;

  thread_loop_c(t,d)
  {
```

```
 if(FLUID_THREAD_P(t))
  {
      begin_c_loop(c,t)
       {
        if (SV_ALLOCATED_P(t,SV_VOF_RG)!=NULL)
         {
            C_CENTROID(x,c,t);
            if((C_VOF(c,t)<0.99)&&(C_VOF(c,t)>0.01)&&(x[0]>dx)&&(x[0]<(2.*dx)))
             {
              grad1 = C_VOF_RG(c,t)[0];
              grad2 = C_VOF_RG(c,t)[1];
              gradmag = sqrt(pow(grad1,2.)+pow(grad2,2.));

              gradnum = gradnum+1.;
              gradtotal = gradtotal+grad1/gradmag;

              veltotal=veltotal+C_V(c,t);
              velnum=velnum+1.;
             }
         }
        totalvol=totalvol+2*M_PI*C_VOLUME(c,t)*C_VOF(c,t);
       }
      end_c_loop(c,t)
  }
}
if(gradnum!=0.)
 {
  contact_angle = acos(gradtotal/gradnum)*180./M_PI;
  CLflag=1;
  if(I_AM_NODE_ZERO_P)
      Message("Node 0!");
  if(I_AM_NODE_ONE_P)
      Message("Node 1!");
  if(I_AM_NODE_SAME_P(2))
      Message("Node 2!");
  if(I_AM_NODE_SAME_P(3))
      Message("Node 3!");
  if(I_AM_NODE_SAME_P(4))
      Message("Node 4!");
  if(I_AM_NODE_SAME_P(5))
      Message("Node 5!");
  if(I_AM_NODE_SAME_P(6))
      Message("Node 6!");
  if(I_AM_NODE_SAME_P(7))
      Message("Node 7!");
  if(I_AM_NODE_SAME_P(8))
```

```
        Message("Node 8!");
    if(I_AM_NODE_LAST_P)
        Message("Last Node!");
  }

 if(CLflag==1)
  Message("Angle is %g \n", contact_angle);

 if(velnum!=0.)
  CL_vel=veltotal/velnum;
 /*Message("CLVel is %g \n", CL_vel);
 Message("veltotal is %g \n", veltotal);
 Message("velnum is %g \n", velnum);*/

  /*Essentially this whole section need to occur only for the node that is looking at the contact
line. Then, somehow I need to tell the new conditions to all the other cores, although it shouldn't
really matter for them, but in case the contact line could move into another node I should keep
them all on the same page*/
 if((CLflag==1)||(I_AM_NODE_ZERO_P))
  {
   if(const_CL==1)
        {
         adv=0;
         rec=0;
         if((contact_angle<=(CA_rec))&&((CL_vel>0.)||(checksource<0.)))
          {
           constCAcount=constCAcount+1;
           Message("CA count = %d \n", constCAcount);
           if(constCAcount>transreq)
                {
                 rec=1;
                 adv=0;
                 const_CA=1;
                 const_CL=0;
                 if(constCLcount>5)
                   constCLcount=0;
                 checksource=0.;
                }
          }
         if((contact_angle>=(CA_adv))&&((CL_vel<0.)||(checksource>0.)))
          {
           constCAcount=constCAcount+1;
           if(constCAcount>transreq)
                {
                 adv=1;
                 rec=0;
```

```
                const_CA=1;
                const_CL=0;
                if(constCLcount>5)
                  constCLcount=0;
                checksource=0.;
               }
            }
           if((adv==0)&&(rec==0))
            {
             constCLcount=constCLcount+1;
             Message("CL count = %d \n", constCLcount);
             if(constCLcount>transreq)
                 {
                  const_CL=1;
                  const_CA=0;
                  if(constCAcount>transreq)
                    constCAcount=0;
                 }
             else
                 {
                  const_CA=1;
                  const_CL=0;
                  if(ABS(contact_angle-CA_rec)<ABS(contact_angle-CA_adv))
                    rec=1;
                  else
                    adv=1;
                 }
            }
          }
     else
         {
          if(rec==1)
            {

/*if(((CL_vel<0.)&&(contact_angle>(CA_rec+2.)))||((CL_vel<0.)&&(checksource<0.)))*/
             if(r_target<x_fix)
                 {
                  constCLcount=constCLcount+1;
                  if(constCLcount>transreq)
                    {
                     const_CA=0;
                     const_CL=1;
                     constCAcount=0;
                    }
                 }
             else
```

```
                {
                 constCAcount=constCAcount+1;
                 const_CA=1;
                 const_CL=0;
                }
            }
           if(adv==1)
            {
              /*if(((CL_vel>0.)&&(contact_angle<(CA_adv-
2.)))||((CL_vel>0.)&&(checksource>0.)))*/
              if(r_target>x_fix)
                {
                 constCLcount=constCLcount+1;
                 if(constCLcount>transreq)
                  {
                   const_CA=0;
                   const_CL=1;
                   constCAcount=0;
                  }
                }
              else
                {
                 constCAcount=constCAcount+1;
                 const_CA=1;
                 const_CL=0;
                }
            }
          }
    Message("CA is %d, CL is %d \n", const_CA, const_CL);
  }
 else
  {
   const_CA=10;
   const_CL=10;
   adv=10;
   rec=10;
   constCAcount=-1;
   constCLcount=-1;
   x_fix = -1.;
   r_target = -1.;
   r_target2 = -1;
   contact_angle = 0.;
  }

 const_CA = PRF_GILOW1(const_CA);
 const_CL = PRF_GILOW1(const_CL);
```

```
  adv = PRF_GILOW1(adv);
  rec = PRF_GILOW1(rec);
  constCAcount = PRF_GIHIGH1(constCAcount);
  constCLcount = PRF_GIHIGH1(constCLcount);
  totalvol = PRF_GRSUM1(totalvol);
  x_fix = PRF_GRHIGH1(x_fix);
  r_target = PRF_GRHIGH1(r_target);
  r_target2 = PRF_GRHIGH1(r_target2);
  contact_angle = PRF_GRHIGH1(contact_angle);

  /*This writing step should only occur on a single node.*/

  if(((stepnum%50)==0)&&(CLflag==1))
    {
      datafile=fopen("datafile.txt","a");
      fprintf(datafile,"%d %g %g %g %g %d %d %g %g \n", stepnum, time, r_target, totalvol,
contact_angle, const_CA, const_CL, dryout_rad, ML_heat_tot);
      fclose(datafile);
    }
  #endif
}

/*%%%%%%%%%%%%%%%%%%%%%%%%%%%%%%%%%%%%%%%%%%%%%%%
%%%%%%%%%%%%%%%%%%%%%%%%%%%%%%%%%%%%%%%%%%%%%%%%
%%*/
/*THIS BEGINS THE PHASE CHANGE UDF MACROS*/
/*%%%%%%%%%%%%%%%%%%%%%%%%%%%%%%%%%%%%%%%%%%%%%%%
%%%%%%%%%%%%%%%%%%%%%%%%%%%%%%%%%%%%%%%%%%%%%%%%
%%*/

DEFINE_ADJUST(store_gradient, domain) /*I MAY NEED TO COMBINE THIS WITH MY
OTHER DEFINE_ADJUST%%%%%%%%%%%%%%%%%%%%%%%%*/
{
 #if !RP_HOST
  Thread *t;
  Thread *t1;
  Thread *tf;
  Thread *tf1;
  Thread **pt;
  cell_t c, c1;
  face_t f, f1;
  real scalint1, scalint2;
  real vfrac, cellvol;
  real count, count2;
  real gas_ava, liquid_ava, radius, mass_flux;
  real area, area_total, area_interface, mass_transfer,heat_flux;
```

```
  real MLEvap;
  real hfg=2257000, rou_v=0.5956, T_sat=373.15,T_goal=373.15, rou_l=957.85, cp_v=2029,
cp_l=4217; /*NEED TO CHECK AND MODIFY THESE
VALUES %%%%%%%%%%%%%%%%%%%%%%%%%%%%%%%%%%%%%%%%%%%%
%%%%%%%%%%%%%%%%%%%%%%%%%%%*/
  int phase_domain_index = 1.;/*domain_index=0 for primary phase, +1 for other domains, I
WILL NEED TO CHANGE TO 1 I THINK BUT I MAY NEED IT TO BE
2 %%%%%%%%%%%%%%%%%%%%%%%%%%%%%%%%%%%%%%%%%%%%%%%%
%%%%%%%%%%%%%%%%%%%%%%%%%%%*/
  int n, i;
  real cell_center[2];
  real delt_T;

  real current_time0 = RP_Get_Real("flow-time");


  Domain *pDomain = DOMAIN_SUB_DOMAIN(domain,phase_domain_index); /*NEED TO
MAKE SURE THIS IS GOING TO OPERATE ON THE PROPER
SUBDOMAIN %%%%%%%%%%%%%%%%%%%%%%%%%%%%%%%%%%%%%%%%%%
%%%%%%%%%%%%%%%%%%%%%%%%%%%%%%%%%%%%%%%%%%%%%*/

  real relax_factor=0.2;

  real scale_gas=1;

  real current_time=RP_Get_Real("flow-time");

  {
    Alloc_Storage_Vars(pDomain,SV_VOF_RG,SV_VOF_G,SV_NULL);
    Scalar_Reconstruction(pDomain, SV_VOF,-1,SV_VOF_RG,NULL);
    Scalar_Derivatives(pDomain,SV_VOF,-
1,SV_VOF_G,SV_VOF_RG,Vof_Deriv_Accumulate);
  }

  {
    Alloc_Storage_Vars(domain, SV_T_RG, SV_T_G,  SV_NULL);
    T_derivatives(domain);
    Free_Storage_Vars(domain, SV_T_RG, SV_NULL);
  }
  time_step=RP_Get_Real("physical-time-step");
  gas_total=gas_total_2=gas_total_1=0;
  liquid_total=liquid_total_2=liquid_total_1=0;


  mp_thread_loop_c (t,domain,pt)
    if (FLUID_THREAD_P(t))
```

```
  {
   {
      Thread *ppt = pt[phase_domain_index];/*the number should be the same as
phase_domain_index; 0 is primary domain, then the C_VOF is the primary domain's fraction*/

      scalint1=scalint2=0;
      count=0;
      volume=volume_source=area_total=area_interface=int_volume_source=0;
      need_fix=0;

      begin_c_loop (c,t)/*ppt is the subdomain, t is the mix-domain*/
        {
          C_UDMI(c,t,0) = C_VOF_G(c,ppt)[0];/* x direction gradient*/
          C_UDMI(c,t,1) = C_VOF_G(c,ppt)[1];/* y direction gradient*/
          C_UDMI(c,t,2) =
C_VOF_G(c,ppt)[0]*C_VOF_G(c,ppt)[0]+C_VOF_G(c,ppt)[1]*C_VOF_G(c,ppt)[1];/* gradient
magnitude ^2*/
          C_UDMI(c,t,2) = sqrt(C_UDMI(c,t,2));/* gradient magnitude*/
          C_UDMI(c,t,3) = C_UDMI(c,t,2)*C_VOLUME(c,t);/*gradient magnitude*cell
volume, surface area I MAY NEED TO CHANGE TO BE AXISYMMETRIC*/
          /*C_UDMI(c,t,11)= C_T_G(c,t)[0];/*x compoent temperature gradient*/
          C_UDMI(c,t,14)=current_time;/*store current simulation time for post process*/
          delt_T=C_T(c,t)-T_sat;
          area_total=area_total+C_UDMI(c,t,3);

/*********************************************************************/
          /*C_UDMI(c,t,15)=C_U(c,t);  /*UDM15 is x velocity*/
          /*C_UDMI(c,t,16)=C_V(c,t);  /*UDM16 is y velocity*/
          /*********************************************************************/
          C_UDMI(c,t,4) = vfrac = C_VOF(c,ppt);/*vapor phase VOF, UDM4 should be the
same as vapor VOF*/
          cellvol = 2*M_PI*C_VOLUME(c,t);

          C_UDMI(c,t,5)=0;/*equal to 1 means interface*/
          C_UDMI(c,t,6)=0;/*liquid mass source*/
          C_UDMI(c,t,7)=0;/*vapor mass source*/
          C_UDMI(c,t,8)=0;/*energy source*/
          C_UDMI(c,t,9)=0;/*mass_flux*/
          C_UDMI(c,t,15)=0;

          C_CENTROID(cell_center, c, t);

          if (C_UDMI(c,t,3)>1e-20 && C_UDMI(c,t,4) < 0.99 && C_UDMI(c,t,4) > 0.1)
/*UDMI5=1 means interface,UDMI5=2 means cells just near the interface*/
            {
              /* if the neck region is broken, please increase 0.1 above correspondingly*/
```

```
                /*//This part is to relax the evaporation rate, try to smooth the evaporation rate
varying with time*/
                C_UDMI(c,t,5)=1;
                if(delt_T>0.005)
                  {
                    C_UDMI(c,t,5)=10;

                    T_goal=T_sat+0.5*C_UDMI(c,t,4)*delt_T;/*0.5 is relaxation factor, try to
decrease it if the simulation is not stable*/
                    Message ("Big Temperature Difference %g\n",(C_T(c,t)-T_sat));
                  }
                /*This part is to relax the evaporation rate, try to smooth the evaporation rate
varying with time*/

                C_UDMI(c,t,8)=(C_UDMI(c,t,4)*rou_v*cp_v*(T_goal-C_T(c,t))+(1-
C_UDMI(c,t,4))*rou_l*cp_l*(T_goal-C_T(c,t)))/time_step;/*energy source to make sure the
temperature is equal to T_sat at the interface,negative means heat sink*/

                gas_total_1=gas_total_1-
C_UDMI(c,t,8)/hfg*(2.*M_PI*C_VOLUME(c,t));/*overall evaporation rate kg/s*/
                liquid_total_1=liquid_total_1+C_UDMI(c,t,8)/hfg*(2.*M_PI*C_VOLUME(c,t));

                C_UDMI(c,t,6)=C_UDMI(c,t,8)/hfg;/*liquid source term, negative for liquid*/

                C_UDMI(c,t,7)=(-1)*C_UDMI(c,t,8)/hfg;

                int_volume_source=(1-vfrac)*cellvol+int_volume_source;
                area_interface=area_interface+C_UDMI(c,t,3);

                T_goal=T_sat;
            }

           else if ( C_UDMI(c,t,4) >0.9 || C_UDMI(c,t,4)==0.9)  /*Vapor, UDMI5=1 means
interface,UDMI5=2 means cells just near the interface*/
             {
                    /* {

                C_UDMI(c,t,5)=2;

                C_UDMI(c,t,8)=(C_UDMI(c,t,4)*rou_v*cp_v*(T_sat-C_T(c,t))+(1-
C_UDMI(c,t,4))*rou_l*cp_l*(T_sat-C_T(c,t)))/time_step;
                /*energy source to make sure the temperature is equal to T_sat at the interface*/


                /*      C_UDMI(c,t,6)=0;
                C_UDMI(c,t,7)=(-1)*C_UDMI(c,t,8)/hfg;
```

```
                gas_total_2=gas_total_2-C_UDMI(c,t,8)/hfg*C_VOLUME(c,t);/*overall
evaporation rate*/
                /*      liquid_total_2=liquid_total_2+C_UDMI(c,t,8)/hfg*C_VOLUME(c,t);

                if(renorm!=0 && renorm!=1) /*NOT SURE WHAT RENORM MEANS
HERE.....*/
                /*   {
                   area = C_UDMI(c,t,3)*2/(1-1/renorm);
                   C_UDMI(c,t,9)=C_UDMI(c,t,7)/area;
                   }*/
                volume_source=vfrac*cellvol+volume_source;
             }

            volume=vfrac*cellvol+volume;/*gas volume or we say primary phase volume*/
           }

         end_c_loop (c,t)

           if (liquid_total_1==0)
             {
              scale_liquid=1;
             }
           else
             {
              scale_liquid=1+liquid_total_2/liquid_total_1;
             }

         if (area_interface==0)
           {
            renorm=2;
           }
         else
           {
            renorm=area_total/area_interface;
           }
     }
   }
  Free_Storage_Vars(pDomain,SV_VOF_RG,SV_VOF_G,SV_NULL);
  gas_total_1=PRF_GRSUM1(gas_total_1);
  gas_total_2=PRF_GRSUM1(gas_total_2);
  liquid_total_1=PRF_GRSUM1(liquid_total_1);
  volume_source=PRF_GRSUM1(volume_source);
  int_volume_source=PRF_GRSUM1(int_volume_source);
```

```
  /*adding in the mass source due to the microlayer evaporation*/
  /*MLEvap = 6.3952*pow((MLSurfTemp-T_sat),0.7736)/pow(dx,2.);*/
  /*gas_total_1 = gas_total_1 + MLEvap/hfg*C_VOLUME(c,t);
    liquid_total_1 = liquid_total_1 - MLEvap/hfg*C_VOLUME(c,t);*/
  /*Message("MLEvap W/m^3 is %g", MLEvap);*/

  #endif
}

DEFINE_ADJUST(ML_tracking, d)
{
  #if !RPHOST
  Thread *t;
  real MLthickness;
  real ML_time;
  real local_heat_flux;
  real local_heat;
  cell_t c;
  real x[ND_ND];
  real time_step = CURRENT_TIMESTEP;
  real k_l = 0.68;
  real radial_area;
  real possible_heat;
  real hfg=2257000, T_sat=373.15, rho_l = 957.85;
  real del_thickness;

  ML_time = CURRENT_TIME + t_off;
  t = Lookup_Thread(d, 15);
  ML_heat_tot = 0.;
  tot_ML_area = 0.;
  tot_ML_vol = 0.;
  dryout_rad = 0.;

  begin_c_loop_all(c,t)
    {
      C_CENTROID(x,c,t);
      if((x[0]>-dx)&&(x[1]<=r_target))
           {
            /*Get current microlayer thickness*/
            if(C_UDMI(c,t,15)<-5.)
              {
                MLthickness = 0.8*sqrt(nu_l*ML_time);
              }
            else
              MLthickness = C_UDMI(c,t,15);
```

```
        if((C_UDMI(c,t,12)>0.)&&(C_UDMI(c,t,15)==0.)) /*retrieves microlayer thickness
that was advanced past due to interfacial oscillation*/
          {
           MLthickness = C_UDMI(c,t,15) = C_UDMI(c,t,12);
           C_UDMI(c,t,12) = 0.;
          }

        /*Message("MLthickness is %g at r = %g \n", MLthickness, x[1]);*/
        /*Calculate microlayer heat transfer*/
        if(MLthickness > 0.)
          {
           local_heat_flux = k_l*((C_T(c,t)-T_sat)/MLthickness);
           radial_area = 2*M_PI*x[1]*dx;
           local_heat = local_heat_flux*radial_area;

           possible_heat = radial_area*MLthickness*rho_l*hfg/time_step;
           tot_ML_area = tot_ML_area + radial_area;
           tot_ML_vol = tot_ML_vol + MLthickness*radial_area;

           /*Message("Location is z = %g, r = %g \n", x[0], x[1]);
           Message("Temperature is %g, MLthickness is %g \n", C_T(c,t), MLthickness);
           Message("Local HF is %g, Possible HF is %g \n", local_heat_flux,
possible_heat/radial_area);*/

           /*Check heat transfer against amount possible and adjust ML thickness accordingly*/
           /*C_UDMI13 is actual local heat transfer, C_UDMI16 is averaged local heat
transfer*/
           if(local_heat<possible_heat)
                {
                 ML_heat_tot = ML_heat_tot + local_heat;
                 C_UDMI(c,t,13) = local_heat_flux;
                 del_thickness = local_heat*time_step/(radial_area*rho_l*hfg);
                 MLthickness = C_UDMI(c,t,15) = MLthickness-del_thickness;
                }
           else
                {
                 ML_heat_tot = ML_heat_tot + possible_heat;
                 MLthickness = C_UDMI(c,t,15) = 0.;
                 C_UDMI(c,t,13) = possible_heat/radial_area;
                }
           /*Message("New MLthickness = %g", MLthickness);*/
          }
        /*track dryout radius*/
        if(MLthickness == 0.)
          {
           C_UDMI(c,t,13) = 0.;
```

```
            if(x[1]>dryout_rad)
                {
                 dryout_rad = x[1];
                 /*Message("Dryout radius is %g \n", dryout_rad);*/
                }
            }
        }

    if((C_UDMI(c,t,15)>0.)&&(x[1]>(r_target))) /*this will lead to some issues if the contact line oscillates back and forth*/
        {
          C_UDMI(c,t,12) = C_UDMI(c,t,15); /*this stores microlayer thickness in case of interfacial oscillations*/
          C_UDMI(c,t,15) = 0.;
        }

   }
 end_c_loop_all(c,t)

 dryout_rad = PRF_GRHIGH1(dryout_rad);
 ML_heat_tot = PRF_GRSUM1(ML_heat_tot);
 #endif
}


DEFINE_SOURCE(gas_mass, c, t, dS, eqn)
{
 #if !RP_HOST
 real source;
 Thread *tm = THREAD_SUPER_THREAD(t);
 real MLEvap;
 real hfg=2257000., T_sat=373.15;

 /*Kunkelmann and Stephen MLEvap*/
 /*MLEvap = 6.3952*pow((MLSurfTemp-T_sat),0.7736)*r_target; /*may need a 2pi here, but I think because volume_source does not include it, it shouldn't be included here either (would cancel out)*/

 /*New MLEvap based on Cooper model and conduction resistance*/
 MLEvap = ML_heat_tot;

 /*Message("MLSurfTemp %g \n", MLSurfTemp);*/

 /*if((MLSurfTemp-T_sat)<0.)
   Message("Negative superheat! \n");*/
```

```
  /*if(isnan(r_target))
    Message("r_target is NaN! \n");

  if(isnan(MLSurfTemp))
  Message("r_target is NaN! \n");*/

  if( C_UDMI(c,t,4) >0.99 || C_UDMI(c,t,4)==0.99) /*made all these 0.99 instead of 0.9*/
    {
     if (volume_source==0)
          {
           source=C_UDMI(c,tm,10)=0;
          }
     else
          {
          /*gas_total_1 = gas_total_1 + MLEvap/hfg;*/
           if(isnan(MLEvap))
             {
               source=C_UDMI(c,tm,10)=(gas_total_1)/volume_source; /*removed gas_total_2 so
that the interior vapor is not kept at saturation*/
               Message("MLEvap Gas source not applied! \n");
             }
           else
             {
               source=C_UDMI(c,tm,10)=(gas_total_1+MLEvap/hfg)/volume_source; /*Not
positive on the added 2pi*/
               /*Message("MLEvap gas Applied! \n");*/
            /*Message("gas_total_1 is %g, MLEvap/hfg is %g \n", gas_total_1, MLEvap/hfg);*/
             }
          }
    }
  else source=C_UDMI(c,tm,10)=0;
  return source;
  #endif
}


DEFINE_SOURCE(liquid_mass, c, t, dS, eqn)
{
  #if !RP_HOST
  real source;
  Thread *tm = THREAD_SUPER_THREAD(t);
  real MLEvap;
  real hfg=2257000., T_sat=373.15;

  /*Kunkelman and Stephan MLEVAP*/
```

```
  /*MLEvap = 6.3952*pow((MLSurfTemp-T_sat),0.7736)*r_target;/*may need a 2pi here, but I
think because volume_source does not include it, it shouldn't be included here either (would
cancel out)*/

  MLEvap = ML_heat_tot;

  if (C_UDMI(c,t,3)>1e-20 && C_UDMI(c,t,4) < 0.99 && C_UDMI(c,t,4) > 0.01)
    {
     if(int_volume_source==0)
          source = 0;
     else
          {
           if(isnan(MLEvap))
             {
              source=C_UDMI(c,tm,11)=(liquid_total_1)/int_volume_source;
              Message("MLEvap liquid source not applied! \n");
             }
           else
             {
              source = C_UDMI(c,tm,11) = (liquid_total_1-MLEvap/hfg)/int_volume_source;
/*Not positive on the added 2*pi*/
              /*Message("MLEvap liquid Applied! \n");*/
              /*Message("liquid_total_1 is %g, MLEvap is %g \n", liquid_total_1, MLEvap/hfg);*/
             }
          }
    }
  else
    {
     source=C_UDMI(c,tm,11)=0;
    }
  return source;
  #endif
}


DEFINE_SOURCE(energy, c, t, dS, eqn)
{
  #if !RP_HOST
  real source;
  real cp_v=2029, cp_l=4217;
  real x[ND_ND];

  C_CENTROID(x,c,t);
```

```
if(((x[0]<dx)&&(x[1]>(r_target+2.*dx)))||((x[0]<(2.*dx))&&(x[0]>dx)&&(x[1]>(r_target2+2.*dx))))
   source = 0;
  else
   source=C_UDMI(c,t,8)+C_UDMI(c,t,11)*cp_l*(C_T(c,t)-298.15)+C_UDMI(c,t,10)*cp_v*(C_T(c,t)-298.15);

  return source;
  #endif
}

DEFINE_SOURCE(microlayer, c, t, dS, eqn)
{
  #if !RP_HOST
  real source;
  real xc[ND_ND];
  real radial_area;
  real MLheat;
  real avgMLthickness;

  C_CENTROID(xc,c,t);

  if((xc[0]>-dx)&&(xc[1]<=r_target)&&(C_T(c,t)>=373.15)&&(C_UDMI(c,t,15)>0.))
    {
     /* Kunkelmann and Stephen Microlayer term*/
     /*source = -6.3952*pow((C_T(c,t)-373.15), 0.7736)/pow(dx,2.);*/

     radial_area = xc[1]*2*M_PI*dx;
     if(tot_ML_area==0.)
          MLheat=0;
     else
          {
           MLheat = ML_heat_tot*radial_area/tot_ML_area;
          }

     /*C_UDMI(c,t,16) = MLheat/(radial_area);*/

     /*source = -MLheat/(2*M_PI*C_VOLUME(c,t)); /*Not sure if this should have a 2*pi in it or not...*/

     /*I think I should try... source = -ML_heat_tot/(tot_ML_area*dx);*/
```

```
    source = -ML_heat_tot/(tot_ML_area*dx);
    C_UDMI(c,t,16) = source*dx;

    avgMLthickness = tot_ML_vol/tot_ML_area;
    /*Message("ML flux is %g \n", source*2*M_PI*C_VOLUME(c,t)/radial_area);*/
   }
  else
   {
    C_UDMI(c,t,16) = 0.;
    source = 0;
   }

  return source;
  #endif
}
```

REFERENCES

[1] N. Zuber, Hydrodynamic Aspects of Boiling Heat Transfer, University of California, Los Angeles, 1959. https://doi.org/10.2172/4175511.

[2] A.E. Bergles, R.M. Manglik, Current Progress And New Developments In Enhanced Heat And Mass Transfer, J. Enhanc. Heat Transf. 20 (2013). https://doi.org/10.1615/JEnhHeatTransf.2013006989.

[3] S. Mori, Y. Utaka, Critical heat flux enhancement by surface modification in a saturated pool boiling: A review, Int. J. Heat Mass Transf. 108, Part B (2017) 2534–2557. https://doi.org/10.1016/j.ijheatmasstransfer.2017.01.090.

[4] Y. Takata, S. Hidaka, M. Masuda, T. Ito, Pool boiling on a superhydrophilic surface, Int. J. Energy Res. 27 (2003) 111–119. https://doi.org/10.1002/er.861.

[5] C.-C. Hsu, P.-H. Chen, Surface wettability effects on critical heat flux of boiling heat transfer using nanoparticle coatings, Int. J. Heat Mass Transf. 55 (2012) 3713–3719. https://doi.org/10.1016/j.ijheatmasstransfer.2012.03.003.

[6] M.M. Rahman, E. Ölçeroğlu, M. McCarthy, Role of Wickability on the Critical Heat Flux of Structured Superhydrophilic Surfaces, Langmuir. 30 (2014) 11225–11234. https://doi.org/10.1021/la5030923.

[7] N.S. Dhillon, J. Buongiorno, K.K. Varanasi, Critical heat flux maxima during boiling crisis on textured surfaces, Nat. Commun. 6 (2015) 8247. https://doi.org/10.1038/ncomms9247.

[8] H. Jo, H.S. Ahn, S. Kang, M.H. Kim, A study of nucleate boiling heat transfer on hydrophilic, hydrophobic and heterogeneous wetting surfaces, Int. J. Heat Mass Transf. 54 (2011) 5643–5652. https://doi.org/10.1016/j.ijheatmasstransfer.2011.06.001.

[9] S. Gong, P. Cheng, Lattice Boltzmann simulations for surface wettability effects in saturated pool boiling heat transfer, Int. J. Heat Mass Transf. 85 (2015) 635–646. https://doi.org/10.1016/j.ijheatmasstransfer.2015.02.008.

[10] Y. Takata, S. Hidaka, T. Uraguchi, Boiling Feature on a Super Water-Repellent Surface, Heat Transf. Eng. 27 (2006) 25–30. https://doi.org/10.1080/01457630600793962.

[11] I. Malavasi, B. Bourdon, P. Di Marco, J. de Coninck, M. Marengo, Appearance of a low superheat “quasi-Leidenfrost” regime for boiling on superhydrophobic surfaces, Int. Commun. Heat Mass Transf. 63 (2015) 1–7. https://doi.org/10.1016/j.icheatmasstransfer.2015.01.012.

[12] M. Zupančič, M. Steinbücher, P. Gregorčič, I. Golobič, Enhanced pool-boiling heat transfer on laser-made hydrophobic/superhydrophilic polydimethylsiloxane-silica patterned surfaces, Appl. Therm. Eng. 91 (2015) 288–297. https://doi.org/10.1016/j.applthermaleng.2015.08.026.

[13] Y. Li, K. Zhang, M.-C. Lu, C. Duan, Single bubble dynamics on superheated superhydrophobic surfaces, Int. J. Heat Mass Transf. 99 (2016) 521–531. https://doi.org/10.1016/j.ijheatmasstransfer.2016.03.098.

[14] E. Teodori, T. Valente, I. Malavasi, A.S. Moita, M. Marengo, A.L.N. Moreira, Effect of extreme wetting scenarios on pool boiling conditions, Appl. Therm. Eng. (2016). https://doi.org/10.1016/j.applthermaleng.2016.11.079.

[15] S. Bhavnani, V. Narayanan, W. Qu, M. Jensen, S. Kandlikar, J. Kim, J. Thome, Boiling Augmentation with Micro/Nanostructured Surfaces: Current Status and Research Outlook, Nanoscale Microscale Thermophys. Eng. 18 (2014) 197–222. https://doi.org/10.1080/15567265.2014.923074.
[16] G. Liang, I. Mudawar, Pool boiling critical heat flux (CHF) – Part 2: Assessment of models and correlations, Int. J. Heat Mass Transf. (2017). https://doi.org/10.1016/j.ijheatmasstransfer.2017.09.073.
[17] G. Liang, I. Mudawar, Pool boiling critical heat flux (CHF) – Part 1: Review of mechanisms, models, and correlations, Int. J. Heat Mass Transf. 117 (2018) 1352–1367. https://doi.org/10.1016/j.ijheatmasstransfer.2017.09.134.
[18] R.C. Chu, R.E. Simons, M.J. Ellsworth, R.R. Schmidt, V. Cozzolino, Review of cooling technologies for computer products, IEEE Trans. Device Mater. Reliab. 4 (2004) 568–585. https://doi.org/10.1109/TDMR.2004.840855.
[19] T.L. Bergman, A.S. Lavine, F.P. Incropera, D.P. Dewitt, Fundamentals of Heat and Mass Transfer, 7th ed., Wiley, n.d.
[20] V.K. Dhir, Boiling Heat Transfer, Annu. Rev. Fluid Mech. 30 (1998) 365–401. https://doi.org/10.1146/annurev.fluid.30.1.365.
[21] J. Kim, Review of nucleate pool boiling bubble heat transfer mechanisms, Int. J. Multiph. Flow. 35 (2009) 1067–1076. https://doi.org/10.1016/j.ijmultiphaseflow.2009.07.008.
[22] P.A. Raghupathi, S.G. Kandlikar, Contact line region heat transfer mechanisms for an evaporating interface, Int. J. Heat Mass Transf. 95 (2016) 296–306. https://doi.org/10.1016/j.ijheatmasstransfer.2015.11.047.
[23] H.K. Forster, N. Zuber, Dynamics of vapor bubbles and boiling heat transfer, AIChE J. 1 (1955) 531–535. https://doi.org/10.1002/aic.690010425.
[24] K. Forster, R. Greif, HEAT TRANSFER TO A BOILING LIQUID MECHANISM AND CORRELATIONS. Progress Report No. 7 (58-40), California. Univ., Los Angeles, CA (United States). Dept. of Engineering, 1958. https://doi.org/10.2172/4298039.
[25] B.B. Mikic, W.M. Rohsenow, A New Correlation of Pool-Boiling Data Including the Effect of Heating Surface Characteristics, J. Heat Transf. 91 (1969) 245–250. https://doi.org/10.1115/1.3580136.
[26] F.D. Moore, R.B. Mesler, The measurement of rapid surface temperature fluctuations during nucleate boiling of water, AIChE J. 7 (1961) 620–624. https://doi.org/10.1002/aic.690070418.
[27] R.L. Judd, K.S. Hwang, A Comprehensive Model for Nucleate Pool Boiling Heat Transfer Including Microlayer Evaporation, J. Heat Transf. 98 (1976) 623–629. https://doi.org/10.1115/1.3450610.
[28] Y. Utaka, K. Hu, Z. Chen, T. Morokuma, Measurement of contribution of microlayer evaporation applying the microlayer volume change during nucleate pool boiling for water and ethanol, Int. J. Heat Mass Transf. 125 (2018) 243–247. https://doi.org/10.1016/j.ijheatmasstransfer.2018.04.044.
[29] P. Stephan, J. Hammer, A new model for nucleate boiling heat transfer, Heat Mass Transf. 30 (1994) 119–125. https://doi.org/10.1007/BF00715018.
[30] P.C. Wayner, Y.K. Kao, L.V. LaCroix, The interline heat-transfer coefficient of an evaporating wetting film, Int. J. Heat Mass Transf. 19 (1976) 487–492. https://doi.org/10.1016/0017-9310(76)90161-7.

[31] E. Wagner, P. Stephan, High-Resolution Measurements at Nucleate Boiling of Pure FC-84 and FC-3284 and Its Binary Mixtures, J. Heat Transf. 131 (2009) 121008-121008–12. https://doi.org/10.1115/1.3220143.
[32] S. Moghaddam, K. Kiger, Physical mechanisms of heat transfer during single bubble nucleate boiling of FC-72 under saturation conditions-I. Experimental investigation, Int. J. Heat Mass Transf. 52 (2009) 1284–1294. https://doi.org/10.1016/j.ijheatmasstransfer.2008.08.018.
[33] T. Yabuki, O. Nakabeppu, Heat transfer mechanisms in isolated bubble boiling of water observed with MEMS sensor, Int. J. Heat Mass Transf. 76 (2014) 286–297. https://doi.org/10.1016/j.ijheatmasstransfer.2014.04.012.
[34] W. Fritz, Maximum volume of vapor bubbles, Phys. Z. 36 (1935) 379–384.
[35] R.L. Mohanty, M.K. Das, A critical review on bubble dynamics parameters influencing boiling heat transfer, Renew. Sustain. Energy Rev. 78 (2017) 466–494. https://doi.org/10.1016/j.rser.2017.04.092.
[36] G. Kocamustafaogullari, M. Ishii, Interfacial area and nucleation site density in boiling systems, Int. J. Heat Mass Transf. 26 (1983) 1377–1387. https://doi.org/10.1016/S0017-9310(83)80069-6.
[37] C.H. Wang, V.K. Dhir, Effect of Surface Wettability on Active Nucleation Site Density During Pool Boiling of Water on a Vertical Surface, J. Heat Transf. 115 (1993) 659–669. https://doi.org/10.1115/1.2910737.
[38] T. Hibiki, M. Ishii, Active nucleation site density in boiling systems, Int. J. Heat Mass Transf. 46 (2003) 2587–2601. https://doi.org/10.1016/S0017-9310(03)00031-0.
[39] C.-Y. Han, P. Griffith, The mechanism of heat transfer in nucleate pool boiling—Part I: Bubble initiaton, growth and departure, Int. J. Heat Mass Transf. 8 (1965) 887–904. https://doi.org/10.1016/0017-9310(65)90073-6.
[40] Y. Nam, J. Wu, G. Warrier, Y.S. Ju, Experimental and Numerical Study of Single Bubble Dynamics on a Hydrophobic Surface, J. Heat Transf. 131 (2009) 121004–121004. https://doi.org/10.1115/1.3216038.
[41] N. Zuber, The dynamics of vapor bubbles in nonuniform temperature fields, Int. J. Heat Mass Transf. 2 (1961) 83–98. https://doi.org/10.1016/0017-9310(61)90016-3.
[42] C.R. Kharangate, I. Mudawar, Review of computational studies on boiling and condensation, Int. J. Heat Mass Transf. 108, Part A (2017) 1164–1196. https://doi.org/10.1016/j.ijheatmasstransfer.2016.12.065.
[43] R.C. Lee, J.E. Nydahl, Numerical Calculation of Bubble Growth in Nucleate Boiling From Inception Through Departure, J. Heat Transf. 111 (1989) 474–479. https://doi.org/10.1115/1.3250701.
[44] S.W.J. Welch, Direct simulation of vapor bubble growth, Int. J. Heat Mass Transf. 41 (1998) 1655–1666. https://doi.org/10.1016/S0017-9310(97)00285-8.
[45] G. Son, V.K. Dhir, N. Ramanujapu, Dynamics and Heat Transfer Associated With a Single Bubble During Nucleate Boiling on a Horizontal Surface, J. Heat Transf. 121 (1999) 623–631. https://doi.org/10.1115/1.2826025.
[46] G. Son, N. Ramanujapu, V.K. Dhir, Numerical Simulation of Bubble Merger Process on a Single Nucleation Site During Pool Nucleate Boiling, J. Heat Transf. 124 (2001) 51–62. https://doi.org/10.1115/1.1420713.

[47] J. Wu, V.K. Dhir, J. Qian, Numerical Simulation of Subcooled Nucleate Boiling by Coupling Level-Set Method with Moving-Mesh Method, Numer. Heat Transf. Part B Fundam. 51 (2007) 535–563. https://doi.org/10.1080/10407790601177763.
[48] G. Son, V.K. Dhir, Numerical simulation of nucleate boiling on a horizontal surface at high heat fluxes, Int. J. Heat Mass Transf. 51 (2008) 2566–2582. https://doi.org/10.1016/j.ijheatmasstransfer.2007.07.046.
[49] E. Aktinol, V.K. Dhir, Numerical Simulation of Nucleate Boiling Phenomenon Coupled with Thermal Response of the Solid, Microgravity Sci. Technol. 24 (2012) 255–265. https://doi.org/10.1007/s12217-012-9308-7.
[50] C. Kunkelmann, P. Stephan, CFD Simulation of Boiling Flows Using the Volume-of-Fluid Method within OpenFOAM, Numer. Heat Transf. Part Appl. 56 (2009) 631–646. https://doi.org/10.1080/10407780903423908.
[51] P.C. Stephan, C.A. Busse, Analysis of the heat transfer coefficient of grooved heat pipe evaporator walls, Int. J. Heat Mass Transf. 35 (1992) 383–391. https://doi.org/10.1016/0017-9310(92)90276-X.
[52] C. Kunkelmann, P. Stephan, Numerical simulation of the transient heat transfer during nucleate boiling of refrigerant HFE-7100, Int. J. Refrig. 33 (2010) 1221–1228. https://doi.org/10.1016/j.ijrefrig.2010.07.013.
[53] Y. Nam, E. Aktinol, V.K. Dhir, Y.S. Ju, Single bubble dynamics on a superhydrophilic surface with artificial nucleation sites, Int. J. Heat Mass Transf. 54 (2011) 1572–1577. https://doi.org/10.1016/j.ijheatmasstransfer.2010.11.031.
[54] S. Gong, P. Cheng, Numerical simulation of pool boiling heat transfer on smooth surfaces with mixed wettability by lattice Boltzmann method, Int. J. Heat Mass Transf. 80 (2015) 206–216. https://doi.org/10.1016/j.ijheatmasstransfer.2014.08.092.
[55] W. Lee, G. Son, J.J. Jeong, Numerical Analysis of Bubble Growth and Departure from a Microcavity, Numer. Heat Transf. Part B Fundam. 58 (2010) 323–342. https://doi.org/10.1080/10407790.2010.522871.
[56] W. Lee, G. Son, Numerical simulation of boiling enhancement on a microstructured surface, Int. Commun. Heat Mass Transf. 38 (2011) 168–173. https://doi.org/10.1016/j.icheatmasstransfer.2010.11.017.
[57] W. Lee, G. Son, H.Y. Yoon, Numerical study of bubble growth and boiling heat transfer on a microfinned surface, Int. Commun. Heat Mass Transf. 39 (2012) 52–57. https://doi.org/10.1016/j.icheatmasstransfer.2011.09.008.
[58] R. Ranjan, J.Y. Murthy, S.V. Garimella, Bubble dynamics during capillary-fed nucleate boiling in porous media, in: 13th Intersoc. Conf. Therm. Thermomechanical Phenom. Electron. Syst., 2012: pp. 1114–1126. https://doi.org/10.1109/ITHERM.2012.6231548.
[59] G. Hazi, A. Markus, On the bubble departure diameter and release frequency based on numerical simulation results, Int. J. Heat Mass Transf. 52 (2009) 1472–1480. https://doi.org/10.1016/j.ijheatmasstransfer.2008.09.003.
[60] A. Georgoulas, M. Andredaki, M. Marengo, An Enhanced VOF Method Coupled with Heat Transfer and Phase Change to Characterise Bubble Detachment in Saturated Pool Boiling, Energies. 10 (2017) 272. https://doi.org/10.3390/en10030272.
[61] J.H. Lienhard, V.K. Dhir, Hydrodynamic Prediction of Peak Pool-boiling Heat Fluxes from Finite Bodies, J. Heat Transf. 95 (1973) 152–158. https://doi.org/10.1115/1.3450013.

[62] J.H. Lienhard, V.K. Dhir, D.M. Riherd, Peak Pool Boiling Heat-Flux Measurements on Finite Horizontal Flat Plates, J. Heat Transf. 95 (1973) 477–482. https://doi.org/10.1115/1.3450092.
[63] I. Kano, Pool Boiling Enhancement by Electrohydrodynamic Force and Diamond Coated Surfaces, J. Heat Transf. 137 (2015) 091006–091006. https://doi.org/10.1115/1.4030217.
[64] M.-C. Lu, C.-H. Huang, C.-T. Huang, Y.-C. Chen, A modified hydrodynamic model for pool boiling CHF considering the effects of heater size and nucleation site density, Int. J. Therm. Sci. 91 (2015) 133–141. https://doi.org/10.1016/j.ijthermalsci.2015.01.011.
[65] Y. Haramura, Y. Katto, A new hydrodynamic model of critical heat flux, applicable widely to both pool and forced convection boiling on submerged bodies in saturated liquids, Int. J. Heat Mass Transf. 26 (1983) 389–399. https://doi.org/10.1016/0017-9310(83)90043-1.
[66] V.S. Nikolayev, D.A. Beysens, Boiling crisis and non-equilibrium drying transition, Europhys. Lett. EPL. 47 (1999) 345–351. https://doi.org/10.1209/epl/i1999-00395-x.
[67] V.S. Nikolayev, D.A. Beysens, G.-L. Lagier, J. Hegseth, Growth of a dry spot under a vapor bubble at high heat flux and high pressure, Int. J. Heat Mass Transf. 44 (2001) 3499–3511. https://doi.org/10.1016/S0017-9310(01)00024-2.
[68] V.S. Nikolayev, D. Chatain, Y. Garrabos, D. Beysens, Experimental Evidence of the Vapor Recoil Mechanism in the Boiling Crisis, Phys. Rev. Lett. 97 (2006) 184503. https://doi.org/10.1103/PhysRevLett.97.184503.
[69] S.G. Kandlikar, A Theoretical Model to Predict Pool Boiling CHF Incorporating Effects of Contact Angle and Orientation, J. Heat Transf. 123 (2001) 1071–1079. https://doi.org/10.1115/1.1409265.
[70] T.G. Theofanous, T.N. Dinh, J.P. Tu, A.T. Dinh, The boiling crisis phenomenon: Part II: dryout dynamics and burnout, Exp. Therm. Fluid Sci. 26 (2002) 793–810. https://doi.org/10.1016/S0894-1777(02)00193-0.
[71] V.V. Yagov, Is a crisis in pool boiling actually a hydrodynamic phenomenon?, Int. J. Heat Mass Transf. 73 (2014) 265–273. https://doi.org/10.1016/j.ijheatmasstransfer.2014.01.076.
[72] B.S. Kim, H. Lee, S. Shin, G. Choi, H.H. Cho, Interfacial wicking dynamics and its impact on critical heat flux of boiling heat transfer, Appl. Phys. Lett. 105 (2014). https://doi.org/10.1063/1.4901569.
[73] R. Blossey, Self-cleaning surfaces — virtual realities, Nat. Mater. 2 (2003) 301–306. https://doi.org/10.1038/nmat856.
[74] R.N. Govardhan, G.S. Srinivas, A. Asthana, M.S. Bobji, Time dependence of effective slip on textured hydrophobic surfaces, Phys. Fluids. 21 (2009) 052001. https://doi.org/10.1063/1.3127123.
[75] J. Wang, B. Wang, D. Chen, Underwater drag reduction by gas, Friction. 2 (2014) 295–309. https://doi.org/10.1007/s40544-014-0070-2.
[76] X. Chen, J.A. Weibel, S.V. Garimella, Exploiting Microscale Roughness on Hierarchical Superhydrophobic Copper Surfaces for Enhanced Dropwise Condensation, Adv. Mater. Interfaces. 2 (2015) n/a-n/a. https://doi.org/10.1002/admi.201400480.
[77] P.S. Mahapatra, A. Ghosh, R. Ganguly, C.M. Megaridis, Key design and operating parameters for enhancing dropwise condensation through wettability patterning, Int. J. Heat Mass Transf. 92 (2016) 877–883. https://doi.org/10.1016/j.ijheatmasstransfer.2015.08.106.

[78] M. Edalatpour, L. Liu, A.M. Jacobi, K.F. Eid, A.D. Sommers, Managing water on heat transfer surfaces: A critical review of techniques to modify surface wettability for applications with condensation or evaporation, Appl. Energy. 222 (2018) 967–992. https://doi.org/10.1016/j.apenergy.2018.03.178.
[79] T. Young, An Essay on the Cohesion of Fluids, Philos. Trans. R. Soc. Lond. 95 (1805) 65–87. https://doi.org/10.1098/rstl.1805.0005.
[80] P.G. de Gennes, F. Brochard-Wyart, D. Quéré, Capillarity and Wetting Phenomena: Drops, Bubbles, Pearls, Waves, Springer, 2004.
[81] R.N. Wenzel, Resistance of Solid Surfaces to Wetting by Water, Ind. Eng. Chem. 28 (1936) 988–994. https://doi.org/10.1021/ie50320a024.
[82] R.N. Wenzel, Surface Roughness and Contact Angle., J. Phys. Colloid Chem. 53 (1949) 1466–1467. https://doi.org/10.1021/j150474a015.
[83] J. Bico, C. Tordeux, D. Quéré, Rough wetting, Europhys. Lett. EPL. 55 (2001) 214–220. https://doi.org/10.1209/epl/i2001-00402-x.
[84] J. Bico, U. Thiele, D. Quéré, Wetting of textured surfaces, Colloids Surf. Physicochem. Eng. Asp. 206 (2002) 41–46. https://doi.org/10.1016/S0927-7757(02)00061-4.
[85] T.P. Allred, J.A. Weibel, S.V. Garimella, A Wettability Metric for Characterization of Capillary Flow on Textured Superhydrophilic Surfaces, Langmuir. (2017). https://doi.org/10.1021/acs.langmuir.7b01522.
[86] Y. Lai, J. Huang, Z. Cui, M. Ge, K.-Q. Zhang, Z. Chen, L. Chi, Recent Advances in TiO2-Based Nanostructured Surfaces with Controllable Wettability and Adhesion, Small. 12 (2016) 2203–2224. https://doi.org/10.1002/smll.201501837.
[87] A.B.D. Cassie, S. Baxter, Wettability of porous surfaces, Trans. Faraday Soc. 40 (1944) 546–551. https://doi.org/10.1039/TF9444000546.
[88] C. Dorrer, J. Rühe, Some thoughts on superhydrophobic wetting, Soft Matter. 5 (2008) 51–61. https://doi.org/10.1039/B811945G.
[89] A. Marmur, Wetting on Hydrophobic Rough Surfaces: To Be Heterogeneous or Not To Be?, Langmuir. 19 (2003) 8343–8348. https://doi.org/10.1021/la0344682.
[90] W. Barthlott, C. Neinhuis, Purity of the sacred lotus, or escape from contamination in biological surfaces, Planta. 202 (1997) 1–8. https://doi.org/10.1007/s004250050096.
[91] H.J. Ensikat, P. Ditsche-Kuru, C. Neinhuis, W. Barthlott, Superhydrophobicity in perfection: the outstanding properties of the lotus leaf, Beilstein J. Nanotechnol. 2 (2011) 152–161. https://doi.org/10.3762/bjnano.2.19.
[92] S. Dash, M.T. Alt, S.V. Garimella, Hybrid Surface Design for Robust Superhydrophobicity, Langmuir. 28 (2012) 9606–9615. https://doi.org/10.1021/la301743p.
[93] E. Celia, T. Darmanin, E. Taffin de Givenchy, S. Amigoni, F. Guittard, Recent advances in designing superhydrophobic surfaces, J. Colloid Interface Sci. 402 (2013) 1–18. https://doi.org/10.1016/j.jcis.2013.03.041.
[94] J.T. Simpson, S.R. Hunter, T. Aytug, Superhydrophobic materials and coatings: a review, Rep. Prog. Phys. 78 (2015) 086501. https://doi.org/10.1088/0034-4885/78/8/086501.
[95] N.A. Patankar, Transition between Superhydrophobic States on Rough Surfaces, Langmuir. 20 (2004) 7097–7102. https://doi.org/10.1021/la049329e.
[96] T. Koishi, K. Yasuoka, S. Fujikawa, T. Ebisuzaki, X.C. Zeng, Coexistence and transition between Cassie and Wenzel state on pillared hydrophobic surface, Proc. Natl. Acad. Sci. 106 (2009) 8435–8440. https://doi.org/10.1073/pnas.0902027106.

[97] D. Murakami, H. Jinnai, A. Takahara, Wetting Transition from the Cassie–Baxter State to the Wenzel State on Textured Polymer Surfaces, Langmuir. 30 (2014) 2061–2067. https://doi.org/10.1021/la4049067.
[98] A. Lafuma, D. Quéré, Superhydrophobic states, Nat. Mater. 2 (2003) 457–460. https://doi.org/10.1038/nmat924.
[99] B. He, J. Lee, N.A. Patankar, Contact angle hysteresis on rough hydrophobic surfaces, Colloids Surf. Physicochem. Eng. Asp. 248 (2004) 101–104. https://doi.org/10.1016/j.colsurfa.2004.09.006.
[100] K.-Y. Yeh, L.-J. Chen, J.-Y. Chang, Contact Angle Hysteresis on Regular Pillar-like Hydrophobic Surfaces, Langmuir. 24 (2008) 245–251. https://doi.org/10.1021/la7020337.
[101] C.R. Szczepanski, F. Guittard, T. Darmanin, Recent advances in the study and design of parahydrophobic surfaces: From natural examples to synthetic approaches, Adv. Colloid Interface Sci. 241 (2017) 37–61. https://doi.org/10.1016/j.cis.2017.01.002.
[102] L. Feng, Y. Zhang, J. Xi, Y. Zhu, N. Wang, F. Xia, L. Jiang, Petal Effect: A Superhydrophobic State with High Adhesive Force, Langmuir. 24 (2008) 4114–4119. https://doi.org/10.1021/la703821h.
[103] H. Jin, Y. Li, P. Zhang, S. Nie, N. Gao, The investigation of the wetting behavior on the red rose petal, Appl. Phys. Lett. 108 (2016) 151605. https://doi.org/10.1063/1.4947057.
[104] S. Yang, J. Ju, Y. Qiu, Y. He, X. Wang, S. Dou, K. Liu, L. Jiang, Peanut Leaf Inspired Multifunctional Surfaces, Small. 10 (2014) 294–299. https://doi.org/10.1002/smll.201301029.
[105] J. Wang, Q. Yang, M. Wang, C. Wang, L. Jiang, Rose petals with a novel and steady air bubble pinning effect in aqueous media, Soft Matter. 8 (2012) 2261–2266. https://doi.org/10.1039/C2SM06705F.
[106] R.L. Webb, The Evolution of Enhanced Surface Geometries for Nucleate Boiling, Heat Transf. Eng. 2 (1981) 46–69. https://doi.org/10.1080/01457638108962760.
[107] S.G. Liter, M. Kaviany, Pool-boiling CHF enhancement by modulated porous-layer coating: theory and experiment, Int. J. Heat Mass Transf. 44 (2001) 4287–4311. https://doi.org/10.1016/S0017-9310(01)00084-9.
[108] A. Jaikumar, S.G. Kandlikar, Enhanced pool boiling heat transfer mechanisms for selectively sintered open microchannels, Int. J. Heat Mass Transf. 88 (2015) 652–661. https://doi.org/10.1016/j.ijheatmasstransfer.2015.04.100.
[109] A. Jaikumar, S.G. Kandlikar, Ultra-high pool boiling performance and effect of channel width with selectively coated open microchannels, Int. J. Heat Mass Transf. 95 (2016) 795–805. https://doi.org/10.1016/j.ijheatmasstransfer.2015.12.061.
[110] A. Jaikumar, S.G. Kandlikar, Pool boiling enhancement through bubble induced convective liquid flow in feeder microchannels, Appl. Phys. Lett. 108 (2016) 041604. https://doi.org/10.1063/1.4941032.
[111] M. Mahamudur Rahman, J. Pollack, M. Mccarthy, Increasing Boiling Heat Transfer using Low Conductivity Materials, Sci. Rep. 5 (2015). https://doi.org/10.1038/srep13145.
[112] M.M. Rahman, M. McCarthy, Boiling Enhancement on Nanostructured Surfaces with Engineered Variations in Wettability and Thermal Conductivity, Heat Transf. Eng. 0 (2016) 1–11. https://doi.org/10.1080/01457632.2016.1242961.
[113] Y. Takata, S. Hidaka, J.M. Cao, T. Nakamura, H. Yamamoto, M. Masuda, T. Ito, Effect of surface wettability on boiling and evaporation, Energy. 30 (2005) 209–220. https://doi.org/10.1016/j.energy.2004.05.004.

[114] A.R. Girard, J. Kim, S.M. You, Pool Boiling Heat Transfer of Water on Hydrophilic Surfaces With Different Wettability, (2016) V008T10A018. https://doi.org/10.1115/IMECE2016-67294.
[115] A.R. Betz, J. Xu, H. Qiu, D. Attinger, Do surfaces with mixed hydrophilic and hydrophobic areas enhance pool boiling?, Appl. Phys. Lett. 97 (2010) 141909. https://doi.org/10.1063/1.3485057.
[116] B. Bourdon, E. Bertrand, P. Di Marco, M. Marengo, R. Rioboo, J. De Coninck, Wettability influence on the onset temperature of pool boiling: Experimental evidence onto ultra-smooth surfaces, Adv. Colloid Interface Sci. 221 (2015) 34–40. https://doi.org/10.1016/j.cis.2015.04.004.
[117] H.S. Ahn, H.J. Jo, S.H. Kang, M.H. Kim, Effect of liquid spreading due to nano/microstructures on the critical heat flux during pool boiling, Appl. Phys. Lett. 98 (2011) 071908. https://doi.org/10.1063/1.3555430.
[118] K.-H. Chu, Y.S. Joung, R. Enright, C.R. Buie, E.N. Wang, Hierarchically structured surfaces for boiling critical heat flux enhancement, Appl. Phys. Lett. 102 (2013) 151602. https://doi.org/10.1063/1.4801811.
[119] C.-H. Choi, M. David, Z. Gao, A. Chang, M. Allen, H. Wang, C. Chang, Large-scale Generation of Patterned Bubble Arrays on Printed Bi-functional Boiling Surfaces, Sci. Rep. 6 (2016) 23760. https://doi.org/10.1038/srep23760.
[120] A.R. Betz, J. Jenkins, C.-J. "CJ" Kim, D. Attinger, Boiling heat transfer on superhydrophilic, superhydrophobic, and superbiphilic surfaces, Int. J. Heat Mass Transf. 57 (2013) 733–741. https://doi.org/10.1016/j.ijheatmasstransfer.2012.10.080.
[121] Q. Li, Y. Yu, P. Zhou, H.J. Yan, Enhancement of boiling heat transfer using hydrophilic-hydrophobic mixed surfaces: A lattice Boltzmann study, Appl. Therm. Eng. 132 (2018) 490–499. https://doi.org/10.1016/j.applthermaleng.2017.12.105.
[122] B. Shen, M. Yamada, S. Hidaka, J. Liu, J. Shiomi, G. Amberg, M. Do-Quang, M. Kohno, K. Takahashi, Y. Takata, Early Onset of Nucleate Boiling on Gas-covered Biphilic Surfaces, Sci. Rep. 7 (2017) 2036. https://doi.org/10.1038/s41598-017-02163-8.
[123] H. Jo, S. Kim, H.S. Park, M.H. Kim, Critical heat flux and nucleate boiling on several heterogeneous wetting surfaces: Controlled hydrophobic patterns on a hydrophilic substrate, Int. J. Multiph. Flow. 62 (2014) 101–109. https://doi.org/10.1016/j.ijmultiphaseflow.2014.02.006.
[124] A. Mukherjee, S.G. Kandlikar, Numerical study of single bubbles with dynamic contact angle during nucleate pool boiling, Int. J. Heat Mass Transf. 50 (2007) 127–138. https://doi.org/10.1016/j.ijheatmasstransfer.2006.06.037.
[125] Y. Chen, R. Mertz, R. Kulenovic, Numerical simulation of bubble formation on orifice plates with a moving contact line, Int. J. Multiph. Flow. 35 (2009) 66–77. https://doi.org/10.1016/j.ijmultiphaseflow.2008.07.007.
[126] T.P. Allred, J.A. Weibel, S.V. Garimella, Enabling Highly Effective Boiling from Superhydrophobic Surfaces, Phys. Rev. Lett. 120 (2018) 174501. https://doi.org/10.1103/PhysRevLett.120.174501.
[127] G.W. Burns, M.G. Scroger, G.F. Strouse, M.C. Croarkin, W.F. Guthrie, Temperature-electromotive force reference functions and tables for the letter-designated thermocouple types based on the ITS-90, National Bureau of Standards, 1993. http://archive.org/details/temperatureelect175burn.

[128] K. Brown, H. Coleman, W. Steele, Estimating Uncertainty Intervals for Linear Regression, in: Proc. 33rd Aerosp. Sci. Meet. Exhib., Reno, NV, 1995. https://arc.aiaa.org/doi/pdf/10.2514/6.1995-796 (accessed August 30, 2017).
[129] H.T. Phan, N. Caney, P. Marty, S. Colasson, J. Gavillet, Surface wettability control by nanocoating: The effects on pool boiling heat transfer and nucleation mechanism, Int. J. Heat Mass Transf. 52 (2009) 5459–5471. https://doi.org/10.1016/j.ijheatmasstransfer.2009.06.032.
[130] T.P. Allred, J.A. Weibel, S.V. Garimella, Control of Pool Boiling Hydrodynamics through Surface Wettability Patterning, in: Proc. 16th Int. Heat Transf. Conf., 2018.
[131] T.P. Allred, J.A. Weibel, S.V. Garimella, Mitigation of film boiling on superhydrophobic surfaces by controlling initial wetting state, Rev. (2018).
[132] T.P. Allred, J.A. Weibel, S.V. Garimella, The petal effect of parahydrophobic surfaces offers low receding contact angles that promote effective boiling, Int. J. Heat Mass Transf. 135 (2019) 403–412. https://doi.org/10.1016/j.ijheatmasstransfer.2019.02.002.
[133] Z.-G. Guo, W.-M. Liu, Sticky superhydrophobic surface, Appl. Phys. Lett. 90 (2007) 223111. https://doi.org/10.1063/1.2745251.
[134] J.Y. Park, D. Ahn, Y.Y. Choi, C.M. Hwang, S. Takayama, S.H. Lee, S.-H. Lee, Surface chemistry modification of PDMS elastomers with boiling water improves cellular adhesion, Sens. Actuators B Chem. 173 (2012) 765–771. https://doi.org/10.1016/j.snb.2012.06.096.
[135] E.W. Weisstein, Spherical Cap, (n.d.). http://mathworld.wolfram.com/SphericalCap.html (accessed May 21, 2018).
[136] Y. Li, K. Zhang, M.-C. Lu, C. Duan, Single bubble dynamics on superheated superhydrophobic surfaces, Int. J. Heat Mass Transf. 99 (2016) 521–531. https://doi.org/10.1016/j.ijheatmasstransfer.2016.03.098.
[137] P.-G. de Gennes, F. Brochard-Wyart, D. Quere, Capillarity and Wetting Phenomena: Drops, Bubbles, Pearls, Waves, Springer-Verlag, New York, 2004. https://www.springer.com/us/book/9780387005928 (accessed May 30, 2019).
[138] S.H. Kim, G.C. Lee, J.Y. Kang, K. Moriyama, H.S. Park, M.H. Kim, The role of surface energy in heterogeneous bubble growth on ideal surface, Int. J. Heat Mass Transf. 108, Part B (2017) 1901–1909. https://doi.org/10.1016/j.ijheatmasstransfer.2016.10.005.
[139] R.G. Picknett, R. Bexon, The evaporation of sessile or pendant drops in still air, J. Colloid Interface Sci. 61 (1977) 336–350. https://doi.org/10.1016/0021-9797(77)90396-4.
[140] E.B. Dussan, On the Spreading of Liquids on Solid Surfaces: Static and Dynamic Contact Lines, Annu. Rev. Fluid Mech. 11 (1979) 371–400. https://doi.org/10.1146/annurev.fl.11.010179.002103.
[141] Y.D. Shikhmurzaev, The moving contact line on a smooth solid surface, Int. J. Multiph. Flow. 19 (1993) 589–610. https://doi.org/10.1016/0301-9322(93)90090-H.
[142] H.N. Oguz, A. Prosperetti, Dynamics of bubble growth and detachment from a needle, J. Fluid Mech. 257 (1993) 111–145. https://doi.org/10.1017/S0022112093003015.
[143] I. Malgarinos, N. Nikolopoulos, M. Marengo, C. Antonini, M. Gavaises, VOF simulations of the contact angle dynamics during the drop spreading: Standard models and a new wetting force model, Adv. Colloid Interface Sci. 212 (2014) 1–20. https://doi.org/10.1016/j.cis.2014.07.004.

[144] C. Galusinski, P. Vigneaux, On stability condition for bifluid flows with surface tension: Application to microfluidics, J. Comput. Phys. 227 (2008) 6140–6164. https://doi.org/10.1016/j.jcp.2008.02.023.
[145] S.S. Deshpande, L. Anumolu, M.F. Trujillo, Evaluating the performance of the two-phase flow solver interFoam, Comput. Sci. Discov. 5 (2012) 014016. https://doi.org/10.1088/1749-4699/5/1/014016.
[146] A. Marmur, From Hygrophilic to Superhygrophobic: Theoretical Conditions for Making High-Contact-Angle Surfaces from Low-Contact-Angle Materials, Langmuir. 24 (2008) 7573–7579. https://doi.org/10.1021/la800304r.
[147] D.M. Qiu, V.K. Dhir, D. Chao, M.M. Hasan, E. Neumann, G. Yee, A. Birchenough, Single-Bubble Dynamics During Pool Boiling Under Low Gravity Conditions, J. Thermophys. Heat Transf. 16 (2002) 336–345. https://doi.org/10.2514/2.6710.
[148] V.P. Carey, Liquid Vapor Phase Change Phenomena: An Introduction to the Thermophysics of Vaporization and Condensation Processes in Heat Transfer Equipment, Second Edition, 2nd ed., Taylor & Francis, 2008. https://www.crcpress.com/Liquid-Vapor-Phase-Change-Phenomena-An-Introduction-to-the-Thermophysics/Carey/p/book/9780203748756 (accessed January 23, 2019).
[149] Z. Pan, J.A. Weibel, S.V. Garimella, A saturated-interface-volume phase change model for simulating flow boiling, Int. J. Heat Mass Transf. 93 (2016) 945–956. https://doi.org/10.1016/j.ijheatmasstransfer.2015.10.044.
[150] M.G. Cooper, A.J.P. Lloyd, The microlayer in nucleate pool boiling, Int. J. Heat Mass Transf. 12 (1969) 895–913. https://doi.org/10.1016/0017-9310(69)90154-9.
[151] S. Jung, H. Kim, An experimental method to simultaneously measure the dynamics and heat transfer associated with a single bubble during nucleate boiling on a horizontal surface, Int. J. Heat Mass Transf. 73 (2014) 365–375. https://doi.org/10.1016/j.ijheatmasstransfer.2014.02.014.
[152] T.A. Otitoju, A.L. Ahmad, B.S. Ooi, Superhydrophilic (superwetting) surfaces: A review on fabrication and application, J. Ind. Eng. Chem. 47 (2017) 19–40. https://doi.org/10.1016/j.jiec.2016.12.016.
[153] T.L. Owens, J. Leisen, H.W. Beckham, V. Breedveld, Control of Microfluidic Flow in Amphiphilic Fabrics, ACS Appl. Mater. Interfaces. 3 (2011) 3796–3803. https://doi.org/10.1021/am201003b.
[154] N.V. Bhat, A.N. Netravali, A.V. Gore, M.P. Sathianarayanan, G.A. Arolkar, R.R. Deshmukh, Surface modification of cotton fabrics using plasma technology, Text. Res. J. 81 (2011) 1014–1026. https://doi.org/10.1177/0040517510397574.
[155] D. Zahner, J. Abagat, F. Svec, J.M.J. Fréchet, P.A. Levkin, A Facile Approach to Superhydrophilic–Superhydrophobic Patterns in Porous Polymer Films, Adv. Mater. 23 (2011) 3030–3034. https://doi.org/10.1002/adma.201101203.
[156] G. Takei, M. Nonogi, A. Hibara, T. Kitamori, H.-B. Kim, Tuning microchannel wettability and fabrication of multiple-step Laplace valves, Lab Chip. 7 (2007) 596–602. https://doi.org/10.1039/B618851F.
[157] K. Tsougeni, D. Papageorgiou, A. Tserepi, E. Gogolides, “Smart” polymeric microfluidics fabricated by plasma processing: controlled wetting, capillary filling and hydrophobic valving, Lab Chip. 10 (2010) 462–469. https://doi.org/10.1039/B916566E.

[158] X. Chen, J. Wu, R. Ma, M. Hua, N. Koratkar, S. Yao, Z. Wang, Nanograssed Micropyramidal Architectures for Continuous Dropwise Condensation, Adv. Funct. Mater. 21 (2011) 4617–4623. https://doi.org/10.1002/adfm.201101302.
[159] N. Miljkovic, R. Enright, Y. Nam, K. Lopez, N. Dou, J. Sack, E.N. Wang, Jumping-Droplet-Enhanced Condensation on Scalable Superhydrophobic Nanostructured Surfaces, Nano Lett. 13 (2013) 179–187. https://doi.org/10.1021/nl303835d.
[160] S. Nishimoto, B. Bhushan, Bioinspired self-cleaning surfaces with superhydrophobicity, superoleophobicity, and superhydrophilicity, RSC Adv. 3 (2012) 671–690. https://doi.org/10.1039/C2RA21260A.
[161] Y. Lai, Y. Tang, J. Gong, D. Gong, L. Chi, C. Lin, Z. Chen, Transparent superhydrophobic/superhydrophilic TiO2-based coatings for self-cleaning and anti-fogging, J. Mater. Chem. 22 (2012) 7420–7426. https://doi.org/10.1039/C2JM16298A.
[162] Z. Guo, W. Liu, B.-L. Su, Superhydrophobic surfaces: From natural to biomimetic to functional, J. Colloid Interface Sci. 353 (2011) 335–355. https://doi.org/10.1016/j.jcis.2010.08.047.
[163] N.A. Patankar, On the Modeling of Hydrophobic Contact Angles on Rough Surfaces, Langmuir. 19 (2003) 1249–1253. https://doi.org/10.1021/la026612+.
[164] J. Drelich, E. Chibowski, D.D. Meng, K. Terpilowski, Hydrophilic and superhydrophilic surfaces and materials, Soft Matter. 7 (2011) 9804–9828. https://doi.org/10.1039/C1SM05849E.
[165] T. Liang, H. Li, X. Su, X. Lai, H. Wu, C. Wang, Y. Wang, M. Zhuang, X. Zeng, A facile fabrication of robust thiol-ene/hierarchically mesoporous silica nanoparticles hybrid superhydrophilic coating films under UV radiation, Prog. Org. Coat. 101 (2016) 423–430. https://doi.org/10.1016/j.porgcoat.2016.09.011.
[166] F.Ç. Cebeci, Z. Wu, L. Zhai, R.E. Cohen, M.F. Rubner, Nanoporosity-Driven Superhydrophilicity: A Means to Create Multifunctional Antifogging Coatings, Langmuir. 22 (2006) 2856–2862. https://doi.org/10.1021/la053182p.
[167] B. Holley, A. Faghri, Permeability and effective pore radius measurements for heat pipe and fuel cell applications, Appl. Therm. Eng. 26 (2006) 448–462. https://doi.org/10.1016/j.applthermaleng.2005.05.023.
[168] E.W. Washburn, The Dynamics of Capillary Flow, Phys. Rev. 17 (1921) 273–283. https://doi.org/10.1103/PhysRev.17.273.
[169] Y. Nam, S. Sharratt, C. Byon, S.J. Kim, Y.S. Ju, Fabrication and Characterization of the Capillary Performance of Superhydrophilic Cu Micropost Arrays, J. Microelectromechanical Syst. 19 (2010) 581–588. https://doi.org/10.1109/JMEMS.2010.2043922.
[170] C. Byon, S.J. Kim, Capillary performance of bi-porous sintered metal wicks, Int. J. Heat Mass Transf. 55 (2012) 4096–4103. https://doi.org/10.1016/j.ijheatmasstransfer.2012.03.051.
[171] D. Deng, Y. Tang, G. Huang, L. Lu, D. Yuan, Characterization of capillary performance of composite wicks for two-phase heat transfer devices, Int. J. Heat Mass Transf. 56 (2013) 283–293. https://doi.org/10.1016/j.ijheatmasstransfer.2012.09.002.
[172] S.J. Kim, M.-W. Moon, K.-R. Lee, D.-Y. Lee, Y.S. Chang, H.-Y. Kim, Liquid spreading on superhydrophilic micropillar arrays, J. Fluid Mech. 680 (2011) 477–487. https://doi.org/10.1017/jfm.2011.210.

[173] C.M. Kunkle, V.P. Carey, Metrics for Quantifying Surface Wetting Effects on Vaporization Processes at Nanostructured Hydrophilic Surfaces, in: Vol. 2 Proc. ASME 2016 Heat Transf. Summer Conf., ASME, July 10-14, 2016, Washington, DC, USA, 2016. https://doi.org/10.1115/HT2016-7203.
[174] T. Yasuda, T. Okuno, H. Yasuda, Contact Angle of Water on Polymer Surfaces, Langmuir. 10 (1994) 2435–2439. https://doi.org/10.1021/la00019a068.
[175] R. Xiao, R. Enright, E.N. Wang, Prediction and Optimization of Liquid Propagation in Micropillar Arrays, Langmuir. 26 (2010) 15070–15075. https://doi.org/10.1021/la102645u.
[176] A.S. Sangani, A. Acrivos, Slow flow past periodic arrays of cylinders with application to heat transfer, Int. J. Multiph. Flow. 8 (1982) 193–206. https://doi.org/10.1016/0301-9322(82)90029-5.
[177] H. Hu, M. Chakraborty, T.P. Allred, J.A. Weibel, S.V. Garimella, Multiscale Modeling of the Three-Dimensional Meniscus Shape of a Wetting Liquid Film on Micro-/Nanostructured Surfaces, Langmuir. (2017). https://doi.org/10.1021/acs.langmuir.7b02837.

VITA

Taylor Allred received his Bachelor of Science (BS) in 2014, his Master of Science in Mechanical Engineering (MSME) in 2018, and his doctorate (Ph.D.) in 2019, all in Mechanical Engineering from Purdue University. He completed his doctoral work under the advisement of Dr. Suresh Garimella and Dr. Justin Weibel. He was awarded the National Defense Science and Engineering Graduate Fellowship from the Department of Defense and the Perry Graduate Fellowship from the School of Mechanical Engineering at Purdue University to support his graduate education. Throughout his graduate work, he received several awards including the Nasser Grayeli Best Poster Award at InterPACK 2019 and his work was featured on the cover of the April 2018 issue of *Physical Review Letters*. His research interests focus on understanding the effects of interfacial dynamics on phase change processes. After graduating with his doctorate, he will begin his career at 3M in the Corporate Research Process Lab.

PUBLICATIONS

T.P. Allred, J.A. Weibel, S.V. Garimella, A Wettability Metric for Characterization of Capillary Flow on Textured Superhydrophilic Surfaces, Langmuir 33 (2017) 7847-7853.

H. Han, M. Chakraborty, T.P. Allred, J.A. Weibel, S.V. Garimella, Multiscale Modeling of the Three-Dimensional Meniscus Shape of a Wetting Liquid Film on Micro-/Nano-Structured Surfaces, Langmuir 33 (2017) 12028-12037

T.P. Allred, J.A. Weibel, S.V. Garimella, Enabling Highly Effective Boiling from Superhydrophobic Surfaces, Phys. Rev. Lett. 120 (2018) 174501.

S. Mancin, L. Doretti, T.P. Allred, J.A. Weibel, G. Righetti, G.A. Longo, Nanoparticle Deposition on Roughened Copper Surfaces via Nanofluid Pool Boiling, Proceedings of the 16th International Heat Transfer Conference (2018).

T.P. Allred, J.A. Weibel, S.V. Garimella, Control of Pool Boiling Hydrodynamics through Surface Wettability Patterning, Proceedings of the 16th International Heat Transfer Conference (2018).

T.P. Allred, J.A. Weibel, S.V. Garimella, The Petal Effect on Parahydrophobic Surfaces offers Low Receding Contact Angles that Promote Effective Boiling, Int. J. Heat Mass Transf. 135 (2019) 403-412.

T.P Allred, J.A. Weibel, S.V. Garimella, Roles of Receding and Advancing Contact Angles during Bubble Growth and Departure (In preparation)

T.P. Allred, J.A. Weibel, S.V. Garimella, The Effect of Dynamic Wetting Behavior on Heat Transfer Mechanisms during Single Bubble Growth (In preparation)